Fundamental Studies on Nano-composite Phase Change Materials (PCM) for Cold Storage Applications

Yaoting Huang

The University of Birmingham

School of Chemical Engineering

Sept, 2018

Abstract

Cold storage, as a sub-subject of thermal energy storage (TES), has been tracked more and more attention due to its growing application possibilities on different scenarios. These scenarios include food reservation and transportation, building air-conditioning, liquid air gasification. etc. Phase change material (PCM) has been considered as a good media in cold storage applications due to its high energy storage density, adjustable temperature range. However, PCMs work at low temperature always suffer from low thermal conductivity, low specific heat and slow freezing and melting rate, which are major properties highly related to the charge/discharge performance of a cold storage system.

In this study, carbon nanotube (CNT) was added into ethylene glycol-water mixture and salt-water mixture to formulate nano-composite PCM with -10 ^{o}C to -30 ^{o}C melting point. Rheological behaviour of all samples was investigated at different CNT concentration, different temperature, and different shear rate. The modified Krieger-Dougher (K-D) model was introduced to explain and fit the experimental viscosity data. Then, the fitting parameter of modified K-D model was used to illustrate the CNT cluster morphology, including cluster size, cluster shape and cluster inner structure.

Thermal conductivity of nano-composite PCM was measured at different CNT concentration and different temperature. The CNT cluster effect was considered to explain the thermal conductivity enhancement mechanism. Firstly, the effective thermal conductivity of one individual CNT cluster was calculated by using Nan's equation with the cluster information from rheological analysis. Then, the effective thermal conductivity of CNT cluster and effective concentration of CNT cluster was applied in Hamilton-Crosser (H-C) model to predict the overall thermal conductivity. The predicted thermal conductivity was approved to show good consistence with the experimental data.

Other thermophysical properties including melting point, specific heat, latent heat and supercooling degree were investigated as well. Conclusions can be drawn that: CNT shows negligible effect on the melting point; specific heat and latent heat decreases linearly with CNT concentration; supercooling degree decreases when CNT concentration increases, but the exact value depends on the method of measuring.

Freezing process was observed under a microscope with temperature control stage. Then, the crystallization rate was calculated. One can see that the appearance of CNT cluster helps accelerating the crystallization rate in salt-water PCM. Also, temperature plays an important role in freezing process. The higher the difference between the temperature and the melting point, the slower the crystallization rate was observed. This phenomenon can be contributed to high viscosity and low Brownian motion at low temperature, which constrain the self-diffusivity of molecular, thus limit the molecular transfer from liquid to solid state.

Acknowledgement

Firstly, I would like to express my special gratitude and thanks to my supervisor, Professor Yulong Ding for accepting me as his PhD student at the beginning, which gave me opportunity to study in UK. Then, I would like to thank for his patience and kind guidance when I ran into the bottleneck, and for supporting me generously when I had trouble in life. Also, I would like to thank the numerous efforts Professor Yulong Ding have made on revising my thesis. I could not have imagined a more conscientious and selfless person to be my Ph.D supervisor.

I would also like to express my appreciation to my co-supervisor, Dr. Yongliang Li, for sharing his experience on keeping balance between doing and thinking, especially when I was distracted by rapidly changing research objectives and ideas inside my brain.

Besides my supervisor and co-supervisor, I would like to thank my thesis examiner: Dr. Jason Zhang and Dr. Wuge Briscoe, for their insightful comments and encouragement, but also for the hard questions which spurred me to widen my research from various perspectives.

Then, I would like to thank my colleagues for all the inspiring ideas we have come up with, for all the efforts we have made working together, and for all the fun we have had in the last four years.

Last but not the least, I would like to thank my family: my parents and my wife for supporting me spiritually throughout writing this thesis and taking care my life with all their love.

Contents

List Of Figures

List Of Tables

List Of Symbols

C	Specific heat (J/g • K)
m	Mass (g)
T	Temperature (^{o}C)
T_m	Melting point (^{o}C)
T_f	Freezing point (^{o}C)
ΔT	Supercooling degree (^{o}C)
t	Time (s)
L	Latent heat (J/g)
k	Thermal conductivity (W/m • K)
a	Thermal diffusivity (m^2/s)
ρ	Density (g/cm^{-3})
η	Dynamic viscosity (mPa • s)
$\dot{\gamma}$	Shear rate (s^{-1})
k_B	Boltzmann constant (J/K)
v	Velocity (m/s)
l	Mean free path (m)
v	Crystal growth rate (μm/s)
φ	Particle volume fraction (Vol %)
φ_{in}	Particle concentration in the cluster
n	Shape factor

D	Fractural index
φ_m	Maximum packing fraction
R	Effective cluster size
r_a	Radius of particle cluster
r	Radius of primary particle
Pe	Peclet number

1 Introduction

1.1 Background

Growing concerns over increased greenhouse gas (GHG) emissions and climate change have triggered attempts to conserve energy at every step of global technological and economic developments. A key step in addressing this is the use of renewable energy sources. The major challenge for this step is the intermittency and fluctuation of energy sources. As a result, scientists, engineers, industrialists, and technologists across the globe have been developing energy-efficient and cost-effective technologies for bridging the gap between the energy supply and end-use energy requirements.

Thermal energy storage (TES) is one of the potential technologies to store (time-shift) and redistribute the energy to meet the less predictable end-user energy demands. The basic concept of TES, wherein the term thermal refers to either heat or cold, is depicted in Fig 1-1. In normal operation, a heat source provides energy to end users directly and a portion of the energy is often wasted during transfer, transport and transformation. The integration of TES on intermediate between heat source and end users

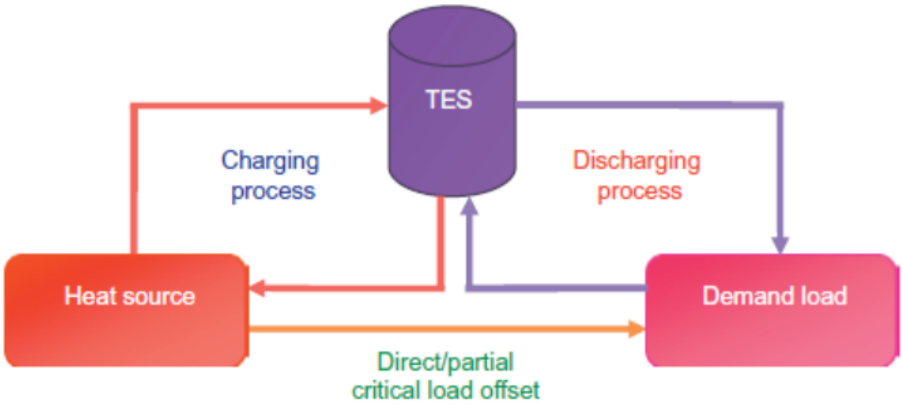

Fig 1-1 The principal and typical operational mode of a TES system.

has the potential to reduce significantly waste of useful thermal energy and hence minimize GHG emissions.

Typically, during off-peak periods, the heat source supply can far exceed the end-user demands. The excess of thermal energy is stored in the TES device which is called the charging process. During peak hours, the energy supply can not meet the end-user demand, the stored thermal energy is retrieved from the TES devices to make up the difference. This is termed discharging process. By incorporating a TES with conventional energy supply systems, the time shift and redistribution of the energy can be effectively achieved. This in turn enables the heat supplier to operate at the nominal capacity and thereby helps enhance energy efficiency, operational performance, and costs.

TES technologies can be divided into three major categories of sensible thermal energy storage (STES), latent thermal energy storage (LTES) and thermochemical energy storage (TCES). The STES works by raising the temperature of a storage material, and the amount of stored thermal energy depends on the specific heat of the storage material, the temperature change during charging/discharging process and the mass of the storage material. This can be quantified by:

$$Q = \int_{T_i}^{T_f} mc_p \, dT \qquad 1\text{-}1$$

where m, c_p, T_f and T_i are the mass, specific heat, final temperature and initial temperature of the storage material, respectively. The LTES works by storing/releasing heat when the storage material undergoes a phase change process, e.g. from solid to liquid or vice versa. Such materials are often termed as phase change materials (PCMs). Different from the STES, the temperature of PCMs is almost constant during the phase change process. Like the STES process, the thermal energy storage capacity of PCMs also depends on the temperature difference if the initial and final temperature of the process alter from the phase change temperature. And in this case, the storage capacity is the sum of both latent heat during

phase change process and the sensible heat caused by the difference between final and initial temperature during the energy storage process. This can be quantified by:

$$Q = \int_{T_i}^{T_{pc}} mc_p \, dT + mH_{pc} + \int_{T_{pc}}^{T_f} mc_p \, dT \qquad 1\text{-}2$$

where T_{pc} and H_{pc} are the phase change temperature and the latent heat of the phase change, respectively. The TCES makes use of reversible reaction and/or sorption processes in which thermal energy is absorbed or released due to breaking or reforming molecular bonds. The thermal energy storage capacity of TCES materials depends on the mass of chemical components, the endothermic/exothermic heat of reaction and the extent of the reaction.

Of these TES technologies, LTES is particularly attractive due to high energy storage density and constant temperature during phase change. However, several technological challenges need to be addressed to bring PCMs to wide industrial applications. Among the challenges, low thermal stability, corrosion, limited crystallization rate and high costs are regarded as the most important factors for industrial uptake of PCM technologies.

1.2 Aims and objectives

The primary aim of work presented in this thesis is to address some of the challenges outlined above. More specifically, this work is to study the thermophysical properties and the phase change behaviour of EG-water and Salt-water based PCMs for cold storage applications, and to investigate the role nano-additives play on the thermophysical properties and the phase change processes. These objectives are detailed in the following:

i) To understand how the composition of base PCMs and concentration of nano-additives affect heat transport properties including thermal conductivity and viscosity.

ii) To understand how the composition of base PCMs and concentration of nano-additives affect heat storage behaviour including melting enthalpy, specific heat and solidification and melting behaviour.

1.3 Methodologies

A combined experimental work and theoretical analysis is used in this work. The experimental work is mainly to investigate thermophysical properties and the phase change behaviour, whereas the theoretical analyses are to establish relationship between concentration of nano-additives and thermal energy storage behaviour and also to interpret the experimental observations.

1.4 Layout of the thesis

This thesis is organised into seven chapters as briefly outlined in the in following:

Chapter two provides a detailed literature review relevant to this work.

Chapter three details the sample preparation and experimental methods.

Chapter four presents the results on thermal conductivity and rheological behaviour of nano-composite PCMs and analyses of the results.

Chapter five provides the results on the melting enthalpy, specific heat, supercooling and crystallization of nano-composite PCMs, and analyses of the experimental results.

Finally chapter seven summarises the main conclusions and gives recommendations for future work.

2 Literature review

PCMs are clearly the most important part of LTES technologies. An ideal PCM should have appropriate thermophysical properties to meet practical applications. These properties includes thermal conductivity, specific heat and latent heat of fusion. The PCM should also have appropriate kinetics during phase change, e.g. nucleation and growth rates, supercooling degree. In addition, chemical properties and economics need also to be considered during material screening stage for large scale industrial applications.

As a subcategory of PCMs, the above criteria are also applicable for cold storage PCMs, and the literature review is focused on these properties and is organised as follows:

a) PCMs for sub-ambient applications

b) Formulation and production of well dispersed nano-composite PCMs

c) Thermal conductivity of nano-composite PCMs

d) Rheological behaviour of nano-suspensions

e) Melting enthalpy, specific heat and crystallization/solidification of nano-composite PCMs

2.1 Phase change materials for sub-ambient temperature applications

In this thesis, cold storage PCMs refers to materials that melts/freezes at a temperature below zero degree Celsius and are mainly used for sub-zero temperature applications, see Fig 2-1. Typical cold storage PCMs include ice, eutectic salt solutions, alcohol solutions, paraffin, alkanone and their multi – component mixtures[1]. These cold storage PCMs have very different physical and chemical

characteristics due to different molecular structure and compositions. The radar charts shown in Fig 2-2 compares major properties of eutectic water-salt PCMs, non-eutectic organic PCMs and ideal PCMs, respectively. It is obvious that typical water-salt solution takes the advantages of high latent heat, high thermal conductivity, high density and non-flammability. However, it suffers from high corrosivity and high supercooling degree. Compared with water-salt PCM, organic PCM has relatively lower harm of corrosion and supercooling degree, but the thermal conductivity and latent heat are sacrificed at the same time. From comparison , one can find that each type of PCM has its own merits and drawbacks, thus leads to the difficulty of formulating an all-purpose PCM.

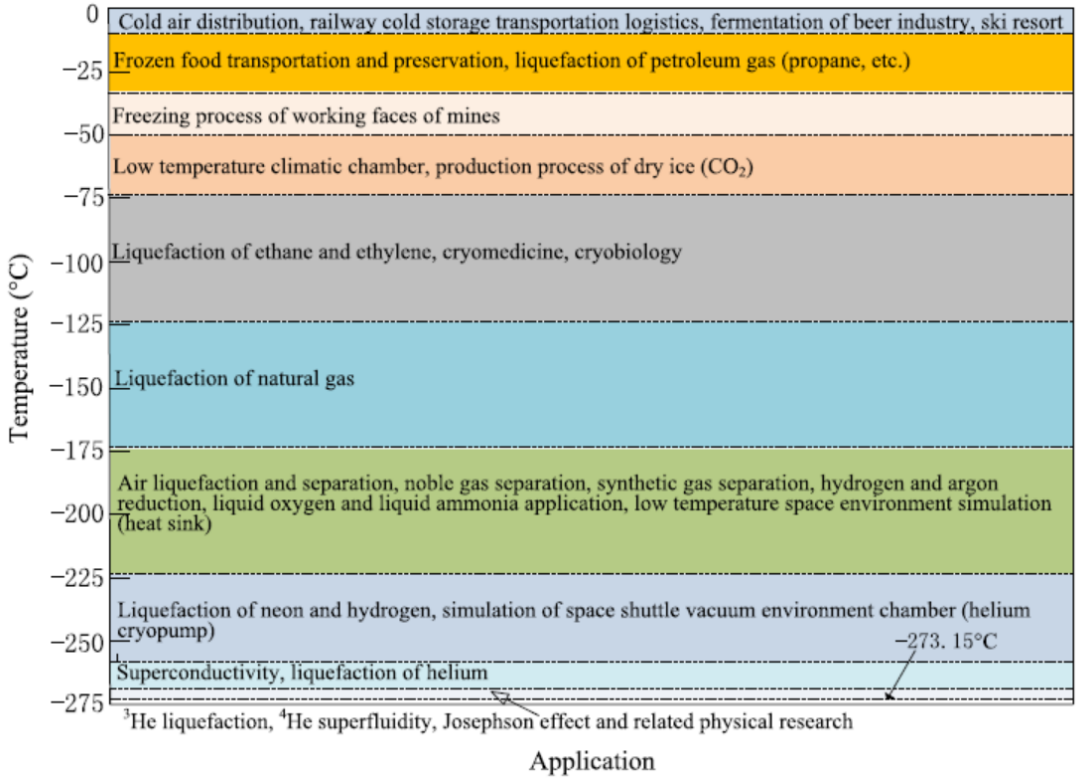

Fig 2-1 Classification of applications of PCMs with different sub-zero phase change temperatures. [1]

This work focuses on water based cold storage PCMs because of their relatively higher latent heat, thermal conductivity, and specific heat, and better chemical stability. More Specifically, eutectic water-salt solutions and water-ethylene glycol (EG) mixtures are chosen for the work.

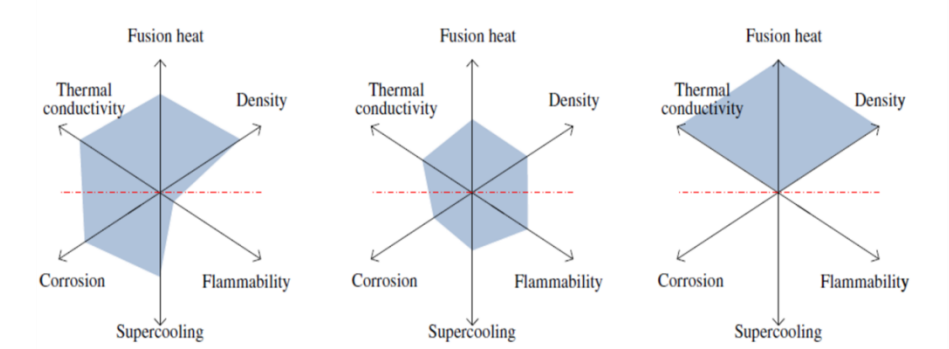

(a) Eutectic water-salt PCM (b) Non-Eutectic organic PCM (c) Ideal PCM

Fig 2-2 Comparison of properties of different PCMs.[1]

2.1.1 Cold storage PCMs: eutectic water-salt solutions

An eutectic water-salt solution is a mixture of water and salt, in particular proportion providing a certain melting/freezing point. By adding a salt the freezing point of water can be depressed and the extent of the depression depends on the concentration of the salt added. Fig 2-3 shows an illustrative relationship between the freezing point and the salt concentration of the water/salt mixture. This figure is often called a phase diagram. In the phase diagram, the freezing curve (solid line MPN) and the dotted line passing through point P parallel to the horizontal axis divides the phase diagram into four zones. The freezing point reduces with increasing salt concentration until the so-called eutectic point P, the lowest

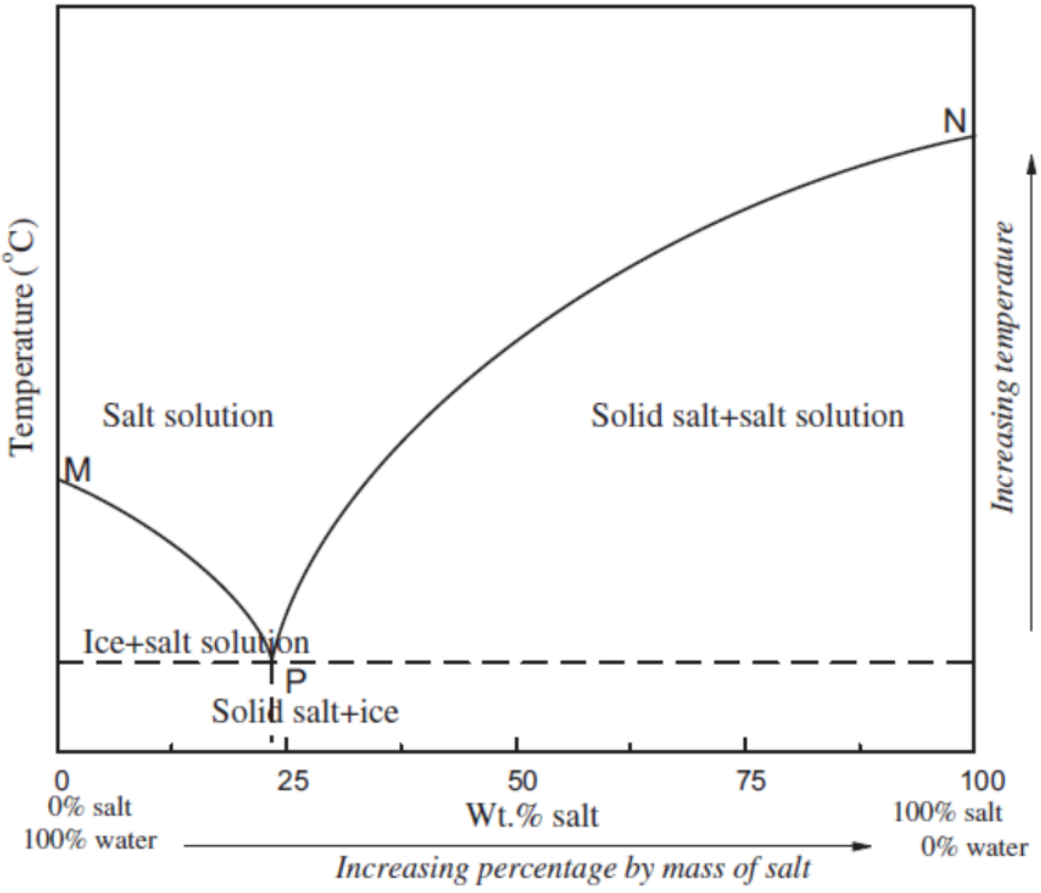

Fig 2-3 Phase diagram for a water-salt mixture.

point on curve MNP, is reached, and beyond which the freezing point increases with increasing salt addition. Theoretically, at the eutectic concentration of the salt, the solution freezes or melts completely at a constant temperature with the cold/hot energy stored or released.

Table 2.1 gives the thermal properties of some typical eutectic water-salt solutions[1]. These PCMs are considered likely suitable candidates for various potential cold storage applications at different temperatures with fairly high latent heat of fusion.

Most cold storage applications of eutectic water-salt PCMs have been investigated with an aim to improve the efficiency of performance of freezers. For example, as early as 1989, Onyejekwe et al. [2] studied the possibility of using eutectic water salt solutions as a PCM on domestic freezers. In their study, $NaCl+H_2O$ was packed and installed in a domestic freezer, and the optimal performance of the cold storage system was investigated by taking into account the volume of the PCM and geometric configuration of the PCM container. Azzouz et al. [3] developed a dynamic mathematical model of the refrigeration system in the presence of an eutectic salt water PCM with a phase change temperature ranging from -9 ℃ to 0 ℃. They claimed that by the incorporation of PCM on the back of the evaporator, as shown in Fig 2-4, they could achieve a higher evaporating temperature and hence a higher coefficient of performance of refrigeration. Later, they [4] conducted an experimental study of the performance of a PCM imbedded household refrigerator. The PCM they used was also an eutectic water salt mixture with a melting temperature of -3 ℃. The results showed an enhancement of the system performance and a reduction of the temperature fluctuation in the refrigerated cell. Gin et al.[5] used NH_4Cl and water (19.5/80.5 wt. %) as a PCM with -15.4 ℃ melting point to maintain a stable temperature in a freezer. They found that the energy consumptions during defrost cycles and door openings could be decreased by 8% and 7% respectively by using the PCM.

The effect of the use of PCM on temperature stability in refrigerated cells has also been a subject of significant research . Gin et al studied[6] the temperature fluctuation in a freezer with and without PCM. They found that the temperature was kept closer to the steady operation temperature of the PCM imbedded freezer, which gave better quality ice cream during a power loss period. Oro et al[7] performed a similar study on the performance of a freezer using PCMs under door opening and power failure scenarios. In their study, a commercial PCM (eutectic of Na_2NO_3 and water) with -18 ^oC melting point was selected. The experimental data showed that the PCM could maintain interior freezer temperature almost constant for a long period when electrical power was cut off and reduce the temperature fluctuation caused by opening doors.

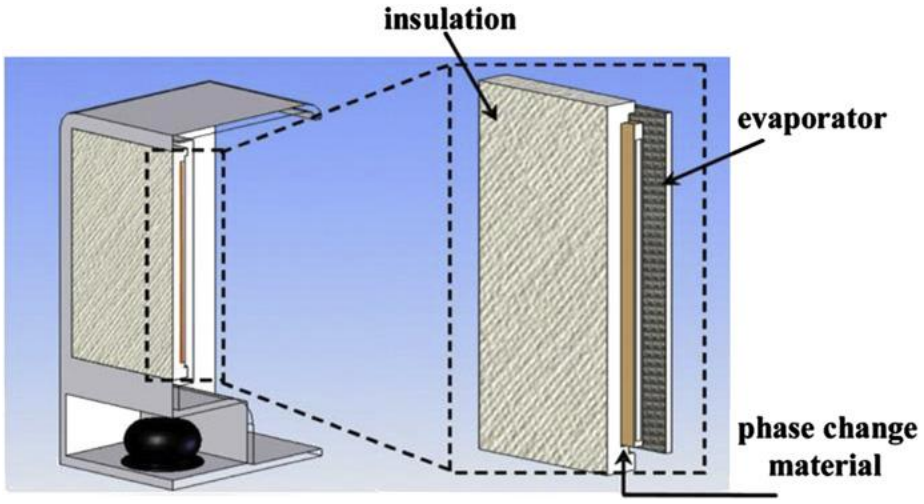

Fig 2-4 Schematic presentation of a refrigerator with a PCM. [3]

Table 2.1 Thermal properties of some selected eutectic water-salt solutions. [1]

Eutectic salt-water	Salt concentration (wt. %)	Eutectic temperature (℃)	Latent heat of fusion (kJ/kg)
$ZnCl_2/H_2O$	51	-62	116.84

$FeCl_3/H_2O$	33.1	-55	155.52
$CaCl_2/H_2O$	29.8	-55	164.93
$CuCl_2/H_2O$	36	-40	166.17
K_2CO_3/H_2O	39.6	-36.5	165.36
$MgCl_2/H_2O$	22	-33.6	221.88
$Al(NO_3)_2/H_2O$	30.5	-30.6	207.63
$Mg(NO_3)_2/H_2O$	34.6	-29	186.93
$Zn(NO_3)_2/H_2O$	39.4	-29	169.88
NH_4F/H_2O	32.3	-28.1	187.83
$NaBr/H_2O$	40.3	-28	175.69
KF/H_2O	21.5	-21.6	227.13
$NaCl/H_2O$	22.4	-21.2	228.14
$(NH_4)_2SO_4/H_2O$	39.7	-18.5	187.75
$NaNO_3/H_2O$	36.9	-17.7	187.79
NH_4NO_3/H_2O	41.2	-17.35	186.29
$Ca(NO_3)_2/H_2O$	35	-16	199.35
NH_4Cl/H_2O	19.5	-16	248.44
K_2HPO_4/H_2O	36.8	-13.5	197.79
$Na_2S_2O_3/H_2O$	30	-11	219.86
KCl/H_2O	19.5	-10.7	253.18
$MnSO_4/H_2O$	32.2	-10.5	213.07

NaH_2PO_4/H_2O	32.4	-9.9	214.25
$BaCl_2/H_2O$	22.5	-7.8	246.44
$ZnSO_4/H_2O$	27.2	-6.5	235.75
$Sr(NO_3)_2/H_2O$	24.5	-5.75	243.15
$KHCO_3/H_2O$	16.9	-5.4	268.54
$NiSO_4/H_2O$	20.6	-4.15	258.61
Na_2SO_4/H_2O	12.7	-3.55	284.95
NaF/H_2O	3.9	-3.5	314.09
$NaOH/H_2O$	19	-2.8	265.98
$MgSO_4/H_2O$	19	-3.9	264.42
KNO_3/H_2O	9.7	-2.8	296.02
Na_2CO_3/H_2O	5.9	-2.1	310.23
$FeSO_4/H_2O$	13.04	-1.8	286.81
$CuSO_4/H_2O$	11.9	-1.6	290.91

Although the benefits of eutectic water-salt based PCMs have been demonstrated in cold storage applications both by experimental and by numerical studies, there are several drawbacks for this type of PCMs including as phase separation, supercooling and corrosion. Practically implementation of the eutectic water-salt based PCMs requires these challenges to be addressed.

2.1.2 Cold storage PCMs: Alcohol solutions

Different from eutectic water-salt based PCMs, alcohol solutions consist of organic compositions. For cold storage in subzero applications, alcohols have been mainly used as freezing point depressants in ice slurry storage system for supermarkets, industry refrigeration, etc. Due to the freezing point depression phenomenon of adding alcohols into water, these type of solutions could be potential PCMs for cold storage applications. Hagg [8]studied effect of the concentration of different alcohols on the freezing point and their results are shown in Fig 2-5. It can be found that different alcohols give a different extent freezing point depression, and thus meet different cold storage requirements.

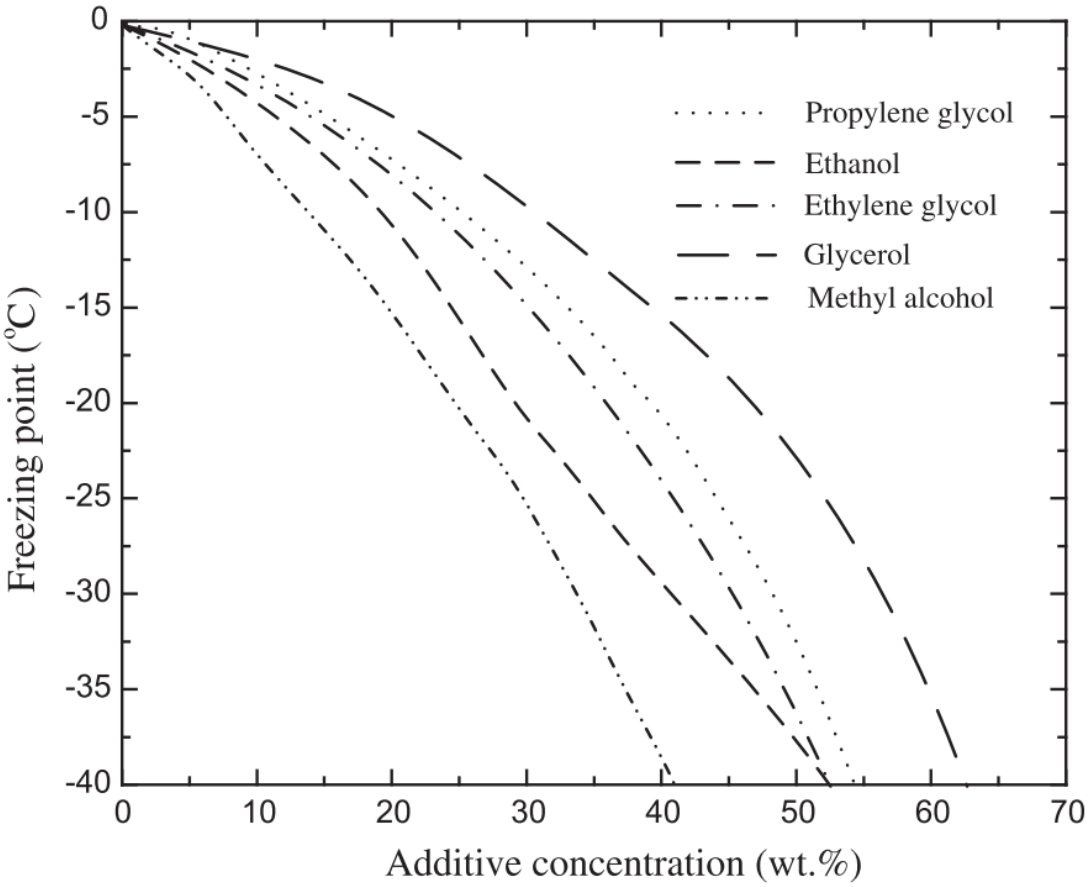

Fig 2-5 Freezing point curves of different alcohols. [8]

Kumano[9] studied the relationship between the degree of freezing point depression and the latent heat of different alcohol solutions. Their results are reproduced in Fig 2-6, which shows that the latent heat

decreases with a decreasing freezing point, and the ethylene glycol solution gives the highest latent heat among the three solutions for a given freezing point.

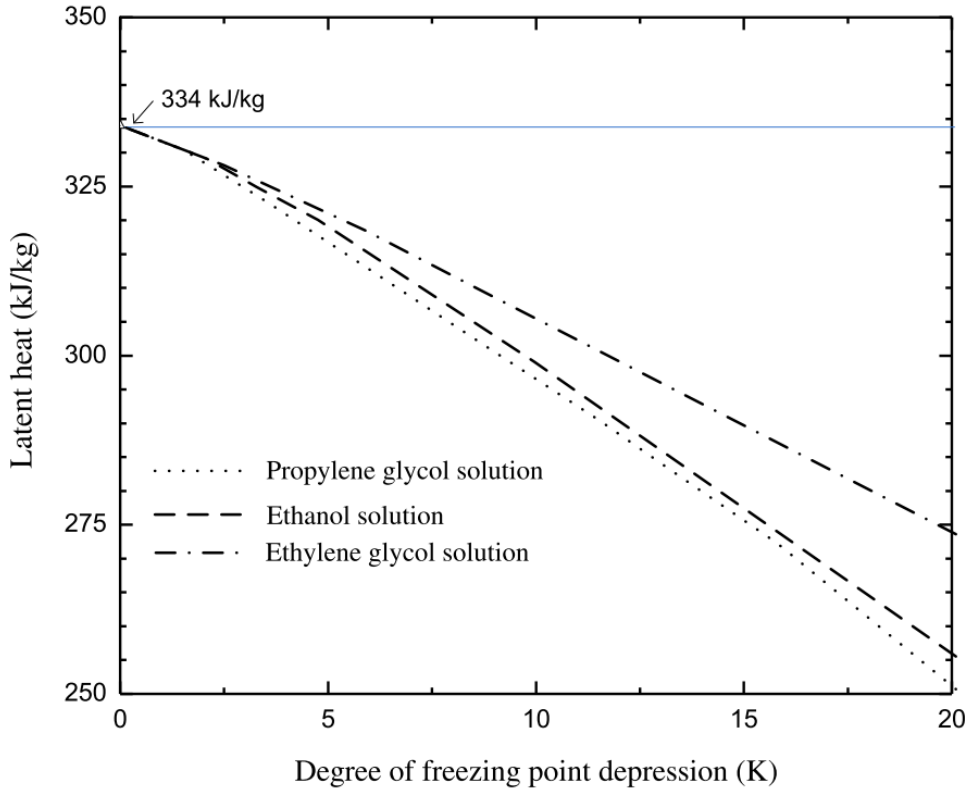

Fig 2-6 Latent heat of different alcohol solutions. [9]

2.2 Formulation of nano-suspensions of PCMs

Recent years have witnessed an increased interest in the emerging nanoscience and nanotechnology areas. Such areas focus on the science and technology related to materials with a characteristic dimension below 100 nm. The properties of these nanoscale materials can be significantly different from their in bulk counterparts, providing great potential for the enhancement of material properties through tailoring the size. More specifically, in thermal energy storage field, the possible applications of nano-composite PCMs are enormous due to their favorable thermophysical properties achieved by embedding nanostructured materials with PCMs.

The nano-composite PCMs can be divided into three major categories of nano-suspension based PCMs, nano-matrix based PCMs and nano-encapsulated PCMs. Fig 2-7 illustrates schematically these materials..

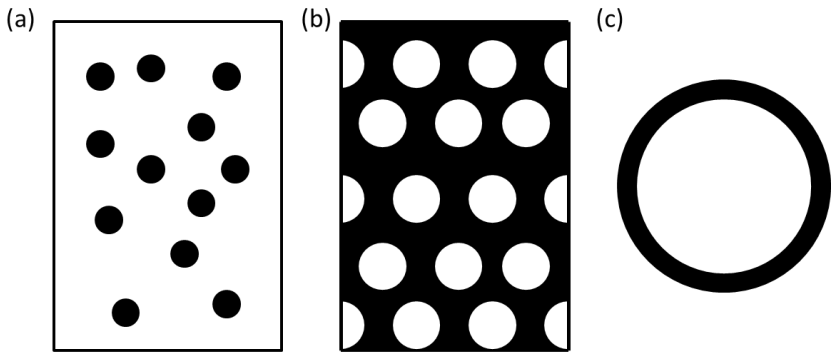

Fig 2-7 Schematics of (a) nano-suspension based PCMs, (b) nano-matrix based PCMs, (c) nano-encapsulated PCMs.

The nano-suspension based PCMs consist of a base liquid with nanomaterials such as nano-particles, nano-tubes and nano-sheets dispersed in the liquid. Nanomaterials in such suspensions properly act as thermal enhancers to improve the performance of thermal energy storage and release processes. The base fluids are made from PCMs to store latent heat. The nano-matrix based PCMs consist of PCMs embedded with a nano-matrix with nano-pores or nano-channels. The nano-encapsulated PCMs have core/shell structure with core being a PCM and shell a polymer in solid state. This work focuses on nano-suspension based PCMs.

2.2.1 Formulation method of nano-suspension based PCMs

Preparing a stable and durable nano-suspension based PCMs is the prerequisite for all potential applications. There are a number of methods for producing such suspensions and they can be divided into two categories of single-step and two-step method.

In single-step method, nanoparticle manufacturing and nano-suspension preparation steps occur simultaneously, which could be continuously. An example of such method is that nanoparticles are

directly produced by physical vapor deposition (PVD), and the in-situ prepared nanoparticles enter the flowing base fluid, forming nanofluids. Fig 2-8 shows schematically the process .

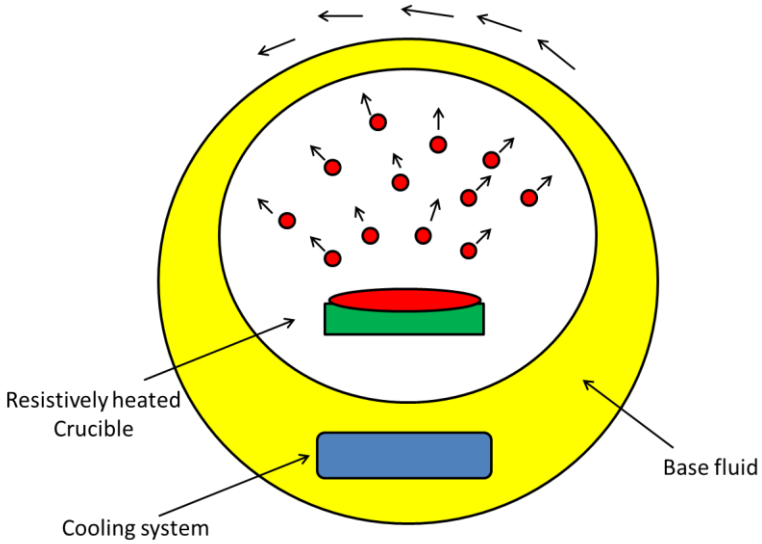

Fig 2-8 Schematic diagram of the single-step nano-suspension production system.

The method used by Akoh et al.[10] in 1978 is a one-step method for producing extremely fine particles, though that is called VEROS (Vacuum Evaporation on Running Oil Substrate) and is shown in Fig 2-9. They claimed that the production rate is several times faster than that of the conventional gas-evaporation method. Later, Eastman et al.[11] modified the VEROS method, and produced Cu nanoparticles in oil with excellent stability. Lo et al.[12] developed a Submerged Arc Nanoparticle Synthesis System (SNSS) to produce nano-suspensions. Such a method involves heating a pure metal rod to melt and vaporize by a submerge arc to a high temperature between 6000 and 12000 ℃. The authors claimed that the SANSS method has advantages of avoiding nanoparticle agglomeration and producing uniform dispersion of nanoparticles.

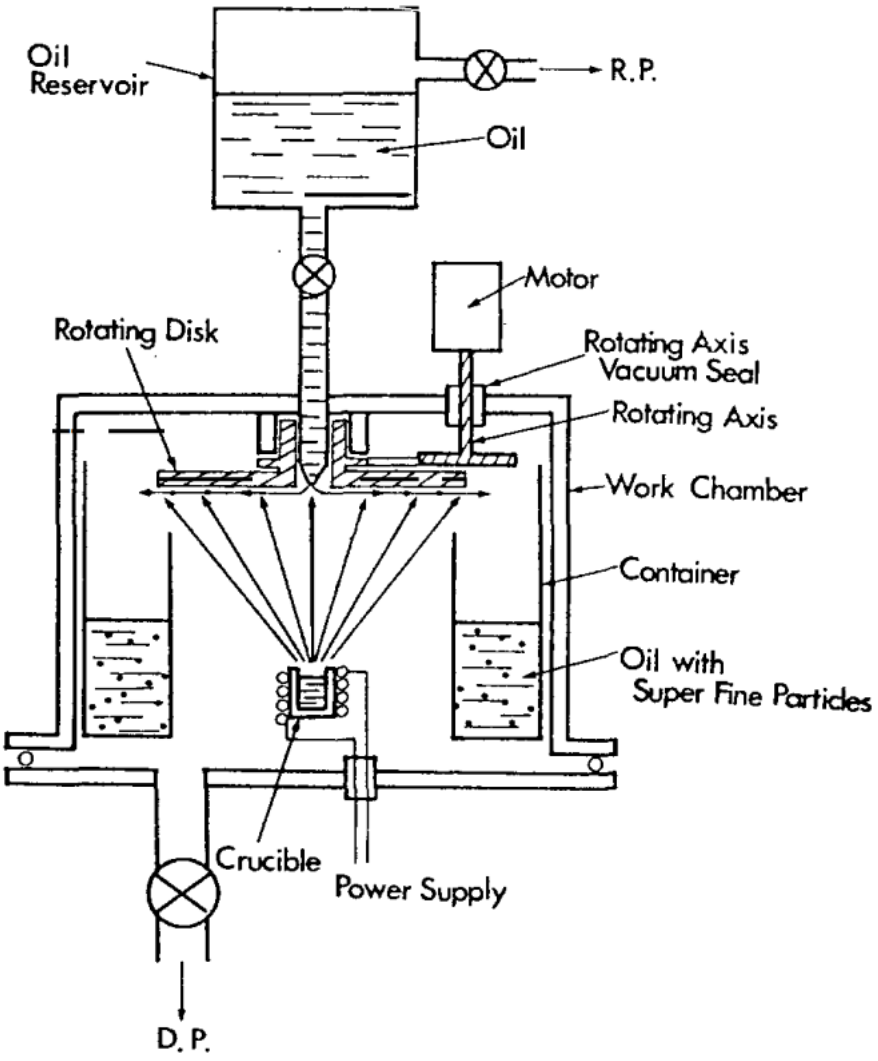

Fig 2-9 A schematic diagram of the VEROS method. [10]

In two-step method, dry nanomaterials are produced first followed by dispersion of the particles. This two-step method is most widely used for the producing nano-suspensions. An unavoidable issue of the two-step method is the aggregation and agglomeration of nanoparticles due to high surface energy of nanoparticles. The aggregation and agglomeration issue makes the redispersion step difficult and later on sedimentation of the aggregated particles if they cannot be broken. As a result, a considerable amount of effort has been made to re-dispersing the agglomerated and aggregated nanoparticles, particularly by ball milling[13]–[21], high shear homogenization[22]–[24], high pressure

homogenization[25], [26] and ultrasonication[27]–[37]. To obtain high quality suspensions, often two or more of the above methods are used in sequence [38]–[42].

So far, a varieties of nanomaterials have been successfully dispersed in different base fluids. Table 2.2 shows a list. This list is incomplete, which aims to show the types of base fluid and nanomaterial used, size range, and concentration range.

Table 2.2 Examples of nanofluids reported in the literature.

Particle	Base fluid	Size	Concentration	Surfactant	Reference
Cu	Water	25 nm	0.0005-0.5 wt.%	SDBS and CTAB	[43]
Al2O3	Water	20 nm,	0.5, 1.0 and 3.0 wt.%	Chitosan	[44]
TiO2	water	21 nm	0.2-2.0 vol.%	CTAB	[45]
MCNTs	water	10-30 nm	0.2 wt.%	Triton X-100	[46]
MCNTs	water	10-20 nm	1.0 wt.%	Gum Arabic	[47]
Fe3O4	water	15-22 nm	0.025-53.0 vol.%	Tetramethylammoniumhydroxide	[48]

2.2.2 Stability of nano-suspensions and inter-particle forces.

Long term stability of nano-suspensions is one of the most important prerequisite for their utilization in thermal energy storage and heat transfer intensification. Yu et al[49] suggested that a good stability mean the nanoparticles aggregate and precipitate at a unnoticeable rate. This is insufficient as there is a lack of time scale in their consideration. This time scale should be relative to the storage time. Aggregation of nanoparticles may deteriorate or enhance the apparent thermophysical properties of the

nano-suspensions. This would, consequently, affects the benefits of nano-suspensions in practical applications. As a result, optimization of the structures of nanoparticles may be needed.

According to DLVO theory[64–66], the stability of a nano-suspension is determined mainly by two inter-particle forces between nanoparticles. One is an attractive force termed van der Waals forces, and the other one is a repulsive force due to electrostatic actions. Fig 2-10 shows schematically the principal of the DLVO theory for two particles, where V_A, V_R and V_T indicates van der Waals attractive potential, electrical double later repulsive potential and the total potential, respectively. One can see three zones from the figure: the primary minimum, the primary maximum and the secondary minimum.

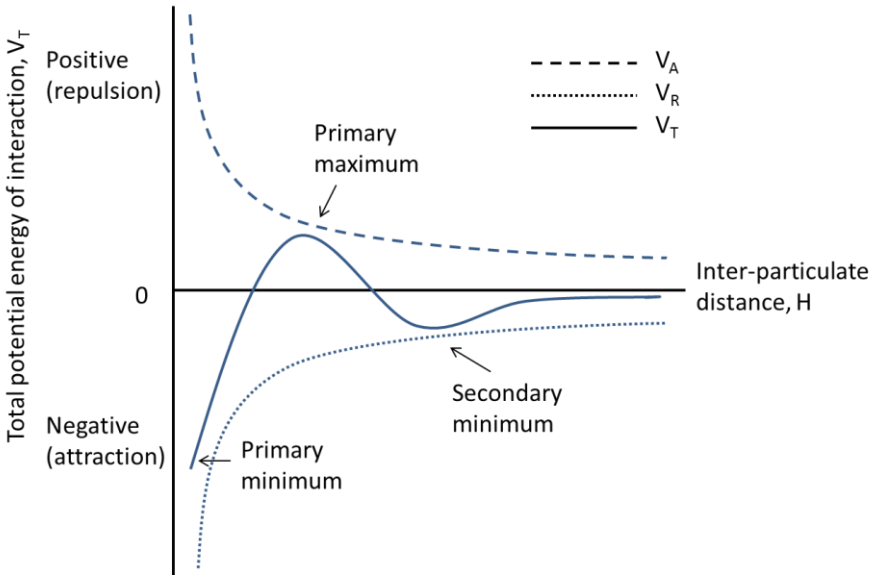

Fig 2-10 Energy interaction between two particles in DLVO theory.

The behavior of the particles depends on the inter-particle distance. For example, if the two particles are very close, so they are in primary minimum area, the total energy is far below zero, indicating a strong attractive force between the particles, and hence a high probability of aggregation. If the particles have a separation distance corresponding to the primary maximum area, the repulsive force overwhelms the attractive force leading to a stable suspension. Note that the primary maximum area is

not a necessary stable zone for suspensions, they can slide to the left side to the primary minimum area when suspended particles are subject to high external kinetic actions that can overcome the total repulsive potential energy barrier. In secondary minimum area, particles could stick to each other forming a loose aggregates, such weak aggregates could be fairly easily broken by external forces.

Apart from the above discussed DLVO forces, non-DLVO forces could also play an important role in the suspension stability[67–72]. This has been a subject of numerous studies. These studies are mainly through modelling , which can be divided into hydration force[73–95], hydrophobic force[96–101] and steric force[102–108]. To summarize all the interaction force between particles in colloidal system, Liang et al. [95] gave comprehensive review on the area covering both DLVO and non-DLVO aspects. Table 2.3 gives some major characteristics of interaction forces between nanoparticles, which are highly relevant to this study.

2.2.3 Stability enhancement methods.

As discussed above, the stability of a nano-suspension depends on the properties of both the nanoparticles, and the base fluid. It is normally easy to disperse hydrophilic particles, (e.g. some metal oxide particles) into polar basefluid (e.g. water). Dispersing hydrophobic particles into water, however, presents challenges because the total repulsive forces between particles may not strong enough to overcome their attractive forces, leading to the formation of aggregation and sedimentation.

To improve the stability, surfactants are often introduced to modify the surface of nanoparticles. The surfactants have functional groups which interacts with nanoparticle surfaces, could increase the repulsive forces between nanoparticles.

Table 2.3 Interaction forces between nanoparticles. [95]

Interaction force	Van der Waals	Electrical double layer	Hydration	Hydrophobic	Steric
Interaction distance	50-100 nm	5-30 nm	10 nm	10 nm	20-200 nm
Type of force	attractive	repulsive	attractive	attractive	repulsive
Interaction energy	$\frac{AR}{12H}$ [1]	$2\pi\varepsilon_a R\varphi_0^2 \ln[1+e^{-\kappa H}]$ [2]	$\pi R h_0 V_1 e^{-\frac{H}{h_0}}$ [3]	$\pi R h_0 V_2 e^{-\frac{H}{h_0}}$ [4]	$\frac{4\pi\kappa T C^2}{3V} \times \left(\frac{1}{2}-\chi\right) \times \left(h-\frac{H}{2}\right)^2 \times \left(3R+2h+\frac{H}{2}\right)$ [5]

[1] A: Hamaker constant.

[2] ε_a: dielectric constant; φ_0 : surface potential of particles; κ: reciprocal of Debye length.

[3] h_0: decay constant; V_1: hydration constant.

[4] V_2: hydrophobic constant.

[5] κ: Boltzmann constant; C: concentration of absorbent; h: thickness of the steric layer; χ: Flory-Huggins interaction parameter.

The surfactants can be divided into three categories according to the charge state of their functional groups: cationic surfactant (positively charge), anionic surfactant (negatively charge) and non-ionic surfactant (neutral). Table 2.4 shows some typical surfactants used in the nano-suspension preparation. Fig 2-11 illustrates how surfactants work to enhance the suspension stability. When particles absorb ionic surfactants molecules on their surface as shown in Fig 2-11 (a), one end of the surfactant molecules attaches to the surface of the particles, whereas the other end with a different charge extends to the base fluid. In this thesis, anionic surfactant SDS was used to enhance the stability of MCNT in EG-water based nanofluids. The hydrophobic chain of SDS was attached to the MCNT surface due to the effect of hydrophobic absorption, while the hydrophilic head was exposed to the water based fluids.

Table 2.4 Some typical surfactants used in the nano-suspension preparation.

Type	surfactant	reference
Anionic	Sodium dodecylbenzene sulphonate (SDBS), sodium dodecylsulphate (SDS), Ammonium lauryl sulphate (ALS), Potassium lauryl aulphate (PLS), Sodium stearate, etc	[110–116]
Cationic	Cetyl trimethyl ammonium bromide (CTAB), dodecyl trimethyl ammonium bromide (DTAB), Cetrimonium chloride, etc	[117–118]
Non-ionic	Gum Arabic (GA), poly vinyl pyrrolidone (PVP), Tween 80, Oleic acid, etc	

A diffuse layer of opposite charged ions therefore forms around the particles, providing additional repulsive force between particles upon approaching each other. The thicker the electrical layer, the stronger the repulsive force among the particles, and hence an enhanced stability due to the use of

surfactants. The use of non-ionic surfactants can also enhance the suspension stability. This works due to steric forces as illustrated in Fig 2-11 (b). Non-ionic surfactants are polymers that have large molecular weight and long polymeric chains. When particles absorb non-ionic surfactant molecules on their surfaces, the polymeric chains can extend to the base fluid to form a barrier to prevent further attraction when the particles approach each other.

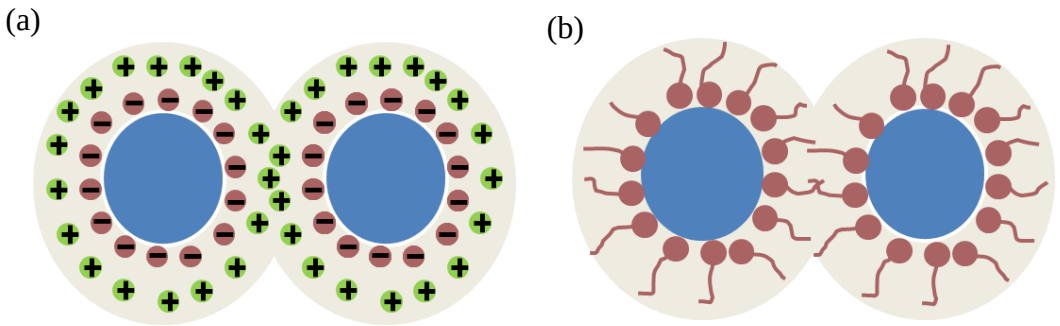

Fig 2-11 Mechanisms of the use of (a) ionic, (b) non-ionic surfactants for suspension stabilisation.

For aqueous suspension of nanoparticles, their stability can be enhanced by adjusting the pH value of the solution. According to the DLVO theory, the electrical double layer around particles contributes to the repulsive force to overcome the van der Waals attractive force. The electrical repulsive potential at the surface of the double layer is called zeta-potential which acts as an indicator of the stability of the particles in the base fluid. Normally, a nano-suspension can be considered stable if the zeta-potential of the particles is larger than +30 mV or smaller than -30 mV[105]. For water based system nano-suspension, zeta-potential is highly related to the pH value of the base fluid. Fig 2-12 shows a typical functional dependence of the zeta-potential on pH.

One can see that the curve passes across the horizontal axis at a point which is commonly known as isoelectric point (IEP). At this point, the zeta potential is zero, indicating no electrical repulsive forces

between suspended particles and hence an instable suspension. By adjusting the pH away from the IEP, the stability of the suspension can be enhanced.

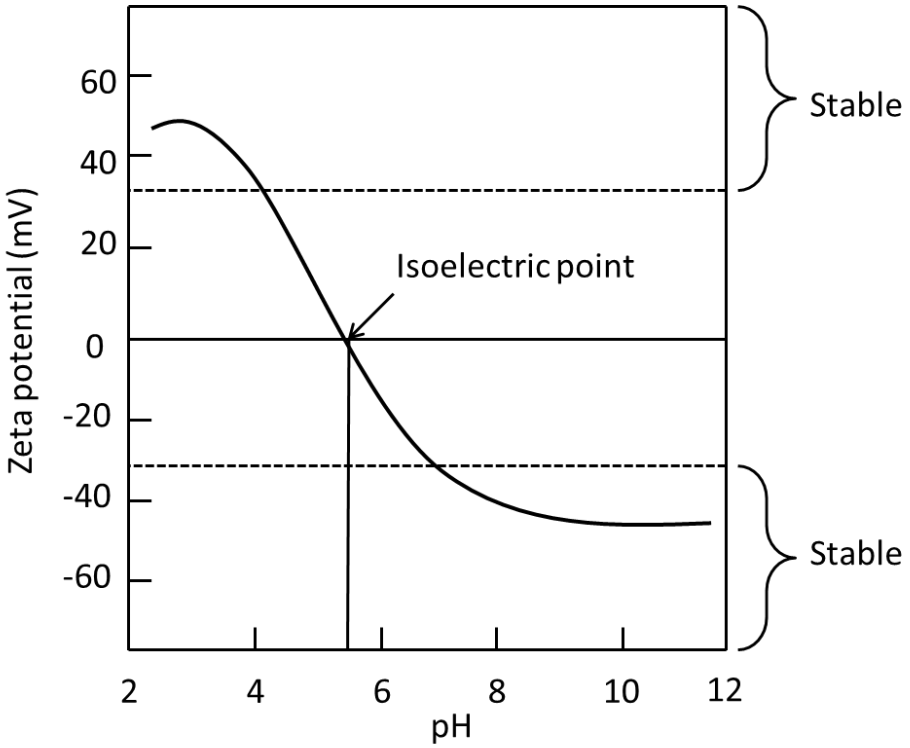

Fig 2-12 Zeta potential vs pH curve.

Suspension stability could also been enhanced from particle aspects, e.g. surface modification. In this method, functional groups are firstly grafted onto the surface of the particles by chemical or physical treatment, followed by dispersing the functionalized particles into the base fluid Table 2.5 shows some reported studies on surface modification for nano-suspension preparation.

Table 2.5 Surface modification for nano-suspension preparation.

nanoparticle	Base fluid	grafted group	reference
CNT	Water, ethylene glycol	C-O-C, C=O	[106]
CNT	Water	-COOH, -OH	[107]
ZnO	Water	-OOCR	[108]

TiO2	Silicone oil	PDMS	[109]
SiO2	Water	PEG	[110]

2.2.4 Characterization of suspension stability

A main and most used method for measuring the stability of nano-suspensions is the visual observation particle sedimentation. Wan et al.[111] studied the stability of graphite/ethylene glycol nano-suspensions. Fig 2-13 shows the photos of different samples taken at different time, illustrating that sample c has a clearly high stability that sample a.

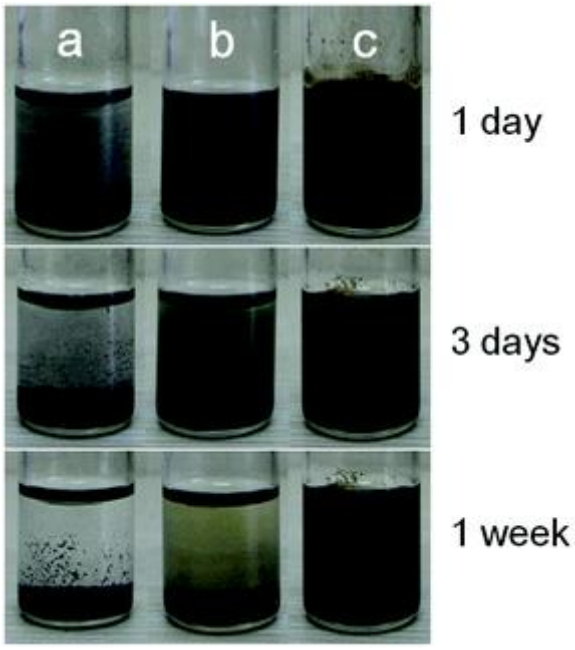

Fig 2-13 Picture of sample a, b and c after 1day, 3 days and 1 week. [111]

Although visually observing particle sedimentation is an easy way to compare stability of suspensions, it is qualitative and less accurate. A more qualitative method is the use of zeta potential measrements according to the DLVO theory. However, such a method is only applicable to polar liquid based suspensions (e.g. water or aqueous solution). It cannot be used for stability of suspensions based the steric forces.

The suspension stability can be quantified by using a UV-VIS spectroscopy. Such a method is based on the Beer-Lambert's Law[112], which shows that the absorbance of a suspension is proportional to the concentration of a suspension. A relationship between the absorbance intensity and particle concentration of the suspension can therefore be established[101]. By recording the absorbance intensity with time, one can then plot the relative concentration of nanoparticles as a function of time of different samples. Fig 2-14 shows an example of such relationship[113].

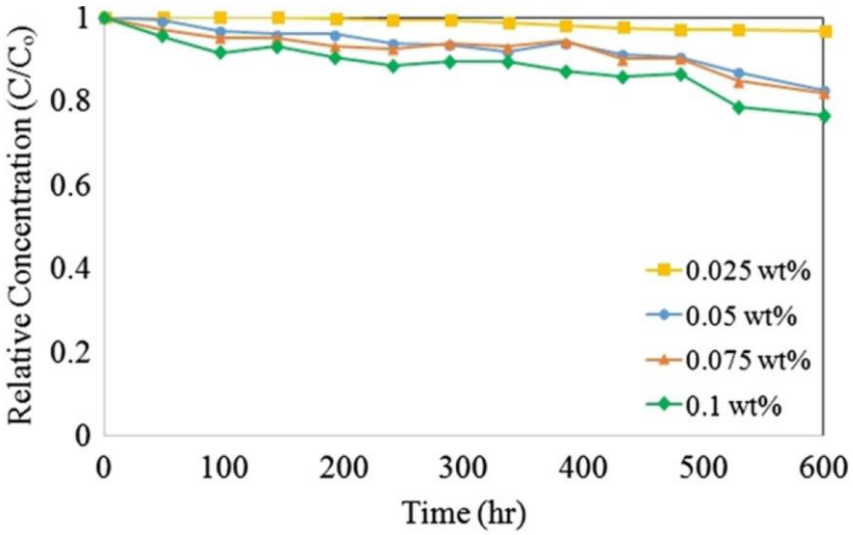

Fig 2-14 Concentration versus sediment time. [113]

The change in concentration illustrates the stability of the nano-suspension.

Other quantitative methods for measuring suspension stability include measuring particle size as a function of time, and measuring particle concentration as a function of time.

2.3 Thermal conductivity enhancement of nano-suspensions

Enhancement of thermal conductivity of PCMs has been at the top of the priority list of most studies as most PCM based devices suffer from low charging/discharging kinetics, and low PCM thermal conductivity contribute a significant potion to such an issue. Recent advances in nanoscience and

nanotechnology has inspired scientists and engineers to introduce nanoparticles into PCM for enhancing their properties.

2.3.1 Experimental observations of thermal conductivity of nano-suspension

A significant amount of studies has been carried out on thermal conductivity enhancement of nano-suspesnions. This section reviews the relevant literatures, particularly the factors that affects the thermal conductivity of naon-suspensions including: nanoparticle concentration, nanoparticle size and shape and nanoparticle materials.

Nanoparticle concentration

The literature reported effect of particle concentration on thermal conductivity enhancement is fairly consistent, see Fig 2-15, for water based Al_2O_3 nanofluids with nanoparticles of the same nominal size, and for water based CuO nanofluids.

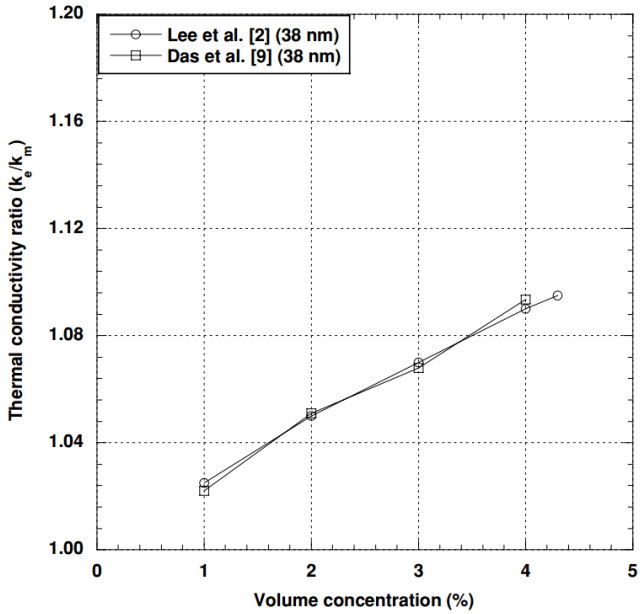

Fig 2-15 Effect of particle volume concentration on thermal conductivity enhancement for water based nanofluids.[114]

Fig 2-15 and Fig 2-16 show a clear functional dependence that the thermal conductivity enhancement increases with increasing particle concentration.

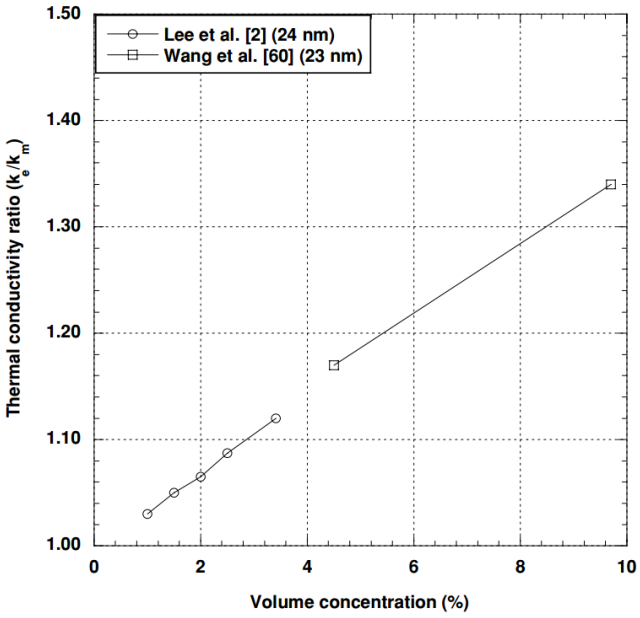

Fig 2-16 Effect of particle volume concentration on thermal conductivity enhancement for water based CuO nanfluids. [114]

Nanoparticle size and shape

The effect of particle size on the thermal conductivity enhancement is still a subject of debate. Fig 2-17 shows an example set of data for water based Al_2O_3 nanofluids. One can see that for a given particle concentration, nanofluids with 60 nm nanoparticles show the highest thermal conductivity enhancement, followed by that with 28 nm nanoparticles, and the 38 nm nanoparticles.

The exact reason for the particle size effect are unclear, but are likely to be associated with the following:

- Interfacial thermal resistance which increases with decreasing particle size;
- Size effect of nanoparticles on thermal conductivity which becomes significant when particle size is close to the mean free path of phonon;
- Inaccurate size measurement and aggregation of particles;

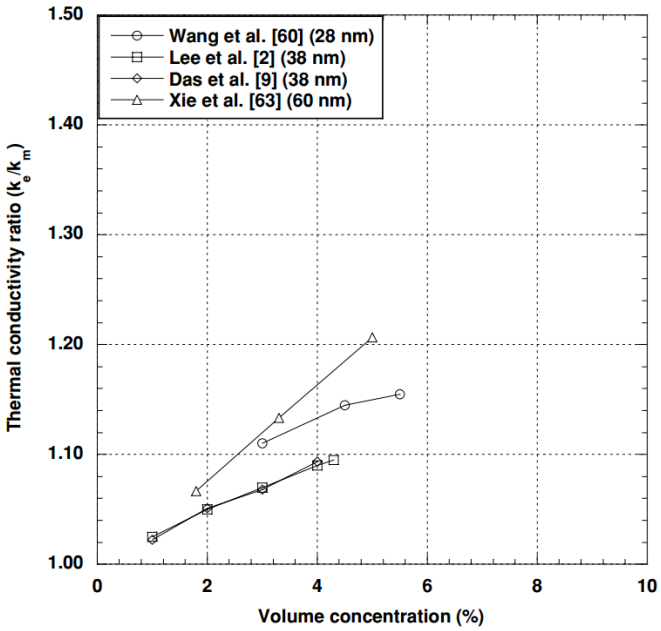

Fig 2-17 Effect of particle size for Al2O3 in water. [114]

The number of studies on the effect of particle shape on the thermal conductivity enhancement is fairly small. However, the results of these studies are fairly consistent. Fig 2-18 shows an example of a set of studies, which demonstrates (though more on qualitative basis) rod-like particle give a higher enhancement.

Nanoparticle materials types

A considerable amount of work has been done on the effect of particle material type on the thermal conductivity enhancement. The results of these studies are not always possible for a meaningful comparison due to more than one variables. Fig 2-19 shows a comparison of these materials with the rest of the variables being the same. One can only see a small effect of the material type.

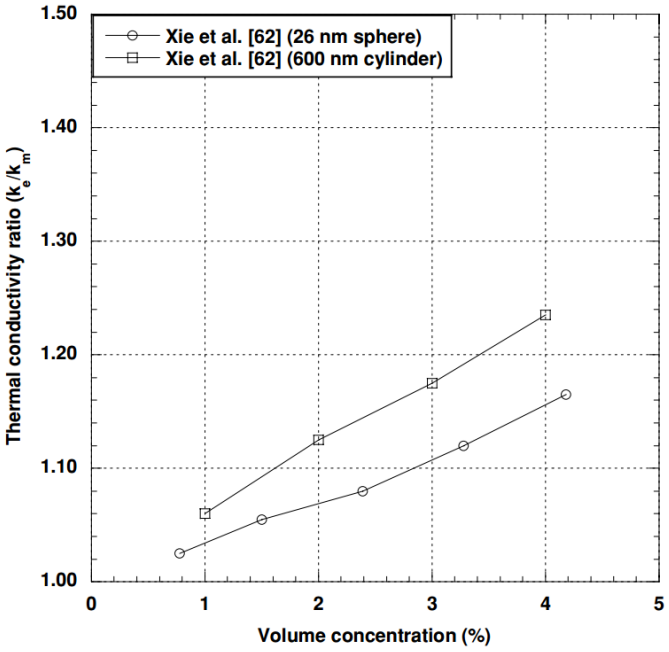

Fig 2-18 Effect of particle shape on thermal conductivity enhancement for water based SiC nanofluids. [114]

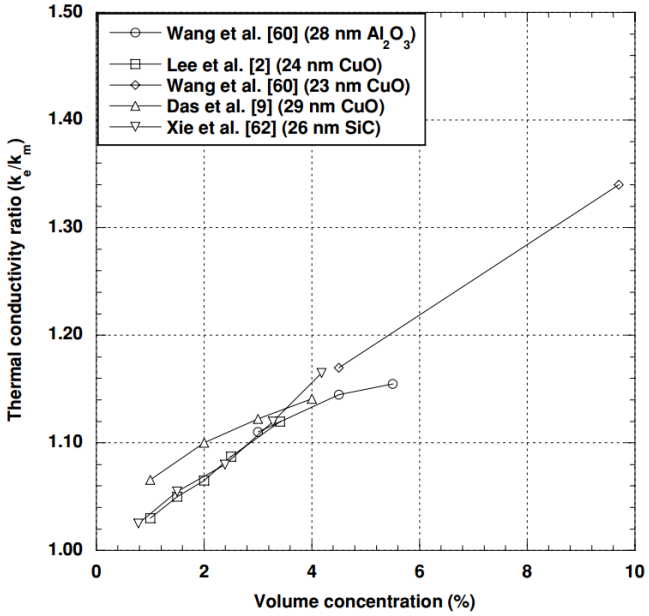

Fig 2-19 Effect of particle material type for water based nanofluids. [114]

However, the situation changes when high thermal conductivity particles are used, as illustrated in Fig 2-20 (a). The data shown in the figure are for two metallic and one oxide particles[14][49][115][116]. The metallic particles produce the same extent of enhancement as the oxide particles but at a much lower volume. Fig 2-20 (b) shows a comparison between nanofluids containing oxide, silicon carbide, and metal alloy particles. One can see a 2.3 times increase in thermal conductivity of metallica alloy based nanofluids at a particle concentration of 2.5%. compared to a much smaller enhancement of metal oxide based nanofluids.

2.3.2 Mechanisms of thermal conductivity enhancement due to introduction of nanoparticles

There are numerous studies on understanding the mechanisms of thermal conductivity enhancement. The most accepted mechanisms are Brownian motion of nanoparticles, clustering of nanoparticles, nano-layering of the liquid at the liquid-nanoparticle interface, and ballistic transport[13][14]. Most of the studies focus on the discussion of the roles of the Brownian motion of the nanoparticles, molecular-scale layering at liquid/particle interface (nano-layer) and nanoparticle clustering. These are briefly reviewed in the following.

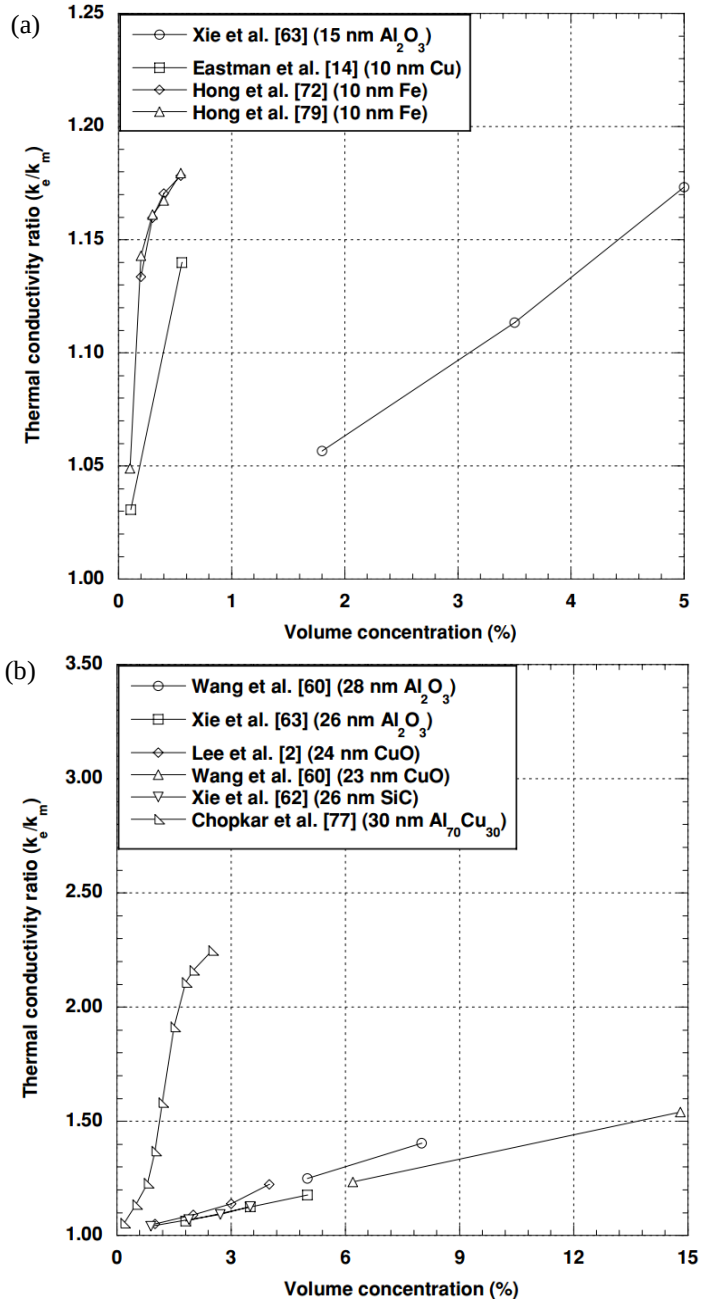

Fig 2-20 Effect of particle material type on ethylene glycol based nanofluids: (a) low concentration, (b) high concentration. [114]

Brownian Motion

The effect of particle Brownian motion is often neglected due to the large sized particles. As particle size reduces, particularly when particles approach the nanometer scale, the particle Brownian motion

and its effect on the surrounding liquids could become significant. The contribution of the Brownian motion enhance thermal conduction could occur in two ways. First, the movement of the nanoparticles transfers heat via convection., Second, the motion of particles induces fluid motion and hence heat transfer around individual nanoparticles. The first one has been shown theoretically to be negligible[117]. The second one has also been shown to have a minor effect on the thermal conductivity by theoretical analysis[118].

Keblinski et al.[119]performed molecular dynamics (MD) simulations to calculate the thermal conductivity of a nanofluid using simplified intermolecular potential model. Their results suggested insignificant effect of nanoparticle Brownian motion on thermal conductivity enhancement. This is consistent with the ratio of thermal diffusion to the Brownian diffusion would indicate. Keblinski et al. also indicated that the Brownian motion may have an effect on the formation of particle cluster, which could improve the thermal conductivity of naonfluids.

Nano-layer

The nano-layer refers to a solid-like liquid layer at the interface between the solid nanoparticles and the surrounding base liquids[120]. An interfacial thermal resistance is known to be present at such interfaces, which is termed as the Kapitza resistance[121]. Although liquid molecules close to a solid surface are easier to form a layered solid-like structure, little is known about the thermal properties of such a nano-layer and interaction between this layer and the base fluid and the solid. According to Yu et al.[122], the layered molecules are in an intermediate physical state between a solid and a base fluid. Therefore, the solid-like nano-layer of liquid molecules would be expected to lead to a higher thermal conductivity than that of the base fluid. This suggests that the solid-like nano-layer would acts as a

thermal bridge between a solid nanoparticle and a base fluid, leading to one of the explanation of the experimentally observed thermal conductivity enhancement.

Although the nanolayer effect is thought by some researchers to play an important role in the thermal conductivity enhancement of nanofluids, experiments and simulations have shown that the thickness of such a layer is only in the order of a few atomic distances (0.5 to 1 nm)[123]. This length scale is smaller than the mean free path of phonons, and hence is not expected to give a dominant effect rather than enhancement.

Clustering

As discussed earlier, nanoparticles are prone to aggregation due to van der Waals forces. This aggregated structure could act as a local percolation mechanism, leading to local enhancement of the effective thermal conductivity of nanofluids.

Clearly, a nanofluid consisting of all nanoparticle clusters would give a high extent of thermal conductivity enhancement, which is difficult to realize in practice, particularly when the fluid is under shear and the cluster can be destroyed. However, local clustering is possible and they have been experimentally observed. These clusters are more thoroughly conductive than the nanofluid made of well dispersed nanoparticles. As a result, the volume fraction of the highly conductive phase is larger than the actual solid volume fraction and may significantly increase the thermal conductivity.

Wang et al.[124] proposed a new model for the thermal conductivity of nanofluids based on the effective medium approximation and the fractal theory for accounting for the effect of nanoparticle clusters. They considered that size effect and the nano-layer in the model. Although their model agrees with the experimental data of CuO-water nanofluid, its validity requires more experimental effort.

Karthikeyan et al[125]. experimentally studied the effect of nanoparticle clustering on the thermal conductivity of CuO nanoparticles based aqueous nanofluid. They showed that the cluster size had a significant effect on the thermal conductivity of the nanofluids, which decreases with time due to the clustering of CuO nanoparticles. Furthermore, they indicated that the finer the particle size with monodispersity, the larger the enhancement in the thermal conductivity of nanofluids. They also noted that the nanoparticle clustering may exert a negative effect on heat transfer enhancement when the clusters start ot settle in the fluid.

Prasher et al[126], by using the effective medium theory, showed that the thermal conductivity of nanofluids can be significantly enhanced by the aggregation of nanoparticles into clusters. They claimed that the observed thermal conductivity of nanofluids can be explained by aggregation kinetics. Their predictions using the effective medium theory were in excellent agreement with detailed numerical calculations on model nanofluids involving fractal clusters and showed the importance of cluster morphology on thermal conductivity enhancements.

Although a lot of work have been done on the development of prediction models for thermal conductivity of nanofluids, most of the models are only valid under their own experimental condition and they are in most cases in disagreement with other literature data.

2.4 Viscosity of nano suspensions

Viscosity is an important fluid property that affects pressure drop and hence pumping power and convective heat transfer of a fluid flows. There have been numerous studies on the area and they are summarized in the following according to the effects of particle shape, particle size, volume fraction and particle aggregation on nanofluids' viscosity.

2.4.1 Effects of particle size and shape on the viscosity

The viscosity of nanofluids is a function of particle size given other conditions. Nguyen et al.[127] studied the viscosity of alumina–water nanofluids. They observed that at 4 % particle volume concentration, 36 and 47 nm alumina/water nanofluids showed almost the same viscosity; however, when the volume concentration was increased, the nanofluids with 47 nm nanoparticles gave a higher viscosity than that with 36 nm particles. Similar results were reported by the same auther for nanofluids with 7 % and 9 % concentration[128]. Their results are in agreement with He et al[129] for aqueous based TiO_2 nanofluids with 95 nm and 145 nm particles.

Namburu et al.[130] reported that the viscosity reduced with increasing particle size for SiO_2 based nanofluids. Similar observations were reported by Chevalier et al.[131] for SiO2–ethanol nano suspensions of three different particle sizes of 35, 94 and 190 nm, Pastoriza-Gallego et al.[40], Lu and Fan[132] and Anoop et al.[133] for CuO–water and Al_2O_3–water nanofluids, respectively. These observations contradict to that of He et al and Nguyen et al, and the exact reason are unclear. Very few studies have been found in the literature on the effect of particle shape on the viscosity of nanofluids. Timofeeva et al.[134] reported that nanofluids with elongated particles had a higher viscosity of nanofluids than that with spherical nanoparticles. Ferrouillat et al.[135] studied the shape factor of nanoparticles on convective heat transfer of water based SiO_2 and ZnO nanofluids. They found that the water based ZnO nanofluids with rod-like nanoparticles had slightly lower viscosity compared to that with polygonal particles, whereas the SiO_2 nanofluids with banana-shaped particles had a viscosity close to that with spherical particles.

2.4.2 Effect of volume concentration

Several studies have been published on the effect of particle loading on the viscosity of nanofluids. Almost all these studies show that the addition of nanoparticles, even at a low volume fraction, increases the viscosity.

Prasher et al.[136] observed that the viscosity of alumina–water nanofluids increased with an increase in nanoparticle volume fraction. Das et al.[137] observed that the alumina-water nanofluids exhibited Newtonian behavior and that the viscosity of the nanoflud increased with particle concentration. Duangthongsuk and Wongwises[138] noticed an increase in the viscosity of TiO_2–water nanofluid by 4–15 % with particle volume concentrations increased from 0.2 % to2.0 %. Similar observation were made by Chevalier et al.[131] on the viscosity of SiO_2–ethanol nanofluids, Schmidt et al.[139] on Al_2O_3 based decane and isoparaffinic polyalphaolefin (PAO) nanofluids, Ding et al.[23] on CNT based aqueous nanofluids; and Chandrasekar et al.[140] on alumina–water nanofluids.

2.4.3 Effect of particle aggregation

The effect of particle aggregation on nanofluid viscosity could be significant. Chen et al.[141] studied this effect using the fractal theory. They introduced the so-called effective particle volume: $\frac{\varphi_{eff}}{\varphi} = (\frac{d_{eff}}{d})^{3-D}$, where d and d_{eff} are diameters of the primary nanoparticles and aggregates, respectively, and D is the fractal index with a typical value of 1.6–2.5 for aggregates of spherical nanoparticles. With this, it was possible to fit the data with a modified Krieger-Dougherty equation by replacing φ with φ_{eff}. This approach was supported by Duan et al.[142]who studied the viscosity of Al_2O_3-water nanofluids and found and the increase in the relative viscosity due to nanoparticle aggregation fits the modified Krieger-Dougherty model.

2.5 Thermal properties of nano-suspensions

Thermal properties related to storage application includes melting point, melting enthalpy, specific heat and supercooling degree and so on. These properties have been studied extensively, particularly for temperatures above the ambient.

2.5.1 Melting point and melting enthalpy

Most reported studies on the area concern the melting point of PCM containing nanoparticles, and the results show little changes to the melting point. For example, Harikrishan et al[143] added TiO_2 nanoparticles into palmitic acid with a particle mass concentration ranging from 0.1 wt% to 0.3wt%, and found that the maximum deviations of melting temperature were 0.19 %. This is consisted with the findings of Wu et al.[144], who observed a maximum change of the melting temperature of 0.6% by adding 2 wt% Cu nanoparticle in paraffin.

The addition of nanoparticles could have significant effect on the latent heat of PCMs. For example, Shuiying et al.[144] found that the latent heat of melting reduced by 11.1 % due to the addition of Cu to paraffin. According to the theory of mixtures, the latent heat of Cu/pafaffin can be calculated by multiplying the latent heat of the pure paraffin with the mass fraction of the PCM in the mixture. However, the experimental latent heat does not agree with theory, as demonstrated in Fig 2-21. From the figure, one can see the deviation increases with increasing mass concentration of nanoparticles. Sari and Karaipekli[145][146] , Ho and Gao[147], and Xie[148] have also observed similar results. The mechanisms for the observation are still subject to further investigation.

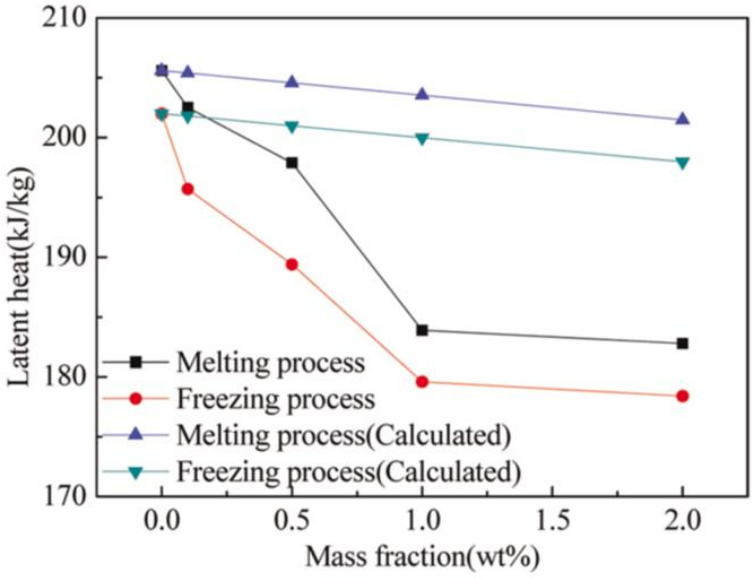

Fig 2-21 Latent heat of Cu/paraffin with different mass fraction.

2.5.2 Specific heat

Besides latent heat, the energy storage capacity of a thermal energy storage system mainly depends on specific heat during no-phase change period. There are reports on the effect of nanoparticle on specific heat of nanofluids. Zhou and Ni[149] found that the specific heat will decrease by adding Al_2O_3 into water, and the decrease is in linear relationship with nanoparticle volume fraction, which is in good agreement with the simple mixing role. Similar observation were found by O'Hanley[150] on water based SiO_2, Al_2O_3 and CuO nanofluids. However, little studies has been carried out on specific heat of PCM at low temperature, especially sub-zero temperature, which forms the motivation of specific heat study in this thesis.

2.5.3 Supercooling degree

Supercooling degree is defined as the difference between the ideal melting point and the real freezing point of PCM. For example, we all know that the melting point of water is 0 ^oC, but the real temperature when water starts turn from liquid to solid can be down to ~-18 ^oC due to the existence of supercooling[151]. Such kind of big delay of freezing point of PCM could cause very large energy cost

on refrigerator side, further lead a low efficiency of the cold storage system. As a result, reducing supercooling degree becomes an important target of using PCM in cold storage area.

Nanoparticle as a nucleation agent has been widely used to reduce supercooling degree. Wu et al.[152] investigated the cold storage performance of an Al_2O_3–H_2O nanofluid and found that adding 0.2% Al_2O_3 nanoparticles can shorten the crystallization time of the nanofluid by 20.5% and reduce its supercooling degree from 7.0 ^oC to 2.3 ^oC. Kumaresan et al.[153] discovered that dispersed multi-walled carbon nanotubes in deionized water can act as a nucleating agent to reduce the supercooling degree of water from 8 ^oC to 4 ^oC.

However, researches on supercooling degree of PCM at sub-zero temperature remains insufficient. He et al.[154] explored the supercooling degree of $BaCl_2$ solution with TiO_2 nanoparticles. They found that adding 1.13 vol% TiO_2 nanoparticles significantly reduce the supercooling degree from 3.78 ^oC to 0.57 ^oC. The lack of experimental study on supercooling degree of sub-zero cold storage PCM forms the motivation of supercooling degree study in this thesis.

2.5.4 Crystallization rate

Crystallization process of water was observed by many researchers and the crystallization rate was calculated based on the observations. Ivall et al.[155] provided an experimental setup to visually observe the freezing of water. The schematic of this experimental apparatus mainly consists a camera with a macro lens, a cooling stage and a sample plate. A droplet of water was deposited on the sample plate and the sample plate was set on the cooling stage. The camera was set aside to record the live image of the droplet during cooling. Then, they measured the solid-liquid front position continuously

and calculated the front velocity, which indicates the crystallization rate. Murray et al.[156] used an optical microscope instead of digital camera and the water droplets were placed in a sealed cell in his experiments. Images were recorded while the droplet-cell was cooled down and the number of frozen droplets was counted, yielding the crystallization rate. Pasieka et al.[157] observed the front moving and mushy zone in cooled water by an infrared camera and the front velocity was calculated afterwards. Although some approaches have been used to observe freezing of water, few research has been carried out on sub-zero PCMs, which forms the motivation of crystallization study in this thesis.

2.6 Summary

This chapter mainly reviewed the basic and typical researches relating to work in this thesis, including: types of sub-zero PCM; formulating methods of nano-suspension; effect of nanoparticle on thermal conductivity, viscosity, melting point, latent heat, specific heat, supercooling degree and crystallization of nano-suspension.

However, existing researches are mainly focusing on properties and mechanisms at ambient temperature, very few work is reported covering sub-zero temperature. In contrast, the growing attention is paid on the cold storage field, leading to a serious need for further knowledge on material side in low temperature area. This forms the motivation of a systematic study on material side concerning cold storage at sub-zero temperature. The work in this thesis presented parts of the efforts of understanding the mechanism of thermal and physical properties in nano-composite PCM at sub-zero temperature.

3 Materials and methodologies

This chapter gives details of materials used in this work as well as methods for preparing nano-suspensions and measuring the preferred thermophysical properties.

3.1 Materials and methods for nano-suspension preparation.

3.1.1 EG-water based MCNT nanosuspensions

Ethylene glycol (EG) with a purity of 99.5 % was purchased from Sigma Aldrich, UK (CAS number: 107-21-1). The multiwalled carbon nanotube (MCNT) with 10 nm outer diamter, 4.5 inner diameter and 3~6 μm length was also purchased from Sigma Aldrich, UK (CAS number: 308068-56-6). Distilled water was obtained from a lab water stiller (Calypso water still, Fistreem International Ltd, UK). Sodium dodecylbenzenesulfonate (SDBS) purchased from Sigma Aldrich (CAS number: 25155-30-0) was used as a surfactant for particle stability enhancement. These materials were used as-received without purification. The EG-water based MCNT nano-suspensions were prepared using the two-step method. EG and distilled water were mixed at to produce basefluids with EG/water ratio of 20/80, 25/75 and 30/70 respectively. A preset amount of MCNT, together with the some amount of SDBS, was then dispersed into the EG-water basefluids. Through this process, nanofluids with MCNT volume concentration of 0.0625%, 0.125%, 0.25% and 0.5% were produced. The corresponding mass of MCNT for a given amount of nanofluids was determined by the following equation:

$$\varphi = \frac{m_{MCNT}/\rho_{MCNT}}{(m_{MCNT}/\rho_{MCNT})+(m_b/\rho_b)} \qquad \text{Eq. 3-1}$$

where φ represents the volume fraction of the nano-suspension; m_{MCNT} and m_b are the mass of MCNT and the base fluid, respectively; and ρ_{MCNT} and ρ_b are the density of the MCNT and base fluid, respectively.

During the preparation of the nano-suspensions, magnetic stirring was applied and a ultrasonication probe(Elmasonic S 70 H, Elma Schmidbauer GmbH) was used to proccess the suspension for one hour with an aim to break down nano-aggregates. The pulse of the ultrasonication was set as 5 s/5 s on/off mode and the samples were placed in a jacked beaker conncected to a chiller. The use of the chiller was to void excessive local temperature rise during the ultrasoniction. Fig 3-1 shows schematically the prepartion process, which also illustrates the effect of surfactant on the stability of the produced nano-suspension.

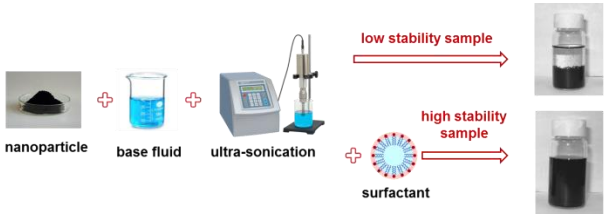

Fig 3-1 A schematic diagram of the nano-suspension preparation process.

3.1.2 Salt-water based MCNT nanofluids

KCl, NaCl and $MgCl_2$ were used to formulate aqueous solutions with different freezing points. These salts were purchased from Sigma Aldrich, UK(CAS number: 7447-40-7, 7647-14-5 and 7786-30-3, respectively). These salts were used as-received without purification. These salts, together with the distilled water, were used to produce salt solution containing 19.5 % KCl, 22.4 % NaCl and 25 % $MgCl_2$. Gum Arabic purchased from Sigma Aldrich was used as the surfactant for the salt-water based MCNT nanofluids production. The method for the nanosuspension production was the same as briefly discussed in 3.1.1.

3.2 Methodologies of nano-suspension characterization

3.2.1 Thermal conductivity

The thermal conductivity of the samples were measured by a Laser Flash Apparatus (LFA), supplied by NETZSCH, Germany(model LFA427). This measurement is equipped with liquid nitrogen cooling control unit which can provide an environment of -196 ^{o}C. The principle of the LFA technology si shown schematically in Fig 3-2. A short laser focuses on the lower flat surface of a disk-shaped sample placed in a temperature and environment controlled chamber. This creates a temperature rise on the upper flat surface of the sample, which is captured by an infrared detector.

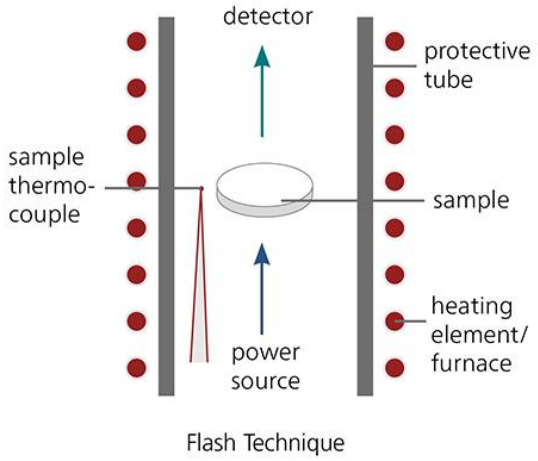

Fig 3-2 Schematic diagram illustrating the principle of a LFA devices.

Fig 3-3 shows a typical temperature response of a measurement, where a is the thermal diffusivity, c_p is the specific heat capacity, m is the mass and d is the thickness of the sample. $t_{1/2}$ represents the time corresponding to the half of the maximum temperature difference. From the equation shown in the figure, one can see that a is proportional to the sample thickness squared, and inversely proportional to the time $t_{1/2.}$ The thermal diffusivity can therefore be obtained if $t_{1/2}$ and d are given, and the thermal conductivity, k can be calculated by using $k = \alpha \cdot \rho \cdot c_p$. These processes are embedded in the software

package of the Netzsch system. The LFA provides a very quick method of measurement of the thermal conductivity, compared with the hot plate and even hot wire methods.

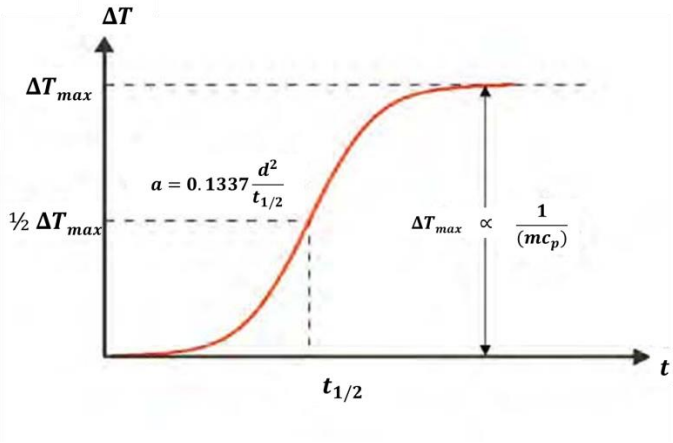

Fig 3-3 A typical temperature response as a function of time, illustrating how the thermal conductivity is obtained.

3.2.2 Rheology

As nano-suspension may exhibit non-Newtonian behavior, the rheological behavior was measured. The measurements gave shear rate and temperature dependence of the shear viscosity of the nano-suspension. An Anton Paar MCR 502 rheometer (Austria) from was used in the work, which is equipped with a liquid nitrogen cooling control unit attached to the measuring chamber, thus enabled the subambiant temperature measurements needed for this work. Fig 3-4 shows a schematic diagram, illustrating the principle and configuration of the MCR502 system. The rheometer was equipped with a measuring cell and this work used a parallel plate (L-PP35/CTD) with a diameter of 35 mm. Nano-suspensions with different concentration (0.0625%-0.5%) by volume for MCNT suspensions were studied using the rheometer at a shear rate of 100-800 s^{-1} and the temperature of the sample was controlled to be between 25 ^{o}C and the freezing points of the suspensions.

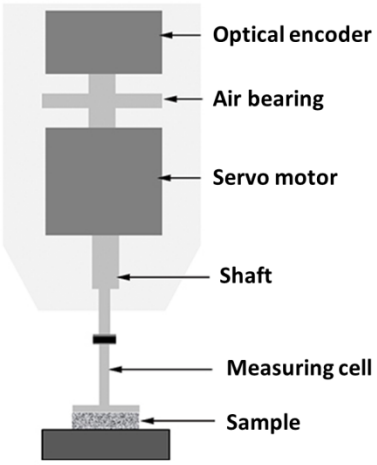

Fig 3-4 Schematic diagram illustrating the principle and configuration of the MCR502 system.

3.2.3 Specific heat

The specific heat was measured by using a differential scanning calorimeter (DSC). The DSC works by measuring the difference in the amount of heat for increasing the temperature of a sample and that of a reference. Fig 3-5 is a schematic diagram showing the principle and configuration of a typical DSC. There are numerous DSC supplier. This work used a DSC 3 from Mettler Toledo, Swiss. Such a device has an immersion cooling system which can provide a temperature environment as low as to -80 ^{o}C. The testing chamber is sealed and can be filled with gas atmosphere if necessary.

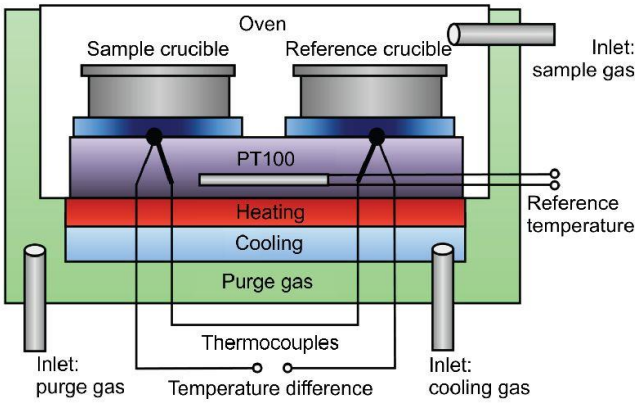

Fig 3-5 A schematic diagram illustrating the principle and configuration of a typical DSC.

Fig 3-6 shows a signal of a typical DSC measurement for the specific heat. Here lines I, II, III and IV represent the heat flow at the first isothermal stage, the second isothermal stage, the dynamic stage for the reference and the dynamic stage for the sample. Ideally, lines I and II overlaps with horizontal axis. The specific heat, c_p, of the measured sample is calculated by using following equation:

$$c_p = \frac{h}{H} \cdot \frac{M}{m} \cdot c_{ps} \qquad \text{Eq. 3-2}$$

where, *h* and *H* are respectively the heat flows of the sample and the reference, *m* and *M* are respectively the mass of the sample and the reference, and c_{ps} is the specific heat of the reference.

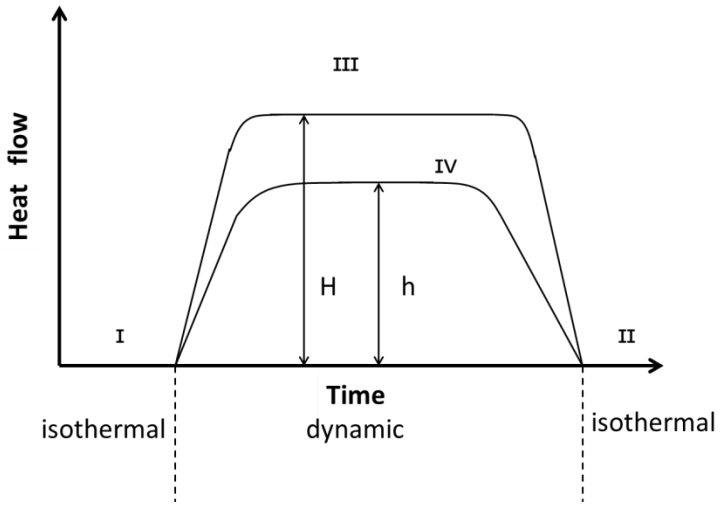

Fig 3-6 A typical DSC signal for the specific heat measurement.

There are a number of type for an measurement of the specific heat. For example, crucibles should be located exactly on the sensors in every measurements. The mass difference of the crucible of sample and that of reference should be as low as possible (<0.01 mg). Good thermal contact is needed between the sample and the crucible, and the heat flow to the sample and that to the reference similar, namely, the

mass and the specific heat of the sample and that of the reference should follow the following relationship $c_p \cdot m \approx c_{ps} \cdot M$.

3.2.4 Melting point/freezing point and melting/solidification enthalpy

The melting/freezing point and the melting enthalpy are also measured by using DSC device. The main difference lies in the dynamic stage of the temperature program due to the freezing and melting processes. A typical DSC signal of a sample undergoing phase change is shown in Fig 3-7. One can see two peaks on the diagram; a freezing or crystallization peak, and a melting peak. The onset of the freezing peak and melting peak is termed as the freezing point, and that of the melting peak is termed as the melting point. The integration of the peaks gives the melting/solidification enthalpy.

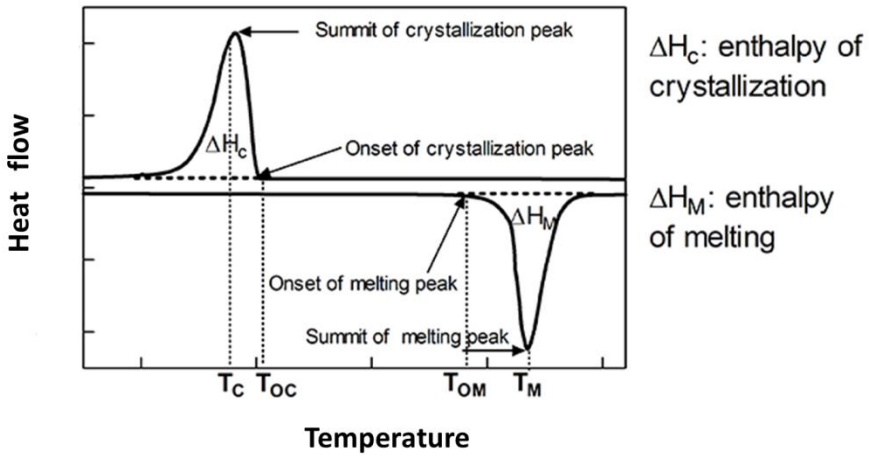

Fig 3-7 A typical signal of a DSC measurement of a sample undergoing phase change.

In this work, all samples are water based solutions. Preliminary experiments indicated that the optimal sample mass for water is very small, ~1 mg or 1 μl in volume. The reason for such a small amount of sample size is because the latent of water is very high ~334 J/g. When a large amount of heat is released, the accuracy will be reduced.

3.2.5 Supercooling degree

Two methods were used to measure the supercooling degree. One is the widely used temperature-history method, and the other is a method proposed by the author, in the following.

The temperature-history method, records the temperature of a PCM samples during the whole freezing period process. Fig 3-8 shows a schematic diagram, illustrating the configuration of a typical Temperature-history measurement device. The cooling bath provides a constant temperature environment for freezing the sample. The Data logger records the temperature history of the sample during freezing. By analyzing the difference between the onset of freezing and the flat (constant) temperature stage, the supercooling degree of the PCM can be obtained.

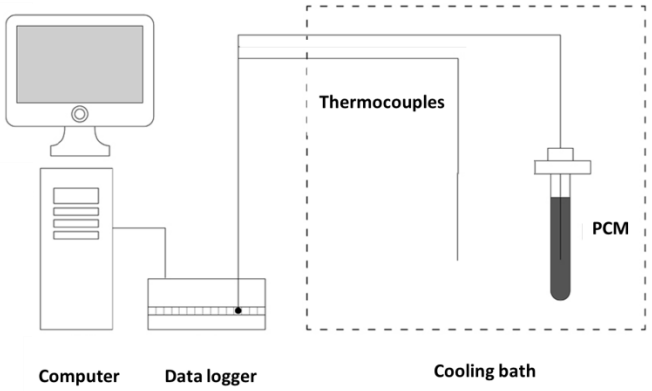

Fig 3-8 A schematic diagram showing the component of a typical temperature-history device.

The modulus-temperature method measuring the supercooling degree indirectly. Such a method records the sudden change of the dynamic modulus of the PCM against temperature using a rheometer as discussed early in this chapter. The turning point of the modulus provides an indication of phase changing either during freezing or melting. A typical modulus-temperature curve is shown in Fig 3-9, in which the red curve I presents the modulus-temperature relationship during the cooling process, and the black curve II represents the modulus-temperature relationship during heating process. Ideally, the dynamic modulus jumps suddenly from a low level to a high level (the freezing processs), so that the

onset of the modulus increase can be identified as the freezing point of the PCM. Conversely, a steep modulus drop from the high level back to the low level (the melting process), makes it easy to define the melting point. The supercooling degree can be obtained by taking the difference between the freeing point and the melting point.

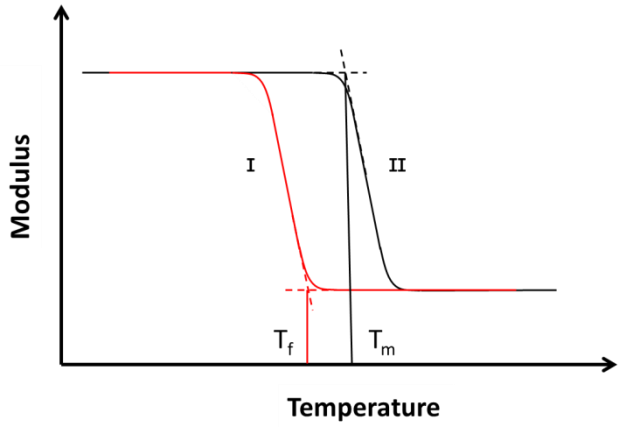

Fig 3-9 A typical freezing and melting curves measured with the modulus-temperature method.

3.2.6 Crystallization rate

The crystallization rate was studied with a transmission optical microscope interfaced to a computer, coupled with a liquid nitrogen cooling stage. The experimental process involved placing the sample on the stage and adjusting the microscope focus to obtain a clear and sharp image, setting up a temperature program of the cooling stage with a proper cooling rate and a targeted temperature. In this work, a digital camera was used to capture the live image of the sample every second during cooling. A software package was used to analyze these images, which involved the marking of the crystal boundary, identifying the size of the crystals as a function of time and calculating the growth rate using the size as a function of time.

3.3 Summary

This chapter briefly explained the method for the formulating and production of nano-suspension, and introduced the methods and associated devices for the characterization of the thermophysical properties of the nano-suspensions, particularly those related to the phase change of the nano-suspensions, including: (a) LFA for thermal conductivity; (b) rheometer for dynamic viscosity and dynamic modulus; (c) DSC for specific heat, melting point and melting enthalpy; (d) temperature-history and modulus-temperature for supercooling degree and (e) temperature controlled microscope for crystal growth observation.

4 Results and discussion (I): rheological behaviour

This chapter presents the viscosity results of salts based and EG based water solutions containing MCNT. Analyses and discussion on these will then be performed with an aim to build a relationship between the measured viscosity and MCNT structure considering temperature and particle concentration effect.

4.1 Experimental results of rheological measurements

In this section, the rheologyical data of liquid PCM suspensions containing nanoparticles are presented first. Theses experimental results are presented in the form of viscosity against shear rate (100 to 800 s^{-1}). Relative viscosity defined as the ratio of the effective viscosity of nano-suspension to the viscosity of the basefluid (all measured at given shear rate 100 s^{-1}) is also calculated and plotted against particle concentration at different temperatures. This section is organised according to the type of different basefluids.

4.1.1 Rheological data of 20% EG-80% water based nano-suspensions

Fig 4-1 to Fig 4-3 show the dynamic viscosity versus shear rate curves for 20/80 EG/water based MCNT nano-suspensions with various particle concentration at 25 ^{o}C, -5 ^{o}C and -10 ^{o}C, respectively. From Fig 4-1, one can see that the viscosity of all samples is nearly constant with increasing shear rate from 100 to 800 s^{-1}, suggesting that the so-called Newtonian behaviour of the suspensions at the room temperature. The measured viscosities are 2.05, 2.06, 2.09, 2.27 and 2.57 mPa • s for 0 %, 0.0625 %, 0.125 %, 0.25 % and 0.5 % volume concentrations of MCNT, respectively.

At -5 ^{o}C, however, as illustratetd in Fig 4-2, the 0.25 % and 0.5 % MCNT suspensions show shear-thickenning behavior during the whole shear rate range. For the 0.25 % sample, the viscsoity

increases approximately linearly from 8.72 to 11.29 mPa • s and for the 0.5% sample, the viscosity climbs from 12.80 to 17.77 mPa • s. The figure also shows that the 0.0625 % and 0.125 % samples still show the Newtonian behaviors.

With decreasing temperature further down to -10 ^{o}C. Very different rheological behavior is observed in Fig 4-3. First, the curve of the 0.125% sample shows the shear thickening behaviour at -10 ^{o}C, which does not occur at -5 ^{o}C. Second, the viscosity of the 0.5% sample at -10 ^{o}C shows an increasing trend at the beginning but followed by declining trend at ~ 400 s^{-1}. at -10 ^{o}C. The reason for the different obserfations at different MCNT concentration under different temperature will be discussed later in this chapter.

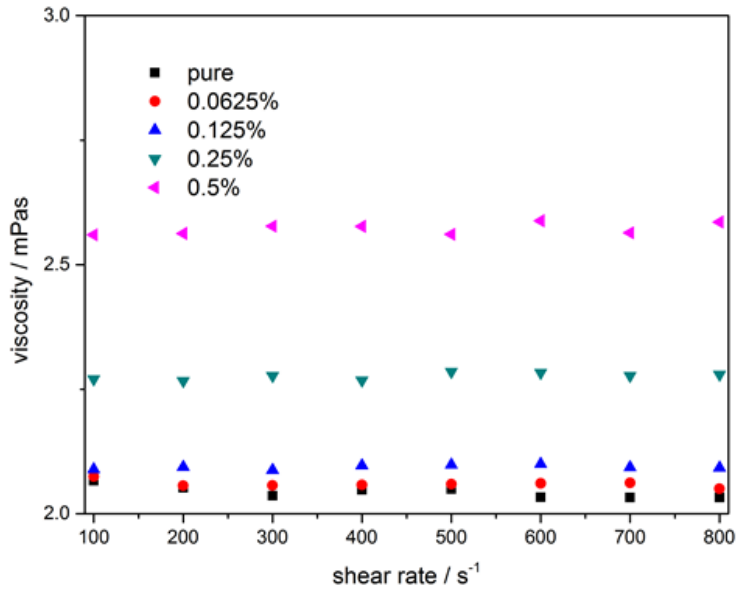

Fig 4-1 Shear viscosity of 20%EG-80%water based nano-suspensions as a function of shear rate at 25 ^{o}C.

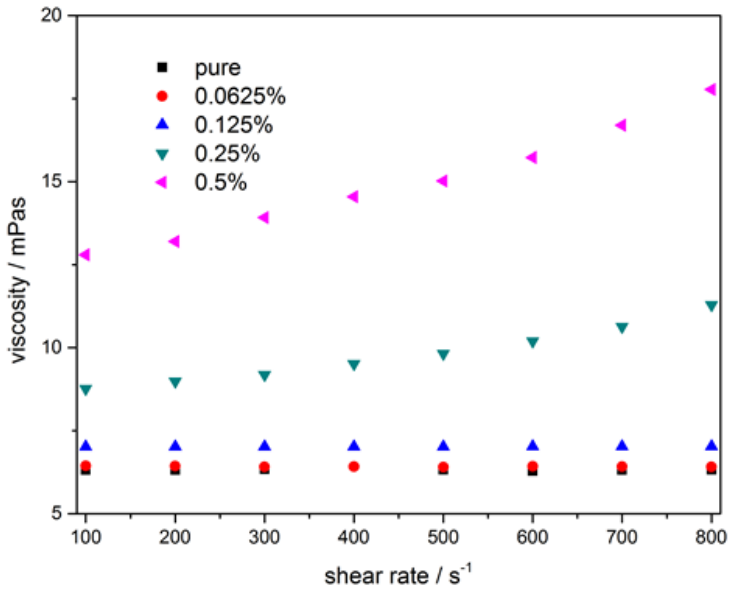

Fig 4-2 Shear viscosity of 20%EG-80%water based nano-suspensions as a function of shear rate at -5 °C.

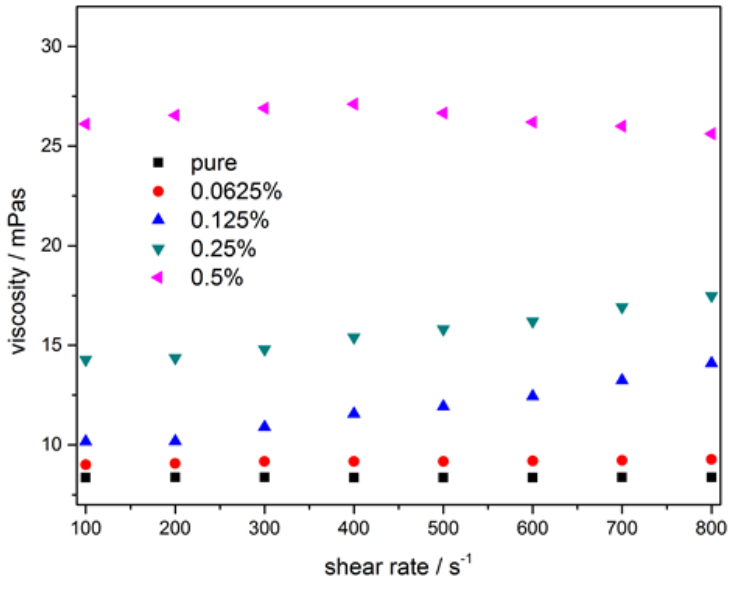

Fig 4-3 Shear viscosity of 20%EG-80%water based nano-suspensions as a function of shear rate at -10 °C.

Fig 4-4 shows the relative viscosity of the nano-suspension. At 25 ^{o}C, the changes ot the realative viscosity is small, especially for 0.0625 % and 0.125 % concentrations. With an increase in the concentration to 0.25 % and 0.5 %, the relative viscosity rises dramatically to 1.10 at 0.25 % suspension and 1.24 at 0.5 % suspension, respectively. This big increase in the relative viscosity does not follow a linear relationship with the particle concentration. This non-linear relationship will be discussed further in a later section of this chapter.

At -5 ^{o}C, the relative viscosity of the 0.0625% concentration sample is ~1.02, which is only slightly higher than that at 25 ^{o}C. However, the samples of other particle concentration show a significantly higher relative viscosity value than that at 25 ^{o}C. The relative viscosities are 1.12, 1.39 and 2.03 respectively for the 0.125 %, 0.25 % and 0.5 % MCNT concentrations at -5 ^{o}C. Which are over ~4 times the respective samples at 25 ^{o}C, signifying the importance of the temperature effect.

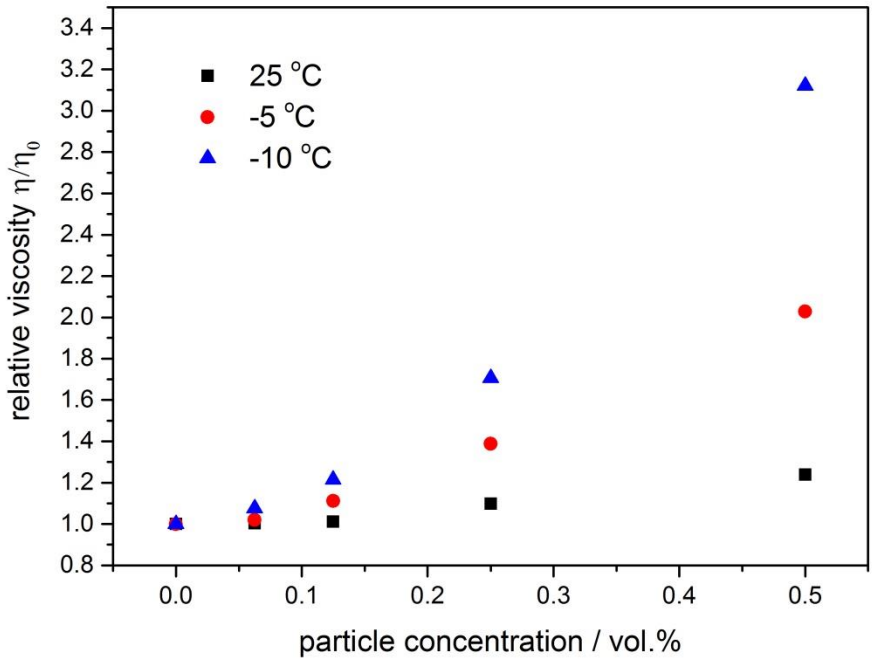

Fig 4-4 Relative viscosity of 20%EG-80%water based nano-suspensions at different tempeartures.

At -10 °C, the relative viscosity of the EG-water-MCNT samples are significantly higher than that at -5 °C., which are 1.07, 1.21, 1.70 and 3.12 respectively for 0.0625 %, 0.125 %, 0.25 % and 0.5 % samples, further reinforcing the important effect of temperature on the viscosity of the nano-suspension.

4.1.2 Rheological behaviour of 25% EG-75% water based nano-suspensions

Fig 4-5 to Fig 4-8 show the dynamic viscosity as a function of shear rate of 25/75 EG/water based MCNT nano-suspensions with various particle volume concentrations at 25 °C, -5 °C, -10 °C and -15 °C respectively. The rheological behavior of the 25.75 EG/water nano-suspensions at 25 °C is similar to that of the 20/80 EG/water based nanofluids at the sample temperature, namely, all samples show a flat curve with increasing shear rate from 100 to 800 s^{-1} as shown in Fig 4-5. The viscosity increases due to the addition of nanoparticles at 25 °C appears to scale with the viscosity of the base liquid. For the 0.5 % MCNT suspensions, the enhancement of viscosity for the 25/75 EG/water system is 13.60 % whereas that for 20/80 EG/water system is 14.00 % at 25 °C.

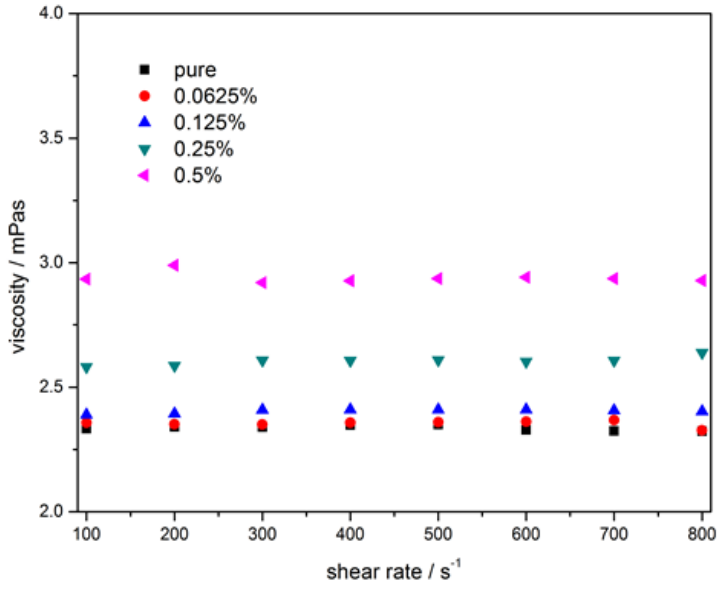

Fig 4-5 Shear viscosity of 25%EG-75%water based nano-suspensions as a function of shear rate at 25 ^{o}C.

At -5 ^{o}C, the shear-thickenning behavior is observed for the 0.25 % and 0.5 % samples as shown in Fig 4-6. This is similar to the observation of the 20/80 EG/water system, but the difference lies in the starting point of the shear thickenning. The 0.25 % and 0.5 % 25/75 EG/water based suspensions starts to show the shear thickenning behaviour at a shear rate of ~300 s^{-1}. Fig 4-6 also shows that the viscosity curve of 0.125 % sample tilts up slightly at shear rate above 600 s^{-1}, while the 0.0625 % sample shows the Newtonian behavior over the whole range of shear rate studied.

The results at -10 ^{o}C are shown in Fig 4-7. Very different behaviour is apparent. For example, the vicsoity of 0.0625 % and 0.125 % samples increase with increasing shear rate; the 0.25 % sample shows an increasing trend first until ~400 s^{-1} where a decreasing trend occur; the 0.5 % sample, however, whos a shear thinning behaviour.

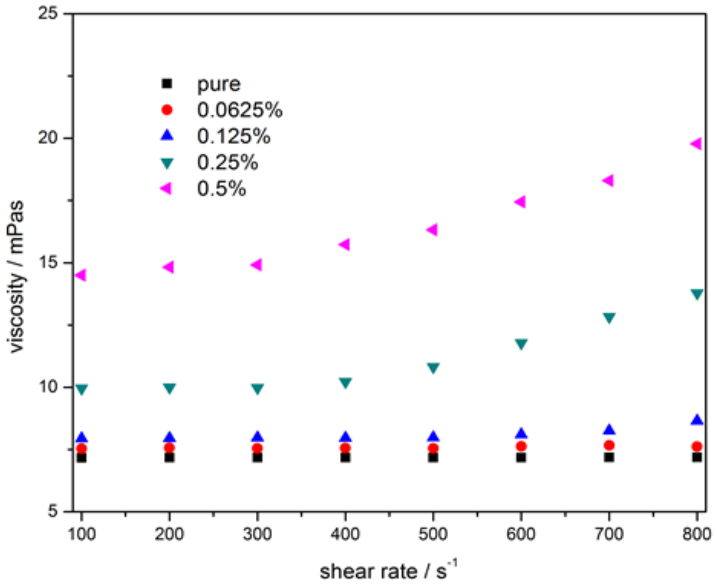

Fig 4-6 Shear viscosity of 25%EG-75%water based nano-suspensions as a function of shear rate at -5 ^{o}C.

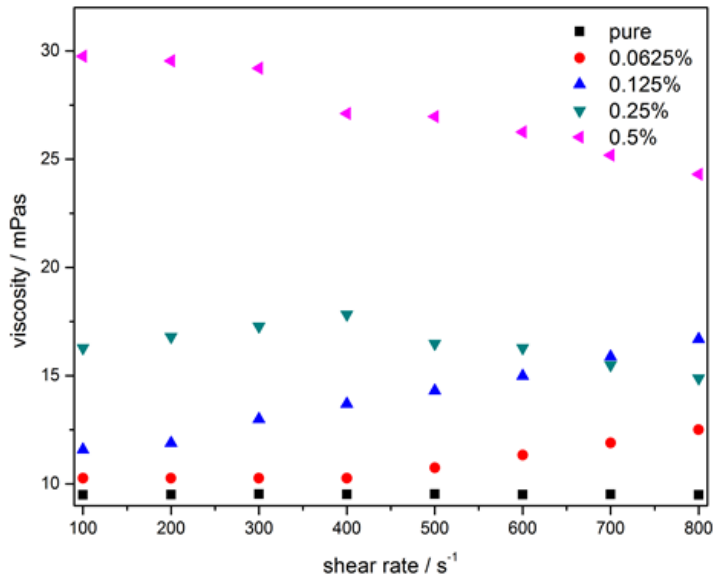

Fig 4-7 Shear viscosity of 25%EG-75%water based nano-suspensions as a function of shear rate at -10 ^{o}C.

When the temperature reduces to -15 ^{o}C, all samples exhibit the shear thinning behavior, except for the base liquid, as illustrated in Fig 4-8.

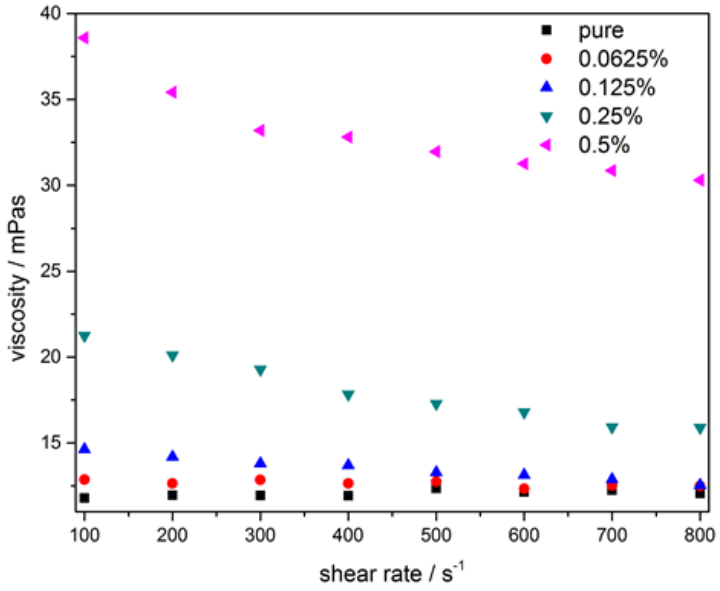

Fig 4-8 Shear viscosity of 25%EG-75%water based nano-suspensions as a function of shear rate at -15 °C.

Although significant difference can be seen in the rheological behaviors of 25/75 EG-water solution based nanofluids from that of the 20/80 samples, similar conclsusions could still be drawn, such as that the viscosity increases monotonously with the particle concentration given other conditions, and that the viscosity increases with decreasing temperature, due to the increased viscosity of 25 % EG-75 % water basefluid from 2.33 to 7.17, 9.50, and 11.80 mPa • s at 25 °C -5 °C, -10 °C and -15 °C, respectively.

Fig 4-9 shows the relative viscosity versus MCNT volume fraction at different temperatures from 25 °C to -15 °C, which is similar to the result shows in Fig 4-4 for the 20%EG-80%water based system. At 25 °C, the viscosity ratio increases from ~1 for 0.0625% concentration sample to 1.25 for the sample with 0.5 % particle concentration. This suggests a non-linear dependence of the viscosity ratio on the particle concentration.

A inspection of Fig 4-4 and Fig 4-9 also shows difference between them. First, the data set for -15 ^{o}C are not in Fig 4-4 as measurements were not done on the 20 % EG-80 % water based samples due to the freezing point. Second, the gap of the data points between -15 ^{o}C and -10 ^{o}C is much smaller than that between -10 ^{o}C and -5 ^{o}C. More discussion on this will be done in section 4.2.

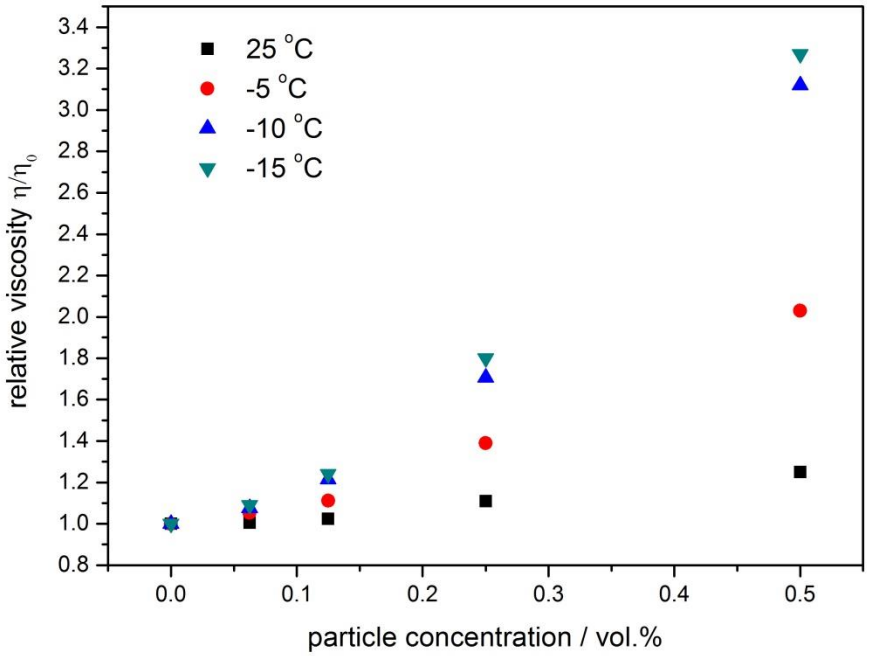

Fig 4-9 Relative viscosity of 25 % EG-75 % water based nanofluids at different tempeartures.

4.1.3 Rheological data for 30% EG-70% water based nano-suspensions

The measured dynamic viscosity data for the 30/70 EG-water based MCNT nanofluids containing different particle volume concentrations and plotted against shear rate in Fig 4-10 to Fig 4-13 at 25 ^{o}C, -5 ^{o}C, -10 ^{o}C and -20 ^{o}C, respectively. The data for 25 ^{o}C is similar to that shown in Fig 4-1 and Fig 4-5, namely, all of 30/70 EG-water based nanofluids behave like a Newtonian fluid.

Fig 4-11 shows clear shear thickenning behavior of the sample at -5 ^{o}C at a shear rate of ~400 s^{-1}, which is larger than that for the 25/75 EG-water sample (300 s^{-1}). Also, the extent of the shear thickening within the shear rate range tested is different. For example, the thickening extent for the 30/70

Eg-water with 0.25% particle is 14%, which is far lower than that for 25/75 system (38%) given other conditions.

All samples exhibit shear thining behavior at -10 ^{o}C to -20 ^{o}C as illustrated in Fig 4-12 and Fig 4-13.

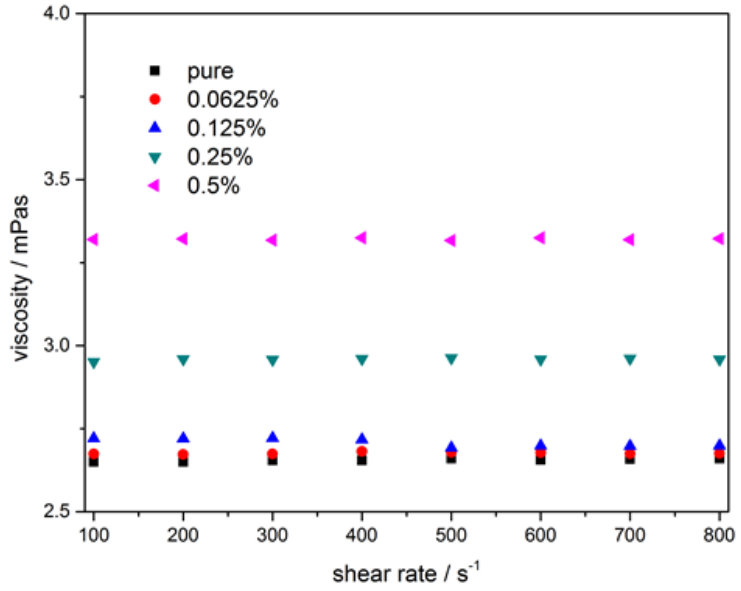

Fig 4-10 Shear viscosity of 30%EG-70%water based nano-suspensions as a function of shear rate at 25 ^{o}C.

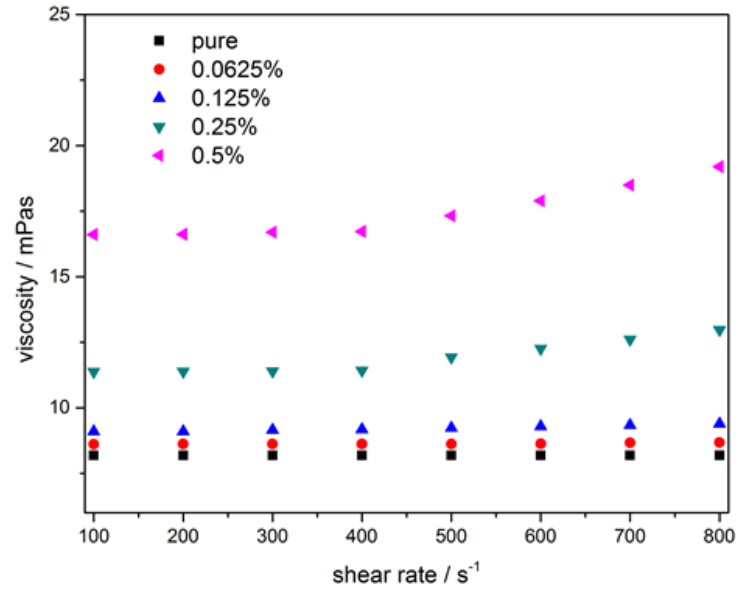

Fig 4-11 Shear viscosity of 30%EG-70%water based nano-suspensions as a function of shear rate at -5 ^{o}C.

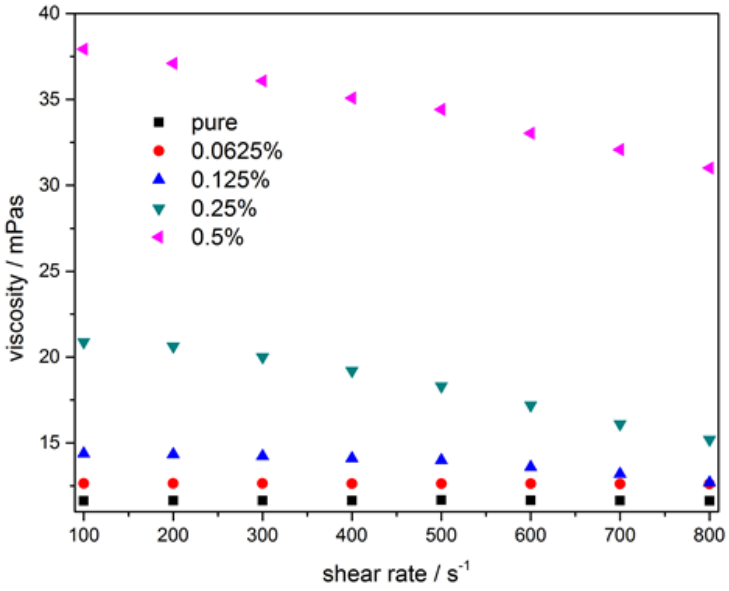

Fig 4-12 Shear viscosity of 30%EG-70%water based nano-suspensions as a function of shear rate at -10 ^{o}C.

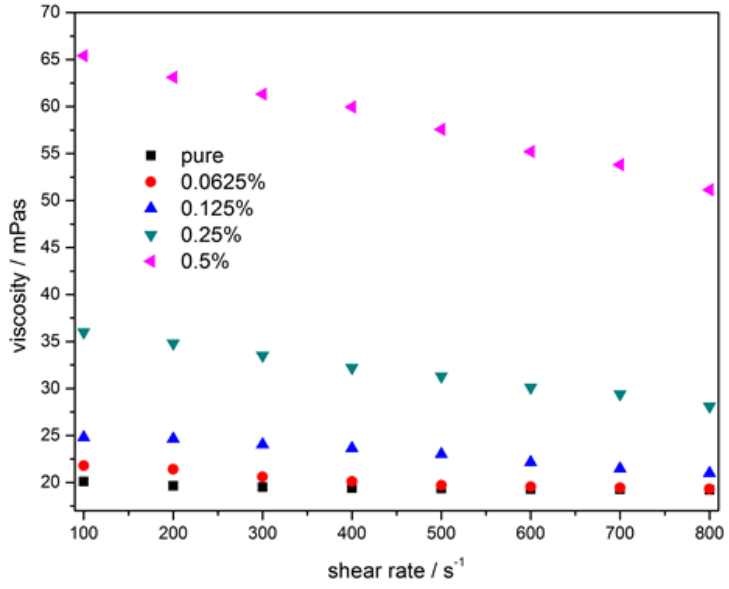

Fig 4-13 Shear viscosity of 30%EG-70%water based nano-suspensions as a function of shear rate at -20 ^{o}C.

Fig 4-14 plots the relative viscosity against MCNT particle volume concentration at 25 ^{o}C, -5 ^{o}C, -10 ^{o}C and -20 ^{o}C. An inspection of data at at 25 ^{o}C, -5 ^{o}C and -10 ^{o}C reveals that the relative viscosities of nanofluids at these temperatures are almost the same as that for 25/75 EG-water and 20/80 EG-water. For example, at 25 ^{o}C, the relative viscosities of the samples with 0.0625 % - 0.5 % concentrations are 1.01, 1.03, 1.12 and 1.25, respectively in Fig 4-9, and they are respectively 1.00, 1.01, 1.10, 1.25 as shown in Fig 4-4.

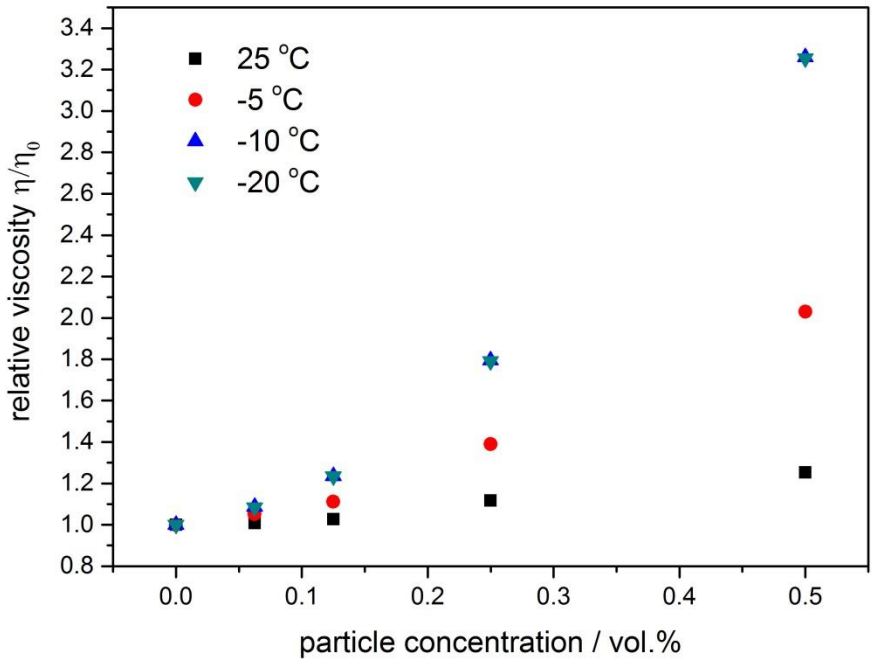

Fig 4-14 Relative viscosity of 30%EG-70%water based nanofluids at different tempeartures.

4.1.4 Rheological data for KCl-water nano-suspensions

This section presents the viscosity data for salt-water based nanofluids. The salt used in this work include KCl, NaCl, $MgCl_2$ and $CaCl_2$. The result are shown according to the type of salt used.

Fig 4-15, Fig 4-16 and Fig 4-17 show the shear viscosity of KCl-water based MCNT nanofluids at 25 ^{o}C, -5 ^{o}C and -10 ^{o}C is presented. At 25 ^{o}C, shear thinning behaviour occurs for all nanofluids. The results for -5 ^{o}C and -10 ^{o}C are similar. The results also indicate that the viscosity decreases with increasing temperature as expected.

The data shown in Fig 4-15, Fig 4-16 and Fig 4-17 can be reprocessed to give relative viscosity as a function of particle concentration. Fig 4-19 shows the results.

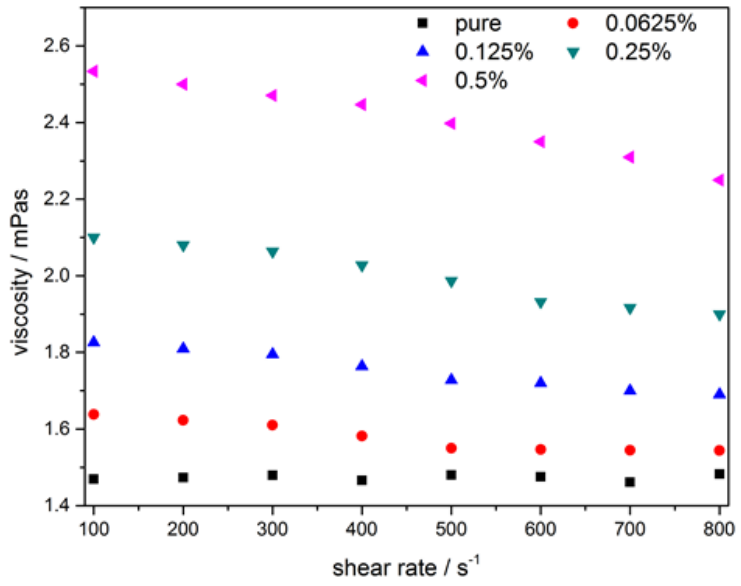

Fig 4-15 Shear viscosity of KCl-water based nano-suspensions as a function of shear rate at 25 ^{o}C.

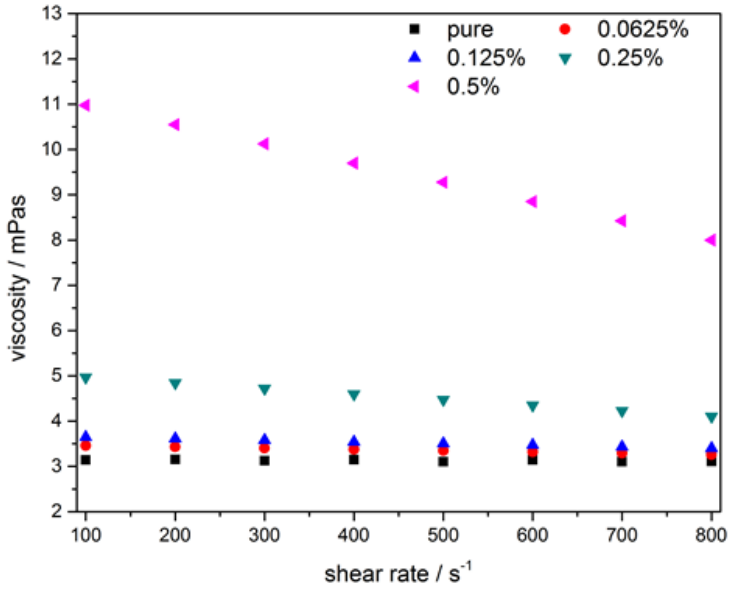

Fig 4-16 Shear viscosity of KCl-water based nano-suspensions as a function of shear rate at -5 ^{o}C.

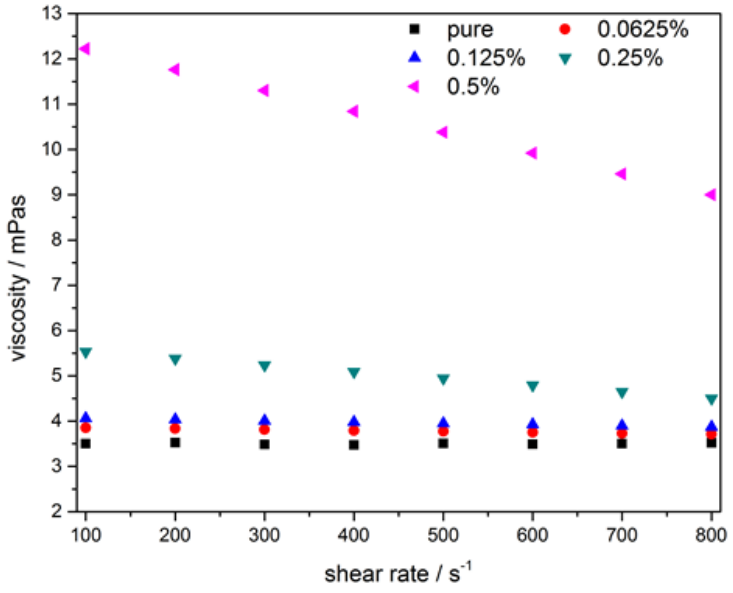

Fig 4-17 Shear viscosity of KCl-water based nano-suspensions as a function of shear rate at -10 ^{o}C.

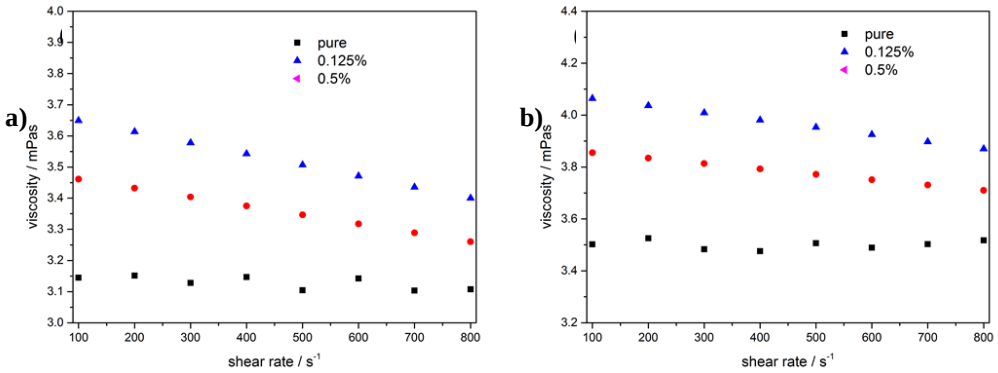

Fig 4-18 Partial enlarged viscosity data of low concentration samples at (a) -5 °C and (b) -10 °C

The dependence of the relative viscosity on particle concentration is similar in trend to that for EG/water based nanofluids as shown in Fig 4-4, Fig 4-9 and Fig 4-14, although the actual relative viscosity is higher for the KCl-water based nanofluids.

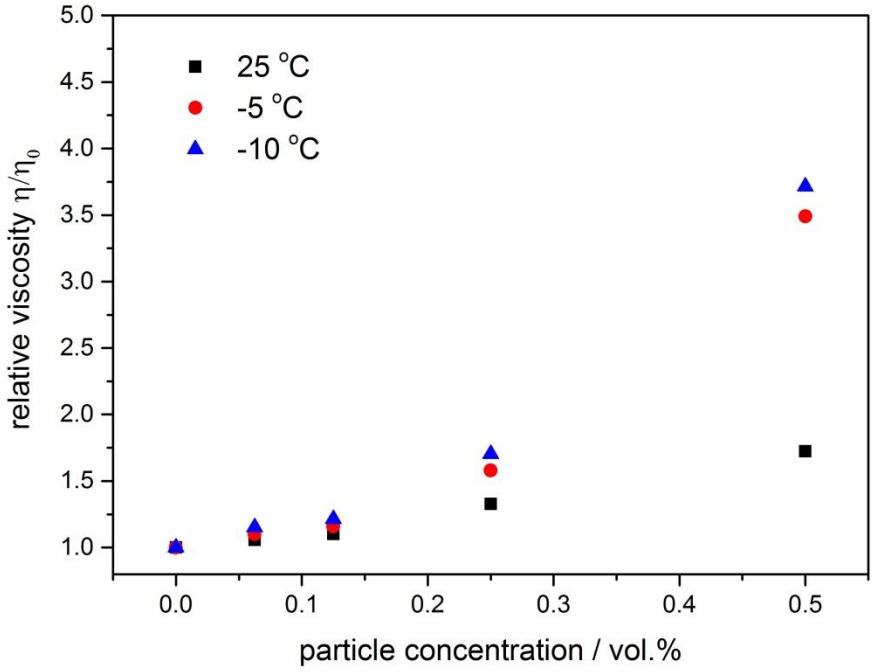

Fig 4-19 relative viscosity of KCl-water based nanofluids at different tempeartures.

4.1.5 Rheological data for NaCl-water based nano-suspensions

The shear viscosity of NaCl-water based MCNT nanofluids is shown in Fig 4-20, Fig 4-21 and Fig 4-22 at 25 ^{o}C, -10 ^{o}C and -20 ^{o}C. Clear shear thinning behaviour is seen, which is similar to the KCl-water based nanofluids. However, the viscositsy of NaCl-water based nanofluids is considerable higher than that of the NaCl-water based nanofluids, and the difference is 45.6 % and 64.6 % higher at 25 ^{o}C and -10 ^{o}C, respectively.

Rearrangement of the data in Fig 4-20, Fig 4-21 and Fig 4-22 gives the relative viscosity, which is illustrated in Fig 4-23. The Results are very similar in numeric values to that for KCl-water based nanofluids at 25 ^{o}C. However, recognizable distinctions can be seen between the KCl and NaCl systems when temperatre decreases to -10 ^{o}C and -20 ^{o}C. First, at -10 ^{o}C, the relative viscosity of NaCl-water based nanofluids is much lower than that of KCl-water based samples. For KCl based samples, the relative viscosities are 1.15, 1.21, 1.70 and 3.71 at 0.0625 %, 0.125 %, 0.25 % and 0.5 % particle volume concentration respectively, whereas the values for the NaCl-water based samples are respectively 1.08, 1.16, 1.39 and 1.98 at -10 ^{o}C. When temperature decreases to -20 ^{o}C (near the freezing point), the increase in the NaCl based nanofluids viscosity still keeps at a relatively low level compared to that of the KCl based nanofluids at a temperature near its own freezing point (-10 ^{o}C).

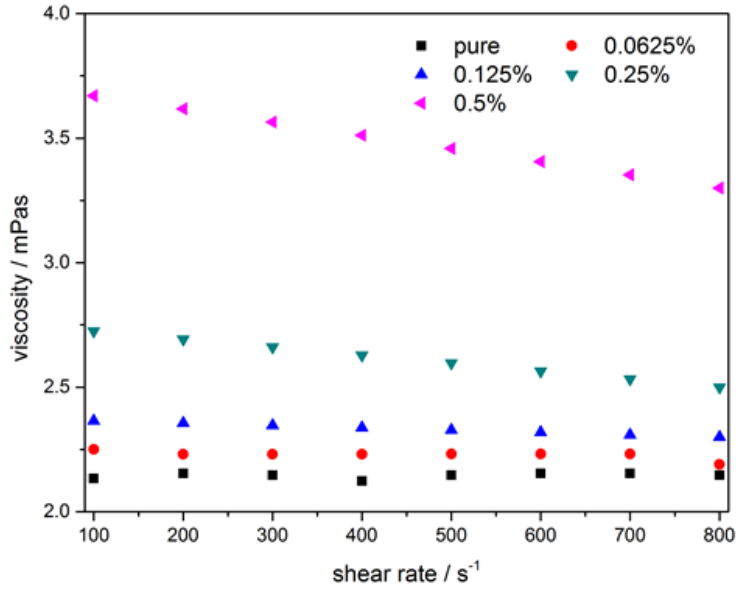

Fig 4-20 Shear viscosity of NaCl-water based nano-suspensions as a function of shear rate at 25 °C.

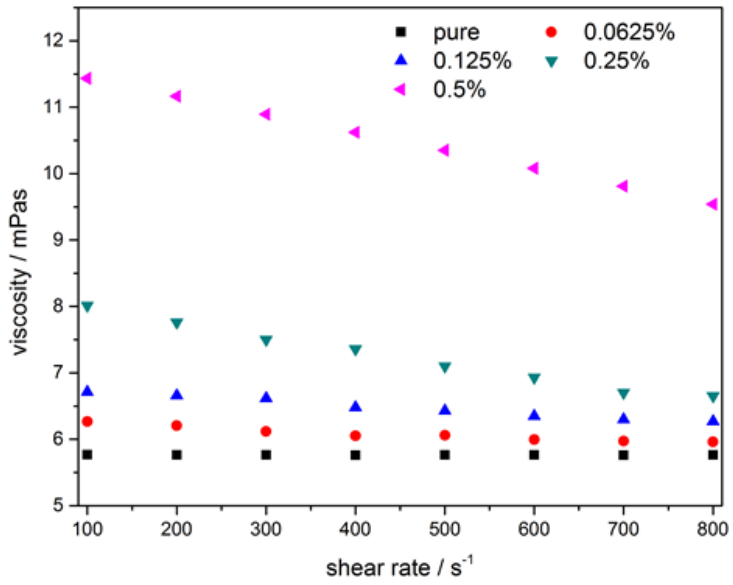

Fig 4-21 Shear viscosity of NaCl-water based nano-suspensions as a function of shear rate at -10 °C.

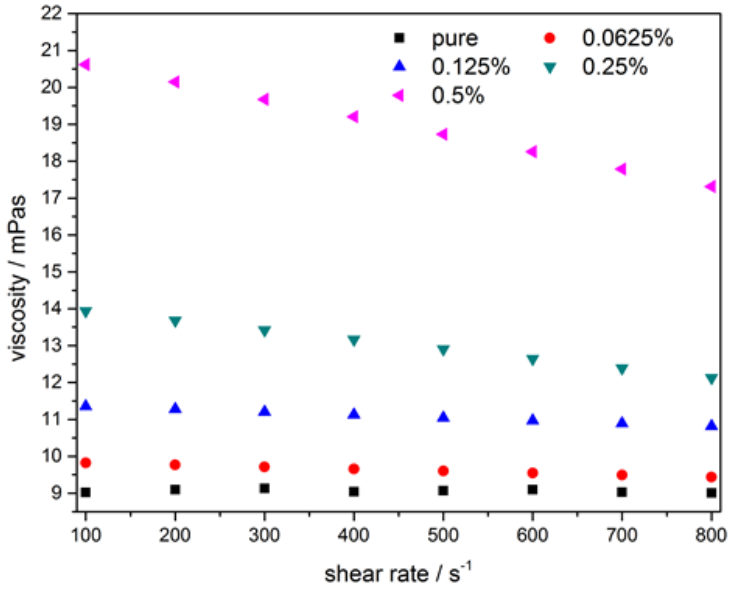

Fig 4-22 Shear viscosity of NaCl-water based nano-suspensions as a function of shear rate at -20 ^{o}C.

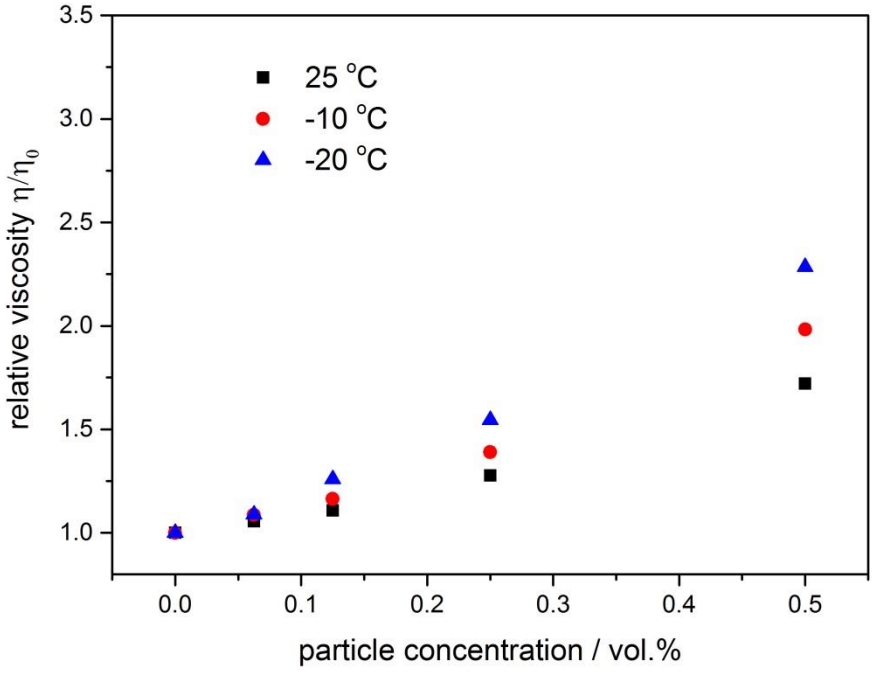

Fig 4-23 Relative viscosity of NaCl-water based nanofluids at different tempeartures.

4.1.6 Rheological data for $MgCl_2$-water based nano-suspensions

The measured shear viscosity of $MgCl_2$-water based MCNT nanofluids is plotted against shear rate in Fig 4-24,Fig 4-25, Fig 4-26 and Fig 4-27 for 25 ^oC to -30 ^oC. The viscosity is 4.12, 14.20, 24.21 and 43.12 mPa • s at 25 ^oC, -10 ^oC, -20 ^oC and -30 ^oC respectively. These are over twice as that of the NaCl-water basefluid, which is respectively 2.14, 5.76 and 9.01 mPa • s at 25 ^oC, -10 ^oC and -20 ^oC.

Similar to the KCl-water and NaCl-water based nanofluids, shear behaviour is shown at all temperature investigated. The results of shear thinning is a function of particle concentration with a higher particle concentration giving a more considerable extent of shear thining as reflected by the slopes.

The relative viscosity of $MgCl_2$-wate based nanofluids are plotted against particle concentration in Fig 4-28. At 25 ^oC, an almost linear dependence can be seen of the relative viscosity on the particle concentration, which is different from that for the NaCl and KCl based nanofluids. A similar trends can be observed at -10 ^oC, -20 ^oC and -30 ^oC.

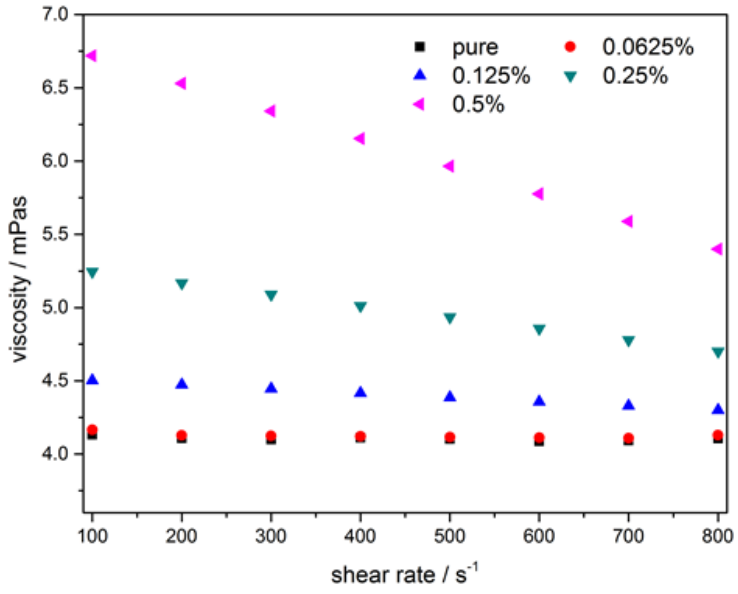

Fig 4-24 Shear viscosity of $MgCl_2$-water based nano-suspensions as a function of shear rate at 25 ^oC.

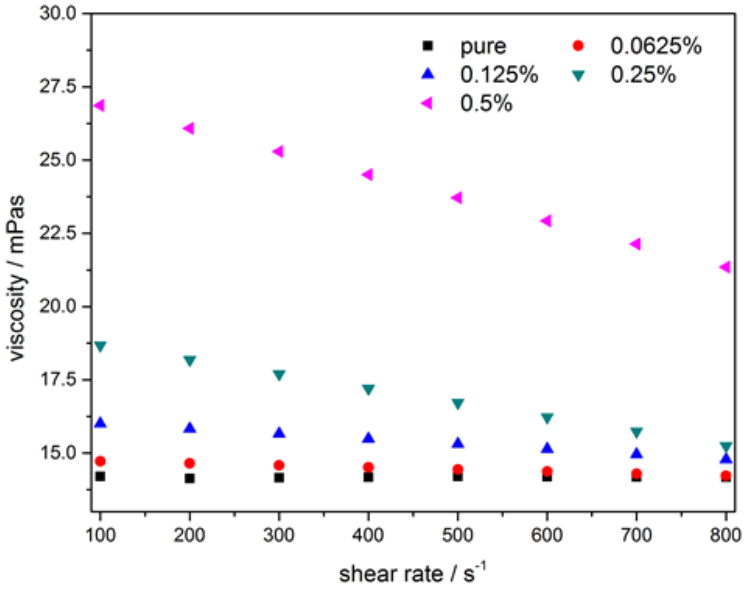

Fig 4-25 Shear viscosity of $MgCl_2$-water based nano-suspensions as a function of shear rate at -10 ^oC.

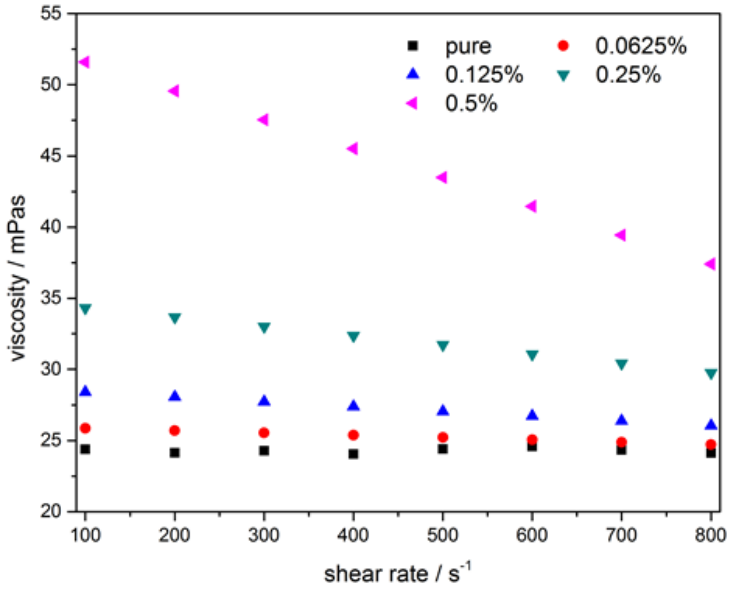

Fig 4-26 Shear viscosity of $MgCl_2$-water based nano-suspensions as a function of shear rate at -20 ^oC.

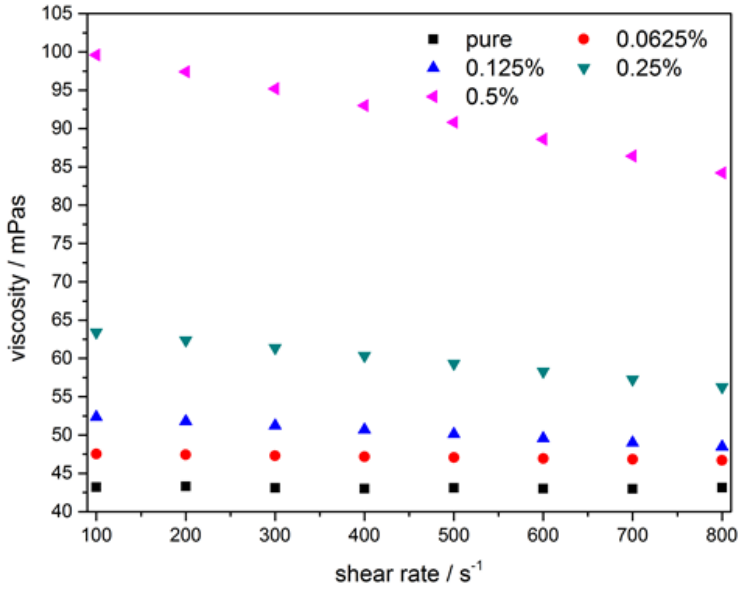

Fig 4-27 Shear viscosity of $MgCl_2$-water based nano-suspensions as a function of shear rate at -30 ^oC.

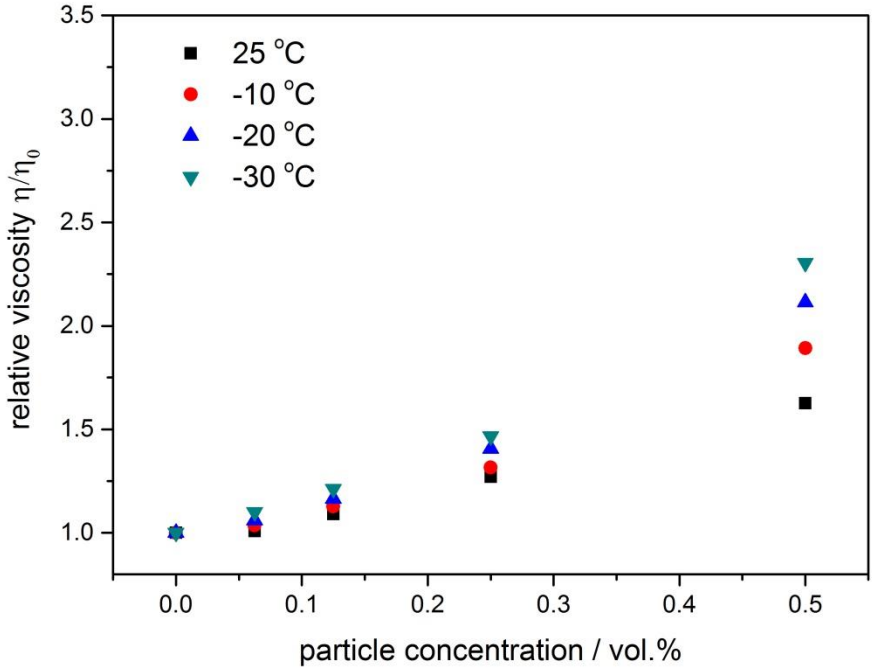

Fig 4-28 Relative viscosity of $MgCl_2$-water based nanofluids at different tempeartures.

4.2 Discussion of the experimental results

Further analysis and discussion on the experimental data presented in 4.1 are performed in this section. First, the data are compared with models for suspensions of nanoparticles. An attempt is then made to fit the data to the most suitable model. Finally, the fitting parameters are linked to the microstructure of particles that may form in the suspensions. The eventual goal is to interpret the experimental data using fundamental physics.

4.2.1 Comparison of experimental data with viscosity models

In Table 4.1, several well-known models of viscosity of nanofluids are listed where the range of applications is also given. Fig 4-29 compares the experimental data for 20/80 EG/water nanofluids with these models at 25 ^{o}C.

Table 4.1 list of viscosity models of suspension containing nano-sized particles.

Model	Expression	Remarks
Einstein[158]	$\eta = \eta_0(1 + 2.5\varphi)$	Applicable for relatively low particle concentration suspensions in which particles are spherical and non-interacting
Batchelor[158]	$\eta = \eta_0(1 + 2.5\varphi + 6.5)$	Applicable for semi-dilute suspensions in which interaction of pair-particles are considered.
Krieger-Dougherty[158]	$\eta = \eta_0(1 - \frac{\varphi}{\varphi_m})^{-[\eta]\varphi_m}$	Full range of concentration of particles，[η] is the intrinsic viscosity with a typical value of 2.5，φ_m is the maximum particle packing fraction.

Modified Krieger-Dougherty[158]	$\eta = \eta_0\left(1-\frac{\varphi_a}{\varphi_m}\right)^{-[\eta]\varphi_m}$ $\varphi_a = \varphi(\frac{r_a}{r})^{3-D}$	Aggregation of particles are considered, r_a and r are the radius of the cluster of particles and primary partilce respectivley, D is the fractal index

Fig 4-29 (a) shows clearly that the Einstein equation, Batchelor equation and Krieger-Dougherty equation all fail to predict the experimental data. An underestimate can be seen for all particle concentration and difference increases with increasing particle concentration. If the low particle concentration region is reproduced with a higher resolution, Fig 4-29 (b) is obtained. One can see that all model reduce to Einstein model at very low particle concentration.

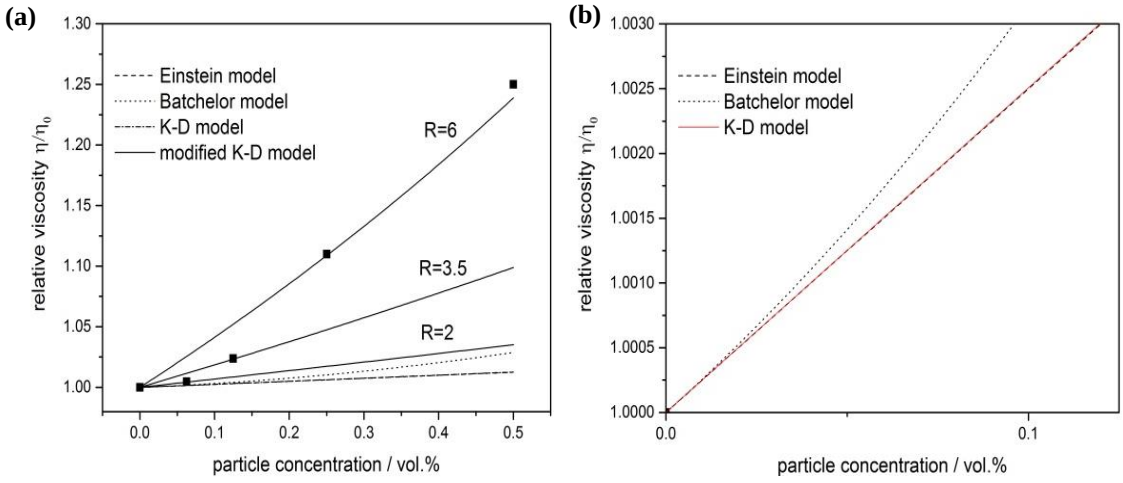

Fig 4-29 Viscosity of 20/80 EG-water-MCNT nanofluids against particle volume fraction at 25 ^{o}C for (a) the whole concentration range, (b) the low concentration range up to 0.125%.

The modified form of K-D equation however can agree well with the experimental data if a right R value is used; see the solid line in Fig 4-29 (a). Detailed explanation of modified K-D equation is

following: η_0 is the viscosity of basefluid, φ_a is the concentration of clusters, which can be calculated by $\varphi_a = \varphi(\frac{r_a}{r})^{3-D}$, where r_a and r is the radius of cluster and particle respectively, φ is the concentration of particle, D is fractal index, which is considered in the range from 1.6 to 1.9 for nanofluids[141]. φ_m is the maximum particle packing fraction, taken between 0.505 to 0.705 due to different shapes of nanoparticle[159]. Fig 4-29 (a) shows a R value of 2 for 0.0625 % sample, 3.5for 0.125 % sample and 6 for 0.25 % and 0.5 % samples, implying that a higher particle concentration gives a larger effective aggregate size.

4.2.2 Further discussion on the modified K-D model

As illustrated in section 4.2.1that the modified K-D model can match the measured viscosity data at 25 ^{o}C for 20/80 EG-water-MCNT nanofluids by adjusting the R value. More discussion is therefore focused on this model for all EG/water and salt/water based nanofliuds at all temperatures.

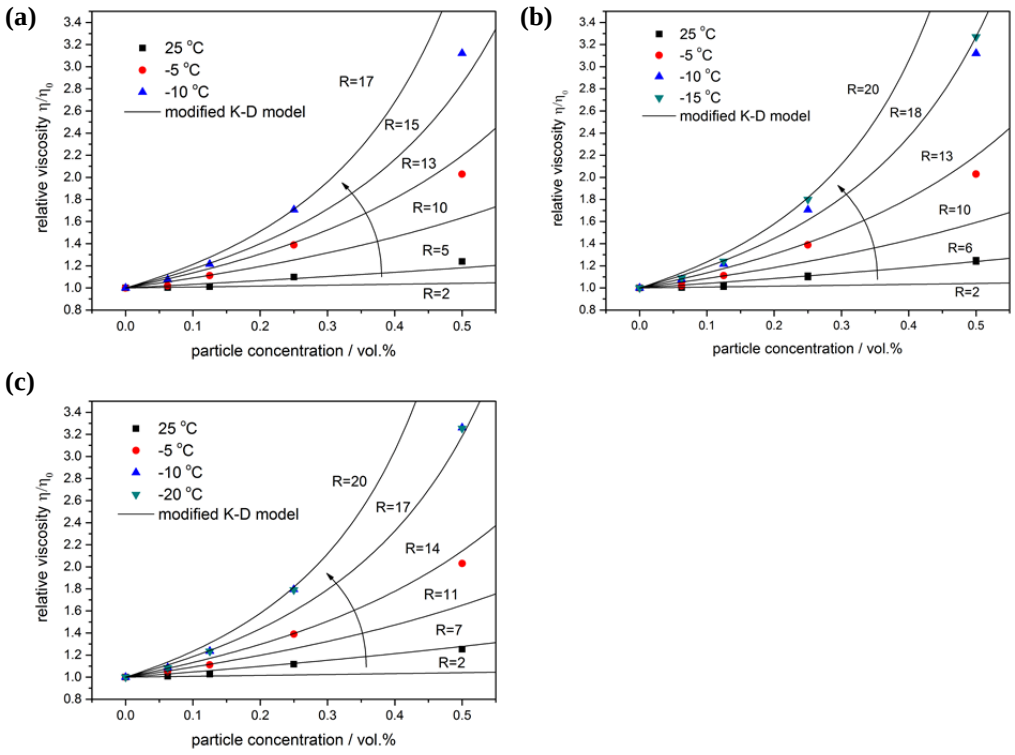

Fig 4-30 Modified K-D model predictions vs experimental data for (a) 20/80, (b) 25/75 and (c) 30/70 EG-water based MCNT nanofluids.

Look at Fig 4-30 (a) first, which is for 20/80 EG-water based nanofluids, the relative viscosity at 25 ^{o}C for the 0.0625 % and 0.125 % samples follows the modified K-D model very well with R=2. This implies that at the room temperature, most of the MCNT particles in the dilute suspensions keep separate from each other with very slight aggregation. As particle concentration increases to 0.25 % and 0.5 %, while temperature is kept at 25 ^{o}C, the fitting parameter R increases to approximately 5, indicating that individual MCNT particles starts aggregating with their close neighbours leading to larger effective cluster dimensions. When the temperature is reduced to -5 ^{o}C, the viscosity data agree with modified K-D model, but the effective cluster size values are higher at at -5 ^{o}C, which are 10 for 0.0625 % and 0.125 % samples and 13 for 0.25 % and 0.5 % samples, respectively. At -10 ^{o}C, the modified K-D model can also reproduce the measured viscosity data for 0.0625 %, 0.125 %, 0.25 % and 0.5 % nanofluids, but corresponding R values are a lot higher, at 13, 15, 17 and 17, respectively.

From the above fitting results, one could obtain two main conclusions, one is that the effective cluster size of nanoparticles is different at a different particle concentration. MCNT particles in concentrated nano suspensions will form larger clusters than that in a dilute nano suspensions. However, there are two data point in Fig 4-30 (a), which are 0.5 % sample at -5 ^{o}C and -10 ^{o}C. The two points are lower than the corresponding predicted line. There are two possible reasons, one is that the large cluster might break to give two or more parts, leading to the reduction in the effective cluster size. The second reason may be associated with the fractural index value D in the modified K-D equation. Even the effective cluster size R keeps unchanged, the change of D value from 1.55 to 1.6 could lead to the lower viscosity as shown on the figure. .

Look now at Fig 4-30 (b) for the relative viscosity of 25/75 EG-water based MCNT nanofluids with the fitted lines by the modified K-D model. A similar trend can be observed as shown Fig 4-30 (a). The effective cluster size R at 25 ^{o}C, -5 ^{o}C and -10 ^{o}C are respectively 6, 13 and 18. It is also noticed that when the temperature drops to -15 ^{o}C, close to the freezing point, the growing rate of the effective cluster size slows down. This could be contributed to the relatively stable structure of the base fluid close to the freezing point which constrains the movement of the MCNT particles, and hence the inhibition of the aggregation process.

Finally, look at Fig 4-30 (c), the validity of the modified K-D model to explain the viscosity increase is further shown. The lowest temperature is now reduced to -20 ^{o}C due to the use of the 30/70 EG-water as the basefluid. One can see relatively small differences of viscosity increase with different EG-water ratio at a given temperature. The effective cluster size of the 30/70 EG-water based samples increases slightly because the more the EG in the basefluid, the higher the viscosity, and hence the harder the Brownian motion to keep particles away from each other, leading to a larger cluster size in 30/70 water-EG based MCNT nanofluids.

Inspection of Fig 4-30 suggests a common phenomenon at the lowest measurement temperature, for example, -15 ^{o}C in Fig 4-30 (b) and -20 ^{o}C in Fig 4-30 (c), the fitted effective cluster size stops becoming larger with cooling. An extreme example is that, at -20 ^{o}C, the relative viscosity of 30/70 EG-water based nanofluids are nearly identical with that at -15 ^{o}C, indicating an almost constant fitted effective particle cluster size. This is because the viscosity of the basefluid at low temperatures, particularly at freezing point is very high, and the Brownian motion and self-diffusion motion are both contained at a very low

level. Therefore, high resistance and low kinetic energy together contribute to the relatively stable cluster sizes of the nanoparticles at low temperatures.

Fig 4-31 shows the measured relative viscosity data of salt-water based MCNT nanofluids at different temperatures together with the fitted curves using the modified K-D model.

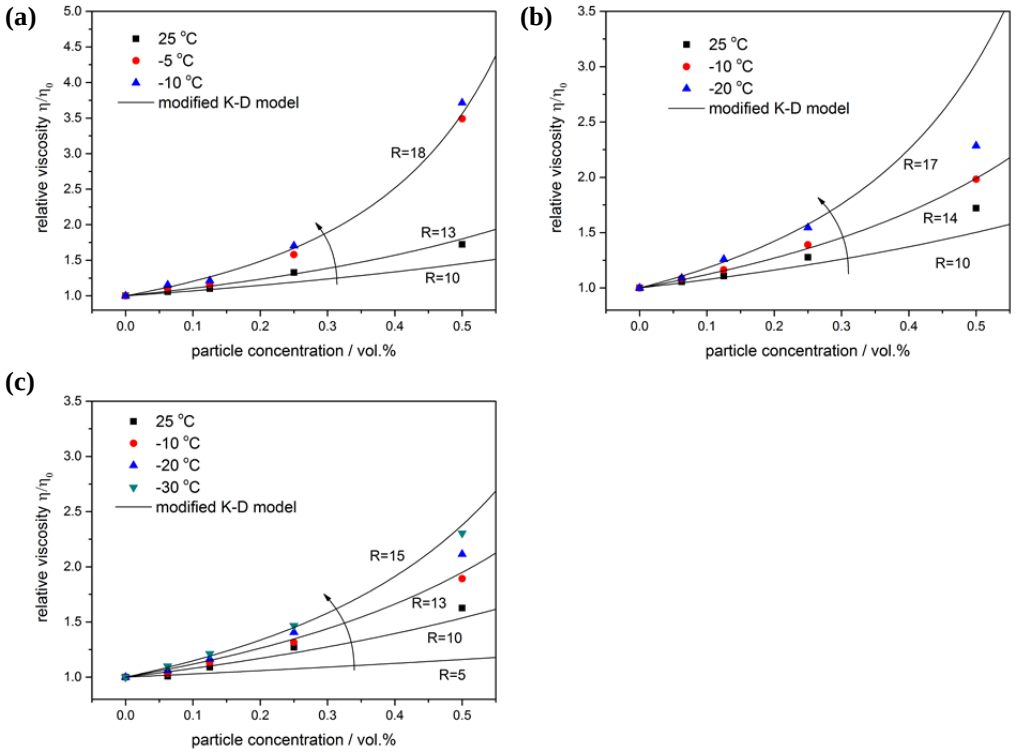

Fig 4-31 Modified K-D model fitting of viscosity data for (a) KCl, (b) NaCl and (c) $MgCl_2$ aqueous solution based MCNT nanofluids.

In Fig 4-31 (a), shows the viscosity data of KCl-water based MCNT nanofluids at 25 ^{o}C, -5 ^{o}C and -10 ^{o}C, together with K-D model fitting. One can notice that the relative viscosity agrees well with the modified K-D model; but the effective cluster size value R is much larger than that for EG-water based samples. The R value is 10 for the 0.0625 % MCNT sample at the room temperature, which is 5 times that of the EG-water based sample. The effective cluster size increases to 13 for 0.25 % and 0.5 % samples. Such a huge difference of R value between the KCl-water and the EG-water based samples is attributed to the

difference in composition of their basefluids. The particles in the EG-water based samples are stabilized by the electrostatic repulsive force. On the contrary, the KCl-water based nanofluids have a high ion concentration compressed the electrical double layers around, leading to a much larger effective cluster size.

When the temperature reduces to -5 ^{o}C, the R value increases to 13 for 0.0625 % and 0.125 % samples, and to 18 for 0.25 % and 0.5 % samples, which are clearly It is clear much larger than that of EG-water based nanofluids at the same temperature. When the temperature decreases to -10 ^{o}C, the relative viscosity data give a fitted R value of 18, which is only slightly larger than that at -5 ^{o}C. Such a small difference in the relative viscosities of the KCl-water based nanofluis between -5 ^{o}C and -10 ^{o}C is probably because that the aggregation extent of MCNT has already reached the upper limit at -5 ^{o}C with an effective cluster size of 18, and the cluster structure becomes fragile when it exceeds the upper limit. This explanation could also apply to the EG-water based nanofluids, for which the upper limit of all EG-water based samples were observed.

In Fig 4-31 (b) shows the results of NaCl-water based MCNT nanofluids at 25 ^{o}C, -10 ^{o}C and -20 ^{o}C respectively. At 25 ^{o}C, the fitted R to the modified K-D model gives a value between 10 and 14.This is similar to the data in Fig 4-31 (a), suggesting that the Na^{+} and Cl^{+} ions play a similar role in compressing the electrical double layer, leading to a similar aggregation extent of MCNT in the nanofluids. However, a difference is observed when temperature is -10 ^{o}C; the fitted R value of NaCl-water based nanofluids is 14, which is smaller than that of KCl-water based nanofluids which is 18. This could be contributed to the difference in the viscosity of the two types of basefluid. At -10 ^{o}C , the

viscosity of the KCl-water basefluids is 3.51 mPa • s while that of the NaCl based nanofluids is 5.76 mPa • s. A high viscosity gives a weak self-diffusion of MCNT making the particles to have a low kinetic energy to move through the liquid to meet other particle at very low temperature. As a result, the extent of aggregation in the NaCl-water nanofluids is lower than that in the KCl-water nanofluids.

Although the cluster size of the KCl-water samples is different from that of the NaCl-water system at -10 ^{o}C, the upper limit of the effective cluster size seems unaffected by the basefluids and the fitted R value is around 17 for NaCl-water based nanofluids, which is very close to that of the KCl-water nanofluids. This can be explained by using the DLVO theory. The electrical double layer of a particle is compressed when ions are added, and the extent of compression is related to the valence of the ions for which bot the NaCl and KCl only have monovalent ions. In specific, ions of the electrolyte have higher valence will have stronger repulsive force on the ions located in the diffusion layer, thus cause thinning of this layer. In this comparative experiment case, the electrolyte that we used to prepare the cold storage basefluid are KCl and NaCl, both of them has only monovalent ions in their aqueous solution.

In Fig 4-31 (c) shows the result of $MgCl_2$-water based MCNT nanofluids at 25 ^{o}C, -10 ^{o}C, -20 ^{o}C and -30 ^{o}C respectively. Comparing the data in Fig 4-31 (a) and (b), one can easily observe that the fitted R values of $MgCl_2$-water based MCNT nanofluids are very similar with that in NaCl-water based samples, and are smaller than that of the KCl-water based nanofluids. These results do not agree with what the DLVO theory predicts for the $MgCl_2$-water based MCNT nanofluids. The R value of $MgCl_2$-water nanofluids should be larger than that of the NaCl and KCl based nanofluids because $MgCl_2$ solutions have Mg^{2+} and Cl^{-} ions and the valence of the magnesium ion is +2.

The fitted R value in $MgCl_2$-water system are almost constant and are smaller than that of the NaCl and KCl nanofluids. Such controversial findings indicates a doubt about validity of both the modified K-D model and the DLVO theory in salt-water nanofluids. The results of this work, however, are insufficient for in-depth discussion on the validity of the DLVO theory and as a result, the following discussion is focused on the K-D model.

The modified K-D model is expressed as: $\eta = \eta_0 \left(1 - \frac{\varphi_a}{\varphi_m}\right)^{-[\eta]\varphi_m}$, where $\varphi_a = \varphi(\frac{r_a}{r})^{3-D}$. One can see that the effective viscosity is determined by three main factors; R, the ratio of r_a to r; D, the fractal index; and φ_m, the maximum packing fraction. The physical meaning of R is easy to understand, it reflects how relatively big the cluster is. D indicates the geometrical properties of a cluster structure. Normally, higher D value means denser structure and higher surface coverage area. Clearly, the use of the R value is not sufficient to reflect the aggregation structure of MCNTs in the nanofluids. The value of D and φ_m also need to define. Based on this thought, the fitting parameters of all the salt-water based MCNT nanofluids are listed for 25 ^oC , -10 ^oC , and -20 ^oC in Table 4.2 to Table 4.4.

Table 4.2 Fitting parameters of salt -water based MCNT nanofluids at 25 ^oC

	KCl-water				NaCl-water				$MgCl_2$-water			
sample	η/η_0	R	D	φ_m	η/η_0	R	D	φ_m	η/η_0	R	D	φ_m
0.0625 %	1.06	10	1.7	0.405	1.05	10	1.7	0.405	1.01	10	1.75	0.605
0.125 %	1.10	10	1.7	0.405	1.11	10	1.7	0.405	1.09	10	1.75	0.405
0.25 %	1.33	12	1.7	0.405	1.28	11	1.7	0.405	1.27	12	1.75	0.405
0.5 %	1.72	12	1.73	0.405	1.72	12	1.73	0.405	1.63	12	1.75	0.405

First, look at the KCl-water based nanofluids at 25 ^{o}C, the fitting parameters of low particle concentrations (0.0625 % and 0.125 %) are the same, with R=10, D=1.7, φ_m=0.405. When particle volume fraction increases to 0.25 %, the effective cluster size R increases to 12 whilst the fractural index D and the maximum packing parameter φ_m keep the same, suggesting the cluster size in the 0.25 % sample increases while the distribution of MCNT in individual clusters and the shape of the clusters have not changed At the highest particle volume concentration investigated in this work, 0.5 %, the R value does not go greater but the fractural index D increases slightly from 1.70 to 1.73. This suggests that the MCNT particle in the clusters formed in the 0.5 % sample are more densely packed. To illustrate how we predict the MCNT aggregation structure with the varying value of R and D in modified K-D model, a brief schematic is drawn as shown in Fig 4-32 illustrates how the aggregated structure changes with varying values of R and D of the modified K-D model. An increase in the R value implies that the total length of the clusters increases, whereas an increased value of D implies more MCNT particles are packed within the clusters.

Focus is now on the columns of the NaCl-water and $MgCl_2$-water nanofluids for which most data are similar and the data could be explained in a similar manner. For example, the effective cluster size in the 0.5 % sample is larger than that in 0.25 % sample due to a large R. On the other hand, the MCNT particles are distributed more evenly in the 0.5 % samples because the D value is larger.

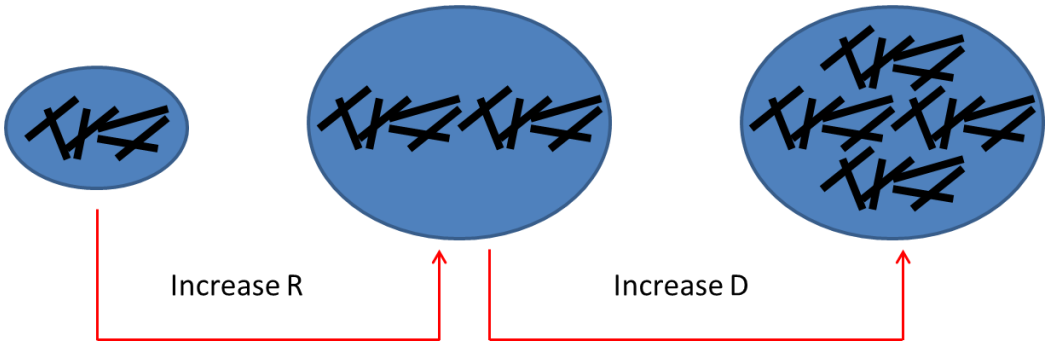

Fig 4-32 A schematic illustration of MCNT clusters with changing R and D.

A specific data point can be seen in the $MgCl_2$-water system at a particle volume fraction of 0.0625 %, with the R, D and φ_m respectively being 5, 1.8 and 0.605, which are very different from that of the KCl-water and NaCl-water samples. The structure of the clusters of this case is speculated to be in Fig 4-33. First look at the left-hand, the MCNTs are aggregated and aligned in one (horizontal) direction, which gives a large effective cluster size R, with a low D because the rest part of the effective cluster volume is empty and a low φ_m due to the elliptic shape of the cluster. On the contrary, low R and φ_m values and and a high D value lead to a more spherical and more dense structure of MCNT clusters as shown in the right-hand side of Fig 4-33.

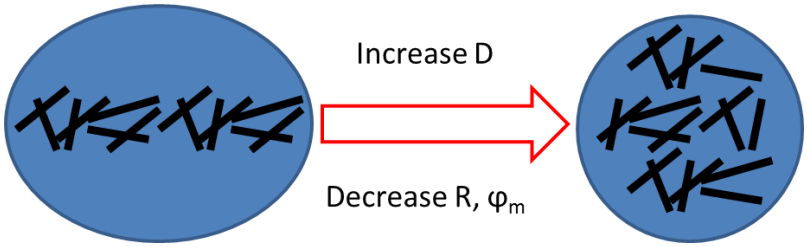

Fig 4-33 Schematic of cluster shape changing

Attention is paid to Table 4.2, one can see that the viscosity (1.01) although the sample has the same particle concentration as the other two samples. This could be explained by a smaller radius and a more spherical shape of the cluster supported by the fitted R, D and φ_m values. For the case shown in the last

row of Table 4.2, all three samples have the same R value but different D values of 1.73, 1.73 and 1.75. This could be explained as that the individual clusters have the same size but there are fewer such clusters in the $MgCl_2$-water based samples, and hence the lower effective viscosity increase in $MgCl_2$-water-0.5 % MCNT nanofluids.

Table 4.3 compare the fitting parameters of all salt solution based nanofluids at -10 ^oC. Comparing with the data in Table 4.2, the fitting parameters of R, D and φ_m have significantly changed, suggesting changes of the structure of the MCNT cluster with temperature. Look at the data of the KCl-water samples in Table 4.2 and Table 4.3. One can easily find that the clusters of MCNT grow significantly and the ellipticity of the clustersalso increase when temperature reduces from 25 ^oC to -10 ^oC. These results provide an explanation of the changes of the fitting parameters of the modified K-D model and hence the high relative viscosity at the KCl-water based MCNT nanofluids at -10 ^oC.

Table 4.3 Fitting parameter of salt-water based MCNT nanofluids at -10 ^oC.

	KCl-water				NaCl-water				$MgCl_2$-water			
sample	η/η_0	R	D	φ_m	η/η_0	R	D	φ_m	η/η_0	R	D	φ_m
0.0625 %	1.15	18	1.72	0.365	1.09	14	1.75	0.390	1.04	9	1.75	0.50
0.125 %	1.21	18	1.72	0.365	1.16	14	1.75	0.390	1.13	13	1.7	0.40
0.25 %	1.70	18	1.72	0.365	1.38	14	1.75	0.390	1.31	13	1.7	0.40
0.5 %	3.71	18	1.72	0.365	1.98	14	1.75	0.390	1.89	13	1.7	0.40

Attention is then paid to the results of different suspensions in Table 4.3 particularly the shape of MCNT clusters. Firstly, one can notice that the fitting parameters of each of the salt solutions do not vary with the particle volume fraction except for 0.0625 % $MgCl_2$-water nanofluid. It is therefore reasonable to assume that the structure of MCNT clusters are approximately the same for a given salt solution at -10 ^oC.

When temperature is -20 ^oC, the KCl-water is excluded from the contrast group because it becomes solid at this temperature. Then, the relative viscosity data Table 4.4 shows that at low temperature the effective cluster size of MCNT in a given salt solution is becoming larger, this relationship between temperature and cluster size has the same trend in EG-water based nanofluids.

Table 4.4 fitting parameter of salt-water based MCNT nanofluids at -20 ^oC.

	KCl-water				NaCl-water				$MgCl_2$-water			
sample	η/η_0	R	D	φ_m	η/η_0	R	D	φ_m	η/η_0	R	D	φ_m
0.0625 %	N/A	N/A	N/A	N/A	1.09	14	1.75	0.390	1.06	11	1.75	0.45
0.125 %	N/A	N/A	N/A	N/A	1.26	17	1.72	0.390	1.16	14	1.7	0.395
0.25 %	N/A	N/A	N/A	N/A	1.54	17	1.72	0.390	1.40	14	1.7	0.395
0.5 %	N/A	N/A	N/A	N/A	2.28	17	1.78	0.400	2.11	14	1.72	0.395

To summarise, an attempt has been made in this section to analyse the experimental data using the modified K-D model and interpret the results using the cluster structure and their changes under different conditions.

4.2.3 Microstructure of particle clusters and rheological behavior

In this section, the rheological behavior of both EG-water and salt-water based MCNT nanofluids is discussed. An attempt is to demonstrate the formation and deformation of microstructures of the MCNT clusters in a dynamic process using the flow behavior.

The rheological data presented before in section 4.1 show three different types of shear behavior; Newtonian, shear-thinning and shear thickening. Such shear behavior is related to particle structure, as demonstrated in the previous section of this study. To simplify the analysis, only the data of such a set of results of 30 % EG-70 % water based nanofluids are taken as an example, and are representative, which includes all three types of shear behavior and covers a wide temperature range from 25 ^{o}C to -20 ^{o}C.

First, a dimensionless Peclet number is introduced, which is defined as the ratio of the rate of advection by the flow to the rate of diffusion by the Brownian motion in a nanofluids. The expressions of the Peclect number, Pe, of nanofluids containing sphere or rod particles are given respectively in the following:

spherical particle:

$$P_e = \frac{6\pi\eta_m\dot{\gamma}a^3}{k_BT} \qquad \text{Eq.4-1}$$

rod-like particle:

$$P_e = \frac{\pi\eta_m\dot{\gamma}L^3}{3k_BT(\ln(L/d)-0.8)} \qquad \text{Eq.4-2}$$

where η_m is the dynamic viscosity of the basefluid, $\dot{\gamma}$ is the shear rate, a is the radius of the sphere, L is the length of the rod-like particles, d is the diameter of the rod, T is temperature and k_B is the Boltzmann

constant. The rheological behaviour is plotted against Pe in Fig 4-34 to Fig 4-37 at different temperatures.

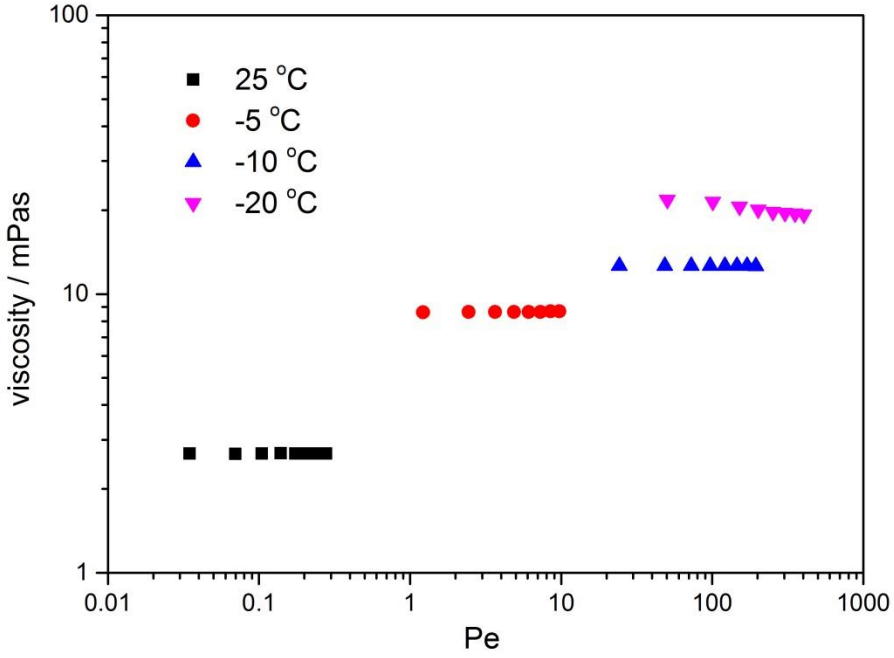

Fig 4-34 Shear viscosity of 30/70 EG-water-0.0625% MCNT nanofluids as a function of Pe at different temperatures.

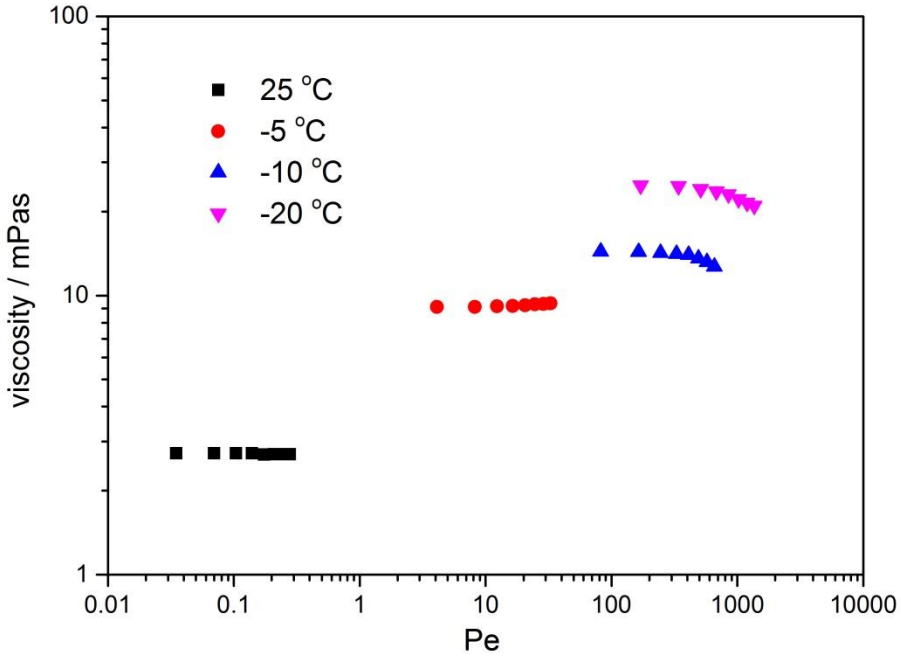

Fig 4-35 Shear viscosity of 30/70 EG-water-0.125% MCNT nanofluids as a function of Pe at different temperatures.

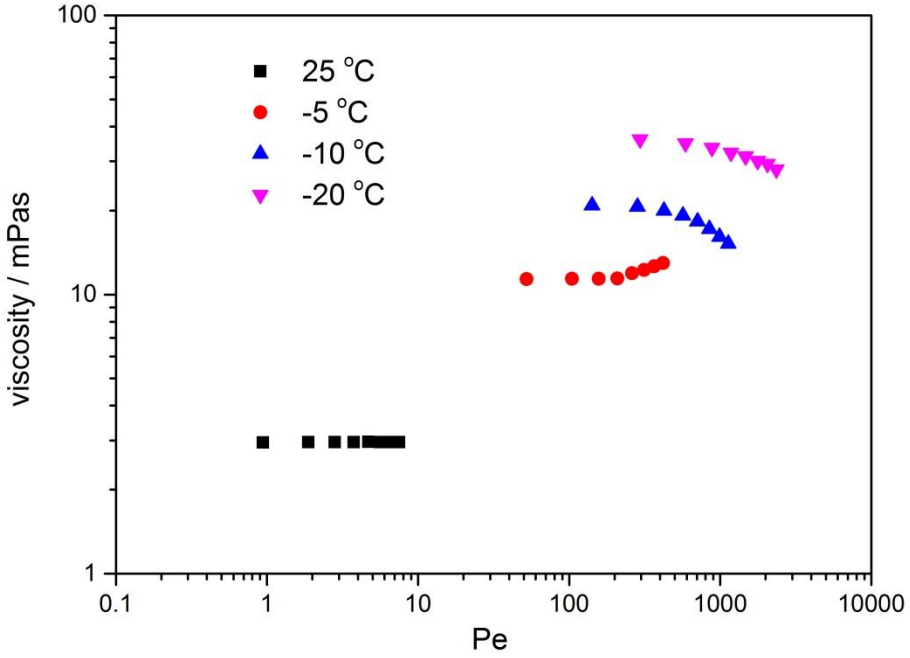

Fig 4-36 Shear viscosity of 30/70 EG-water-0.25% MCNT nanofluids as a function of Pe at different temperatures.

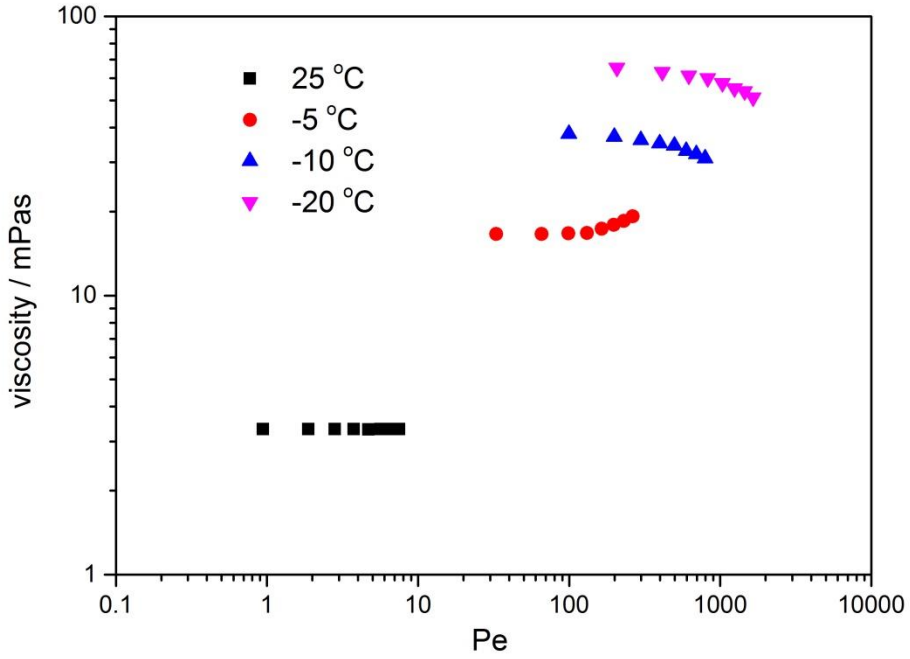

Fig 4-37 Shear viscosity of 30/70 EG-water-0.5% MCNT nanofluids as a function of Pe at different temperatures.

Look at Fig 4-34 first, the data at different temperatures are seen to cover different ranges of Pe number demonstrating that the relative importance of the hydrodynamic advection and Brownian motion varies with not only the shear rate, but also the temperature. The Brownian motion effect plays an important role at 25 ^{o}C, but this effect reduces with reducing temperature, leading to a more dominant role of the convection due to shear at -10 ^{o}C and -20 ^{o}C.

Fig 4-34 also shows that the 0.0625 % MCNT nanofluids behaves as a Newtonian fluid over Pe=0.01-100 and a weak shear thinning behaviour occurs at Pe>100. The Newtonian behaviour of the 0.0625 % samples at temperature between 25 ^{o}C and -10 ^{o}C illustrates that the MCNT particles are likely to be aggregated to give spherical shaped clusters which do not grow due to the Brownian motion and hydrodynamic advection. However, the high Pe number at -20 ^{o}C suggests that the hydrodynamic advection contribution overtakes that due to the Brownian motion. This is likely to lead to the formation of small elliptical clusters by the shear flow, such elliptical clusters would rearrange to give a more aligned orientation with increased shear rate, leading to the shear thinning behaviour. Fig 4-38 illustrates the morphology evolution of MCNT clusters in both Newtonian fluids and shear thinning fluids with a particle volume fraction of 0.0625 %. The red zig-zag lines in Fig 4-38 (b) are intended to indicate weak connections between particles in a large MCNT cluster.

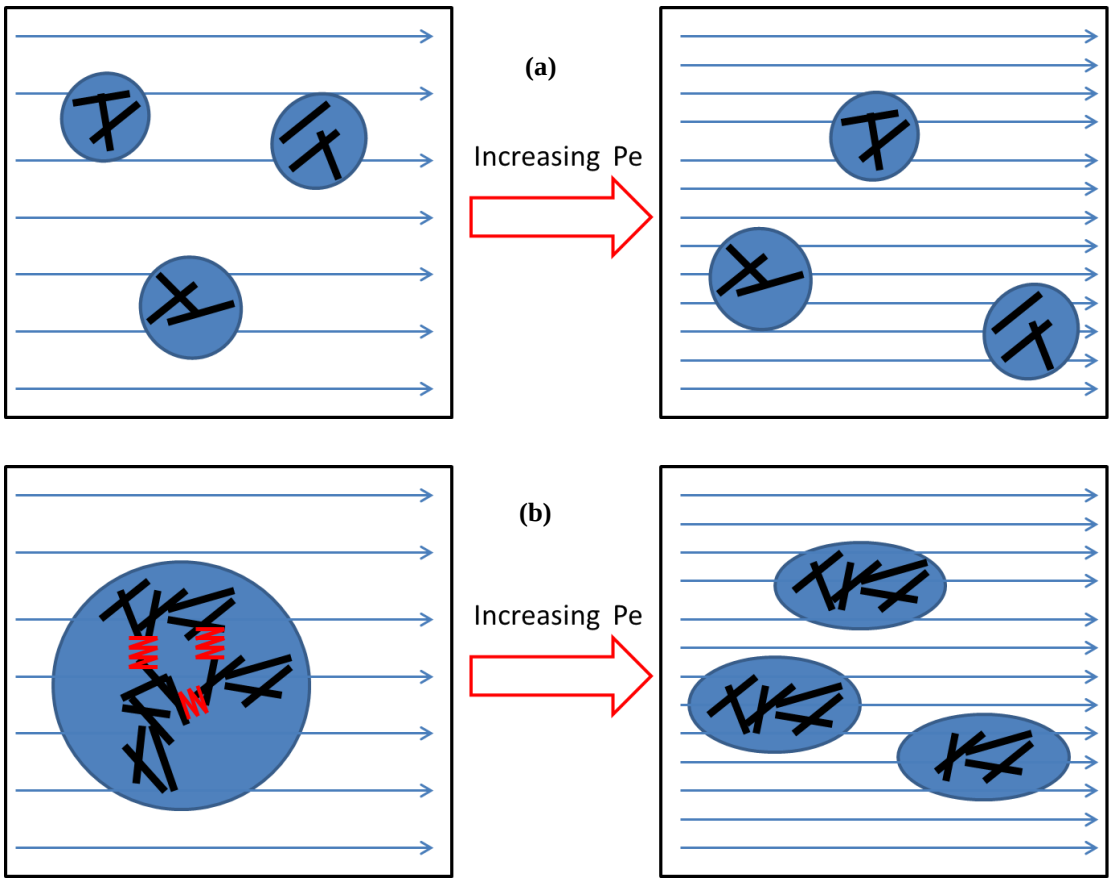

Fig 4-38 A schematic illustration of the morphology evolution of MCNT clusters in (a) Newtonian and (b) shear thinning nanofluids containing 0.0625 % MCNT.

Look then at Fig 4-35, which shows similar behavior of the 0.125 % samples to that of the 0.0625% samples. Newtonian behavior is observed at 25 ^{o}C and -5 ^{o}C while shear thinning behaviour occurs at -10 ^{o}C and -20 ^{o}C. However, clear difference can be also be noticed for the 0.125% sample, the shear shinning behaviour started to occur at -10 ^{o}C at which the 0.0625% sample remains Newtonian. It is also noticed that the Peclet number at which the shear thinning occurs in both samples are the same, around 200 to 300. This implies that only temperature is not sufficient to determine the shear behaviour, other factors such as the particle cluster size are also important. This reflects the beauty of the Pe number, which combines the effects of various factors.

Now attention is on Fig 4-36 and Fig 4-37, one notice a controversial phenomenon. At -5 ^{o}C and Peclet number in a range of 100 to 300, the 0.25 % and 0.5 % samples show shear thickening behaviour. This is clearly different from that of the 0.125% samples and discussed above that dominant hydrodynamic advection should have occurred at Pe>200 which would have broken the aggregation leading to shear thinning. To interpret this controversial observation, one needs to look the schematic of the cluster structure displayed in Fig 4-38. There is an important requirement for such a mechanism, the existence of the intra cluster weak bonds. In 0.125 % sample, the proposed structure could be approved by the observed shear thinning behaviour. Such weak bonds may not be there or less important and the morphology change of the structure is proposed in Fig 4-39.

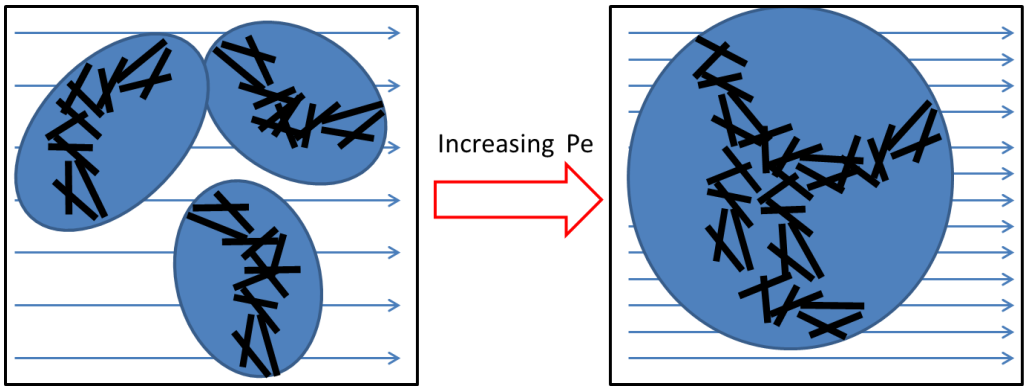

Fig 4-39 A schematic illustration of morphology evolution of MCNT cluster in shear thickening nanofluids.

In the proposed mechanism as shown in Fig 4-39, the MCNT particles tend to form a rod like cluster at a relatively low Pe number which is dispersed stably in the basefluid. While the contribution of the hydrodynamic advection increases, the rod like clusters could be forced together to form large loose aggregate with a large effective size. Such shear induced large clusters would give a higher viscosity, and therefore, the shear thickening behaviour is observed at -5 ^{o}C.

4.3 Summary

In this chapter, the experimentally measured viscosity data are presented for both EG-water and salt-water based MCNT nanofluids at a shear rate from 100 s^{-1} to 800 s^{-1}. The relative viscosity was then calculated and fitted to the modified K-D model to explain the viscosity data. The fitted parameters of the modified K-D model, R, D and φ_m are then used to analysis the cluster structures of MCNTs in the different basefluids and at different temperatures. Finally, the Peclet number is used to explain the experimentally observed rheological behaviour. Through the experimental study and analysis, the structure of MCNT clusters is linked to the rheological behaviour of the nanofluids, leading to plausible interpretation of the results.

5 Results and discussion (II): thermal conductivity

In this chapter, we will investigate the thermal conductivity of nano-compostie PCMs, which are salts and ethylene glycol aqueous solution containing varying amount of MCNT. The detailed procedure of sample preparation and equipment and methods of characterization of thermal conductivity have already been clearly illustrated in the previous methodology chapter 3. Therefore, in this chapter we will directly present the measured data of thermal conductivity of different samples. After that, we will discuss the mechanism of thermal conductivity enhancement in different nanofluids based on the predicted MCNT cluster structure we achieved in chapter 4.

5.1 Experimental results of thermal conductivity measurement

In this section, we will display the measured thermal conductivity data of both EG-water and salt-water based MCNT nanofluids separately. Firstly, all of the thermal conductivity data of nanofluids with varying particle concentration will be plotted against temperature. Then, the relative thermal conductivity ,which is the ratio of the effective thermal conductivity of nanofluid to the original thermal conductivity of basefluid will be calculated and plotted against particle volume fraction of MCNT (from 0.0625 to 0.5 %) at varying temperature. In the following paragraph, we will display thermal conductivity results of EG-water and salt-water based MCNT nanofluids in sequence.

5.1.1 EG-water based nanofluids

Before showing the thermal conductivity results of nanofluids, we will study the relationship between EG concentration and the thermal conductivity of EG-water basefluid at both liquid and solid state. In Fig 5-1, the measured thermal conductivity data versus ratio of EG to water is plotted. And the thermal conductivity is decreasing monotonically with the increasing proportion of EG. For example, when EG

concentration is 0, we get 0.590 W/m • K for pure water, then the number drops to 0.527, 0.505 and 0.488 when the proportion of EG is 20%, 25 % and 30 % respectively. We also find that this thermal conductivity data can match the mixing theory very well, which considers the overall thermal conductivity of a mixture as the weighted average of thermal conductivity of each composition in the mixture.

However, in Fig 5-2, we find a totally different trend of thermal conductivity with increasing EG ratio. The tested thermal conductivity data of solid EG-water does not follow the mixing theory, on the contrary, it deviates far below the expected value. As a result, the relationship between thermal conductivity of solid sample and EG concentration is no longer linear, but follows a new equation, $k = Aexp\left(-\frac{x}{B}\right) + C$, in which k is thermal conductivity of the mixture, x is the ratio of EG to water, A,B and C are the fitting parameters.

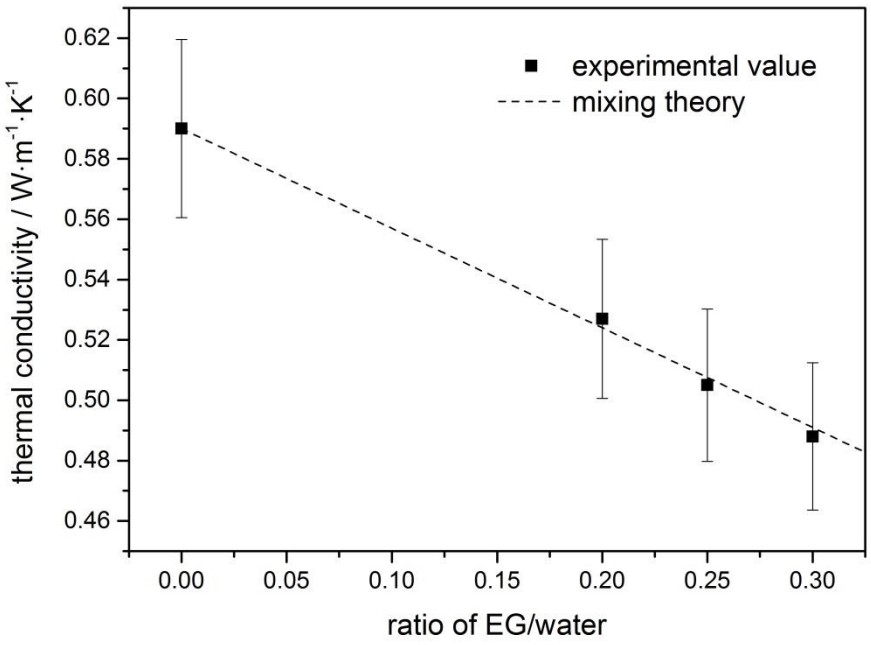

Fig 5-1 Thermal conductivity of EG-water mixture at liquid state.

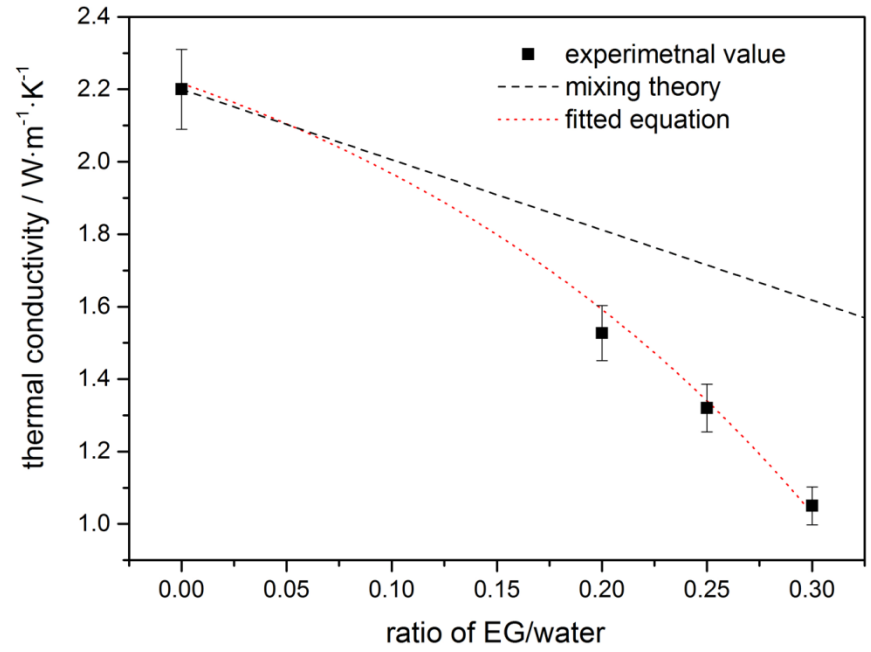

Fig 5-2 Thermal conductivity of EG-water mixture at solid state.

The unexpected phenomenon could be contributed to the function of -OH in the EG. Due to the existence of -OH group in EG, some water molecular are attached to the EG molecular by hydrogen bonding force, and the 'trapped' water molecular cannot form ordered crystal structure like ice when the temperature reaches the freezing point. In addition, the mechanism of heat conduction in non-metal matters is most dominated by vibration of phono, which is an imaginary carrier of energy, and the thermal conductivity can be expressed as, $k = \frac{1}{3}Cvl$, in which l is mean free path, v is velocity and C is heat capacity of phonon. Among them, mean free path is a highly sensitive value with crystal structure, therefore we could built relationship between the extra reduction of thermal conductivity in solid EG-water and the shortened mean free path of phonon in the disordered water molecular cage surrounding the EG molecular.

5.1.2 20EG-80water

Fig 5-3 shows the measured thermal conductivity data of 20EG-80water based MCNT nanofluids, and the data at temperature from 25 ^{o}C to -10 ^{o}C is zoomed in and shown in the inserted figure. In the whole temperature range from 25 ^{o}C to -40 ^{o}C, the thermal conductivity first keeps at a low level of nearly 0.5 W/m • K until temperature reaches -10 ^{o}C, and then it suddenly jumps to over 1.7 W/m • K when temperature is -40 ^{o}C. This over three times difference on the boost of thermal conductivity can be contributed to the occurrence of phase change of the samples from liquid to solid state during cooling, as we know, normally, solid material has better heat conduction than liquid material.

It can be also seen on the inserted figure that the thermal conductivity of 20EG-80water basefluid is decreasing during cooling process. For example, at 25 ^{o}C, the measured k value is 0.518 W/m •K, and the number decreases to 0.511, then to 0.502 at -5 ^{o}C and -10 ^{o}C. This observed relationship between

temperature and thermal conductivity is in accordance with most of other researcher's work in nanofluids. They also find that thermal conductivity of EG-water mixture will increase with temperature although their experiments were conducted at above room temperature. However, we find that in samples containing MCNT particles, the case is not always the same.

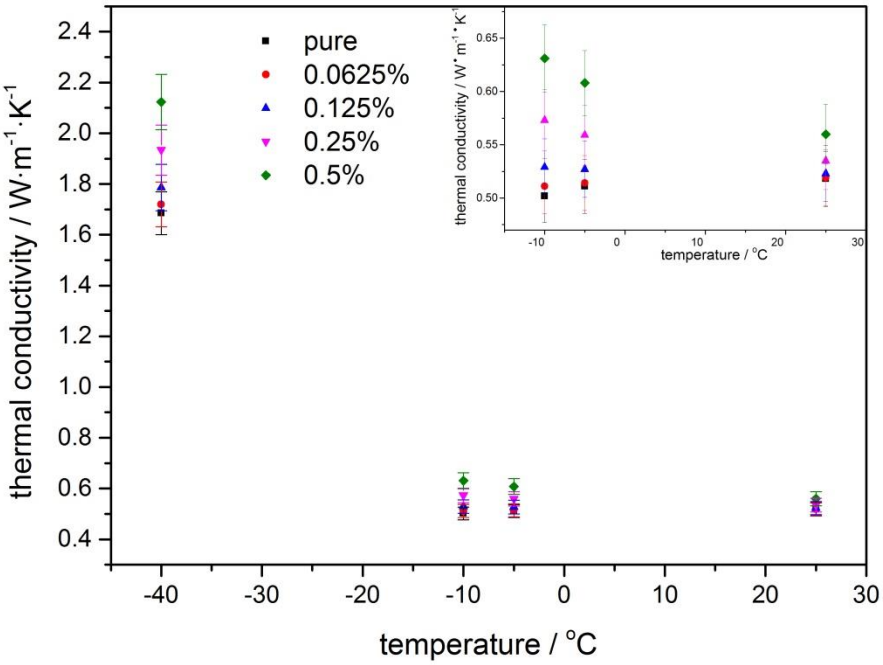

Fig 5-3 Thermal conductivity of 20/80 EG-water based MCNT nanofluids.

To be specific, in 0.0625 % sample, the trend of thermal conductivity is the same with the basefluid, increasing with temperature, while in 0.125 %, 0.25 % and 0.5 % samples, thermal conductivity decreases with temperature contrarily, and the rate of the reduction rises with particle volume fraction. To illustrate the relationship between thermal conductivity and temperature numerically, we compute the percentage of the cooling induced change (both increasing and decreasing) of k. The variation are

exhibited with the original experimental k value together in Table 5.1, in this table, we only considerate samples at liquid state.

Table 5.1 Thermal conductivity of 20/80 EG-water based MCNT nanofluids.

Temperature	25 °C	-5 °C	-10 °C	Variation at -5	Variation at
% MCNT	Thermal conductivity / W/m • K			°C	-10 °C
0	0.518	0.511	0.502	-1.3%	-3.1%
0.0625	0.519	0.514	0.511	-1.0%	-1.5%
0.125	0.523	0.527	0.529	+1.0%	+1.1%
0.25	0.535	0.559	0.573	+4.5%	+6.6%
0.5	0.560	0.608	0.631	+8.6%	+12.7%

From the table, we can notice that the higher the MCNT volume fraction in the nanofluids, the higher the cooling induced enhancement of thermal conductivity at both -5 °C and -10 °C. For example, when temperature is cooled to -5 °C and -10 °C, the enhancement of k in 0.125 % sample is 1.0 % and 1.1 %, significantly improving to 8.6% and 12.7% by adding 0.5 % MCNT. This displayed phenomenon of thermal conductivity trend changing with particle concentration was not observed before and we will discuss it in the later section.

In addition, to show the particle concentration effect on the thermal conductivity, we calculated the ratio of the effective thermal conductivity k_{eff} of nanofluids to the basefluid thermal conductivity k_0. The

results are plotted in Fig 5-4. It is easy to find that the thermal conductivity is increasing with MCNT volume fraction at each given temperature. And we also observe that the degree of the enhancement caused by MCNT is highly related with temperature. For instance, in 0.5 % sample, the enhancement at 25 ^{o}C and -40 ^{o}C is 8.1 % and 26.0 % respectively and in 0.25 % sample, it is 3.2 % and 14.8 %. All of the calculated relative thermal conductivity data demonstrates that when particle volume fraction is given, the lower the temperature, the higher the thermal conductivity enhancement, especially when samples is cooled to frozen.

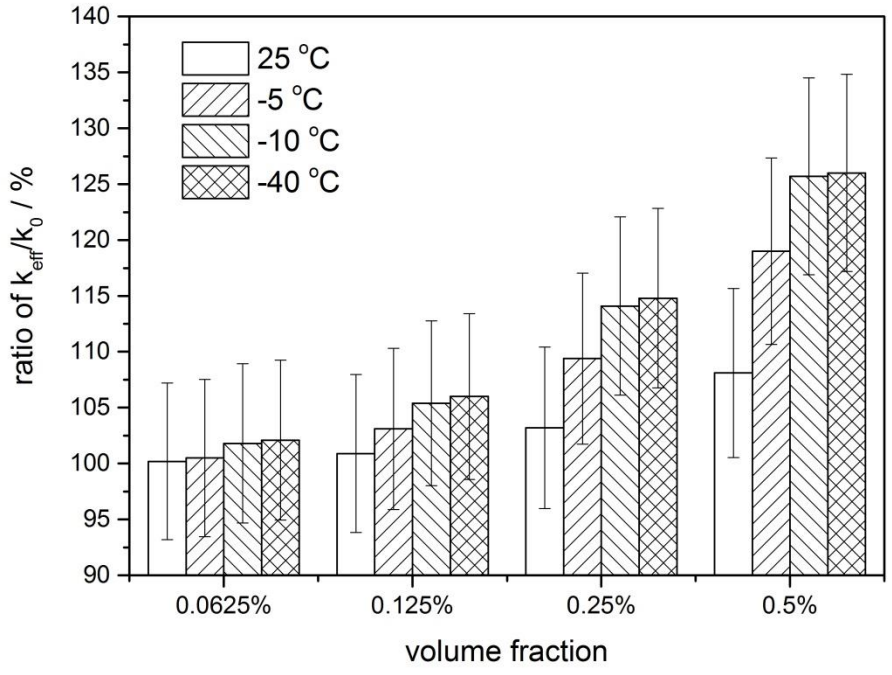

Fig 5-4 Relative thermal conductivity of 20/80 EG-water based MCNT nanofluids.

5.1.3 25EG-75water

Similarly, Fig 5-5 shows the measured thermal conductivity data of 25EG-75water based MCNT nanofluids. The same as we observed in 20/80 EG-water based samples, in the inserted figure of Fig 5-5, the thermal conductivity of basefluid and 0.0625 % nanofluids is increasing with temperature while others are decreasing with temperature. And the details of experimental k value of 25/75 EG-water based

MCNT nanofluids at liquid state are also listed in Table 5.2. One can still draw the same conclusion that at a certain MCNT volume fraction, the enhancement of thermal conductivity is higher at lower temperature. However, compared with the apparently large enhancement from -5 ^{o}C to -10 ^{o}C, it becomes negligible from -10 ^{o}C to -15 ^{o}C.

Also in Fig 5-6, relative thermal conductivity of all 25/75 EG-water based MCNT nanofluids samples are plotted against particle volume fraction. The figure shows that thermal conductivity is increasing with MCNT concentration at each set temperature. And at a given particle concentration, thermal conductivity is increasing with decreasing temperature, particularly in solid samples.

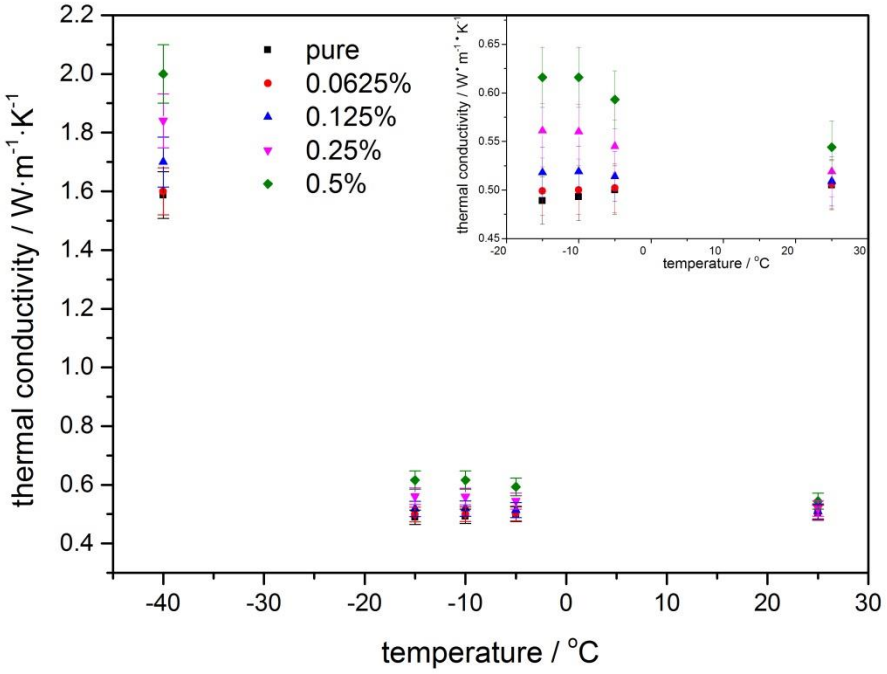

Fig 5-5 Thermal conductivity of 25/75 EG-water based MCNT nanofluids.

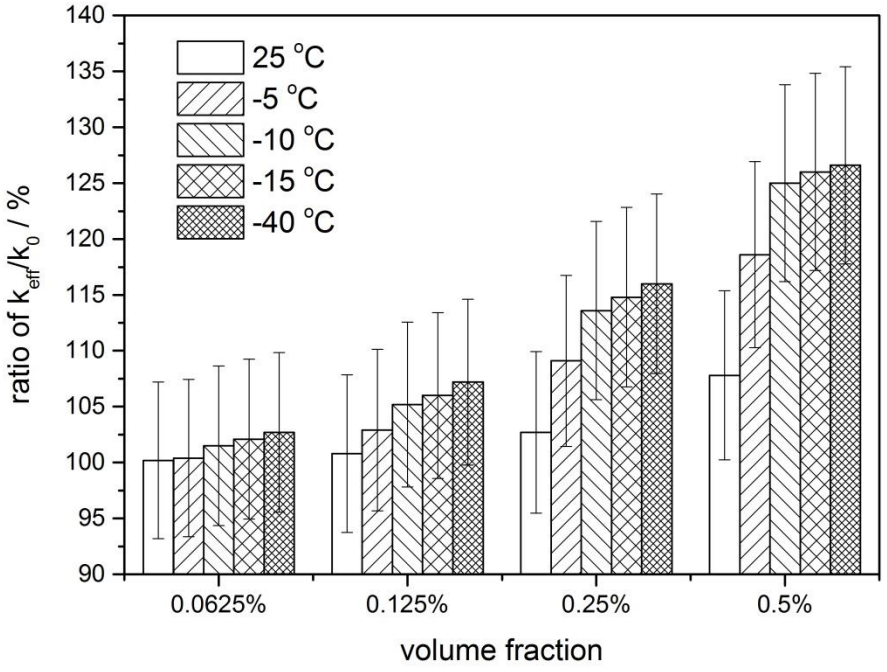

Fig 5-6 Relative thermal conductivity of 25/75 EG-water based MCNT nanofluids.

Table 5.2 Thermal conductivity of 25/75 EG-water based MCNT nanofluids.

Temperature	25 °C	-5 °C	-10 °C	-15 °C	Variation at	Variation at	Variation at
% MCNT	Thermal conductivity / W/m • K				-5 °C	-10 °C	-15 °C
0	0.505	0.500	0.493	0.489	-1.0%	-2.4%	-3.1%
0.0625	0.506	0.502	0.500	0.499	-1.0%	-1.2%	-1.4%
0.125	0.509	0.514	0.519	0.519	+1.0%	+1.9%	+1.9%
0.25	0.519	0.545	0.560	0.561	+5.0%	+7.9%	+8.1%
0.5	0.544	0.593	0.616	0.616	+9.0%	+13.2%	+13.2%

5.1.4 30EG-70water

Fig 5-7 shows the measured thermal conductivity data of 30EG-70water based MCNT nanofluids. And Fig 5-8 presents the relative thermal conductivity against MCNT volume fraction. Detailed experimental value of thermal conductivity are listed in Table 5.3. Similarly, we can observe the thermal conductivity is increasing with particle volume fraction, and the enhancement of k arises when temperature drops. Particularly, from Fig 5-8, the increasing rate of each concentration is accelerating very fast during 25 °C to -10 °C, and slows down when temperature is lower than -10 °C. However, a difference we could find from Table 5.3 is that, when particle volume fraction is given, the thermal conductivity is no longer increasing with cooling, but reaches highest point at -10 °C and drops down slightly at -15 °C.

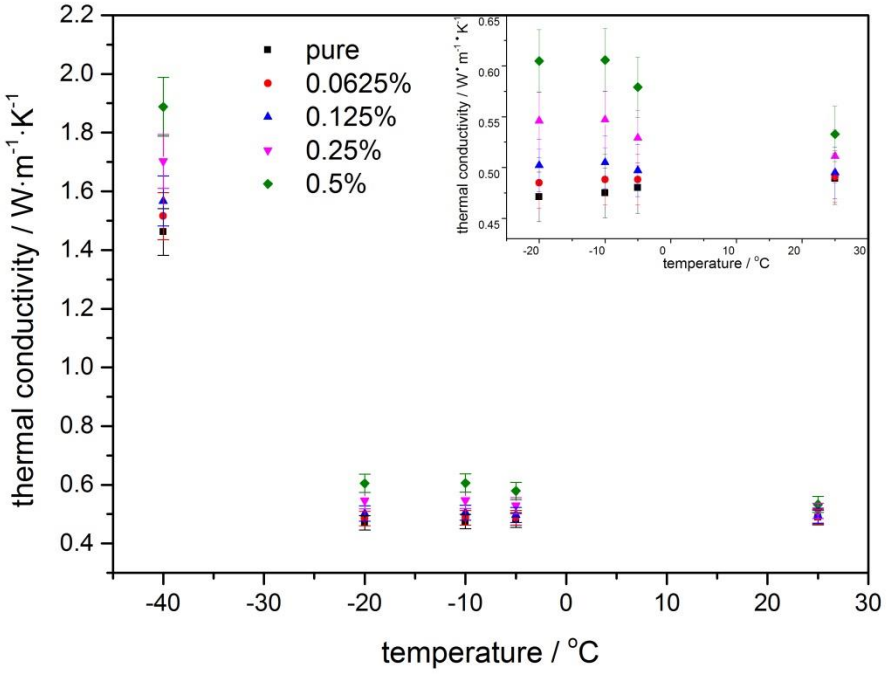

Fig 5-7 Thermal conductivity of 30/70 EG-water based MCNT nanofluids.

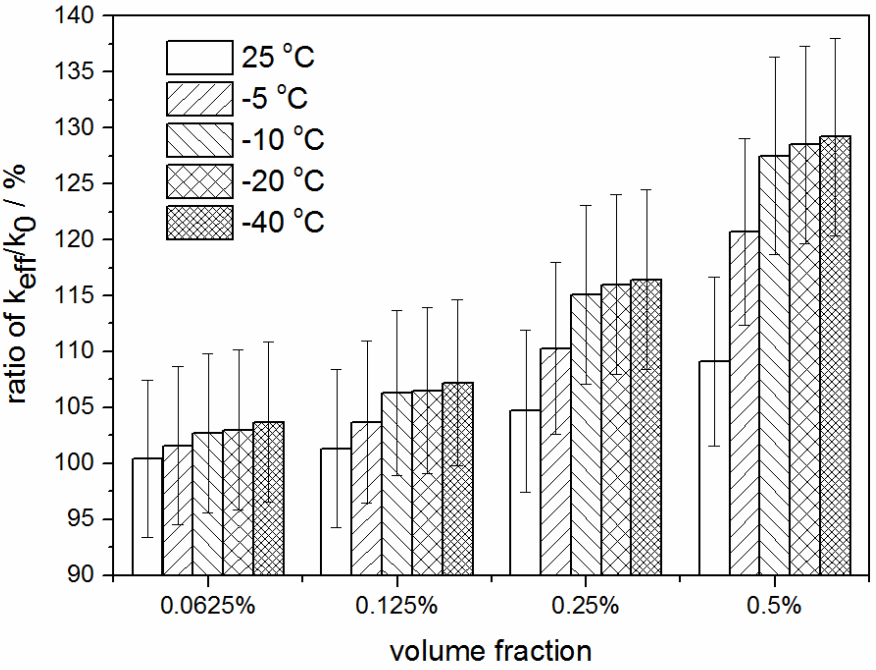

Fig 5-8 Relative thermal conductivity of 30/70 EG-water based MCNT nanofluids.

Table 5.3Tthermal conductivity of 30/70 EG-water based MCNT nanofluids.

Temperature	25 °C	-5 °C	-10 °C	-20 °C	Variation at	Variation at	Variation at
% MCNT	Thermal conductivity / W/m • K				-5 °C	-10 °C	-20 °C
0	0.489	0.480	0.475	0.471	-1.8%	-2.9%	-3.7%
0.0625	0.491	0.488	0.487	0.485	-0.6%	-0.8%	-1.2%
0.125	0.495	0.497	0.505	0.502	+0.4%	+2.0%	+1.4%
0.25	0.511	0.529	0.547	0.546	+3.5%	+7.0%	+6.8%
0.5	0.533	0.579	0.606	0.607	+8.6%	+13.7%	+13.9%

5.1.5 KCl-water

Fig 5-9 shows the measured thermal conductivity data of KCl-water based MCNT nanofluids. From the plots in the inserted figure and one can easily find that nanofluids samples containing different amount of MCNT show varying trend of thermal conductivity over temperature. For example, in KCl-water basefluid, thermal conductivity decreases when temperature is falling from 25 °C to -5 °C then to -10 °C. Similarly, in 0.0625 % sample, thermal conductivity decreases by 0.8 % during the first cooling stage from 25 °C to -5 °C, and on the contrary, increases by 0.2 % when temperature is further dropped to -10 °C. The same situation happens in 0.125 % sample, thermal conductivity firstly decreases by 0.1 % at -5 °C, and then, at -10 °C, restored to the room temperature level. Unlike 0.0625 % and 0.125 % samples, nanofluids containing 0.25 % and 0.5 % MCNT exhibits a monotonically increasing trend during the whole cooling process from 25 °C to -10 °C. Especially in 0.5 % sample, apparent enhancement of 9.4 % and 9.7 % are observed at -5 and -10 respectively.

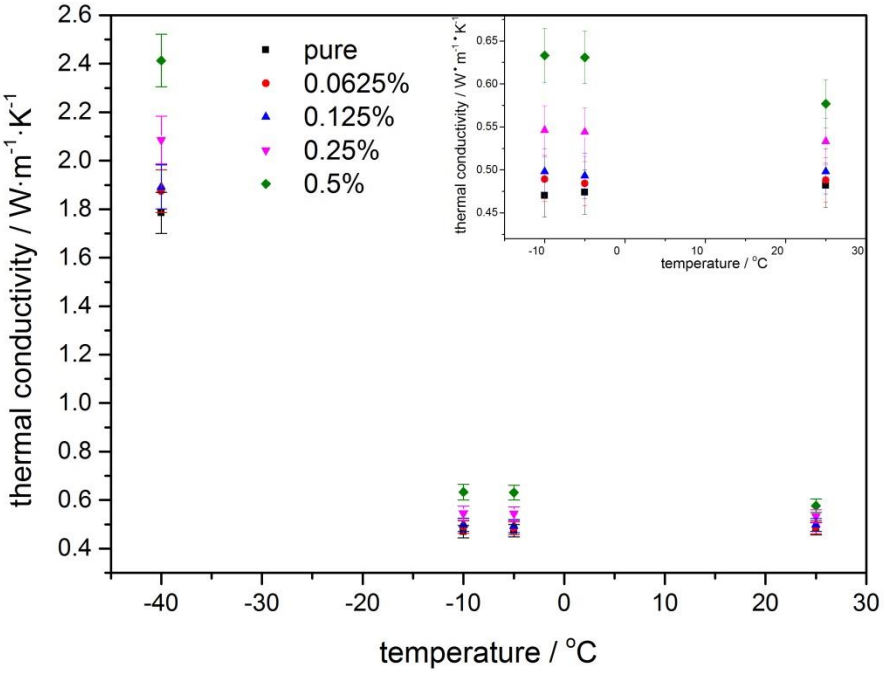

Fig 5-9 Thermal conductivity of KCl-water based MCNT nanofluids.

Table 5.4 Thermal conductivity of KCl-water based MCNT nanofluids.

Temperature	25 °C	-5 °C	-10 °C	Variation at -5	Variation at
% MCNT	Thermal conductivity / W/m • K			°C	-10 °C
0	0.482	0.474	0.470	-1.7%	-2.5%
0.0625	0.488	0.484	0.489	-0.8%	+0.2%
0.125	0.498	0.493	0.498	-1.0%	+0.0%
0.25	0.533	0.544	0.546	+2.1%	+2.4%
0.5	0.577	0.631	0.633	+9.4%	+9.7%

In addition, the relative thermal conductivity against MCNT volume fraction is plotted in Fig 5-10. It is easy to see that at each temperature series, thermal conductivity keeps increasing with the particle volume fraction although the increasing rate is different at different temperature. Generally speaking, lower temperature leads to higher enhancement in thermal conductivity, except data in 0.125 % and 0.25 % samples at -10 ^{o}C. Particularly, an obvious much higher enhancement of thermal conductivity is found when temperature is -60 ^{o}C in 0.5 % sample. This result demonstrates that the solidification process could significantly improve the MCNT induced enhancement of thermal conductivity in KCl-water based nanofluids.

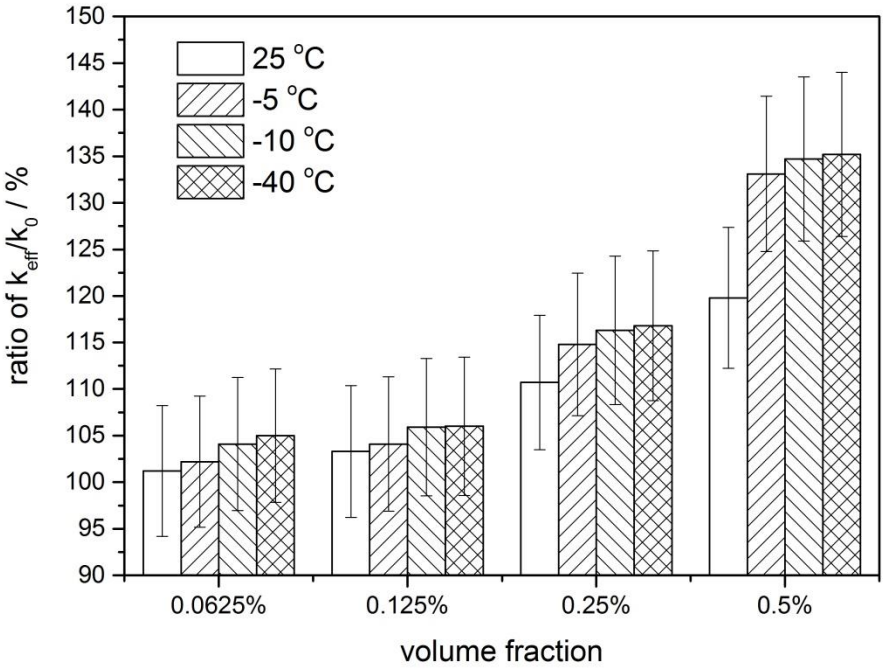

Fig 5-10 Relative thermal conductivity of KCl-water based MCNT nanofluids.

5.1.6 NaCl-water

Fig 5-11 shows the measured thermal conductivity data of NaCl-water based MCNT nanofluids. Table 5.5 lists the raw data of thermal conductivity and temperature caused change of thermal conductivity in liquid state samples. Compared with 0.482 W/m • K in KCl-water base fluid, NaCl-water basefluid has

higher room temperature thermal conductivity which is 0.572 W/m • K. Also higher solid state thermal conductivity of 2.10 W/m •K in NaCl-water is found when temperature is -40 ^{o}C, which is 17.6 % greater than thermal conductivity in solid state KCl-water sample.

Additionally, In Table 5.5, different from previous samples, we firstly find the cooling induced reduction of thermal conductivity in 0.0625 % samples are same at both -10 ^{o}C, and -20 ^{o}C, of which percentage is 2.1 %. Likewise, the enhancement at both temperature in 0.25 % samples are same as well, the percentage is 1.2 %. However, in 0.125 % and 0.5 % samples; the trend of thermal conductivity against temperature is still in accordance with that in KCl-water based nanofluids, namely, lower temperature promotes the MCNT role on enhancing the thermal conductivity of nanofluids.

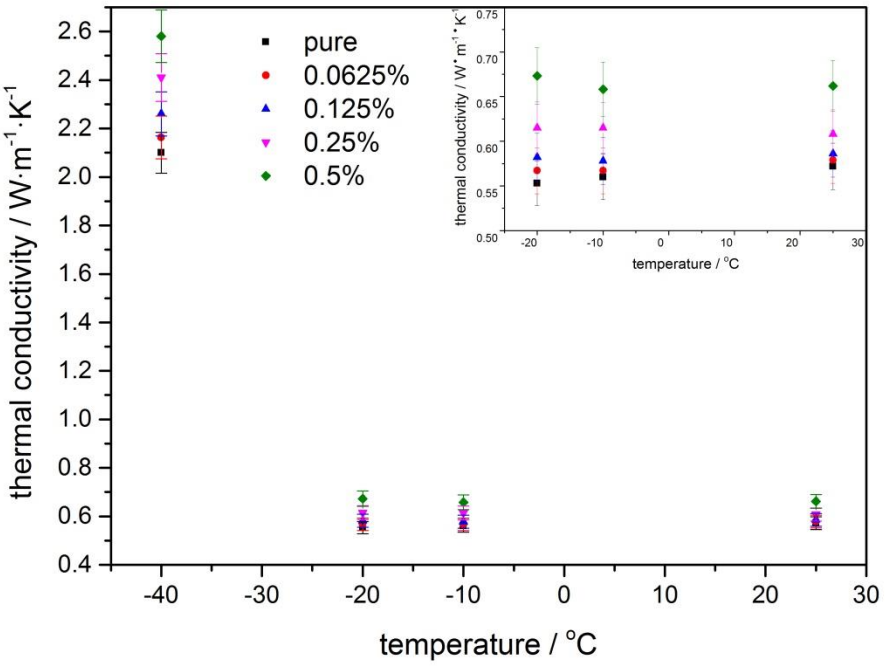

Fig 5-11 Thermal conductivity of NaCl-water based MCNT nanofluids.

Table 5.5 Thermal conductivity of NaCl-water based MCNT nanofluids.

Temperature	25 °C	-10 °C	-20 °C	Variation at	Variation at
% MCNT	Thermal conductivity / W/m • K			-10 °C	-20 °C
0	0.572	0.560	0.553	-2.1%	-3.3%
0.0625	0.579	0.567	0.567	-2.1%	-2.1%
0.125	0.586	0.578	0.582	-1.4%	-0.7%
0.25	0.608	0.615	0.615	+1.2%	+1.2%
0.5	0.662	0.658	0.673	-0.6%	+1.7%

In addition, the relative thermal conductivity against MCNT volume fraction is plotted in Fig 5-12. Without exception, the highest enhancement of thermal conductivity of each samples with given MCNT volume fraction is found to appear at -40 ^{o}C, which means in solid state, the contribution of MCNT on thermal conductivity is much higher than in liquid state at room temperature. Besides this, an interesting phenomenon can be found in each samples when temperature is -20 ^{o}C. At this temperature, the effective thermal conductivity is much higher than that at room temperature, some can even reach the level in solid state at -40 ^{o}C, although at -20 ^{o}C, the sample is still in liquid state. The observed high thermal conductivity at -20 ^{o}C in NaCl-MCNT nanofluids could be contributed to the similar MCNT structure

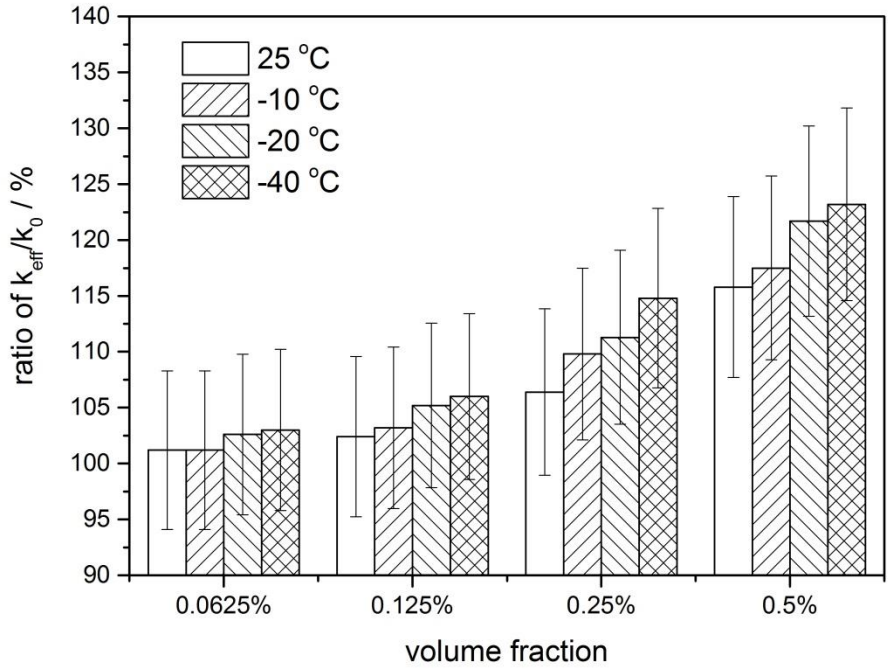

Fig 5-12 Relative thermal conductivity of NaCl-water based MCNT nanofluids.

in nanofluids at both -20 ^{o}C and -40 ^{o}C. As we know, the thermal conductivity enhancement is highly depended on the MCNT aggregation condition, thus similar MCNT structure will cause similar overall effective thermal conductivity.

5.1.7 $MgCl_2$-water

Fig 5-13 shows the measured thermal conductivity data of $MgCl_2$-water based MCNT nanofluids. Table 5.6 lists the raw data of thermal conductivity and temperature caused change of thermal conductivity in liquid state samples. From the measured data, we noticed that the thermal conductivity of $MgCl_2$-water basefluid at room temperature is 0.547 W/m • K, which is higher than that of KCl-water, but lower than NaCl-water basefluid, although $MgCl_2$-water has the lowest freezing point. This result shows that, on the contrary to EG-water system, the thermal conductivity of salt solution does not have the same trend with its freezing point. Additionally, the solid state thermal conductivity of $MgCl_2$-water is also found between that of solid state KCl-water and solid state NaCl-water.

In Table 5.6, we can clearly compare the different effect of MCNT particle on thermal conductivity of $MgCl_2$-water during cooling from 25 ^oC to -30 ^oC. We found that when the particle volume fraction is 0.0625 %, although the thermal conductivity is decreasing with cooling, the decreasing rate is slowing down when temperature drops lower and lower. And in 0.125 % and 0.25 % sample, we found at cooling stage from 25 ^oC to -10 ^oC, thermal conductivity is decreasing when temperauter is dropping, however, during the stage when the temperature is further cooled to -30 ^oC, the thermal conductivity shows a opposite relationship with temperature, namely, thermal conductivity is increasing with decreasing temperature. In 0. 5 % sample, we found that cooling no longer causes decreasing of thermal conductivity, in anther word, thermal conductivity in samples containing 0.5 % MCNT at both -10 ^oC and -30 ^oC is higher than that of pure basefluid.

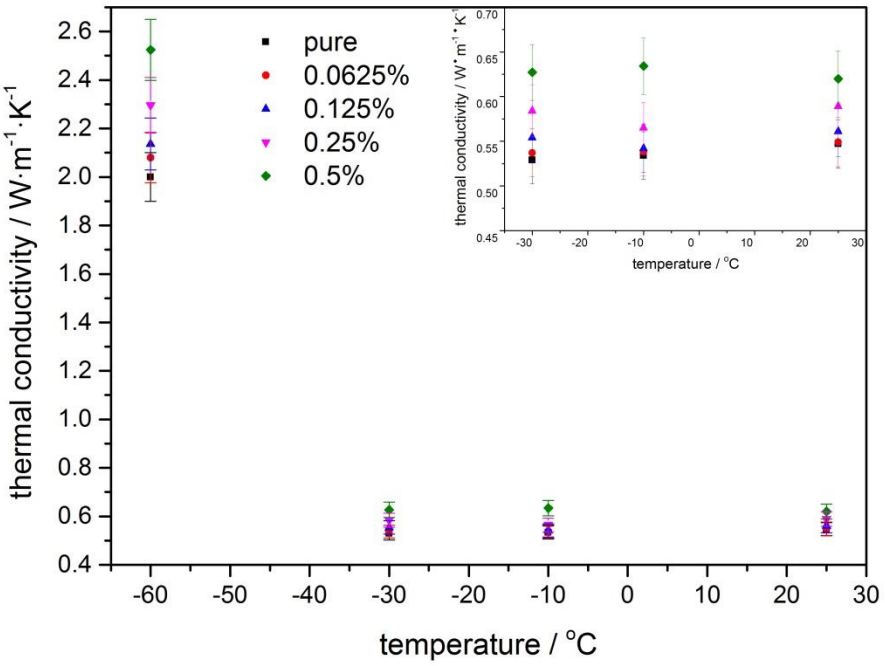

Fig 5-13 Thermal conductivity of $MgCl_2$-water based MCNT nanofluids.

Table 5.6 Thermal conductivity of $MgCl_2$-water based MCNT nanofluids.

Temperature	25 °C	-10 °C	-30 °C	Variation at	Variation at
% MCNT	Thermal conductivity / W/m • K			-10 °C	-30 °C
0	0.547	0.534	0.529	-2.4%	-3.3%
0.0625	0.549	0.538	0.537	-2.0%	-2.2%
0.125	0.561	0.542	0.554	-3.4%	-1.2%
0.25	0.589	0.565	0.584	-4.1%	-0.8%
0.5	0.620	0.634	0.627	+2.3%	+1.1%

In addition, the relative thermal conductivity against MCNT volume fraction is plotted in Fig 5-14. Similar with we observed in KCl-water and NaCl-water based nanofluids, it is apparent that the effective thermal conductivity is increasing with MCNT concentration at each setted temperature. Also, regardless of the MCNT volume fraction, all of relative thermal conductivity of frozen $MgCl_2$-water MCNT

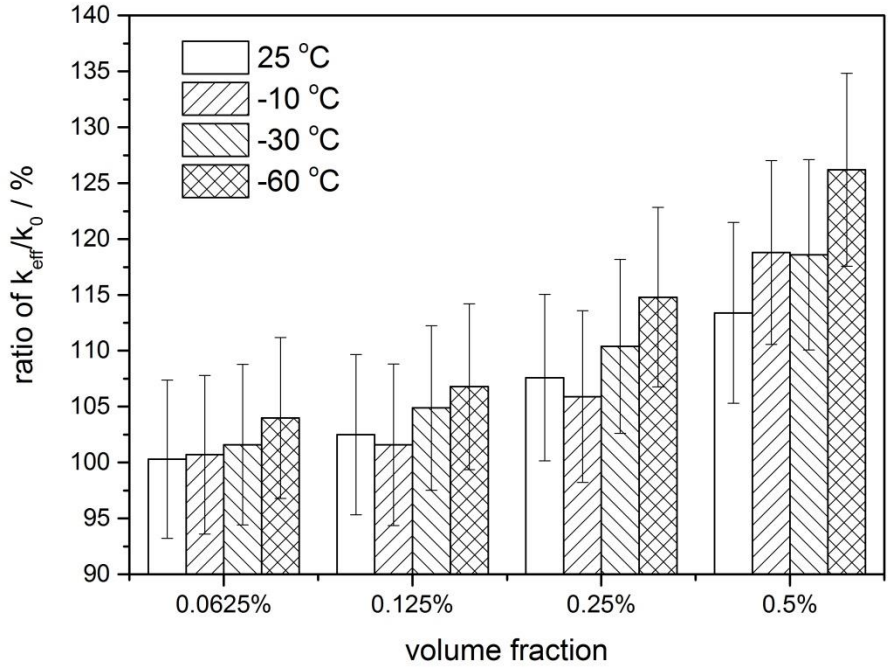

Fig 5-14 Relative thermal conductivity of $MgCl_2$-water based MCNT nanofluids.

nanofluids measured at -60 ^oC is much higher than its counterparts in liquid state. For example, when particle volume fraction is 0.5 %, the ratio of effective thermal conductivity to thermal conductivity of basefluid at room temperature is 113.4 %, and this number climbs to 126.2 % at -60 ^oC when all of the sample has become solid. Particularly, some abnormal data is found in 0.125 % and 0.25 % samples at -10 ^oC, instead of being higher than the room temperature thermal conductivity, it is even lower. This unusual result could be caused by the randomly distributed MCNT structure at 25 ^oC due to relatively strong Brownian motion.

5.2 Discussion of the Experimental results of thermal conductivity measurement

In this section, we will investigate the mechanism of thermal conductivity enhancement in both EG-water and salt-water based MCNT nanofluids, according to the measured thermal conductivity data which have been shown in the previous experimental results section. To conduct the research, firstly, we will compare the experimental data in our work with several well-known thermal conductivity models which have been proposed before and choose the most applicable model for subsequent study. Then, we will substitute the MCNT structure parameter predicted in last chapter by rheological behaviour of nanofluids into the thermal conductivity model which has aggregation term in the functional expression. Lastly, we will check the validity of the method of using rheological behaviour to predict thermal conductivity of nanofluids. Below we will divide the discussion into two parts: EG-water and salt-water, and will study both thermal conductivity mechanism separately.

5.2.1 EG-water based nanofluids

In this part, we will focus on the discussion of the particle effect on the thermal conductivity of EG-water based MCNT nanofluids. To begin with, several traditional and typical thermal conductivity models will be listed as the candidate of our following research. As mentioned in literature review chapter, the well-studied models including Maxwell-Garnett model (MG), Hamilton-Crosser model (HC) and Nan's model will be considered in our following study. The expression of function of these models are listed in Table 5.7.

Firstly, we will compare the predicted thermal conductivity value by MG model and HC model with the measured thermal conductivity value respectively. To simplify the comparison, we will only select 20/80

EG/water based MCNT nanofluids as a representative and the result is plotted in Fig 5-15. From the result, it can be found that the predicted thermal conductivity by MG model is much lower than the measured value and the gap between the predicted data and measured data keeps enlarging with increasing MCNT particle volume fraction. As we know, the MG model is only applicable for two phase suspensions containing spherical particle, and moreover, there is also a limitation on the particle volume fraction. Both of these factors could lead to the underestimation of the thermal conductivity of MCNT nanofluid in our study.

Since MG model fails to predict the thermal conductivity of nanofluids containing tube-like particles, HC model which considers particle shape factor is further used to calculate the thermal conductivity. However, from the result, we can observe that although the theoretical thermal conductivity value calculated by HC model is higher than that by MG model, the gap between the experimental data and theoretical data remains unfilled. In HC model, the value of shape factor n is 10 for MCNT in our case. Based on above findings, the conclusion is clear that traditional MG model and HC model are not valid anymore in our MCNT based nanofluids due to their limitation on particle shape and particle volume fraction. Thus, a new model is needed to give a reasonable prediction of thermal conductivity of MCNT nanofluids.

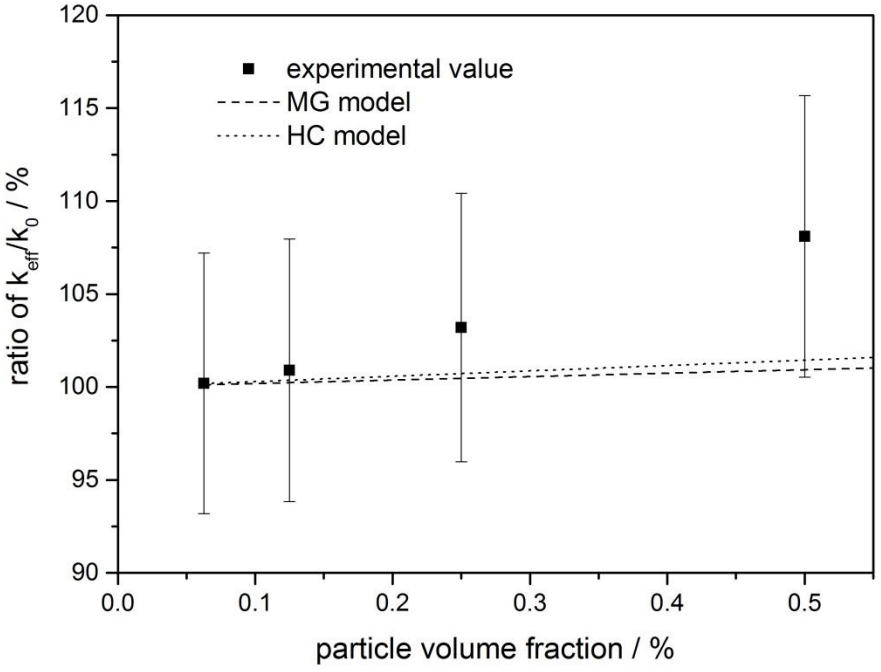

Fig 5-15 Relative thermal conductivity of 20/80 EG-water based MCNT nanofluids at 25 °C.

Table 5.7 Models on thermal conductivity of nanofluids

Investigator	Expression	Comments
Maxwell-Garnett[160]	$\frac{k_{eff}}{k_b} = \frac{k_p + 2k_b + 2(k_p - k_b)\varphi}{k_p + 2k_b - (k_p - k_b)\varphi}$	For spherical particles and low particle concentration
Hamilton-Crosser[161]	$\frac{k_{eff}}{k_b} = \frac{k_p + (n-1)k_b - (n-1)(k_b - k_p)\varphi}{k_p + (n-1)k_b + (k_b - k_p)\varphi}$	For non-spherical particles and low particle concentration, n is shape factor
Nan[162]	$\frac{k_a}{k_b} = \frac{3 + \varphi_{in}[2\beta_x(1 - L_x) + \beta_z(1 - L_z)]}{3 - \varphi_{in}[2\beta_x L_x + \beta_z z]}$ Where, $\beta_x = (k_x - k_b)/[k_m + L_x(k_t - k_m)]$ $\beta_z = (k_z - k_b)/[k_m + L_z(k_t - k_m)]$	For the randomly oriented ellipsoidal particles, and has no limitation on the particle concentration

Among all of advanced thermal conductivity models considering Brownian motion effect, nano-layer effect and clustering effect trying to explain the abnormal high enhancement of thermal conductivity of nanofluids, the aggregation model has been widely studied and its feasibility has been successfully demonstrated in many reports as well. In our work, we will choose Nan's model to compute the thermal conductivity of MCNT aggregation and further predict the effective thermal conductivity of MCNT nanofluids, the functional expression of Nan's model is listed in Table 5.7.

As mentioned above, we will use Nan's model to predict the effective thermal conductivity of MCNT cluster, and subsequently, use otherwise the HC model to calculate the effective thermal conductivity of the whole MCNT nanofluid. The equation of Nan's model is written like $\frac{k_a}{k_b} = \frac{3+\varphi_{in}[2\beta_x(1-L_x)+\beta_z(1-L_z)]}{3-\varphi_{in}[2\beta_x L_x+\beta_z L_z]}$, where $\beta_x = (k_x - k_b)/[k_b + L_x(k_t - k_b)]$ and $\beta_z = (k_z - k_b)/[k_b + L_z(k_t - k_b)]$. In the function, k_a is the thermal conductivity of the MCNT aggregation, k_b is the thermal conductivity of the basefluid, φ_{in} is the concentration of MCNT in an individual cluster, k_x, k_y and k_t is the thermal conductivity of MCNT along the transverse and longitudinal directions and isotropic thermal conductivity of the MCNT respectively. In our research, k_x, k_y and k_t are considered the same as the thermal conductivity k_p of MCNT. And L_x and L_z are well-known geometrical factors dependent on the MCNT aspect ratio and expressed as $L_x = \frac{0.5r^2}{r^2-1} - 0.5rcosh^{-1}r/(r^2-1)^{\frac{2}{3}}$ and $L_z = 1 - 2L_x$, in which r is the ratio of the length of the MCNT to the diameter of the MCNT.

If we rewrite the left part of Nan's equation we can get expression as following: $\frac{k_a}{k_b} = 1 + \frac{\varphi_{in}[2\beta_x+\beta_z]}{3-\varphi_{in}[2\beta_x L_x+\beta_z L_z]}$. This term 1 plus a fractional term means that the effective thermal conductivity of nanofluids with cluster is alway larger than the thermal conductivity of the basefluid.

Furthermore, the fractional term means that the enhancement of thermal conductivity is highly related with the geometrical factors L_x and L_z, which determines the value of β_x and β_z.

Among all of the parameters mentioned in the last paragraph, most of them are inherent properties or can be derived from given parameters except the value of φ_{in}. The concentration of MCNT in the cluster is the key factor for predicting the thermal conductivity of nanofluids using Nan's model, which is difficult to be observed directly from experimental methods. In our work, to obtain the value of the φ_{in}, we will quantify the microstructure of MCNT cluster by the rheological analyses. Below, we will discuss the procedure of linking rheological property with thermal conductivity of MCNT nanofluids based on different EG-water basefluids in sequence.

5.2.2 20EG-80water

From the rheological analyse in chapter 4, the conclusion has been achieved that by fitting the experimental data of viscosity with modified K-D model, we can quantify the parameters describing the MCNT cluster structure, such as R, the ratio of the effective size of cluster to the size of a primary particle and D, the fractural index. Having the value of R and D, we can further calculate the value of φ_{in} based on the equation $\varphi_{in} = R^{(D-3)}$. All of the MCNT cluster parameters at 25 ^{o}C, -5 ^{o}C and -10 ^{o}C are listed in Table 5.8.

From the data in Table 5.8, if we look vertically comparing the fitting parameters of samples containing different amount of MCNT, we will find that the amount of MCNT particle contained in the cluster is not always the same, for example, in 0.0625 % and 0.125 % samples, the value of φ_{in} is 0.366, while in

0.25 % and 0.5 % sampels, the value of φ_{in} shrinks to one-fourth to 0.089, namely, much less of MCNT is located in an individual cluster.

Table 5.8 Fitting parameters of MCNT cluster in 20EG-80water basefluid.

Temperature	25 °C			-5 °C			-10 °C		
% MCNT	R	D	φ_{in}	R	D	φ_{in}	R	D	φ_{in}
0.0625	2	1.55	0.366	5	1.50	0.089	13	1.50	0.021
0.125	2	1.55	0.366	10	1.45	0.028	13	1.50	0.021
0.25	5	1.50	0.089	13	1.55	0.024	17	1.55	0.016
0.5	5	1.50	0.089	13	1.58	0.026	17	1.60	0.019

Since we have already known the concentration of MCNT contained in an individual cluster through the rheology analysis in chapter 4, subsequently, we will apply the value of φ_{in} into Nan's model to compute the effective thermal conductivity of the MCNT cluster, which is k_a. And we can also get the concentration of MCNT cluster in the whole nanolfuids by using equation $\varphi_a = \frac{\varphi_p}{\varphi_{in}}$. After this, we will substitute the calculated k_a for the thermal conductivity of particle k_p and substitute φ_a for the particle concentration φ_p in H-C model, then the function becomes as $\frac{k_{eff}}{k_b} = \frac{k_a+(n-1)k_b-(n-1)(k_b-k_a)\frac{\varphi_p}{\varphi_{in}}}{k_a+(n-1)k_b+(k_b-k_a)\frac{\varphi_p}{\varphi_{in}}}$. By this way, the predicted thermal conductivity considering cluster effect can be obtained and the results are plotted in Fig 5-16 showing with the experimental value together. We can observe that the H-C model modified taking into account the MCNT cluster by Nan's model, agrees very well with the experimental results at each temperature.

Also in Fig 5-16, we can notice that at all temperature, the predicted thermal conductivity data of samples containing various concentration of MCNT are all located within the range of the experimental error and the variation between the predicted value and the average experimental value is slight as well. However, one can see that there is no predicted value when temperature is -40 ^{o}C, this is because our prediction of φ_{in} is derived from the shear viscosity measurement and the shear viscosity test is not achievable at -40 ^{o}C due to the solidifying of the sample. As a result, we didn't show the prediction of thermal conductivity at -40 ^{o}C. However, from the results showed before in Fig 5-4, we know that thermal conductivity at -40 ^{o}C shows similar value with that at -10 ^{o}C. This is due to the microstructure of MCNT cluster does not migrate very much during the cooling from the freezing point to a further low temperature, in this case, from -10 ^{o}C to -40 ^{o}C.

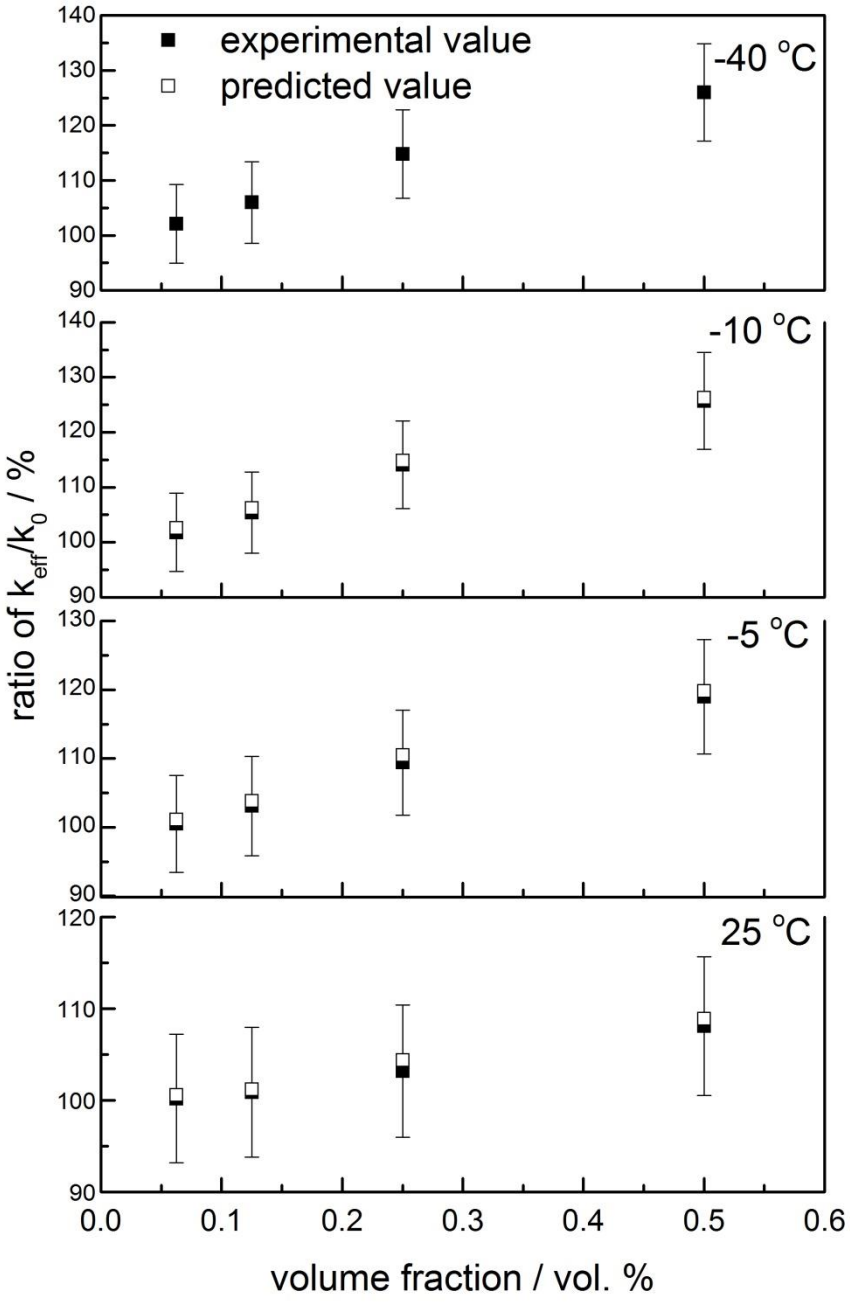

Fig 5-16 Effective thermal conductivity of 20/80 EG-water based MCNT nanofluids.

5.2.3 25EG-75water

Similar with the discussion in 20/80 EG-water based MCNT nanofluids, in this section, firstly, the results of rheology analysis is also presented in Table 5.9. The different thing is that we applied -15 ^{o}C in 25/75 EG-water based samples, so that we can have more information to build relationship between thermal

conductivity and viscosity that covers a wide temperature range. In aspect of the value of R and D, generally, people can notice some distinction caused by changing the ratio of EG to water in basefluid. For example, when temperature is 25 ^{o}C, the value of the fractal index D has increased from 1.55 to 1.60 even though the relative particle size keeps the same number in 0.0625 % and 0.125 % samples. That leads to a higher value of φ_{in} which will further influence the prediction of thermal conductivity afterwards. Also, we can find that, at a given temperature, the value of R in 25/75 EG-water based sampels are always higher, if not equal, than that in 20/80 EG-water based samples. This indicates that more EG in the basefluid could promote the aggregation of MCNT particles which subsequently affects the fitting parameter derived from the viscosity data. The positive correlation between EG concentration and particle aggregation status is due to the MCNT is attached with the hydrophobic end of the surfactant and the hydrophilic end stretches out into the basefluid. Thus, the surfactant coated MCNT presents a hydrophilic behaviour, and the compatibility between MCNT and the basefluid is better when the whole system contains more water, in another word, more EG will cause a less stable dispersion condition of MCNT, which turns out to facilitate aggregating of particle.

Table 5.9 Fitting parameters of MCNT cluster in 25EG-75water basefluid.

Temperature	25 ^{o}C			-5 ^{o}C			-10 ^{o}C			-15 ^{o}C		
% MCNT	R	D	φ_{in}	R	D	φ_{in}	R	D	φ_{in}	R	D	φ_{in}
0.0625	2	1.60	0.379	6	1.55	0.074	13	1.55	0.024	13	1.55	0.024
0.125	2	1.60	0.379	10	1.57	0.037	15	1.55	0.020	15	1.55	0.020

0.25	6	1.55	0.074	13	1.55	0.024	18	1.52	0.014	18	1.55	0.015
0.5	6	1.55	0.074	13	1.58	0.026	18	1.61	0.018	18	1.56	0.016

Although increasing the proportion of EG in the basefluid makes worse stability of MCNT in the suspension, to some extent, the further aggregation of particle could help promoting the heat conduction of MCNT cluster, thus enhancing the total thermal conductivity of the nanofluids. The effective thermal conductivity results are shown in Fig 5-17. We can see that the predicted thermal conductivity data matches well with the experimental results at all particle concentration and it manages to follow the trend that the lower the temperature, the higher the effective thermal conductivity. That is, the method of predicting thermal conductivity through rheology analysis has been successfully demonstrated its advantages of explaining the temperature effect on enhancement of thermal conductivity.

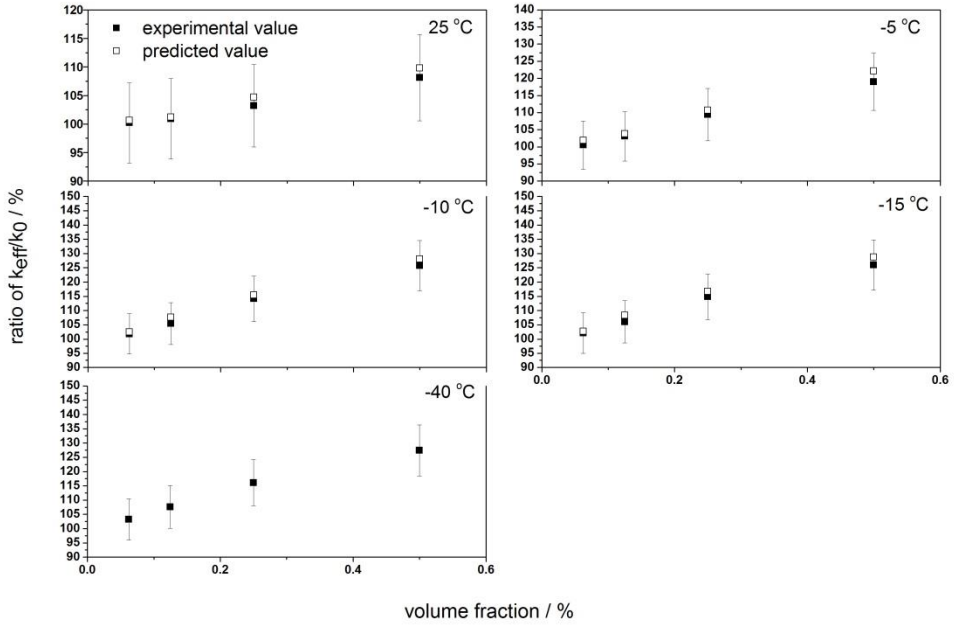

Fig 5-17 Effective thermal conductivity of 25/75 EG-water based MCNT nanofluids.

In addition, if we look at the numbers in depth, we will find that the ratio of effective thermal conductivity to that of basefluid increases almost linearly with MCNT volume fraction at each temperature. However, it doesn't show the same trend with temperature. For example, for samples containing 0.5 % MCNT, the enhancement of thermal conductivity at 25 ^{o}C is 7.8 %, increases to 18.6 % at -5 ^{o}C, then to 25.0 % at -10 ^{o}C, and then keeps nearly unchanged at 26.0 % and 26.6 % at -15 ^{o}C and -40 ^{o}C. It is obvious that at the early stage of cooling, like from 25 ^{o}C to -5 ^{o}C, the temperature dropping induced thermal conductivity increasing is very fast, while during the later cooling stage, like from -10 ^{o}C to -15 ^{o}C, the enhancement of the effective thermal conductivity tends to keep increasing very slow, even to a far lower temperature beyond the freezing point of the sample, the thermal conductivity is still not increasing very much. This observing could be explained when we refer to the microstructure of MCNT cluster. According to the fitting parameters of 0.5 % sample in Table 5.9, we can easily find that during the cooling from 25 ^{o}C to -5 ^{o}C, the value of R increases from 6 to 13 with only a little change in D, this leads to a big drop in φ_{in}, from 0.074 to 0.026. The variation of these parameters indicates that during this cooling stage, the MCNT cluster has more than doubled in its effective volume while including the same amount of particle, which means that the pathway of heat contributed by MCNT has been extended and spread to over twice as its original coverage rate in the base fluid. As a result, the total thermal conductivity of MCNT naonfluids will increase more at -5 ^{o}C than at 25 ^{o}C.

However, the effective cluster size R in 0.5 % sample at -10 ^{o}C and -15 ^{o}C doesn't show difference and the only change is the slight increase of D from 1.56 to 1.61, which leads to an almost stable φ_{in}. As we have already known the relationship between the value of φ_{in} and the thermal conductivity of MCNT

cluster, the little change in thermal conductivity at -10 °C and -15 °C could be contributed to the relatively stable amount of MCNT particles in the cluster.

5.2.4 30EG-70water

Table 5.10 lists the fitting parameter of MCNT cluster in 30/70 EG-water basefluid derived from the modified K-D model. Compared with that in 25/75 EG-water basefluid, MCNT particles in 30/70 EG-water basefluid tend to aggregate more closely and the cluster structure tend to be tighter. In terms of fitting parameters by rheology analysis, the higher concentration of EG plays a restricting role on the dispersion of MCNT, thus leads to higher effective cluster size R and fractural index D. The reason is the same as we illustrated in last section, that is, more EG makes the compatibility between surfactant coated MCNT and basefluid worse, therefore particles tend to aggregate to form a larger and tighter cluster.

Table 5.10 Fitting parameters of MCNT cluster in 30EG-70water basefluid.

Temperature	25 °C			-5 °C			-10 °C			-20 °C		
% MCNT	R	D	φ_{in}	R	D	φ_{in}	R	D	φ_{in}	R	D	φ_{in}
0.0625	3	1.60	0.215	8	1.55	0.049	13	1.55	0.024	14	1.60	0.025
0.125	3	1.60	0.215	9	1.60	0.046	15	1.55	0.020	16	1.55	0.018
0.25	6	1.60	0.081	14	1.60	0.025	18	1.52	0.014	20	1.60	0.015
0.5	6	1.65	0.089	14	1.62	0.026	18	1.61	0.018	20	1.67	0.018

Fig 5-18 displays the effective thermal conductivity of 30/70 EG-water based MCNT nanofluids and the predicted thermal conductivity by rheology analysis. From this figure, we can also draw the same

conclusion that predicted value can match the experimental value very well even when temperature goes to -20 ^{o}C.

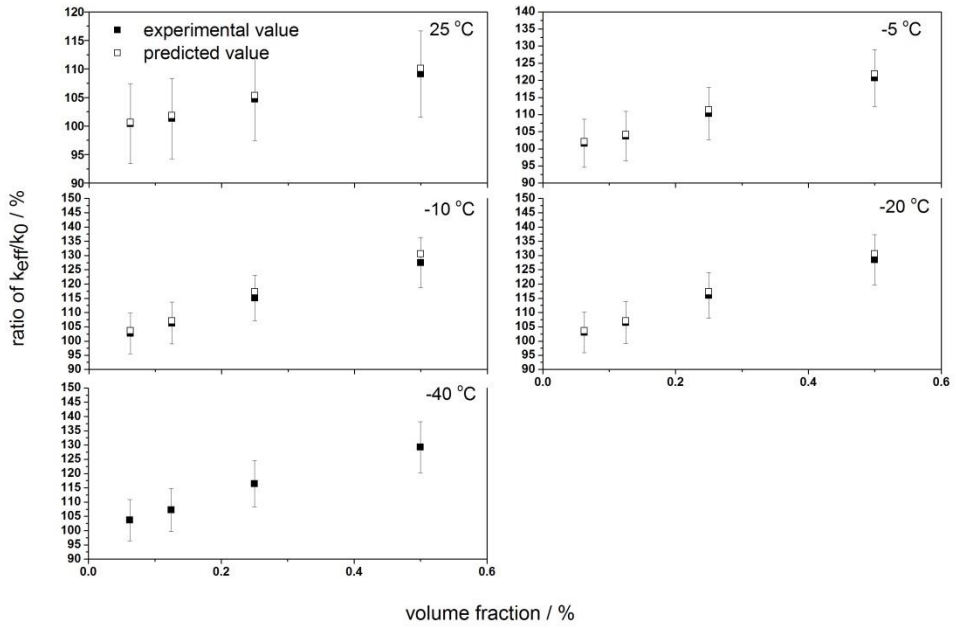

Fig 5-18 Effective thermal conductivity of 30/70 EG-water based MCNT nanofluids

However, the predicted value at all temperature overestimated the thermal conductivity a bit, especially when the MCNT volume concentration is high, like 0.25 % and 0.5 %. This is because the method we used to predict the microstructure of MCNT cluster is based on the shear viscosity, although the viscosity data can reveal the information of the cluster indirectly, the shear force applied in the measurement might also affect the cluster distribution, which is considered as an inevitable artefact. Due to the existing shear force, the MCNT particles in the viscosity test is dispersed in a more stretched pattern than in the still crucible in LFA test for thermal conductivity, thus the better thermal conductivity enhancement is observed in the predicted value from rheology analysis.

5.2.5 Salt-water based nanofluids

In this section, we will discuss the thermal conductivity results of salt-water based MCNT nanofluids. As cold storage phase change material, the freezing point range of the salt-water based basefluid covers from -10 ^{o}C to -33 ^{o}C, including KCl, NaCl and $MgCl_2$ aqueous solution. We will discuss the results in the sequence of the type of salt in the following subsections.

5.2.6 KCl-water

At first, we will talk about KCl-water based MCNT nanofluids. And to start with, the structure information of MCNT cluster in KCl-water baseflud is shown in terms of fitting parameter of modified K-D model in Table 5.11. Comparing with that in EG-water based samples, we could find that the R and D value is relatively higher in KCl-water based samples, for example, at 25 ^{o}C, the effective size is 10 and the fractural index is 1.70 in 0.0625 % sample, compared with 3 and 1.6 in its counterpart in 30/70 EG-water based samples. This means the MCNT cluster is larger and denser in salt-water based nanofluids of which the reason has already been discussed and explained in chapter 4.

In addition, we could find another different phenomenon in KCl-water based MCNT nanofluids. Especially in the -5 ^{o}C column, we can notice that although the value of R grows gradually from 15 to 18 with the increasing particle volume fraction, the value of fractural index keeps the same at 1.70. This is a sign that the structure of MCNT cluster at different volume fraction are similar with each other as the inner density of the MCNT are same. And even in -10 ^{o}C column, we can find all of the samples share the same R and D, which indicates that the MCNT cluster in all samples have identical inner inclusion.

Table 5.11 Fitting parameters of MCNT cluster in KCl-water basefluid.

Temperature	25 ^{o}C	-5 ^{o}C	-10 ^{o}C

% MCNT	R	D	φ_{in}	R	D	φ_{in}	R	D	φ_{in}
0.0625	10	1.70	0.050	15	1.70	0.029	18	1.72	0.025
0.125	10	1.70	0.050	15	1.70	0.029	18	1.72	0.025
0.25	12	1.70	0.039	17	1.70	0.025	18	1.72	0.025
0.5	12	1.73	0.042	18	1.70	0.023	18	1.72	0.025

Based on above findings, it is convenient to draw the conclusion that the structure of MCNT cluster in KCl-water basefluid is more rigid than in EG-water based samples, and the structure doesn't change very much with particle concentration. And from the results in Fig 5-19, we could also claim that the combination of Nan's model and H-C model could successfully predict the experimental value of thermal conductivity.

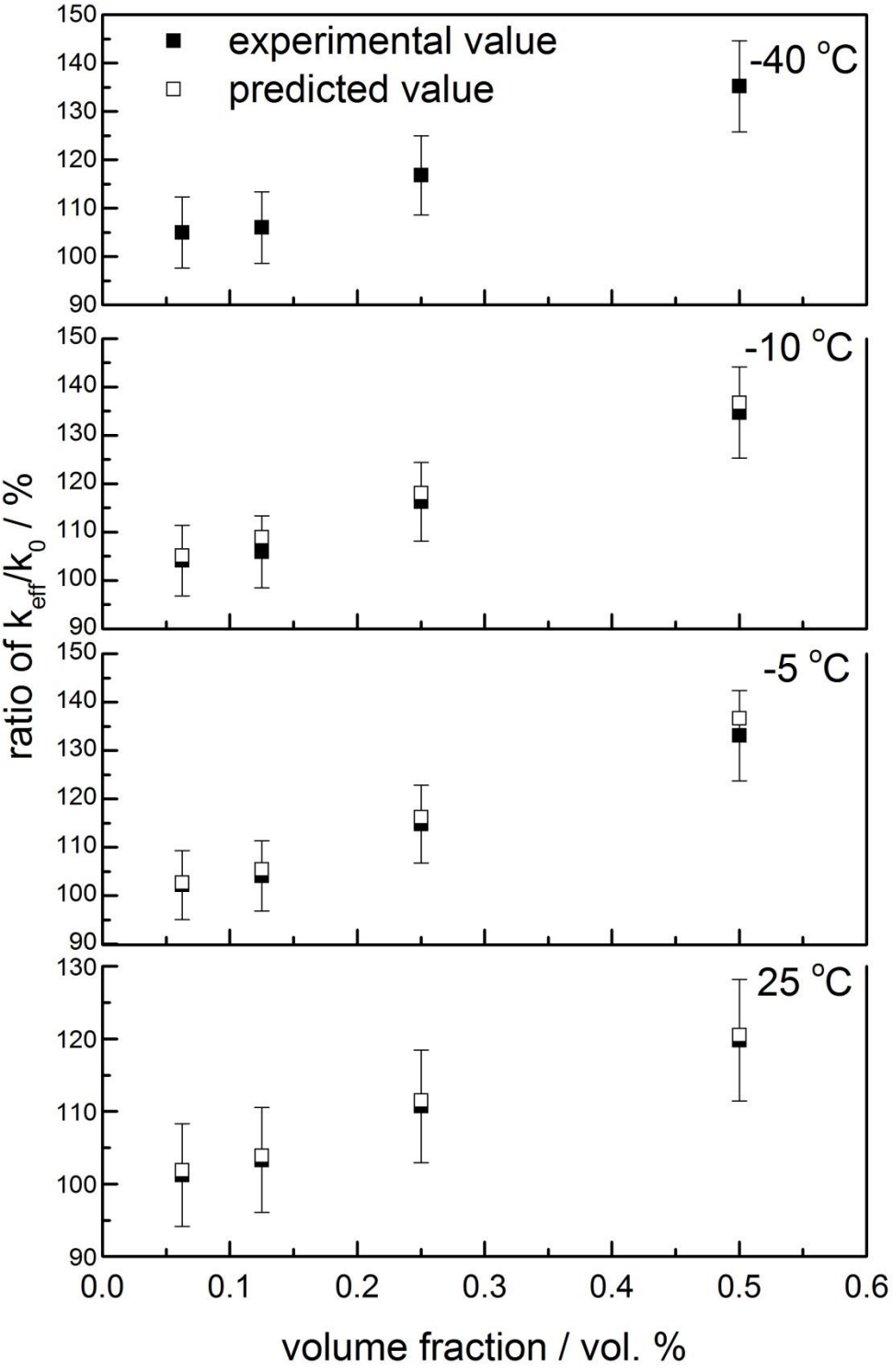

Fig 5-19 Relative thermal conductivity of KCl-water based MCNT nanofluids

5.2.7 NaCl-water

In this section, we will display the structure information of MCNT cluster in NaCl-water based nanofluids and compare the predicted thermal conductivity with the measured thermal conductivity. Firstly, the fitting parameters of MCNT cluster is presented in Table 5.12 which covers a wide temperature range from 25 ^{o}C to -20 ^{o}C. From the data in below table, we could find that like in KCl-water based samples, the NaCl-water based nanofluids have the ability to maintain a fixed effective MCNT cluster size. For example, nanofluids containing different amount of MCNT shows very similar R values if we only look at results in one given temperature, especially at -10 ^{o}C and -20 ^{o}C, R values are 15 and 18 for varying particle concentration respectively. On the other hand, in terms of fractural index D, the fitting value shows a clear increasing trend with the volume fraction of MCNT, particularly at low temperature conditions. For instance, when temperature is -10 ^{o}C, D value increases gradually from 1.73 to 1.76 during the volume fraction grows from 0.0625 % to 0.5 %. Also, the same trend is found when temperature is -20 ^{o}C.

Table 5.12 Fitting parameters of MCNT cluster in NaCl-water basefluid.

Temperature	25 ^{o}C			-10 ^{o}C			-20 ^{o}C		
% MCNT	R	D	φ_{in}	R	D	φ_{in}	R	D	φ_{in}
0.0625	10	1.70	0.052	14	1.75	0.032	14	1.75	0.025
0.125	10	1.70	0.052	14	1.75	0.032	17	1.72	0.025
0.25	11	1.70	0.043	14	1.75	0.033	17	1.72	0.025
0.5	12	1.73	0.043	14	1.75	0.035	17	1.78	0.029

As we have already known the MCNT cluster structure, then we can apply the fitted parameters into the Nan's model and H-C model to obtain the theoretical thermal conductivity value of NaCl-water based

MCNT nanofluids. As plotted in Fig 5-20, predicted thermal conductivity with experimental thermal conductivity are presented together at 25 ^{o}C, -10 ^{o}C and -20 ^{o}C. At first, from the general point of view, we can find that all of the predicted thermal conductivity value overestimates the experimental thermal conductivity value in a noticeable degree, particularly when particle concentration is above 0.125 %. As we know, the predicted value is computed by applying φ_{in} into Nan's model, in which the value of φ_{in} is derived from the fitting parameter R and D in modified K-D model via rheology analysis. Also, as shown in Table 5.12, R and D doesn't vary significantly, thus the value of φ_{in} remains steady in a narrow range, consequently, the MCNT volume fraction becomes the major factor that dominates in the prediction of thermal conductivity. As a result, we can observe an approximately linear relationship between the predicted thermal conductivity and the particle concentration.

However, in the real case, the MCNT cluster structure in NaCl-water basefluid might not be steady as illustrated from the fitting parameter via modified K-D model. This uncertainty makes us have to rethink the applicability of the predicting method.

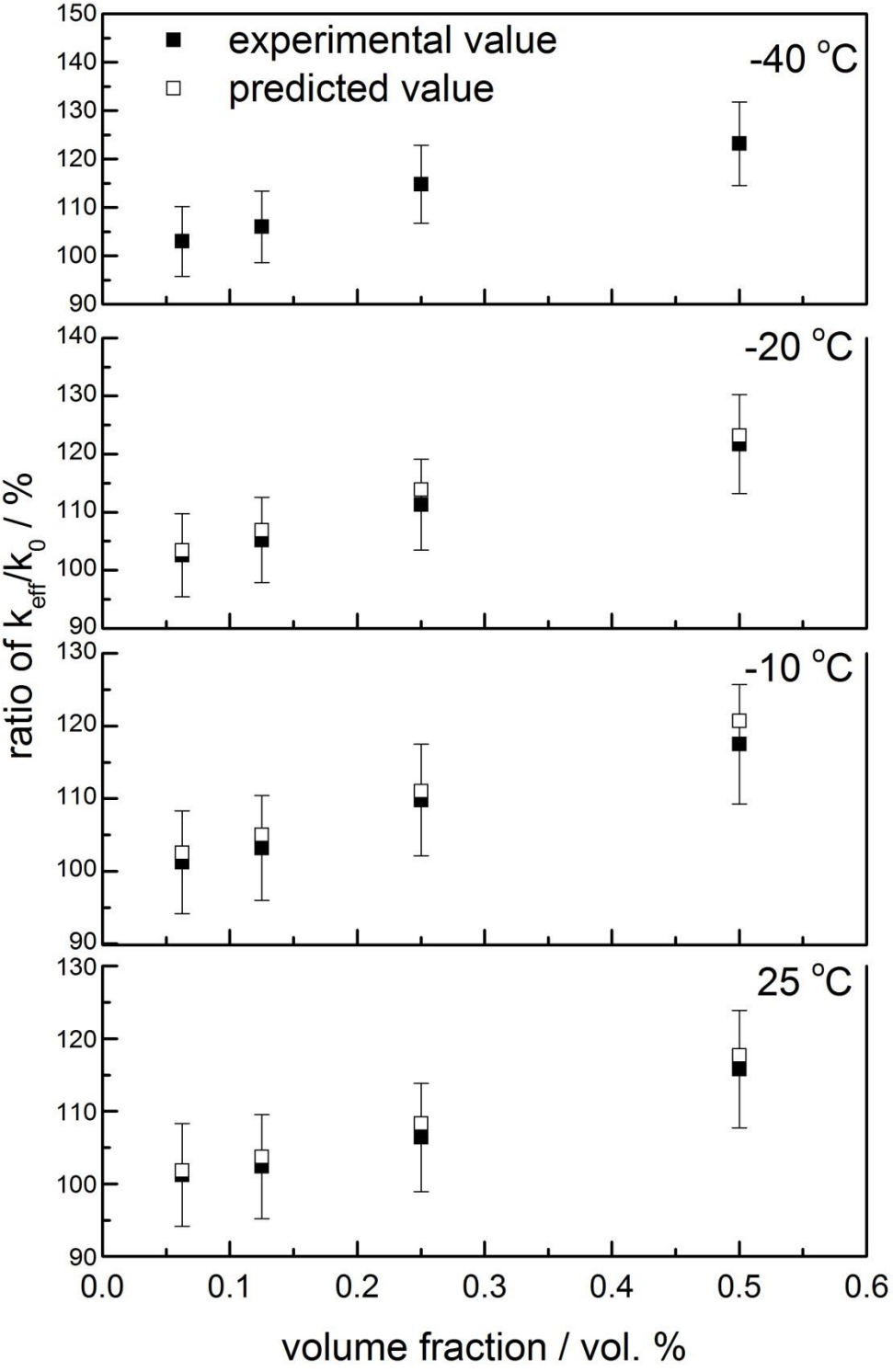

Fig 5-20 Relative thermal conductivity of KCl-water based MCNT nanofluids

As proved in EG-water based MCNT nanofluids, the predicted thermal conductivity follows well with the measured thermal conductivity. In this case, when the basefluid has been change to NaCl-water solution, the thermal conductivity predicting method shows its own limitations. Hypothetically speaking, the deviation of the predicted value could be mainly contributed to the variability occurs at rheology analysis part during the thermal conductivity predicting procedure. Specifically, the overestimated thermal conductivity could be caused by the artefact due to the shear flow when we apply the modified K-D model to predict the MCNT cluster structure. As we mentioned in chapter 4, the NaCl-water we use is a high ion concentration system, which prevents the particle from arranging evenly in the basefluid when left to stand. Thus, the applied shear force might play a positive role on the homogeneous distribution of the MCNT cluster, which causes the higher value of predicted thermal conductivity than the experimental thermal conductivity measured on the still condition.

5.2.8 $MgCl_2$-water

Table 5.13 shows the fitting parameter of modified K-D model of MCNT cluster in $MgCl_2$-water basefluid. The temperature range covers from 25 ^oC to -30 ^oC. Comparing the data in Table 5.13 and Table 5.12, we can find that both naonfluids shows stable fitting parameters of fractural index D at same temperature but various MCNT volume fraction. In addition, not like fractural index, the value of effective cluster size is increasing slowly with the adding of particle concentration, and also with the cooling of the nanofluid. This trend illustrates that although the MCNT cluster size will change with temperature and particle fraction, the amount of particles included in the cluster tends to keep constant.

Table 5.13 Fitting parameters of MCNT cluster in $MgCl_2$-water basefluid.

Temperature	25 ^oC	-10 ^oC	-30 ^oC

% MCNT	R	D	φ_{in}	R	D	φ_{in}	R	D	φ_{in}
0.0625	10	1.75	0.054	9	1.75	0.054	17	1.73	0.027
0.125	10	1.75	0.054	13	1.70	0.043	17	1.73	0.027
0.25	12	1.75	0.043	13	1.70	0.035	17	1.73	0.027
0.5	12	1.75	0.043	13	1.70	0.035	17	1.73	0.027

Based on the fitting parameters of MCNT cluster, we calculated the thermal conductivity of $MgCl_2$-water based nanofluids using Nan's model and H-C model. And the relative thermal conductivity is plotted in Fig 5-21. It is obvious that the prediction of thermal conductivity can generally follow the experimental data at each temperature and particle concentration. However, the predicted value overestimated the real value in some cases. The reason could be contributed to the limitation of the method being used to get the MCNT cluster structure, as we have already mentioned in last section, the shear force has taken part in to affect the cluster distribution during the process of using modified K-D model to predict the cluster structure.

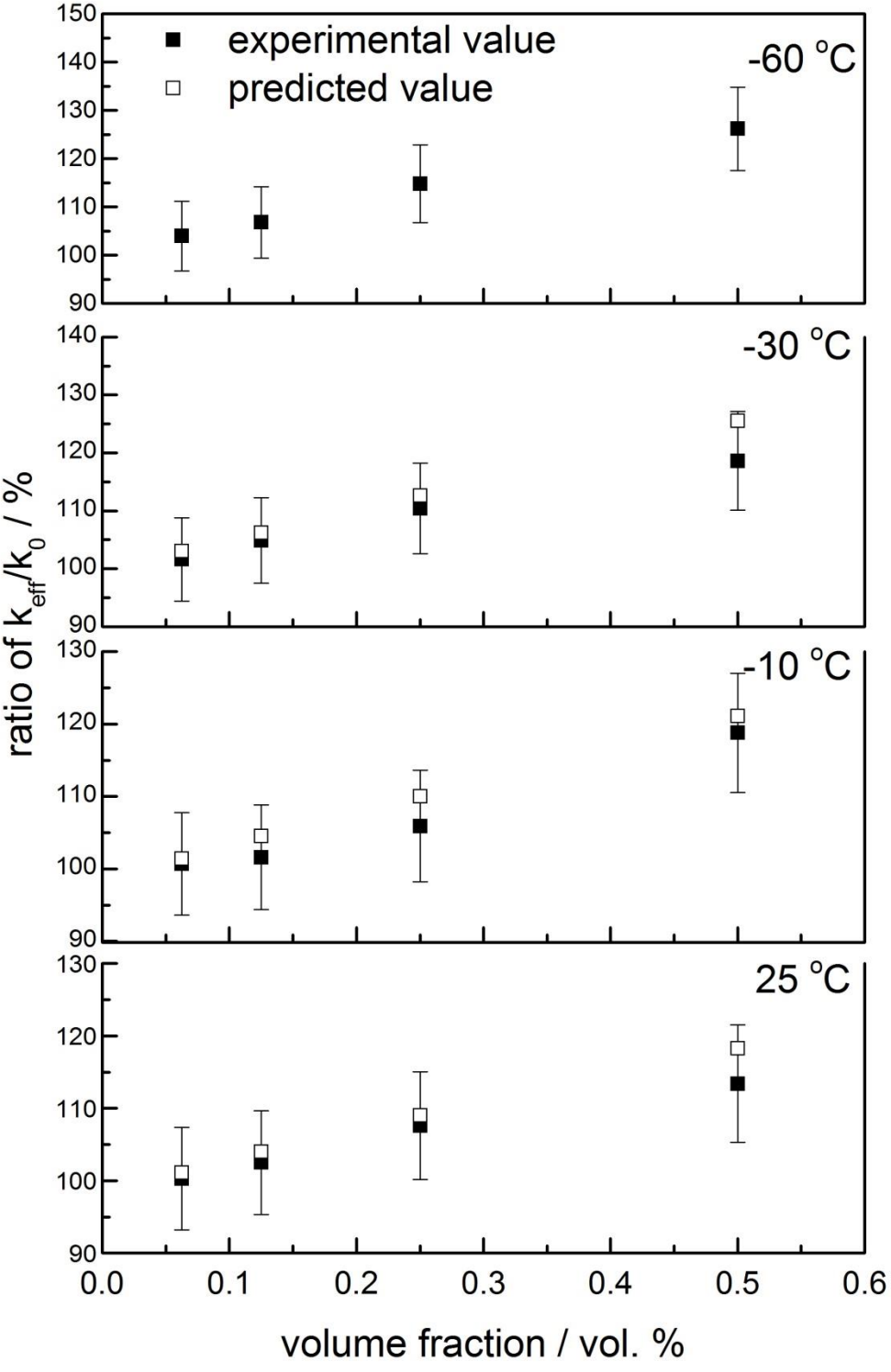

Fig 5-21 Relative thermal conductivity of $MgCl_2$-water based MCNT nanofluids

5.3 Summary

To summarize this chapter, first we presented the experimental thermal conductivity data of both EG-water and salt-water based MCNT nanofluids measured at different temperatures. Then, we listed the temperature induced thermal conductivity variation in tables and plotted the enhancement of thermal conductivity in bar charts. We found that the thermal conductivity of nanofluid with different base fluid shows different relationship with temperature, and the enhancement of nanofluid is higher at lower temperature. All of above findings illustrates that the effective thermal conductivity of nanofluids not only relies on the particle concentration, but also depends on the particle cluster structure, which is highly related with the sample temperature.

Based on this knowledge, we applied the cluster structure parameters which have been studied in chapter 4 into Nan's model and H-C model to predict the value of thermal conductivity. In addition, we compared the predicted thermal conductivity with the experimental thermal conductivity of all samples and found that in most cases, the theoretical value could match the experimental value very well. To conclude, from the study of this chapter, we can link the MCNT cluster structure with the enhancement of thermal conductivity of nanofluids, and use the cluster information through rheology analysis to complete the prediction of thermal conductivity by Nan's model and H-C model.

6 Results and discussion (III): thermal properties

In this chapter, we will investigate the thermal properties of EG-water and salt-water based MCNT nano-composite PCMs. The thermal properties mentioned here include specific heat, melting enthalpy, supercooling degree and crystallization behaviour, all of which are very important properties influencing the thermal storage performance of the nano-composite PCMs. The detailed procedure of sample preparation and equipment and methods of characterization of above thermal properties have already been clearly illustrated in the previous methodology chapter 3. As a results, in this chapter, we will only display the tested data, and then discuss the results in sequence. At the end of this chapter, we will give the conclusion that how MCNT particle affects the specific heat, melting enthalpy, supercooling and crystallization.

6.1 Experimental results and discussion of specific heat

In this section, we will display the measured data of specific heat of both EG-water and salt water based MCNT nanofluids in both liquid and solid state. Then, we will match the experimental value of specific heat with the predicted value by traditional model. Because the numbers of samples are very large, so we will divide all samples into two section: EG-water and salt-water based nanofluds, and only present the data of specific heat measured at room temperature, namely, at 25 ^{o}C.

6.1.1 EG-water based nanofluids

In Fig 6-1, the measured results of specific heat of EG-water based MCNT nanofluids are shown with error bar. We can see that although the error bar is large, the trend of specific heat of basefluid samples with different EG-water ratio is very clear. That is, the specific heat of the mixture will decrease with the amount of adding EG into water. For example, the 20/80 basefluid has the highest specific heat in

our experiment, which is 3.930 J/g • K, and this value decreases to 3.830 J/g • K in 25/75 sample, then to 3.750 J/g • K in 30/70 one. The drop of specific heat follows the mixing rule of EG and water, the similar observation has also been demonstrated in others researches. In aspect of effect of nanoparticle, we noticed that the specific heat of nanofluids is also reducing gradually with concentration of MCNT. The detail will be shown and discussed in the following paragraph.

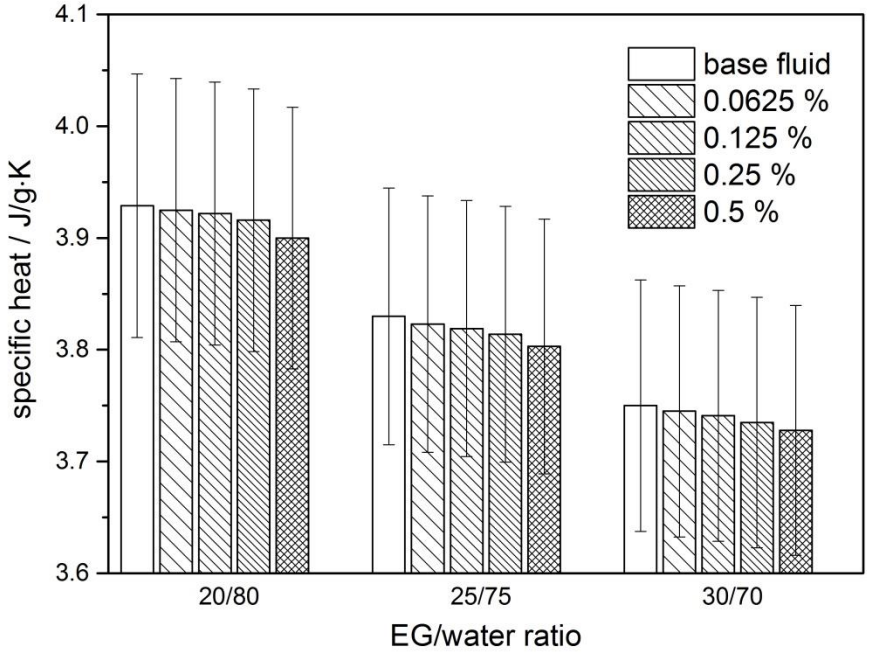

Fig 6-1 Specific heat of EG-water based MCNT nanofluids at 25 °C.

As shown in Fig 6-2, the experimental data and theoretical value of specific heat of EG-water based MCNT nanofluids is plotted together in solid point and dash line respectively, error bar is not shown to make the figure clear and simple. In this section, the model we used to predict specific heat of nanofluds is the conventional mixing rule, which is expressed as $c_p = (1-\varphi)c_{pb} + \varphi c_{pp}$, where c_p, c_{pb} and c_{pp} are specific heat of nanofluid, basefluid and nanoparticle respectively. φ is the volume concentration of MCNT.

On the figure, we noticed that both the experimental specific heat data and the theoretical data are decreasing with the volume fraction of MCNT. And the reduction in specific heat at all particle concentration is bigger than the predicted value, which means the mixing theory underestimates the realistic value. For example, in 20/80 EG-water based samples, the one containing 0.0625 % MCNT presents a very similar specific heat value with the predicted data, they are 3.925 J/g • K and 3.927 J/g •K. The difference is only 0.002 J/g •K. However, in 0.5 % sample, the experimental and theoretical value are 3.900 J/g • K and 3.914 J/g • K, the gap broadens to 0.014 J/g • K.

The main reason of the slight gap between the measured data and predicted data is that when we were preparing the nanofluid samples, we introduced the surfactant SDS into the system, so the dissolved SDS could affect the specific heat of the EG-water mixture, thus the experimental specific heat value of the whole system drops as well. In addition, the amount of SDS in each sample is related with the concentration of particle, in another word, the more MCNT particle, the more SDS was added. As a result, the gap between the experimental value and the theoretical value at high concentration is bigger than that at low concentration which is obviously shown on the figure.

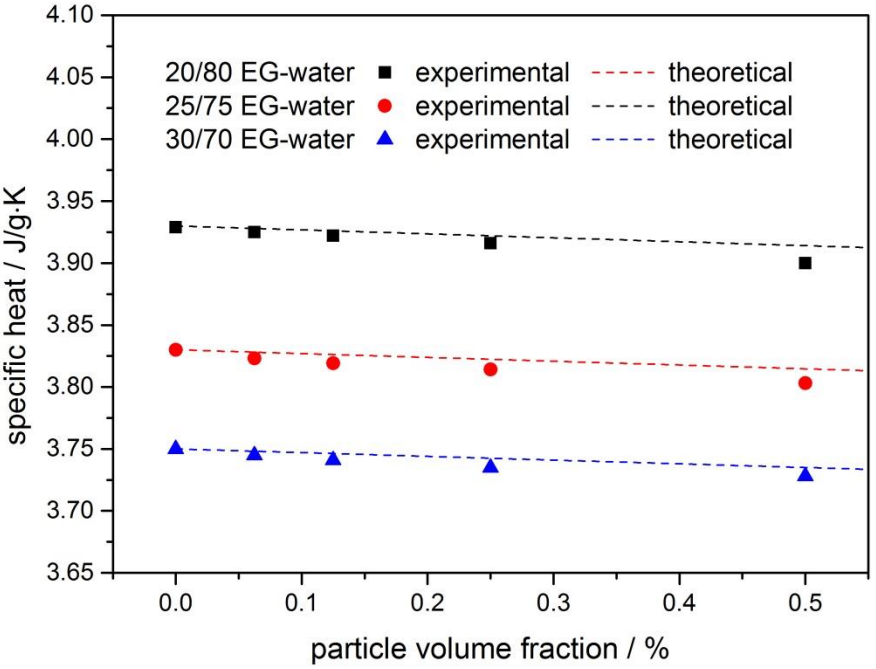

Fig 6-2 Experimental and theoretical data of specific heat of EG-water based MCNT nanofluids at 25 ^{o}C.

6.1.2 Salt-water based nanofluids

In Fig 6-3, we plotted the experimental specific heat results of KCl, NaCl and $MgCl_2$ solution based MCNT nanofluids, the same as EG-water based samples, we only considerate the specific heat at room temperature. As mentioned in last section, the specific heat of EG-water basefluid presents a linear relationship with the EG concentration, and we know that freezing point will decrease with the EG/water ratio. As a result, we can draw the conclusion that specific heat of EG-water will decrease with the freezing point of them. Contrarily, at the very first sight of the data, we can find that the specific heat of these three types of salt-water doesn't show a clear trend with their freezing point. For example, KCl-water solution used in our study has the highest -10 ^{o}C freezing point, but its specific heat locates in the middle of three salt solutions, which is 3.244 J/g • K. And the NaCl-water possesses the highest specific heat, 3.425 J/g • K while its freezing point is -21 ^{o}C, lower than -33 ^{o}C of $MgCl_2$-water solution. The reason of the irregular specific heat of salt solutions could be contributed to

the combining effect of many factors, including the weight fraction of the salt in the water, the molar mass of the salt, the volume of the ions dissolved in water and so on. All of above makes it very hard to predict the specific heat precisely by theoretical model, thus, experimental study is the most convenient way to know the specific heat of different salt solutions.

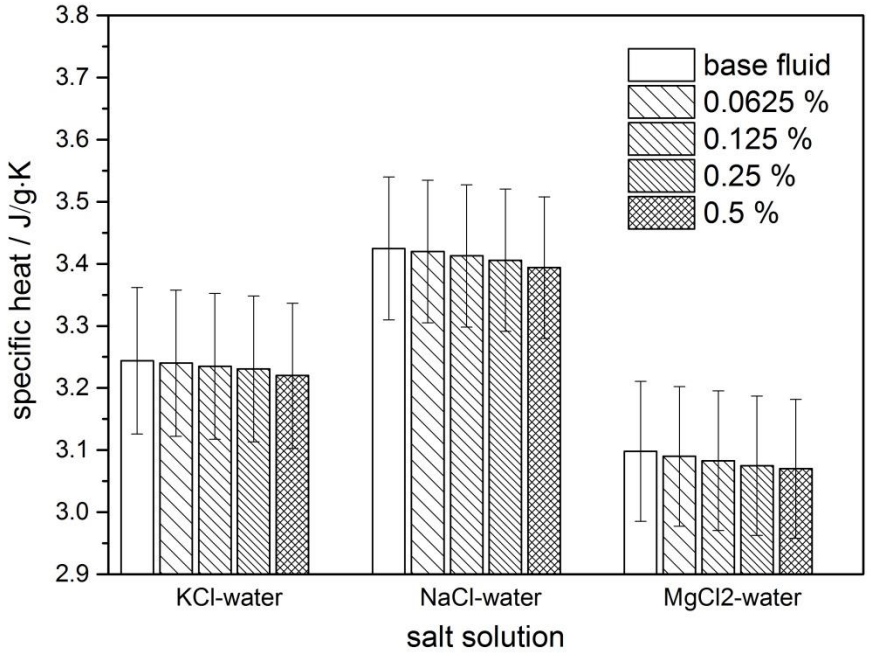

Fig 6-3 Specific heat of salt-water based MCNT nanofluids at 25 ^{o}C.

In addition, we also plotted the experimental specific heat data with the theoretical data together against the MCNT volume fraction, which is shown in Fig 6-4 without error bar for convenience. It is apparent that all of the salt-water based nanofluids show the same relationship between specific heat and particle volume fraction, namely, specific heat decreases with particle concentration. For example, the specific heat of NaCl-water based MCNT nanofluids is 3.425, 3.420, 3.413, 3.406 and 3.394 J/g • K in basefluid, 0.0625 %, 0.125 %, 0.25 % and 0.5 % samples respectively. Besides that, like in EG-water based nanofluids, the mixing model has been approved to be applicable for predicting the

specific heat of salt-water based nanofluds although an insignificant gap occurs when particle concentration is high.

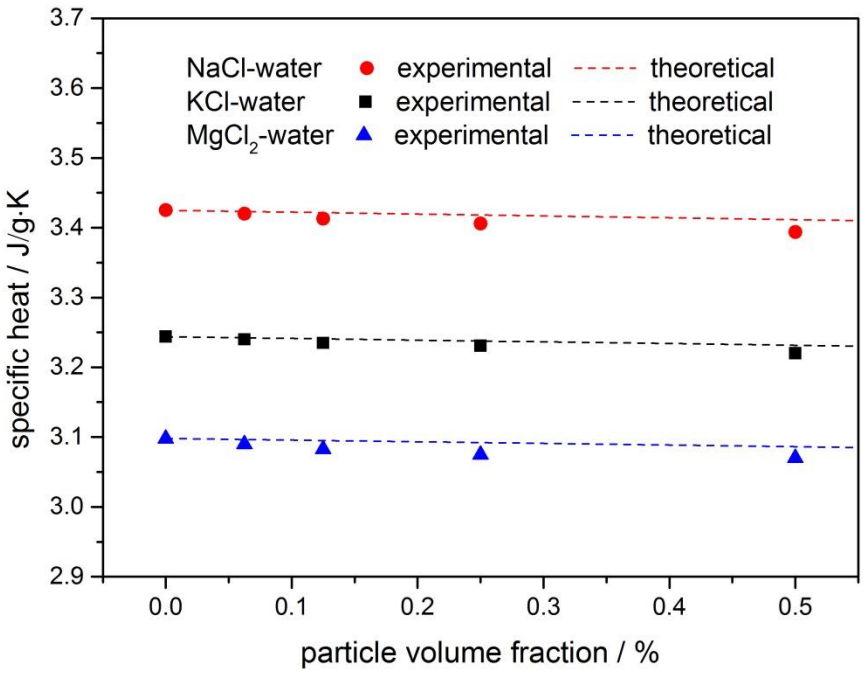

Fig 6-4 Experimental and theoretical data of specific heat of salt-water based MCNT nanofluids at 25 °C.

6.2 Experimental results and discussion of melting point and melting enthalpy

In this section, we will display the experimental results of the melting point and melting enthalpy of both EG-water and salt-water based MCNT nanofluids. First, in aspect of basefluid type, we will divide our samples into two parts: EG-water and salt-water based nanofluids. Then, in each part, we will show the DSC curves during the melting stage, consequently, based on these curves, we can obtain the melting point and melting enthalpy.

6.2.1 EG-water based nanofluids

To start the works of this part, we investigated the relationship between the EG/water ratio and the melting point and melting enthalpy. In Fig 6-5, the effect of EG on the melting point depression is clearly shown with the fitting trend line. The melting point is -15.7 ^{o}C, -22.1 ^{o}C and -25.4 ^{o}C in 20/80, 25/75 and 30/70 EG-water mixture respectively. Also, we can find that the degree of melting point depression follows a linear relationship with the concentration of EG. This finding could be explained very well by the melting point depression theory, which claims that in an ideal solution, the degree of melting point decrease of the solvent (in our case is water) depends only on the solute (in our case is salt) concentration that can be estimated by a linear relationship.

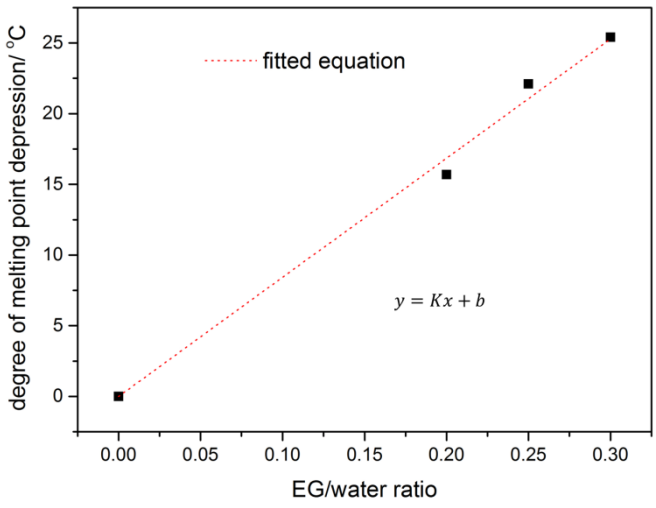

Fig 6-5 Degree of melting point depression of EG-water basefluid.

Apart from melting point, we presents the measured melting enthalpy of EG-water basefluid in Fig 6-6. Interestingly, when we come to look at the experimental data of melting enthalpy, the result shows a big discrepancy with the value predicted by simply using the mixing theory. It is apparently that the melting enthalpy is decreasing dramatically with EG/water ratio and fits an exponential correlation instead of

following the linear trend. For example, the measured melting enthalpy is 334.0 J/g in water, and it has dropped by more than half to 141.0 J/g by adding only 20% EG, and when the ratio is 30/70, the melting enthalpy data has shrunk drastically to 85.5 J/g. Moreover, the fitted equation is shown on the figure with parameter of A= 319.22, B=0.2 and C=14.46. The reason of this abnormal phenomenon could be explained by considering the –OH group in ethylene glycol, which traps the water molecular through hydrogen bonding force thus leading less water molecular to attend the freezing process, as a result, the overall melting enthalpy will be diminished due to the existence of some 'unfrozen' water molecular.

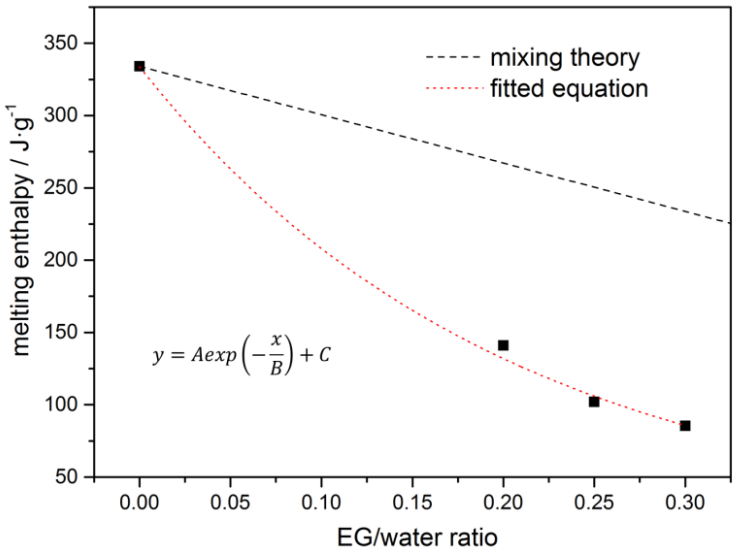

Fig 6-6 Melting enthalpy of EG-water basefluid.

Then, we will study the effect of nanoparticle on the melting point and melting enthalpy of EG-water based samples. Results of samples at different EG/water ratio are shown in Fig 6-7 (a)-(c). Firstly, to find the relationship between the MCNT volume fraction and the melting point, we only look at the red circle symbol in each figure. It is obvious that the data of the melting point at different particle

concentration in each figure keeps almost unchanged with only a little fluctuation. This observation indicates that the amount of the MCNT does not play a very significant role on the melting point of the nano-composite samples. In the nanofluids system, the nanoparticle can be considered as an introduced impurity which does not affect the physical properties of the basefluid itself.

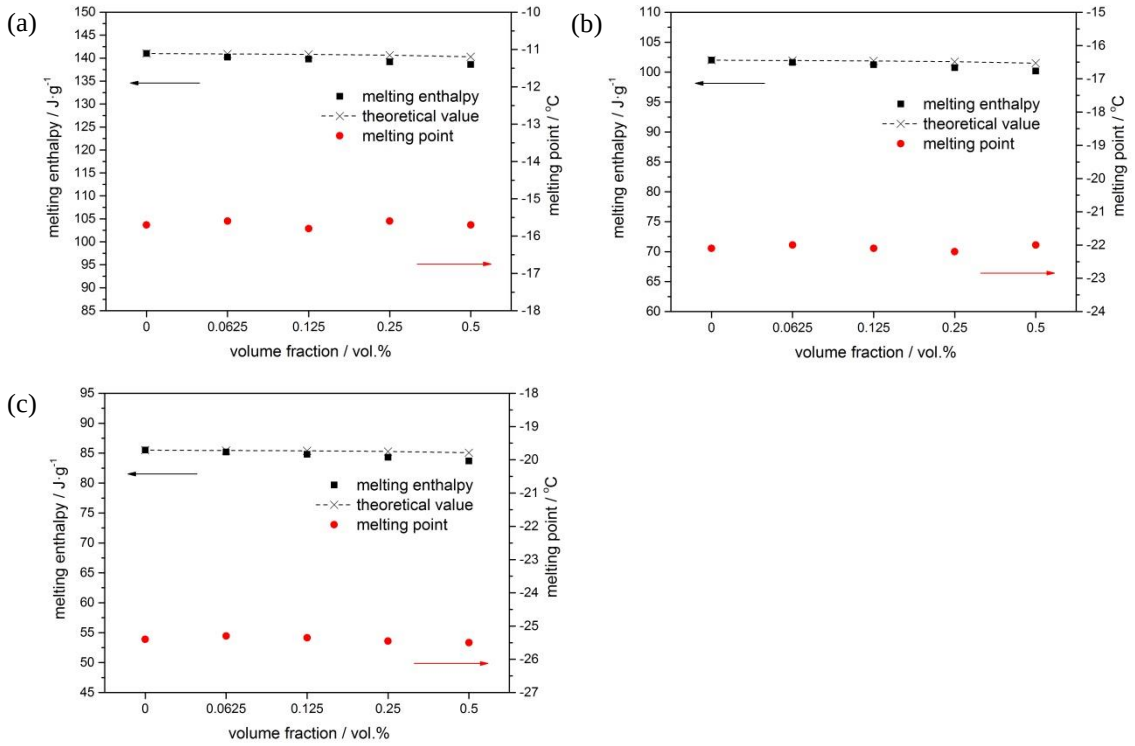

Fig 6-7 Melting point and melting enthalpy of (a) 20/80, (b) 25/75 and (c) 30/70 EG-water based MCNT nanofluids.

In terms of melting enthalpy, data are plotted in figures using black square symbol, the predicted value are also shown together with the experimental data. From the results, we can easily find that the melting enthalpy will decrease with the adding of MCNT in nanofluids based on EG/water mixture of any ratio. Luckily, the loss of the melting enthalpy is very few which is at an acceptable, if not negligible level in the industrial cold storage application. For example, the largest melting enthalpy loss

among all EG-water based samples happens in 20/80 EG-water containing 0.5 % MCNT, which is only 2.4 J/g. Besides that, we also find that the decreasing of melting enthalpy matches well with the theoretical value calculated by mixing theory, the same one we used to predict specific heat before. Because added MCNT particles does not participate into the process of melting, thus the effective phase changing proportion in the whole nano-composite PCM will reduce to some extent corresponding to the amount of MCNT added into the base material.

6.2.2 Salt-water based nanofluids

For salt-water based MCNT nanofluids, we don not study the effect of salt concentration on the change of melting enthalpy and melting point. Because as mentioned in the materials and methodology chapter, the salt solution we used in this study are all at their eutectic point, which means for each type of salt, an exact salt/water ratio was chosen to make the basefluids has the lowest freezing point. However, we still study effect of adding different types of salt on the melting point and melting enthalpy of pure water. As we all know, adding impurity into the water will depress the melting point of the water itself. However, the melting enthalpy of salt solution is not simply as we expected by only summing the latent heat of fusion of the salt and the water. That is because, the salt has already become ionic state when dissolved in the water, and these ions are all surrounded by water molecules. So, the amount of bond energy stored in the solid state salt has been transferred into the 'hydrated ions', and this part of energy will not participate in the process of the melting and freezing of the salt solution. That is why the total amount of melting enthalpy of salt solution is reduced based on the original value of pure water, but no matter with the melting enthalpy of the salt very much. As shown in Fig 6-8, we can have a clear look at the reduction of both melting point and melting enthalpy of different types of salt solution. The percentage of reduction of melting point is calculated by dividing the degree of the melting point

depression of the salt solution with the melting point of water (273 K). And also, the percentage of reduction of melting enthalpy is obtained using the same method.

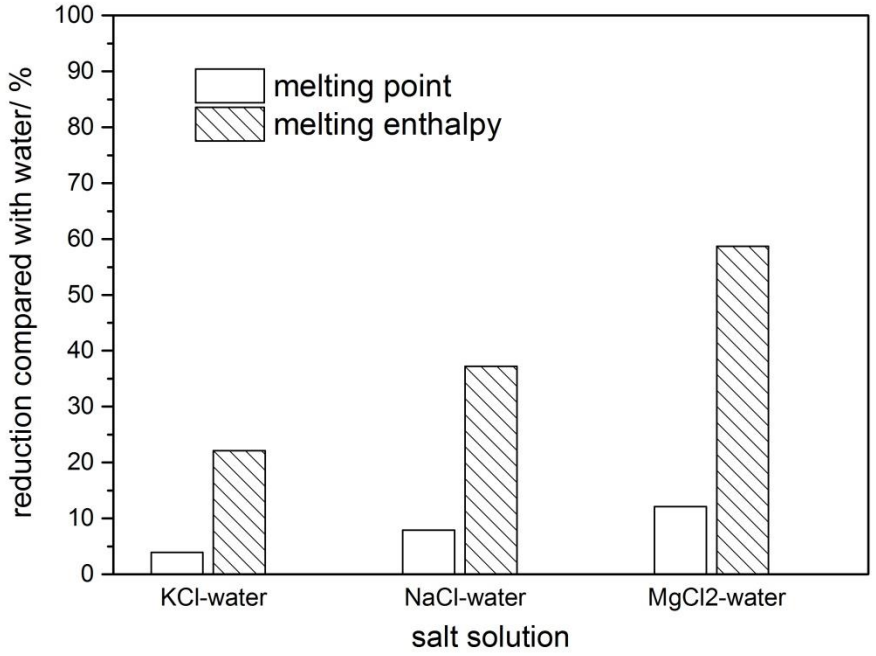

Fig 6-8 Reduction of melting point and melting enthalpy.

From the results, it is clear that the degree of reduction of melting point is linearly increasing from KCl-water to NaCl-water, then to MgCl2-water solutions, while the degree of reduction of melting enthalpy is also increasing at the same time. However, the extent of both dropping of melting point and melting enthalpy of each salt solution is very different. For example, in KCl-water, melting point has been decreased by 3.95 % to -10.78 oC , while the melting enthalpy 22.13 %, which is 260.1 J/g. And in NaCl-water, the melting point and melting enthalpy is -21.54 ^{o}C and 209.8 J/g, decreased by 7.89 % and 37.19 % respectively. Also in $MgCl_2$-water, only 12.15 % depression of melting point brings an over half loss on melting enthalpy, the heat of fusion is only 137.8 J/g. From above results, we know

that to achieve a lower melting point PCM, melting enthalpy can be sacrificed a lot, thus, a balance between the working temperature and the energy storage density need to be considered carefully when we choose a PCM for the real cold storage applications.

After that, we will study the effect of MCNT concentration on the melting point and melting enthalpy of salt solutions based nanofluids, results are listed in Fig 6-9. From the figure, we find that the melting point in three different salt solution based nanofluids does not vary with the particle volume fraction very much, namely, adding nanoparticles into the PCM will not affect the feasibility of the material to be used in a particular temperature range. However, the melting enthalpy of all nanofluids tend to decrease with the amount of added MCNT particles. For examples, in Fig 6-9 (a), a much huger reduce in melting enthalpy than the predicted value can be observed in KCl-water based MCNT nanofluid, especially in high particle concentration samples. For example, at 0.0625 %, the measured melting enthalpy is 257.6 J/g, while the theoretical value is 259.9 J/g, the gap is 2.3 J/g. And at 0.5 %, the experimental data is 250.2 J/g, 8.6 J/g lower than the theoretical value. Based on the results, it seems that the rate of descend of the experimental melting enthalpy against particle concentration is much higher than the predicted value using mixing theory. Moreover, the similar trend of melting enthalpy can be found in NaCl-water and $MgCl_2$-water based nanofluids as well. The experimental results of melting enthalpy of all samples are listed in Table 6.1

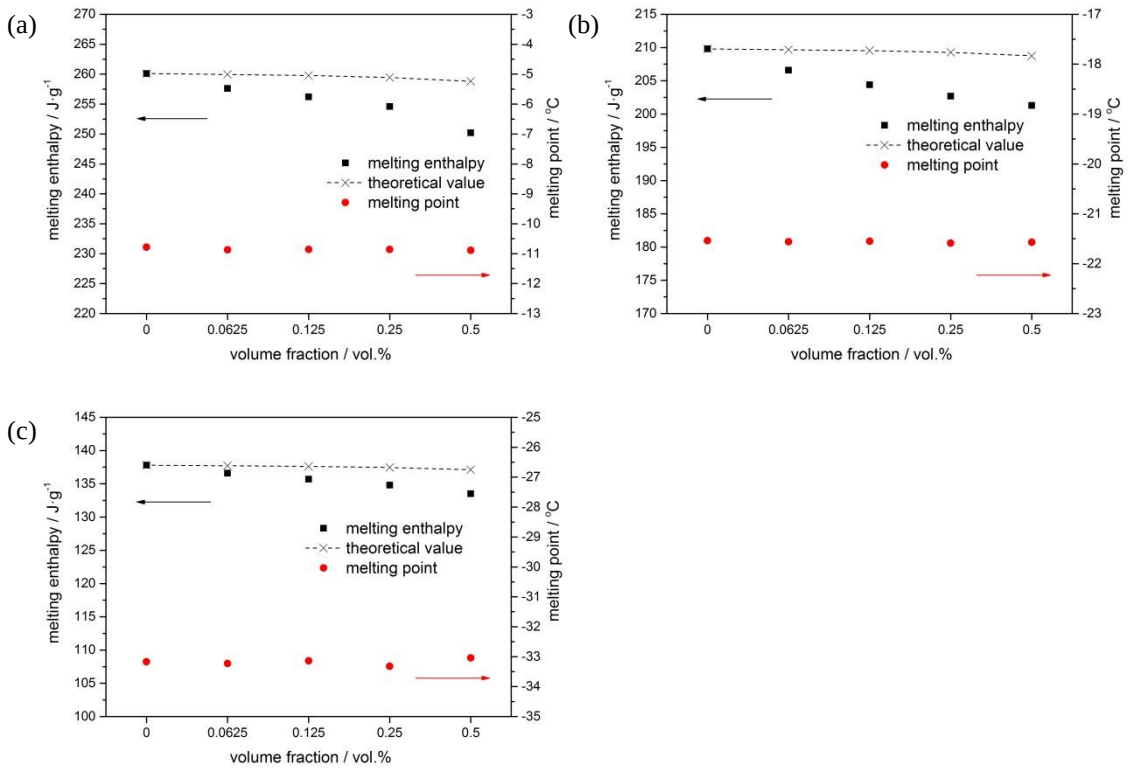

Fig 6-9 Melting point and melting enthalpy of (a) KCl, (b) NaCl and (c) $MgCl_2$ -water based MCNT nanofluids.

Compared with the melting enthalpy results of EG-water based samples, we can find the value in salt-water based samples scatters far from the value predicted by mixing theory. This could be caused by the different types of surfactants used in two different systems. In former case, SDS was used to enhance wettability of MCNT in the EG-water mixture, while in later, Gum Arabic was applied to thicken the salt solution to keep the MCNT particles well isolated from each other. Similar with adding EG into water, the thickening agent itself will demise the latent heat of fusion, due to the –OH groups in Gum Arabic will capture water molecules to constrain their participation in the phase changing process. Therefore, an alternative way should be figured out to formulate stable salt solution based nano-composite PCMs without sacrificing the melting enthalpy severely.

Table 6.1Melting enthalpy of salt-water based MCNT nanofluids.

samples	melting enthalpy (J/g)				
	pure	0.0625%	0.125 %	0.25 %	0.5 %
KCl-water	260.1	257.6	256.2	254.6	250.2
NaCl-water	209.8	206.6	204.4	202.7	201.3
$MgCl_2$-water	137.8	136.6	135.7	134.8	133.5

6.3 Experimental results and discussion of supercooling

In this section, we will display the degree of supercooling of EG-water and salt-water based MCNT nanofluids. As we have already mention in methodology chapter, we used two kinds of method to characterize the supercooling degree of nano-composite PCMs. One of them is called Temperature-history method, a very traditional and commonly used method to achieve onset of freezing temperature. The other is a novel method firstly proposed by us, and we name it Modulus-temperature method. In this work, we will compare the experimental results using both methods and discuss the results based on two categories of basefluids: EG-water and salt water.

6.3.1 EG-water based nanofluids

Firstly, we will present the experimental results of EG-water based samples. The group of EG-water based nanofluids can be further divided into three subgroups according to the ratio of EG to water, which are 20/80, 25/75 and 30/70.

20/80 EG-water

In Fig 6-10, the Temperature-history curves of 20/80 EG-water based MCNT nanofluids are plotted. We can see that the temperature drops below the ideal freezing temperature (equals to the melting point) until a lowest point and then rise up to the ideal freezing point again, which illustrates the

supercooling phenomenon in all samples. Not only us, this kind of Temperature-history curve is also presented by other researchers, which is a clear and visual demonstration of the existence of supercooling phenomenon during freezing of PCMs. To be clear and specific, we enlarge the supercooling zone on all curves in Fig 6-10 (a), results are plotted in Fig 6-10 (b). In the zoom-in view, we can point out the bottom of each curve, namely, the onset of freezing of each 20/80 EG-water based sample, and these data are listed in Table 6.2.

As shown in Table 6.2, the supercooling degree in the pure 20/80 EG-water mixture is 5.9 ^{o}C, which can be further reduced to 5.3 ^{o}C, 4.8 ^{o}C, 3.7 ^{o}C and 2.6 ^{o}C by adding 0.0625 %, 0.125 %, 0.25 % and 0.5 % MCNT in volume fraction. The degree of supercooling reduction can be explained by the heterogeneous crystallization mechanism, which is caused by the introducing of MCNT particles.

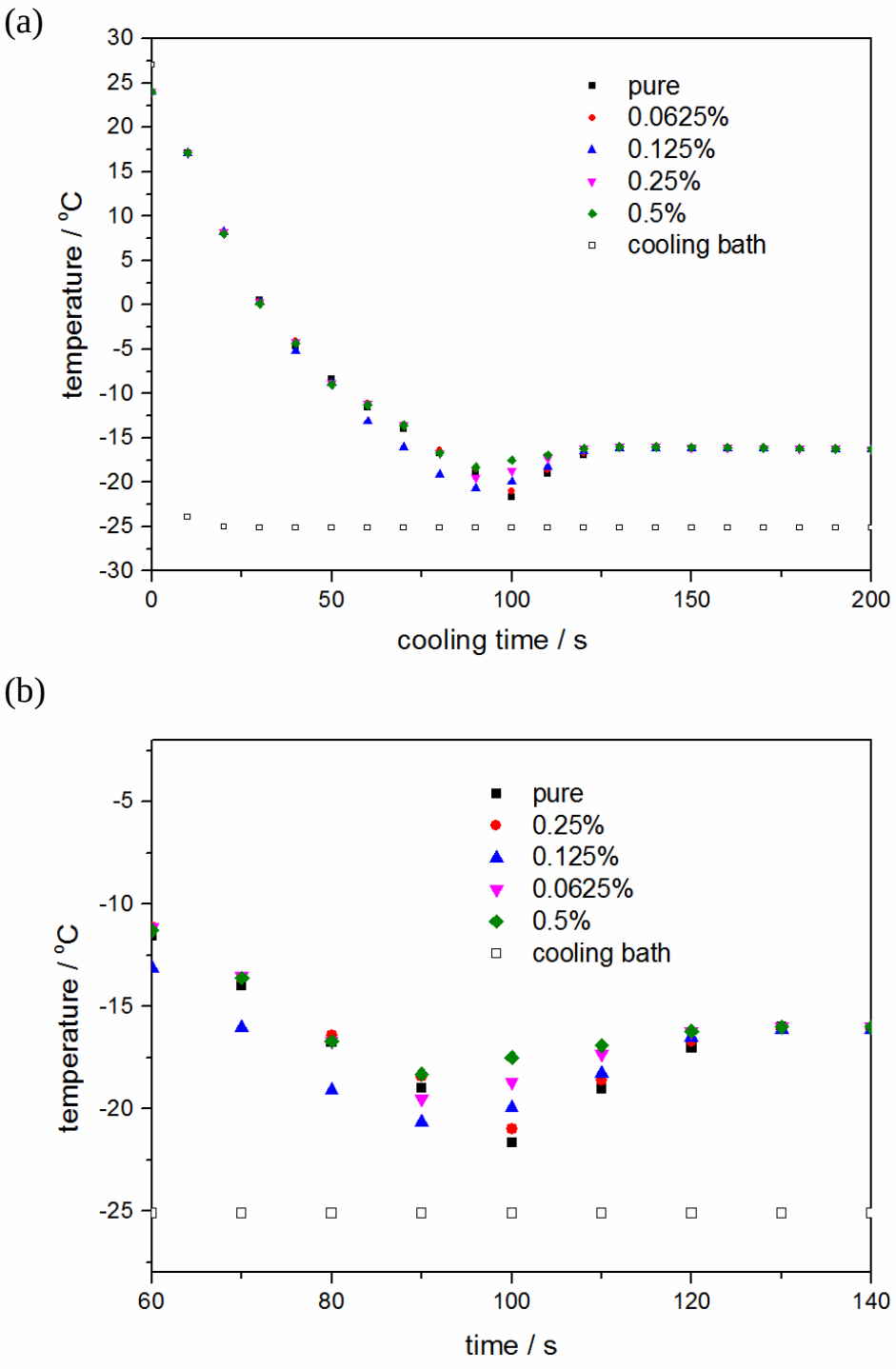

Fig 6-10 Temperature-history results of 20/80 EG-water based MCNT nanofluids (a) whole view, (b) zoom-in view.

Table 6.2 Freezing point and supercooling degree of 20/80 EG-water based MCNT nanofluids by Temperature-history.

Vol %	Onset of T_f (^{o}C)	Δ T (^{o}C)
0	-21.6	5.9
0.0625	-21.0	5.3
0.125	-20.5	4.8
0.25	-19.4	3.7
0.5	-18.3	2.6

Another way of measuring supercooling degree is also conducted via rheological analysis and the detailed principle of this method is already explained in chapter 3. Simply speaking, that is, by detecting the change of the storage modulus of the samples with temperature, we will know the state of the material at temperature, thus, we can get melting/freezing point by finding the turning point of solid/liquid to liquid/solid state on the modulus-temperature curve. For example, Fig 6-11 shows the modulus-temperature curves of 20/80 EG-water based nanofluids during both freezing and melting process. It is clear that, in melting stage, all of the curves drop down stiffly at approximately the same temperature, from an enormous modulus to a 6 orders of magnitude less modulus, which means that samples containing different amount of MCNT have the same melting point. In the other hand, in freezing stage, we can observe a similar step of modulus in all samples, but contrarily, from low level to high level, indicating the transformation of the PCM from liquid to solid state. Moreover, it is also shown that the onset of the transformation happens at different temperature in samples with different particle volume concentration. The specific data are listed in Table 6.3. The results show the existence of supercooling phenomenon in every samples, and the supercooling degree is decreasing with the adding amount of MCNT. For example, the supercooling degree is 11.3 ^{o}C, 10.7 ^{o}C, 8.8 ^{o}C, 5.9 ^{o}C and 3.2 ^{o}C in samples without and containing 0.0625 % to 0.5 % MCNT.

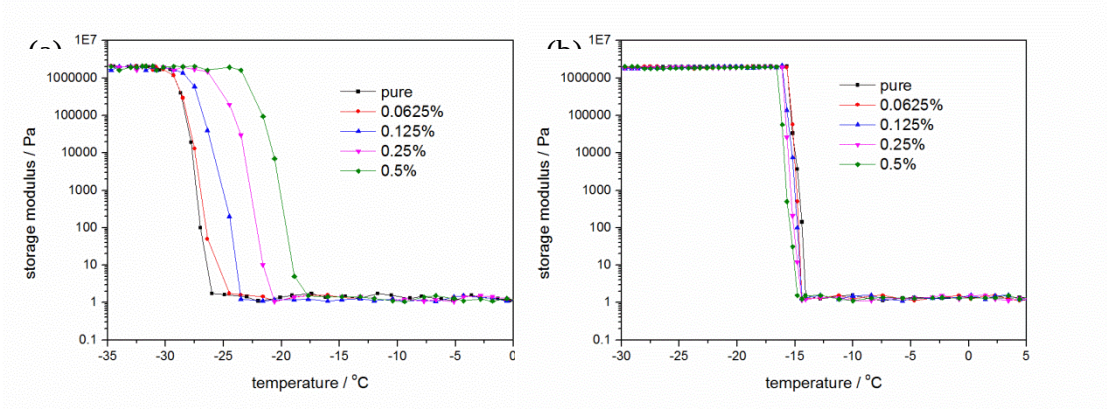

Fig 6-11 Modulus-temperature curves of 20/80 EG-water based MCNT nanofluids:

(a) freezing and (b) melting process.

It is worth to mention that, the measured onset of freezing using two different methods are quite different, like -21.6 ^{o}C and -27 ^{o}C in temperature-history and modulus-temperature respectively. However, the onset of melting shows good consistency in two methods. The discrepancy between the two methods are related to many factors, such as the volume of sample being measured and the geometry of the sample holder. Among them the most influential difference is the freezing condition, in temperature-history method, samples are set into a cooling bath with constant temperature while in modulus-temperature method, the sample chamber and the sample was cooled down simultaneously, namely, it is a nonisothermal crystallization process.

Table 6.3 Freezing point and supercooling degree of 20/80 EG-water based MCNT nanofluids by modulus-temperature method.

Vol %	Onset of T_f (^{o}C)	Δ T (^{o}C)
0	-27.0	11.3
0.0625	-26.4	10.7
0.125	-24.5	8.8
0.25	-21.6	5.9
0.5	-18.9	3.2

25/75 EG-water

For 25/75 EG-water based samples, of which melting point is -22.1 ^{o}C, we set the cooling bath temperature to -35 ^{o}C to ensure a large enough temperature difference for isothermal crystallization. After the experiments, the temperature-history curves are shown in Fig 6-12, and the real freezing point and supercooling results are listed in Table 6.4. From the results, we know that although the melting point of EG-water mixtures are different, the difference of supercooling degree of the counterparts in each group are not that big. For examples, in 20/80 EG-water basefluid, supercooling degree is 5.9 ^{o}C while in 25/75 sample, it is 6.5 ^{o}C, the difference is less than 1 ^{o}C. This is because both of the basefluids use the EG-water mixture system, thus the freezing mechanism are similar in each group of samples.

Also, the modulus-temperature methods was applied on 25/75 EG-water based samples, curves are shown in Fig 6-13, and the supercooling results are listed in Table 6.5. Clearly, supercooling phenomenon can be observed from the freezing and melting curves. And the rightwards shifting of freezing curve by adding MCNT particles in Fig 6-13 (a) indicates that the onset of freezing can be moved to earlier stage in nanofluids samples and the degree of the movement is related with the particle volume fraction. Also, similar with that in 20/80 EG-water based samples, the results measured by modulus-temperature method shows obvious discrepancy with that by temperature-history method, especially in basefluid and diluted nanofluids samples. Anyway, regardless of the difference in detailed experimental data, we can still conclude that introducing MCNT into the EG-water mixture system could reduce the supercooling degree.

(a)

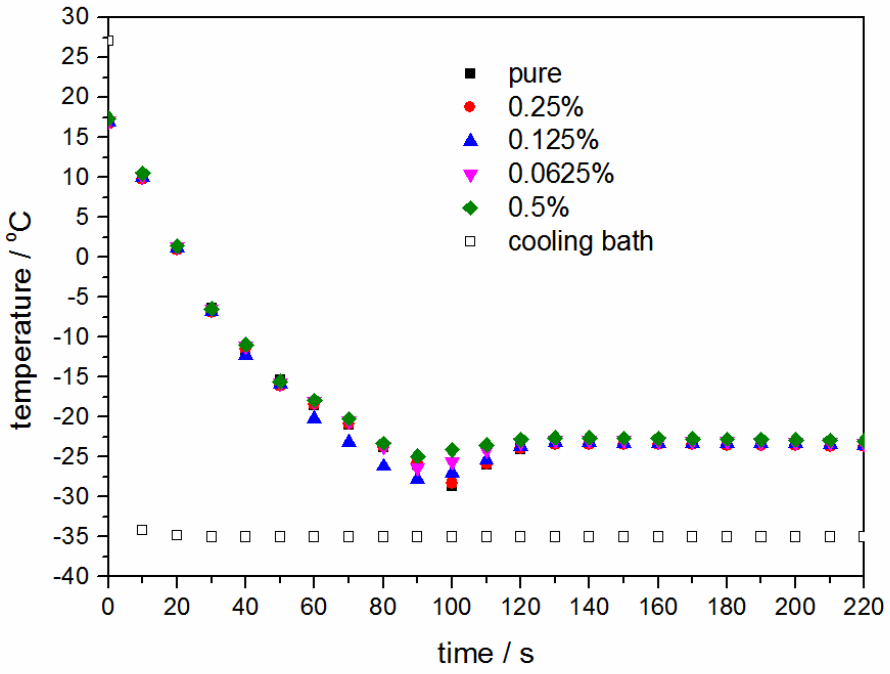

(b)

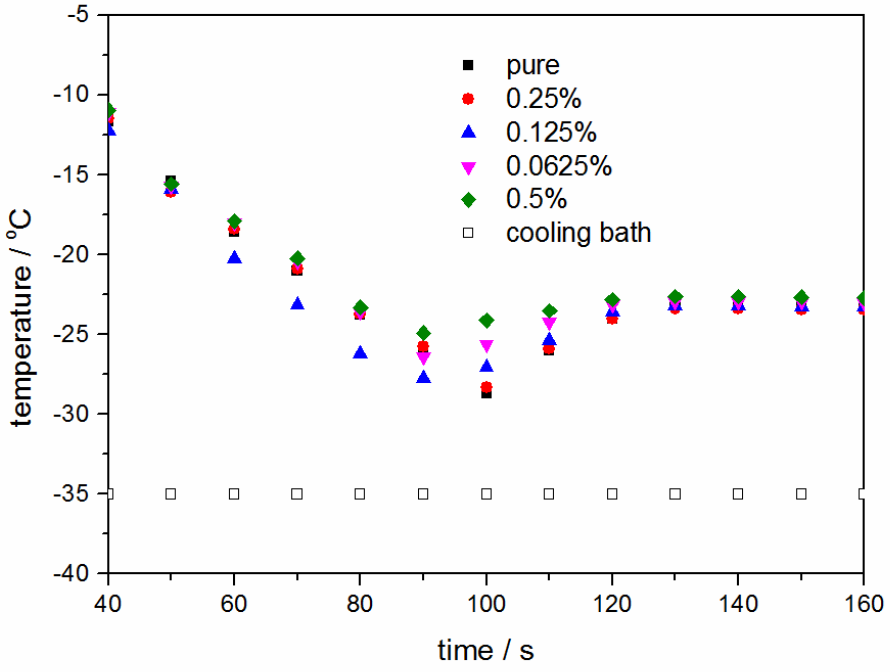

Fig 6-12 Temperature-history results of 25/75 EG-water based MCNT nanofluids (a) whole view, (b) zoom-in view.

Table 6.4 Freezing point and supercooling degree of 25/75 EG-water based MCNT nanofluids by Temperature-history.

Vol %	Onset of T_f (^oC)	Δ T (^oC)
0	-28.6	6.5
0.0625	-28.3	6.2
0.125	-27.7	5.6
0.25	-26.4	4.3
0.5	-24.9	2.8

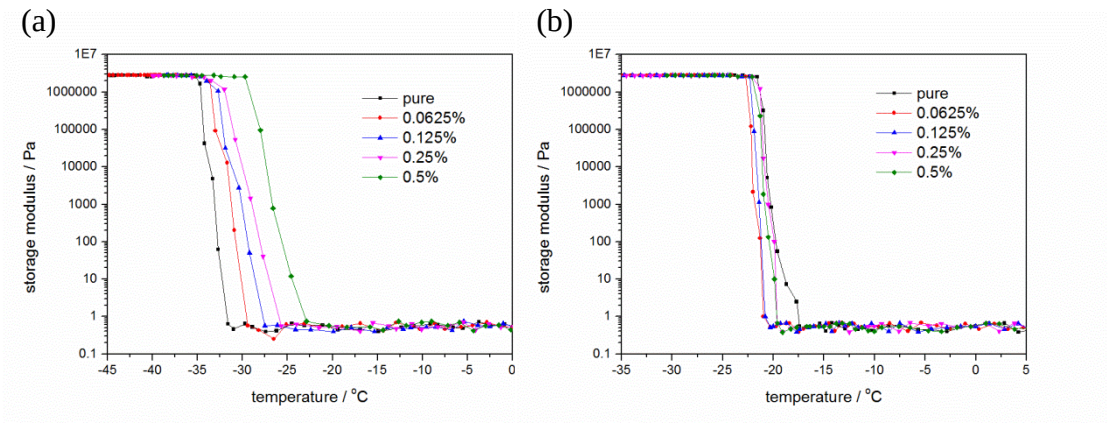

Fig 6-13 Modulus-temperature curves of 25/75 EG-water based MCNT nanofluids:

(a) freezing and (b) melting process.

Table 6.5 Freezing point and supercooling degree of 25/75 EG-water based MCNT nanofluids by modulus-temperature.

Vol %	Onset of T_f (^oC)	Δ T (^oC)
0	-32.7	10.6
0.0625	-30.9	8.8
0.125	-29.2	7.1
0.25	-27.7	5.6
0.5	-24.6	2.5

30/70 EG-water

In Fig 6-14, the cooling curves of 30/70 EG-water based MCNT nanofluids are plotted. Onset of freezing temperature of each sample can be detected in Fig 6-14 (b). Apparently, the gap between the onset of freezing, namely, the bottom of the temperature curve and the flat stage is decreasing with the concentration of MCNT. In another word, the supercooling phenomenon can be constrained by adding MCNT particles. Numerically, the supercooling degree in 0% to 0.5 % sample ranges from 7.2 ^{o}C to 3.1 ^{o}C. Comparing the experimental data in 25% and 20% EG based samples, we can find that the reduction extent of supercooling degree is very close in samples containing same amount of MCNT particles, indicating that the supercooling reduction mechanism is mainly related with the MCNT concentration, and is weakly influenced by other factors.

However, the tested supercooling degree is higher in most samples except 0.5 % sample, which were measured through modulus-temperature method based on the curves in Fig 6-15. The experimental results of supercooling degree is 14.3 ^{o}C, 10.5 ^{o}C, 7.8 ^{o}C, 4.7 ^{o}C and 2.7 ^{o}C in basefluid, 0.0625 %, 0.125 %, 0.25 % and 0.5 % samples respectively. This finding is similar with that in previous experiments, which shows obvious discrepancy in supercooling degree between temperature-history and modulus temperature method. To understand the reason of the difference, we will compare the results of all samples in this thesis in afterwards section.

(a)

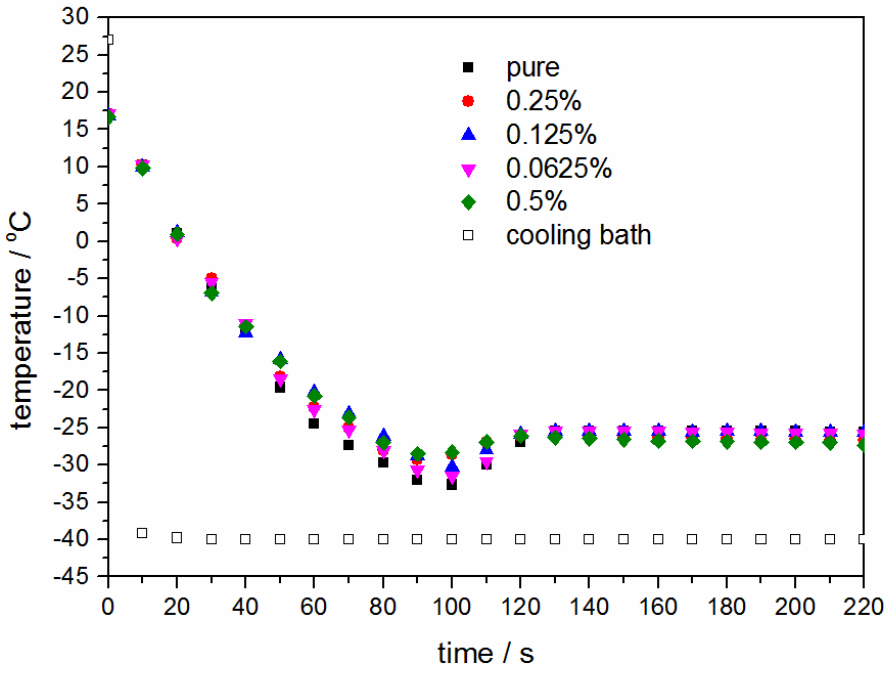

(b)

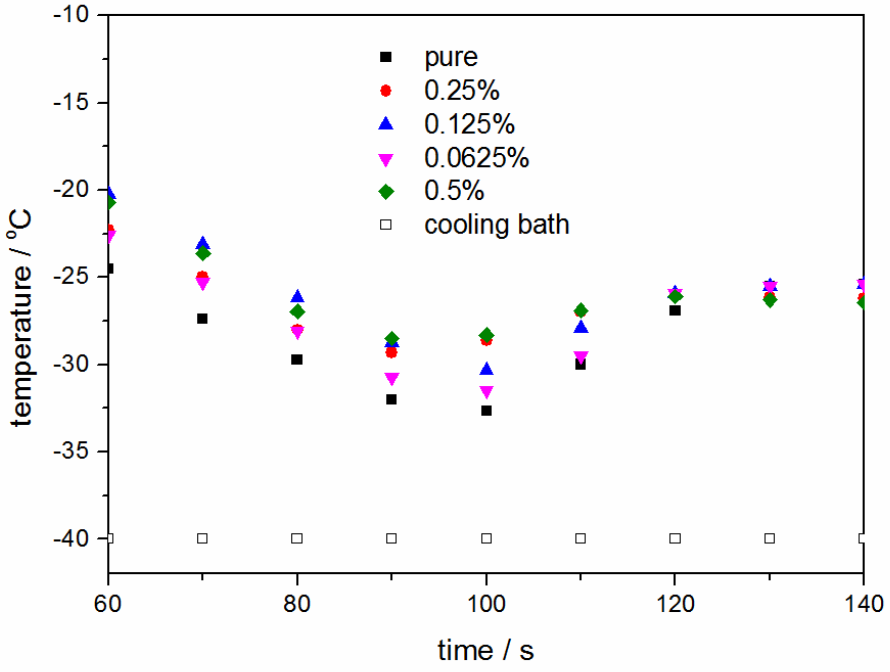

Fig 6-14 Temperature-history results of 30/70 EG-water based MCNT nanofluids (a) whole view, (b) zoom-in view.

Table 6.6 freezing point and supercooling degree of 30/70 EG-water based MCNT nanofluids by Temperature-history.

Vol %	Onset of T_f (^oC)	Δ T (^oC)
0	-32.6	7.2
0.0625	-31.5	6.1
0.125	-30.3	4.9
0.25	-29.3	3.9
0.5	-28.5	3.1

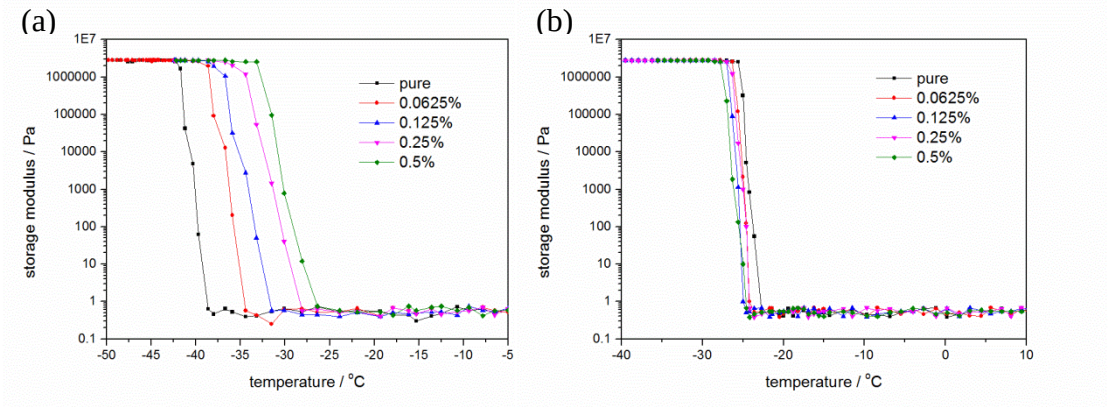

Fig 6-15 Modulus-temperature curves of 30/70 EG-water based MCNT nanofluids:

(a) freezing and (b) melting process.

Table 6.7 Freezing point and supercooling degree of 30/70 EG-water based MCNT nanofluids by modulus-temperature.

Vol %	Onset of T_f (^oC)	Δ T (^oC)
0	-39.7	14.3
0.0625	-35.9	10.5
0.125	-33.2	7.8
0.25	-30.1	4.7
0.5	-28.1	2.7

6.3.2 salt-water based nanofluids

Then, we will present the experimental results of salt-water based samples. The group of salt-water based nanofluids will be classified into three subgroups according to the types of the salt, which are KCl, NaCl and $MgCl_2$.

KCl-water

As shown in Fig 6-16, the live temperature changing of the KCl-water based nanofluids samples were recorded against the time, and the cooling bath temperature was also recorded. From the curves in Fig 6-16 (a), we find that the temperature of all samples keeps dropping until it reaches a certain point and then increases rapidly to a higher temperature. In addition, the lowest point of each samples can be different regarding to the concentration of particle additives, while the plateau stage overlaps at a constant temperature.

In Fig 6-16 (b), we can see more details of the onset temperature of freezing by focusing on the 'valley' area on the curves. The onset of the freezing process, namely, the lowest temperature on the curve of all samples are picked out, consequently, the degree of supercooling can be easily acquired by calculating the gap between the plateau line and the lowest point, which is listed in Table 6.8. From the results, we find that the degree of supercooling of KCl-water without MCNT particles is the highest among all the samples, and it decrease with volume fraction of added MCNT particles, which means that adding MCNT is an effective way to move freezing point to a higher temperature. For example, pure KCl-water basefluids freezes at -15.5 ^{o}C, while the sample containing 0.5 % MCNT starts freezing in advance at -12 ^{o}C.

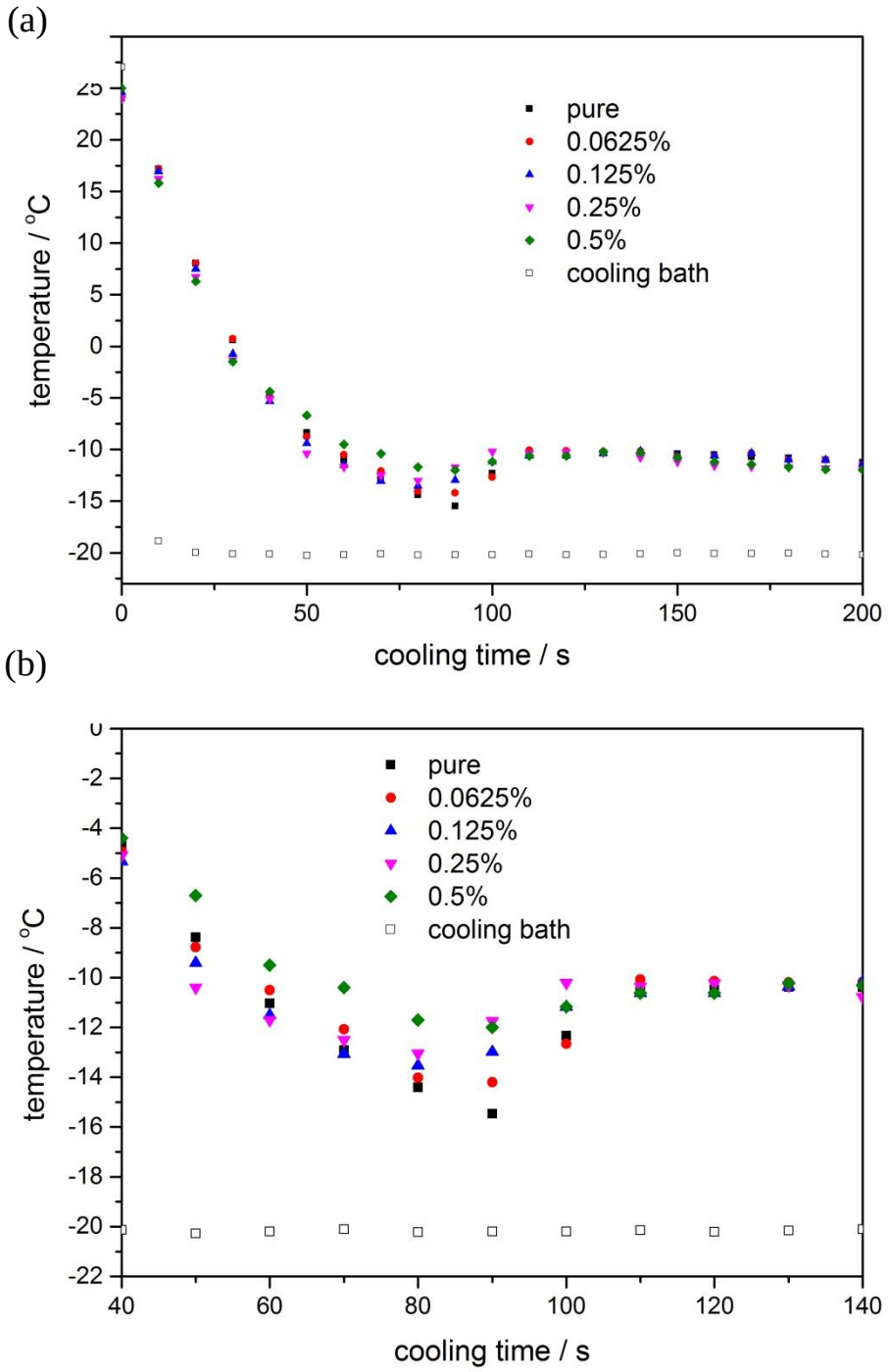

Fig 6-16 Temperature-history results of KCl-water based MCNT nanofluids (a) whole view, (b) zoom-in view.

Table 6.8 Freezing point and supercooling degree of KCl-water based MCNT nanofluids by Temperature-history.

Vol %	Onset of T_f (°C)	Δ T (°C)

0	-15.5	5.2
0.0625	-14.2	3.9
0.125	-13.5	3.2
0.25	-13.0	2.7
0.5	-12.0	1.7

Modulus-temperature curve of KCl-water based MCNT nanofluids are plotted in Fig 6-17. Clearly, the melting curves in Fig 6-17 (b) tell us that introducing MCNT does not change the melting point of our nano-composite PCMs, because all of the samples behaves a step drop in storage modulus at approximately the same temperature, indicating they have the same melting point. But when we look at the freezing curves in Fig 6-17 (a), the situation is very different, each curves jumps up at different turning point, represents that each sample starts transforming from liquid to solid at different temperatures. To compare with results by getting Temperature-history, the freezing point and supercooling degree data using modulus-temperature are presented in Table 6.9.

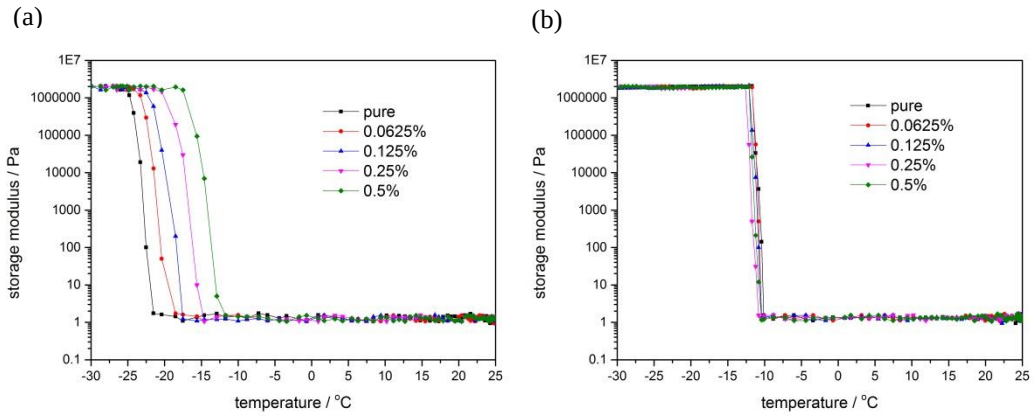

Fig 6-17 Modulus-temperature curves of KCl-water based MCNT nanofluids: (a) freezing and (b) melting process.

Table 6.9 Freezing point and supercooling degree of KCl-water based MCNT nanofluids by modulus-temperature.

Vol %	Onset of T_f (^oC)	Δ T (^oC)
0	-21.5	9.8
0.0625	-20.4	8.7
0.125	-18.5	6.8

0.25	-15.6	3.9
0.5	-12.9	1.2

Not as we expected, the onset of freezing point here is much lower than that in Temperature-history method. For example, in pure KCl-water, the freezing point is -21.5 ^{o}C and -15.5 ^{o}C in modulus-temperature and temperature-history method respectively. Not to mention, results of other samples also shows bias in different extent. Such kind of difference could be caused by many reasons, like the amount of sample, the geometry of the measuring cell and the temperature control method. All of above will affect the heat conduction pattern in the sample, thus causing the bias between the real temperature and the measured temperature. To summarize these two methods of characterizing supercooling degree,we will discuss this comprehensively at the end of this section.

NaCl-water

Temperature-history results of NaCl-water based MCNT nanofluids are displayed in Fig 6-18. On the whole view graph in Fig 6-18 (a), we notice that the trend of the temperature-history curves are similar with that in KCl-water based samples, that is, all of them are decreasing slowly to the bottom of the curve, following by an rapid increase up to a plateau stage. This illustrates that the supercooling phenomenon also exists in NaCl-water based PCMs. However, an obvious distinction is the length of the period between the point when temperature firstly reaches the ideal freezing point and the point when temperature reaches the lowest position. We can find that such a period is approximately 90 s in NaCl-water basefluid, but only one-third in KCl-water basefluid, which means the KCl-water is much easier to freeze than NaCl-water when used as a PCM.

Additionally, in Fig 6-18 (b), we can take a close look at the very bottom of the curve of each sample to get the onset temperature of freezing and supercooling degree subsequently. The results are listed in Table 6.10, it is clear that the onset of freezing could be moved forward by adding MCNT particles, and the degree of advance is proportional to the volume fraction of added particles. For example, the supercooling degree is 5.6, 5.2, 4.1, 3.0 and 2.3 in pure, 0.0625 %, 0.125 %, 0.25 % and 0.5 % samples respectively. The linear reduction of supercooling degree can be contributed to the heterogeneous nucleation mechanism caused by introducing particle interface.

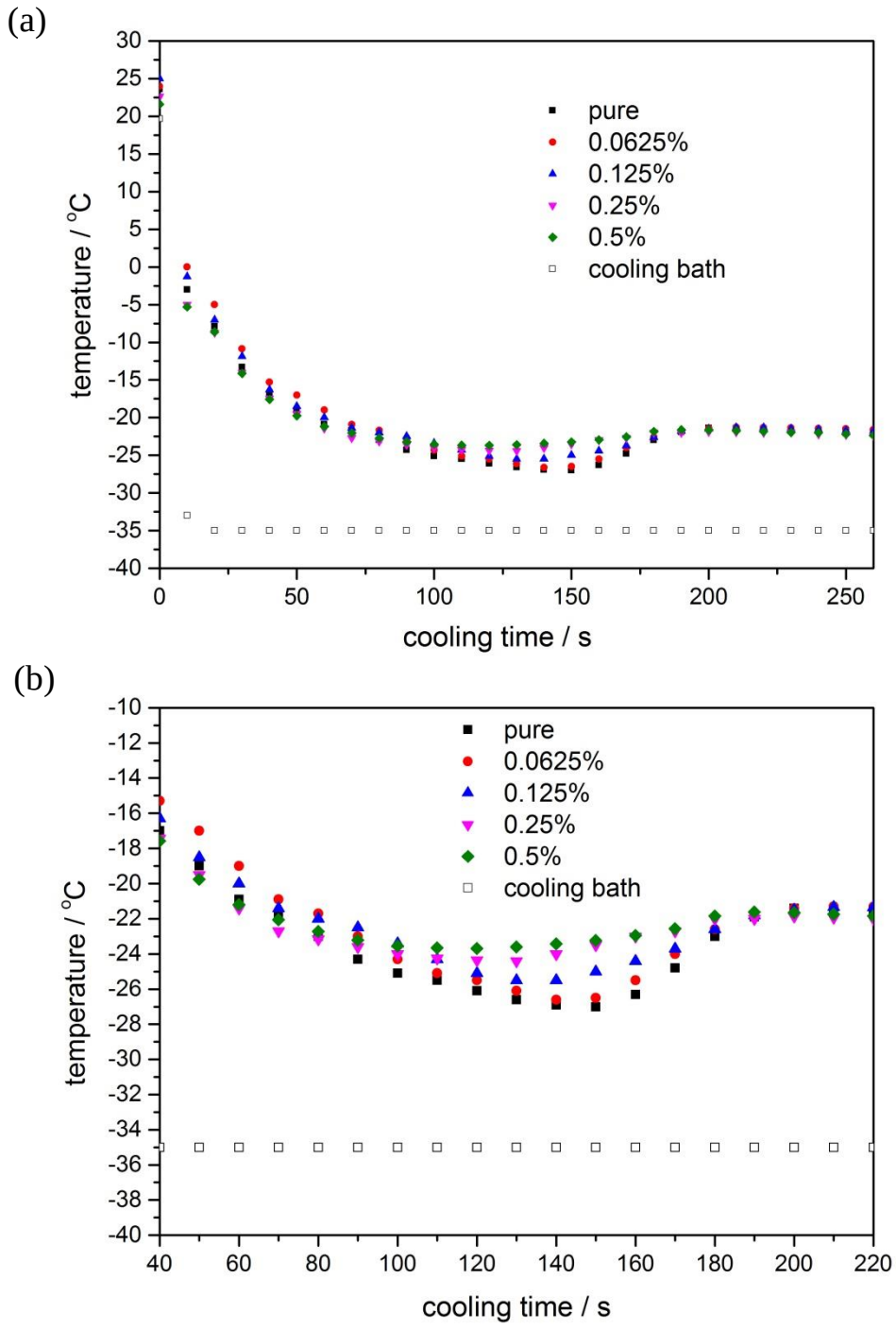

Fig 6-18 Temperature-history results of KCl-water based MCNT nanofluids (a) whole view, (b) zoom-in view.

Table 6.10 Freezing point and supercooling degree of NaCl-water based MCNT nanofluids by Temperature-history.

Vol %	Onset of T_f (^oC)	Δ T (^oC)
0	-27.0	5.6
0.0625	-26.6	5.2
0.125	-25.5	4.1
0.25	-24.4	3.0
0.5	-23.7	2.3

Besides that, the modulus-temperature method is also conducted and the results are plotted in Fig 6-19. The shape of the plot is similar with that in KCl-water based samples. During melting, the storage modulus of all samples drop steeply from solid level to liquid level at almost the same temperature, while during freezing, the transformation from liquid to solid happens at different turning point.

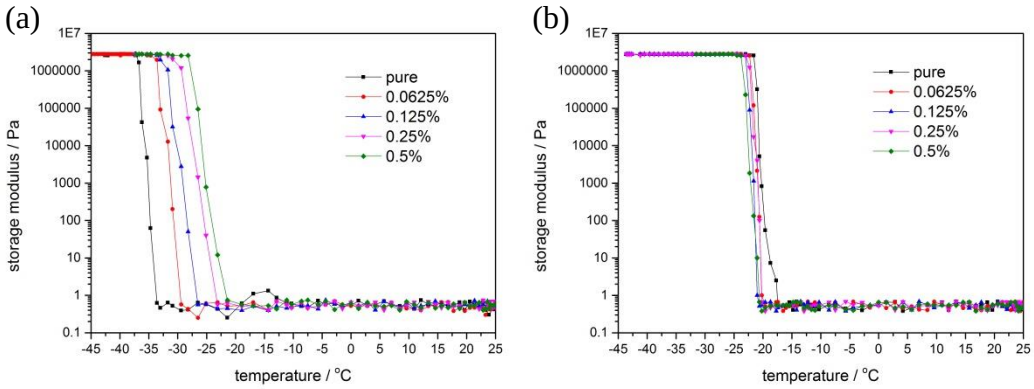

Fig 6-19 Modulus-temperature curves of NaCl-water based MCNT nanofluids:

(a) freezing and (b) melting process.

To be specific, the exact onset of transforming from liquid to solid with the corresponding supercooling degree of all NaCl-water based nanofluids is listed in Table 6.11. Comparing the results with that in Temperature history method, we can find that all the measured onset of freezing by modulus-temperature method is lower, except that in 0.5 % sample. However, the nanoparticle function of decreasing supercooling degree of nano-composite PCMs is well demonstrated in this method.

Table 6.11 Freezing point and supercooling degree of NaCl-water based MCNT nanofluids by modulus-temperature.

Vol %	Onset of T_f (^oC)	Δ T (^oC)
0	-34.7	13.2
0.0625	-30.9	9.4
0.125	-28.2	6.7
0.25	-25.1	3.6
0.5	-23.1	1.6

$MgCl_2$-water

Fig 6-21 shows the Temperature-history results of $MgCl_2$-water based MCNT nanofluids. The cooling bath temperature was set constant at -50 ^oC to provide enough driving force for the phase changing process. As shown in the figure, the supercooling is very severe in pure $MgCl_2$-water basefluid, which is 11.8 ^oC. And the period between the start of supercooling phenomenon and the onset of the phase change platform is 90s, which is similar with that in NaCl-water, much longer than that in KCl-water. Such a long delay in phase changing from liquid to solid will cause higher charging cost, as a results, constrains the application of using $MgCl_2$-water as an industrial low temperature cold storage PCM.

To compensate the large gap between the real freezing temperature and the ideal designed temperature while shortening the supercooling duration, MCNT was introduced by different dosage. The partial enlarged details are shown in Fig 6-21 (b) to get onset temperature of freezing. And the onset of the freezing temperature and the supercooling degree results are listed in Table 6.12. It is obvious that pure $MgCl_2$-water basefluid has a very large supercooling degree, which is 11.8 ^oC. And the supercooling degree is decreasing with the amount of MCNT particles, especially in

(a)

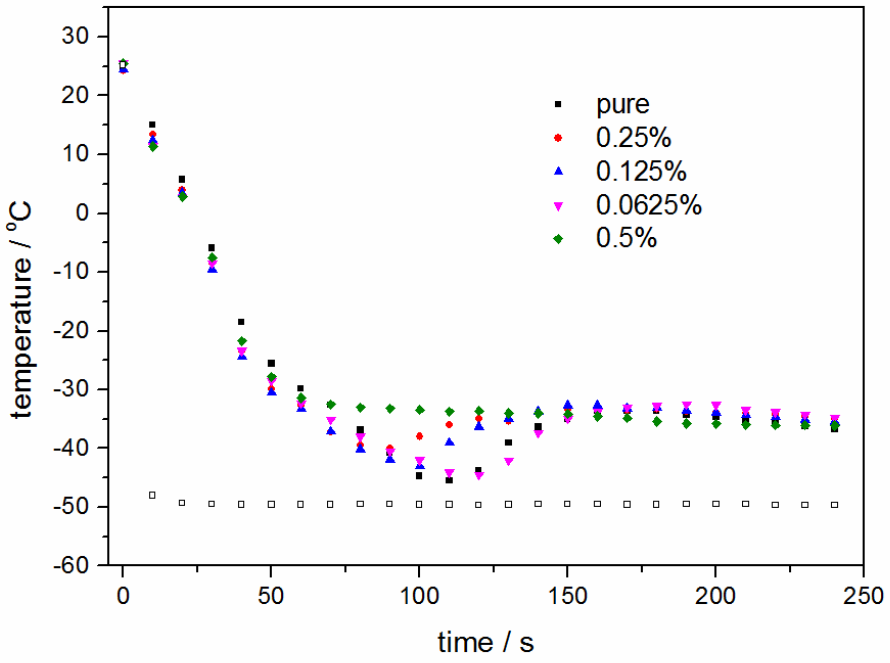

(b)

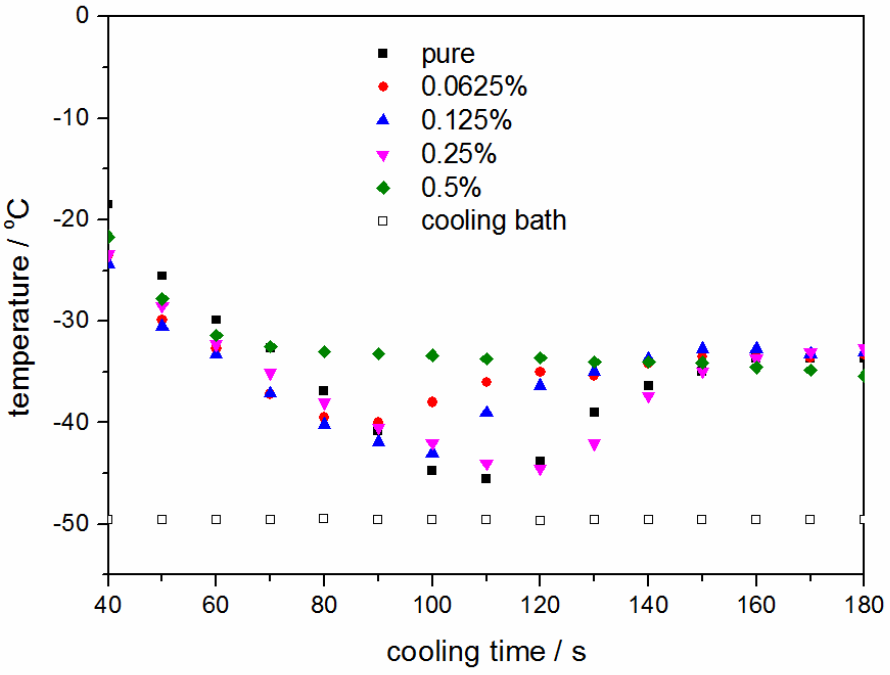

Fig 6-20 Temperature-history results of $MgCl_2$-water based MCNT nanofluids (a) whole view, (b) zoom-in view.

Table 6.12 Freezing point and supercooling degree of $MgCl_2$-water based MCNT nanofluids by Temperature-history.

Vol %	Onset of T_f (^oC)	Δ T (^oC)
0	-45.5	11.8
0.0625	-44.5	10.8
0.125	-43.0	9.3
0.25	-40.0	6.3
0.5	-33.7	0.0

0.5 % samples, a direct freezing without supercooling is observed on its Temperature-history curve. The significant decrease on supercooling degree in 0.5 % sample could be contributed to the special arrangement of MCNT cluster, which might form a more thermal conductive pathway to release the heat generated during freezing, thus accelerates the freezing rate.

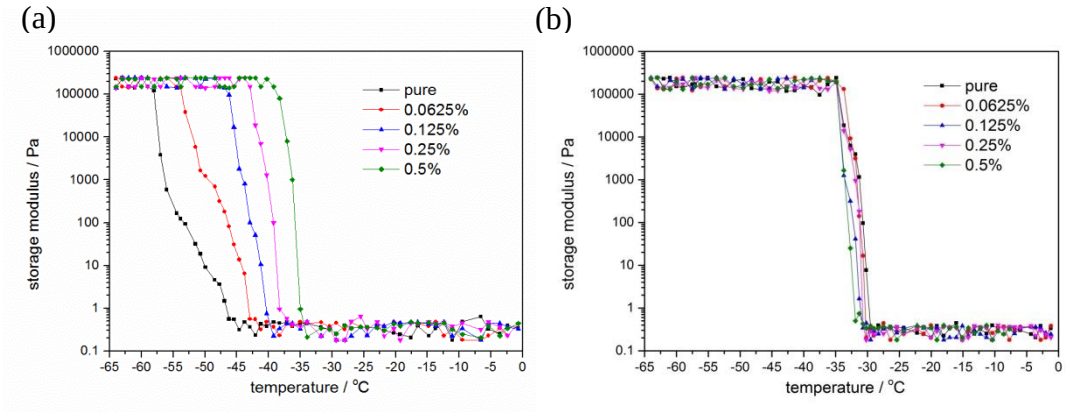

Fig 6-21 Modulus-temperature curves of $MgCl_2$-water based MCNT nanofluids:

(a) freezing and (b) melting process.

Besides that, we applied modulus-temperature method on $MgCl_2$-water based smaples as well, results are shown in Fig 6-21. The findings are apparent that no big difference in curves in Fig 6-21 (b), which

means the melting point of all samples are unaffected by the adding of MCNT. However, in Fig 6-21 (a), the curves separated a lot with each other, which means the adding of MCNT affects the freezing point of each sample. Summarily, the supercooling degree and freezing point results are concluded in Table 6.13. We find that in this method, the relationship between supercooling degree and MCNT volume fraction is the same with that in temperature-history method, although there are some little deviation on measured onset of freezing. For example, the supercooling degree in 0.5 % sample in modulus-temperature method is 2.6 ^{o}C while its 0 ^{o}C in temperature-history method. The reason of this inconsistency between these two methods is caused by different setup of the testing device.

Table 6.13 Freezing point and supercooling degree of $MgCl_2$-water based MCNT nanofluids by modulus-temperature.

Vol %	Onset of T_f (^{o}C)	Δ T (^{o}C)
0	-47.7	14.0
0.0625	-44.6	10.9
0.125	-41.2	7.5
0.25	-39.2	5.5
0.5	-36.3	2.6

Comparison of two methods

Summarily, as demonstrated above, both of the temperature-history and the modulus-temperature methods can identify the supercooling phenomenon in EG-water and salt-water based MCNT nanofluids. However, the supercooling degree results obtained from modulus-temperature method is larger than that via temperature-history methods. The discrepancy is manly caused by the different setting-up of the test device in these two methods. The temperature-history method is using isothermal freezing while the modulus-temperature methods nonisothermal freezing. And the sample volume in temperature-history method is much greater than that in modulus-temperature method. As a result,

based on the requirements of industrial application, temperature-history methods is a preferable way to characterize the supercooling degree of the PCM. On the other hand, the modulus-temperature methods has its own advantages. For example, we can get very accurate value of the onset temperature of freezing and melting, and we can also check phase separation because the state the sample is very sensitive to the modulus, any slight variation of the phase can be detected and reflected by the modulus value. Thus, modulus-temperature methods can be applied on particular situations for better resolution of the phase transition and phase change temperature.

6.4 Experimental results and discussion of crystallization process

In this section, the live image of crystallization process and MCNT cluster morphology are presented for only salt-water based suspensions. Moreover, these images of crystal growth of three different types of salt-water based PCMs without and with nanoparticle are displayed in chronological order. The reason for excluding EG-water based samples are explained in previous methodology chapter. That is the phase changing of EG-water based sample is too fast to be record by our microscope.

6.4.1 Crystallization of salt-water pure solutions

Firstly, crystal growth time-lapse images of KCl, NaCl and $MgCl_2$ based aqueous solutions are presented in Fig 6-22. At the same time, the distance of the boundary expansion of three types of basefluids were measured and displayed on the figure with the scale bar. In addition, the time interval between each image was chosen as 5 s and the cooling stage temperature for each sample was set 20 degree below the corresponding ideal melting point, thus we can ensure sufficient cooling power.

In images of KCl-water sample in Fig 6-22, we can observe a clear trend that the boundary of the growing crystal expands from left side to right side in parallel. This phenomenon indicates that in KCl-water basefluid, the freezing process is directional and continuous, in another word, the solid phase always appear and enlarge from the liquid phase basing on the earlier formed solid phase. Not only in KCl-water, the similar findings are also observed in NaCl-water and $MgCl_2$-water samples, which further approves the above conclusion.

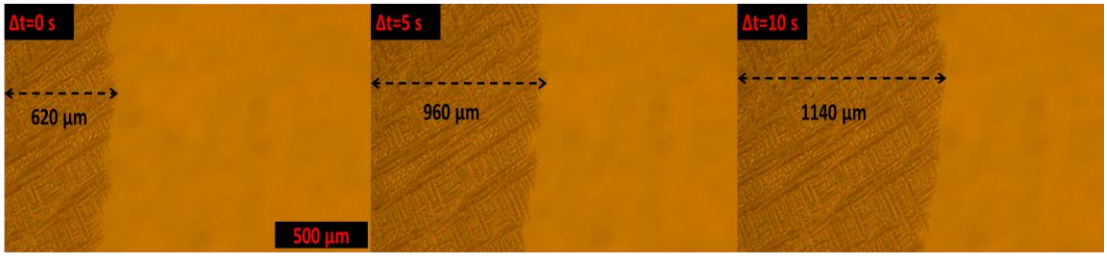

KCl-water

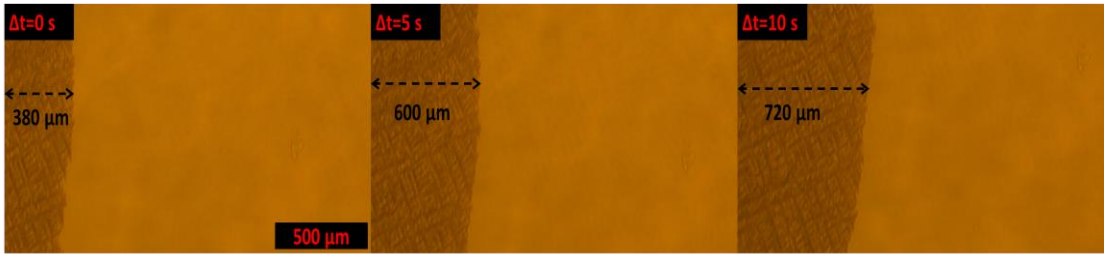

NaCl-water

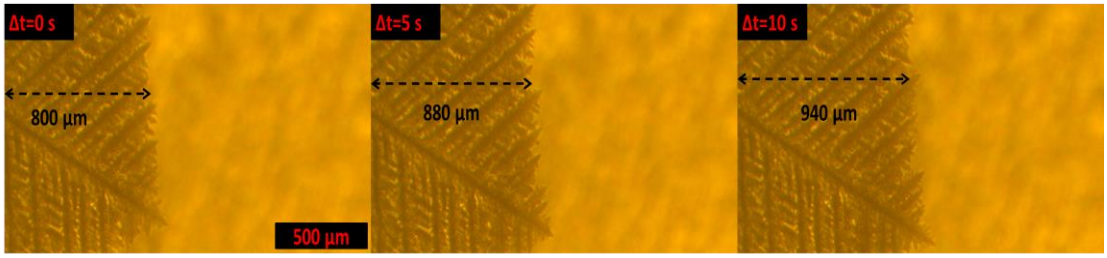

$MgCl_2$-water

Fig 6-22 Crystal growth time-lapse image of salt-water basefluid.

From the observing of the live image under microscope, we found that although the crystal growing mode of KCl-water, NaCl-water and $MgCl_2$-water shows similarity, there is apparent difference on the

crystal growth rate of these three types of salt-water. To quantify the crystal growth rate, we measured the relative position of the solid phase boundary at 0 s, 5 s and 10 s, and calculated the velocity of the boundary movement during 0 s to 5 s, 5 s to 10 s and 0 s to 10 s respectively, which are presented as $v_{0\text{-}5}$, $v_{5\text{-}10}$, $v_{0\text{-}10}$ correspondingly. The results of boundary position and crystal growth rate of KCl-water, NaCl-water and $MgCl_2$-water are listed in Table 6.14. By this way, we can compare the crystal growth rate of each samples numerically. From the results, it is clearly shown that the crystal growth rate is the fastest in KCl-water when we only look at the data in first 5 seconds, which is 68 μm/s, nearly 1.5 times of 44μm/s in NaCl and 4 times of 16 μm/s in $MgCl_2$-water.

Table 6.14 Crystal boundary position and growth rate of salt-water basefluid.

Sample	Boundary position (μm)			Crystal growth rate (μm/s)		
	t=0 s	t=5 s	t=10 s	$v_{0\text{-}5}$	$v_{5\text{-}10}$	$v_{0\text{-}10}$
KCl-water	620	960	1140	68	36	52
NaCl-water	380	600	720	44	24	34
$MgCl_2$-water	800	880	940	16	12	14

Moreover, we can find that the crystal growth rate is much slower during 5 s to 10 s, that is, $v_{5\text{-}10}$ is less than $v_{0\text{-}5}$. For example, in KCl-water, $v_{5\text{-}10}$=36μm/s while $v_{0\text{-}5}$=68 μm/s. Also in NaCl-water, $v_{5\text{-}10}$=24 μm/s, almost half of $v_{0\text{-}5}$. The significant decrease in crystal growth rate during the second 5 s is because the self-limitation of nucleation constrains the forming of the solid phase when the liquid-solid phase change is happening. To be specific, freezing process will release heat, and if the heat could not be conducted away from where the phase change is happening, the local temperature will increase and affect the nucleation rate consequently. Thus, increasing the thermal conductivity is important for

enhancing the charging and discharging performance of cold storage PCM from both heat transfer property aspect and nucleation aspect as well.

6.4.2 Crystallization of salt-water based MCNT suspensions

In this section, we will present the crystal growth images of KCl-water, NaCl-water and $MgCl_2$-water based MCNT suspensions with 0.5 % particle volume concentration, the figures are shown in Fig 6-23. On the figure, we can clearly see the morphology of MCNT clusters in the basefluids. It is obviously that these clusters are in different shapes and structures although the total concentration of MCNT particles are same in three different types of salt water solution. The difference in the morphology of MCNT clusters could be partially contributed to the different electric charge of ions in the basefluids which can affect the stability of particles in the suspension system. However, the electrical repulsive force does not play the main role on keeping particles away in the high concentration salt solution system which are explained in the literature review chapter before. The supposed reason of the discrepancy of the MCNT cluster structure is that the self-diffusion extent of the particles are different due to the viscosity of these three basefluids are different at the corresponding freezing temperature, thus the arrangement of the MCNT particles present different patterns in different basefluids. For example, in KCl-water based nanofluids in Fig 6-23, the MCNT clusters can be found in relatively small size and isolated from each other. But in NaCl-water based sample, the clusters tend to agglomerate together and expand in certain direction (horizontal in the figure). Also, in $MgCl_2$-water system, we can observe MCNT cluster is large and in round-shape, and the particles in the cluster are densely contacted with each other. These findings are similar with the prediction of the MCNT cluster structure in chapter 5.

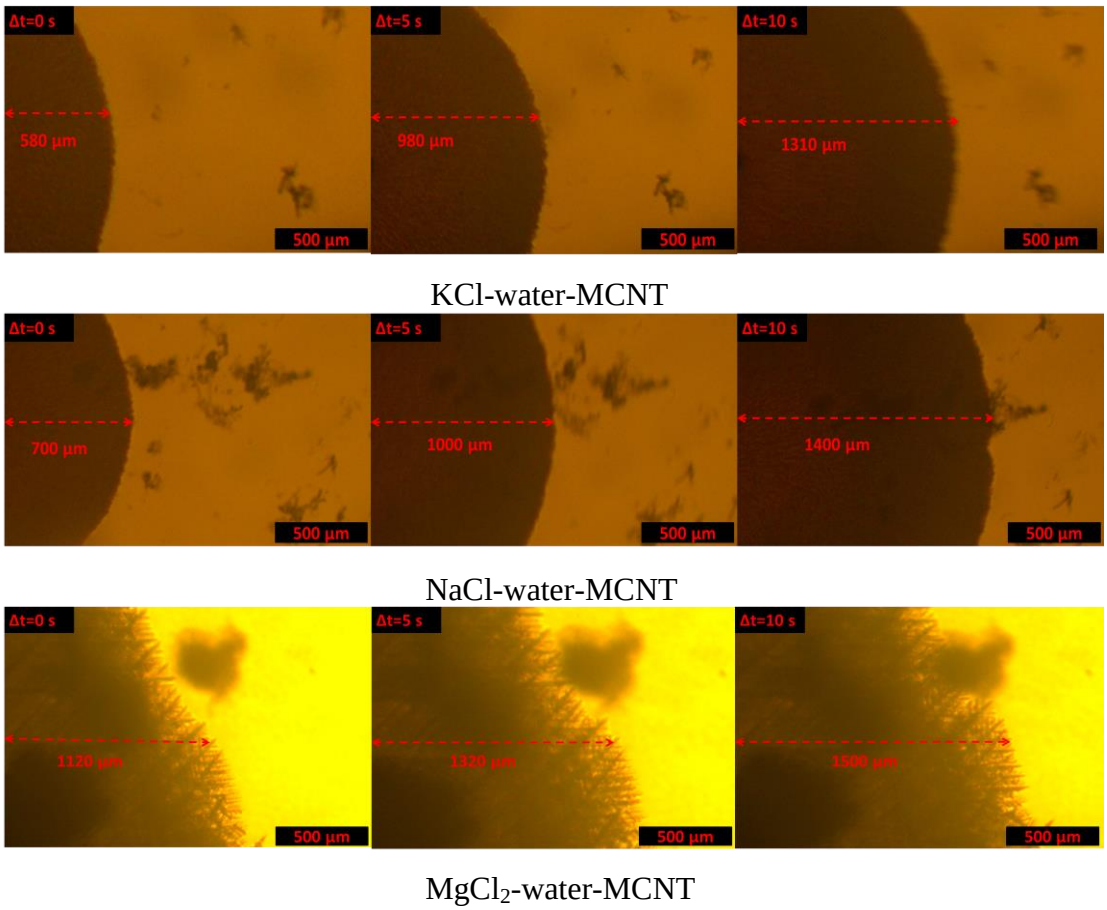

Fig 6-23 Crystal growth time-lapse image of salt-water based nanofluid with 0.5 % MCNT.

In addition, the crystal growth rate was calculated and the results are shown in Table 6.15 to study the effect of MCNT cluster on the nucleation of KCl-water, NaCl-water and $MgCl_2$-water based nanofluids. From the data, we can find the crystal growth rate $v_{0\text{-}5}$ and $v_{5\text{-}10}$ of KCl-water-MCNT is 80 μm/s and 66 μm/s, which is higher than 68 μm/s and 36 μm/s in the pure basefluid. Similarly, crystal growth rate are all enhanced in NaCl-water-MCNT and $MgCl_2$-water-MCNT samples. To compare the enhancement of the crystal growth rate at different time, we plotted both the value of $v_{0\text{-}5}$ and $v_{5\text{-}10}$ in bar chart, as shown in Fig 6-24. It is clear that the crystal growth rate of KCl-water, NaCl-water and $MgCl_2$-water samples are in high to low order, both basefluids and nanofluids.

Table 6.15 Crystal boundary position and growth rate of salt-water based MCNT nanofluids.

Sample	Boundary position (μm)			Crystal growth rate (μm/s)		
	t=0 s	t=5 s	t=10 s	v_{0-5}	v_{5-10}	v_{0-10}
KCl-water-MCNT	580	980	1310	80	66	73
NaCl-water-MCNT	700	1000	1400	60	80	70
$MgCl_2$-water-MCNT	1120	1320	1500	40	36	38

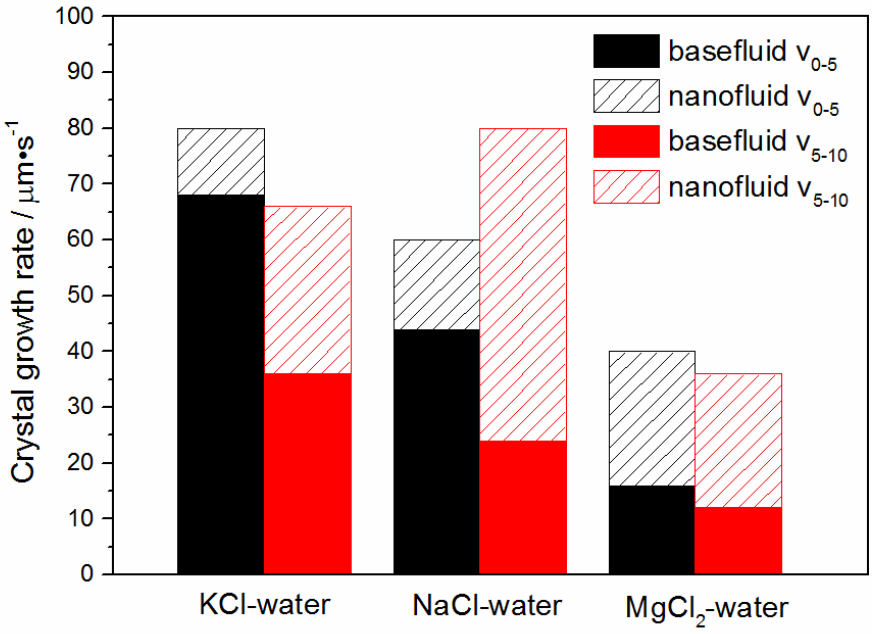

Fig 6-24 Crystal growth rate of salt-water based samples.

However, it is worth to mention that the enhancement of crystal growth rate is not in the same pace at the different period of phase changing. For example, in KCl-water samples, the height of v_{5-10} is only half of v_{0-5} in basefluid, while the gap between v_{0-5} and v_{5-10} is significantly reduced due to the higher enhancement of crystal growth rate happens in 5 s to 10 s period when KCl-water-MCNT is freezing.

Also in NaCl-water, although the trend of basefluid data is similar, an dramatic inversion is found in nanofluids samples. In another word, the MCNT induced enhancement not only bridge the gap between the $v_{0\text{-}5}$ and $v_{5\text{-}10}$, but also put $v_{5\text{-}10}$ much higher than $v_{0\text{-}5}$. The extremely high increasing of crystal growth rate in NaCl-water-MCNT at 5 s to 10 s period is due to the directionally arranged MCNT clusters in local area. The MCNT cluster is allocated along the direction of crystal growing, thus the heat generated from the freezing process can be scattered away from the nucleation center efficiently, which consequently the reduces self-limiting of the nucleation and increases the crystal growth rate. Moreover, the MCNT caused heterogeneous nucleation is also a promotive factor on crystal growth process.

Not like above two salt-water systems, in $MgCl_2$-water result in the bar chart, we find that the crystal growth rate increases a lot in both 0 s to 5 s period and 5 s to 10 s period, by 150 % and 200 % respectively. This consistence of crystal growth rate in different periods of freezing is because the structure of the MCNT cluster is solid and isotropy, which leads to more stable and predictable changes on the nucleation process.

6.5 Summary

In this chapter, we discussed the results of specific heat, melting point, melting enthalpy, supercooling degree and crystallization of both EG-water and salt-water based MCNT nanofluids.

1) The specific heat of EG-water based nanofluids is decreasing proportionally with the concentration of both EG and MCNT, which matches the conventional mixing theory. Also, salt-water presents

the similar trend on relationship between specific heat and MCNT concentration. However, comparing with KCl-water, an abnormal higher specific heat was observed in NaCl-water based samples, of which freezing point is lower than that in KCl-water contrarily, which indicates that the specific heat of salt-water is not always decreasing with decreasing freezing point.

2) The melting point of EG-water and salt-water based MCNT nanofluids do not change very much when MCNT was added. However, the latent heat of fusion will be affected by adding particles, meanwhile, the surfactant. Also, lowering the freezing point of EG-water and salt-water based samples will cause adverse effect on the value of melting enthalpy significantly.

3) The supercooling degree of EG-water and salt-water based samples can be reduced by adding MCNT particles. The depression of supercooling degree is increasing with the adding amount of MCNT in all samples. However, the measured supercooling degree by temperature-history method and modulus-temperature method have different values due to different samples setting and cooling setting. Although, results of both two methods approve that adding MCNT is efficient to narrow the gap between the real onset of freezing and the ideal freezing point of our cold storage PCM.

4) The crystallization process of salt-water basefluid and nanofluid was observed and recorded under an optical microscope with cooling stage. We found that the crystal growth rate are quite different in different salt-water basefluid, which are 68μm/s, 44μm/s and 16μm/s in KCl-water, NaCl-water and $MgCl_2$-water respectively. In addition, adding 0.5 % MCNT in each salt-water basefluids can promote the crystal growth rate to 80μm/s, 60μm/s and 40μm/s. We also explained the discrepancy on enhancement of crystallization rate in different salt-water nanofluids, that is, different structure of MCNT cluster leads to different heat conduction behaviour and different specific area of MCNT

cluster. Specifically, the MCNT cluster aggregated and expanded in the direction of crystal growing will significantly facilitate the liquid-solid transforming of nearby PCMs, while evenly and non-directionally distributed clusters will slow the increasing of freezing process but affect more PCMs in larger area.

7 Conclusions and furture work

7.1 Conclusions

The fitted parameters of the modified K-D model, R, D and φ_m can be used to analysis the cluster structures of MCNTs in the different basefluids and at different temperatures. The Peclet number can be used to explain the experimentally observed rheological behaviour. Through the experimental study and analysis, the structure of MCNT clusters is linked to the rheological behaviour of the nanofluids, leading to plausible interpretation of the results.

The thermal conductivity of nanofluid with different base fluid shows different relationship with temperature, and the enhancement of nanofluid is higher at lower temperature. The effective thermal conductivity of nanofluids not only relies on the particle concentration, but also depends on the particle cluster structure, which is highly related with the temperature. The MCNT cluster structure can be linked with the enhancement of thermal conductivity of nanofluids, and use the cluster information through rheology analysis to complete the prediction of thermal conductivity by Nan's model and H-C model.

The specific heat of EG-water based nanofluids is decreasing proportionally with the concentration of both EG and MCNT, which matches the conventional mixing theory. Also, salt-water presents the similar trend on relationship between specific heat and MCNT concentration. The melting point of EG-water and salt-water based MCNT nanofluids do not change very much when MCNT was added.

The supercooling degree of EG-water and salt-water based samples can be reduced by adding MCNT particles. The depression of supercooling degree is increasing with the adding amount of MCNT in all samples.

The crystallization process of salt-water basefluid and nanofluid was observed and recorded under an optical microscope with cooling stage. The crystal growth rate are quite different in different salt-water basefluid, which are 68μm/s, 44μm/s and 16μm/s in KCl-water, NaCl-water and $MgCl_2$-water respectively. In addition, adding 0.5 % MCNT in each salt-water basefluids can promote the crystal growth rate to 80μm/s, 60μm/s and 40μm/s. And different structure of MCNT cluster leads to different heat conduction behaviour and different specific area of MCNT cluster.

7.2 Future works

Although some interesting results have been obtained in this thesis, there are still a number of fields worth to be further investigated. They are listed as following:

(1) To formulate PCMs working at cryogenic temperature: This thesis studied PCM based on EG-water and salt-water, the temperature range is from -10 ^{o}C to -30 ^{o}C. However, cold storage application at much lower temperature raises the demand of corresponding PCM candidates. For example, in liquid natural gas gasification system, the large amount of vaporizing latent heat needs to be stored at some temperature below -100 ^{o}C, which poses challenges to researchers to find a proper PCM.

(2) To study the nanoparticle cluster visually: In this thesis, nanoparticle structure was imagined based on the fitting parameters from rheology analysis. This method only gives generally structure of the

cluster. In order to understand the detailed aggregation condition of the nanoparticle, a visual measurement should be designed. To achieve this goal, an in-situ TEM with temperature control unit could be used.

(3) To measure the thermal conductivity with more precise technique: The scatter of thermal conductivity data in this thesis is large. In order to draw a more solid and accurate conclusion on the mechanism of thermal conductivity of nano-composite material, a technique with high resolution and repeatability should be used.

(4) To study the crystallization mechanism of cold storage PCM and study other approaches for promoting crystallizing: In this thesis, MCNT was used as nucleating agent to reduce supercooling degree and increase crystallization rate. The principal of this method is introducing heterogeneous crystallization and enhancing heat conduction by adding MCNT. However, further knowledge on factors influencing crystallization should be understood. For example, the type of nanoparticle, the synergistic effect of nucleation and growth on crystallization.

(5) To study the application of PCM in specific cold storage system: This thesis focuses on the fundamental study of nano-composite PCM for cold storage. However, further efforts should be made on the design of a realistic cold storage system and the performance evaluation of the PCM embedded system.

Reference

[1] G. Li, Y. Hwang, R. Radermacher, and H.-H. Chun, “Review of cold storage materials for subzero applications,” *Energy*, vol. 51, pp. 1–17, 2013.

[2] D. C. Onyejekwe, “Cold storage using eutectic mixture of NaCl/H2O: An application to photovoltaic compressor vapour freezers,” *Sol. Wind Technol.*, vol. 6, no. 1, pp. 11–18, 1989.

[3] K. Azzouz, D. Leducq, and D. Gobin, “Performance enhancement of a household refrigerator by addition of latent heat storage,” *Int. J. Refrig.*, vol. 31, no. 5, pp. 892–901, 2008.

[4] K. Azzouz, D. Leducq, and D. Gobin, “Enhancing the performance of household refrigerators with latent heat storage: An experimental investigation,” *Int. J. Refrig.*, vol. 32, no. 7, pp. 1634–1644, 2009.

[5] B. Gin, M. M. Farid, and P. K. Bansal, “Effect of door opening and defrost cycle on a freezer with phase change panels,” *Energy Convers. Manag.*, vol. 51, no. 12, pp. 2698–2706, 2010.

[6] B. Gin and M. M. Farid, “The use of PCM panels to improve storage condition of frozen food,” *J. Food Eng.*, vol. 100, no. 2, pp. 372–376, 2010.

[7] L. Miro, “Improving thermal performance of freezers using phase change materials” *Int. J. Refrig.*, vol. 35, pp. 984–991, 2012.

[8] C. Hägg, “Ice Slurry as Secondary Fluid in Refrigeration Systems”, *thesis*, 2005.

[9] H. Kumano, T. Asaoka, A. Saito, and S. Okawa, “Study on latent heat of fusion of ice in aqueous solutions,” *Int. J. Refrig.*, vol. 30, no. 2, pp. 267–273, 2007.

[10] H. Akoh, Y. Tsukasaki, S. Yatsuya, and A. Tasaki, “Magnetic properties of ferromagnetic ultrafine particles prepared by vacuum evaporation on running oil substrate,” *J. Cryst. Growth*, vol. 45, pp. 495–500, 978.

[11] J. A. Eastman, U. S. Choi, S. Li, L. J. Thompson, and S. Lee, “Enhanced thermal conductivity through the development of nanofluids,” *MRS Proc.*, vol. 457, 1996.

[12] C.-H. Lo, T.-T. Tsung, L.-C. Chen, C.-H. Su, and H.-M. Lin, “Fabrication of copper oxide nanofluid using submerged arc nanoparticle synthesis system (SANSS),” *J. Nanoparticle Res.*, vol. 7, no. 2, pp. 313–320, 2005.

[13] S. Suwanboon, P. Amornpitoksuk, and P. Bangrak, “Synthesis, characterization and optical properties of Zn(1−x)TixO nanoparticles prepared via a high-energy ball milling technique,” *Ceram. Int.*, vol. 37, no. 1, pp. 333–340, 2011.

[14] B. Wang, X. Wang, W. Lou, and J. Hao, “Thermal conductivity and rheological properties of graphite/oil nanofluids,” *Colloids Surfaces A Physicochem. Eng. Asp.*, vol. 414, pp. 125–131, 2012.

[15] H. Xie and L. Chen, “Adjustable thermal conductivity in carbon nanotube nanofluids,” *Phys. Lett. A*, vol. 373, no. 21, pp. 1861–1864, 2009.

[16] B. Munkhbayar, M. Bat-Erdene, B. Ochirkhuyag, D. Sarangerel, B. Battsengel, H. Chung, and H. Jeong, “An experimental study of the planetary ball milling effect on dispersibility and thermal conductivity of MWCNTs-based aqueous nanofluids,” *Mater. Res. Bull.*, vol. 47, no. 12, pp. 4187–4196, 2012.

[17] B. Munkhbayar, M. J. Nine, S. Hwang, J. Kim, K. Bae, H. Chung, and H. Jeong, “Effect of grinding speed changes on dispersibility of the treated multi-walled carbon nanotubes in aqueous

solution and its thermal characteristics," *Chem. Eng. Process. Process Intensif.*, vol. 61, pp. 36–41, 2012.

[18] B. Munkhbayar, M. J. Nine, J. Jeoun, M. Bat-Erdene, H. Chung, and H. Jeong, "Influence of dry and wet ball milling on dispersion characteristics of the multi-walled carbon nanotubes in aqueous solution with and without surfactant," *Powder Technol.*, vol. 234, pp. 132–140, 2013.

[19] L. Zhang, Y. Jiang, Y. Ding, M. Povey, and D. York, "Investigation into the antibacterial behaviour of suspensions of ZnO nanoparticles (ZnO nanofluids)," *J. Nanoparticle Res.*, vol. 9, no. 3, pp. 479–489, 2007.

[20] C. Choi, H. S. Yoo, and J. M. Oh, "Preparation and heat transfer properties of nanoparticle-in-transformer oil dispersions as advanced energy-efficient coolants," *Curr. Appl. Phys.*, vol. 8, no. 6, pp. 710–712, 2008.

[21] L. Chen and H. Xie, "Silicon oil based multiwalled carbon nanotubes nanofluid with optimized thermal conductivity enhancement," *Colloids Surfaces A Physicochem. Eng. Asp.*, vol. 352, no. 1–3, pp. 136–140, 2009.

[22] D. Wen and Y. Ding, "Natural convective heat transfer of suspensions of titanium dioxide nanoparticles (nanofluids)," *IEEE Trans. Nanotechnol.*, vol. 5, no. 3, pp. 220–227, 2006.

[23] Y. Ding, H. Alias, D. Wen, and R. A. Williams, "Heat transfer of aqueous suspensions of carbon nanotubes (CNT nanofluids)," *Int. J. Heat Mass Transf.*, vol. 49, no. 1–2, pp. 240–250, 2006.

[24] D. Wen and Y. Ding, "Formulation of nanofluids for natural convective heat transfer applications," *Int. J. Heat Fluid Flow*, vol. 26, no. 6, pp. 855–864, 2005.

[25] E. P. Bandarra Filho, O. S. H. Mendoza, C. L. L. Beicker, A. Menezes, and D. Wen, "Experimental investigation of a silver nanoparticle-based direct absorption solar thermal system," *Energy Convers. Manag.*, vol. 84, pp. 261–267, 2014.

[26] D. D. H. Fontes, G. Ribatski, E. B. Filho, and E. P. Bandarra Filho, "Experimental evaluation of thermal conductivity, viscosity and breakdown voltage AC of nanofluids of carbon nanotubes and diamond in transformer oil," *Diam. Relat. Mater.*, vol. 58, pp. 115–121, 2015.

[27] A. Ghadimi and I. H. Metselaar, "The influence of surfactant and ultrasonic processing on improvement of stability, thermal conductivity and viscosity of titania nanofluid," *Exp. Therm. Fluid Sci.*, vol. 51, pp. 1–9, 2013.

[28] A. T. Utomo, H. Poth, P. T. Robbins, and A. W. Pacek, "Experimental and theoretical studies of thermal conductivity, viscosity and heat transfer coefficient of titania and alumina nanofluids," *Int. J. Heat Mass Transf.*, vol. 55, no. 25–26, pp. 7772–7781, 2012.

[29] S. Chakraborty, S. K. Saha, J. C. Pandey, and S. Das, "Experimental characterization of concentration of nanofluid by ultrasonic technique," *Powder Technol.*, vol. 210, no. 3, pp. 304–307, 2011.

[30] H. Ghodsinezhad, M. Sharifpur, and J. P. Meyer, "Experimental investigation on cavity flow natural convection of Al2O3???water nanofluids," *Int. Commun. Heat Mass Transf.*, vol. 76, pp. 316–324, 2016.

[31] R. Mondragon, J. E. Julia, A. Barba, and J. C. Jarque, "Characterization of silica-water nanofluids dispersed with an ultrasound probe: A study of their physical properties and stability," *Powder Technol.*, vol. 224, pp. 138–146, 2012.

[32] A. Mariano, M. J. Pastoriza-Gallego, L. Lugo, L. Mussari, and M. M. Pi??eiro, “Co3O4 ethylene glycol-based nanofluids: Thermal conductivity, viscosity and high pressure density,” *Int. J. Heat Mass Transf.*, vol. 85, pp. 54–60, 2015.

[33] A. Hernández Battez, J. L. Viesca, R. González, a. García, T. Reddyhoff, and a. Higuera-Garrido, “Effect of Shear Rate, Temperature, and Particle Concentration on the Rheological Properties of ZnO and ZrO2 Nanofluids,” *Tribol. Trans.*, vol. 57, no. 21, pp. 489–495, 2014.

[34] K. S. Hwang, S. P. Jang, and S. U. S. Choi, “Flow and convective heat transfer characteristics of water-based Al2O3 nanofluids in fully developed laminar flow regime,” *Int. J. Heat Mass Transf.*, vol. 52, no. 1–2, pp. 193–199, 2009.

[35] M. E. Meibodi, M. Vafaie-Sefti, A. M. Rashidi, A. Amrollahi, M. Tabasi, and H. S. Kalal, “The role of different parameters on the stability and thermal conductivity of carbon nanotube/water nanofluids,” *Int. Commun. Heat Mass Transf.*, vol. 37, no. 3, pp. 319–323, 2010.

[36] J. Qu, H. ying Wu, and P. Cheng, “Thermal performance of an oscillating heat pipe with Al2O3-water nanofluids,” *Int. Commun. Heat Mass Transf.*, vol. 37, no. 2, pp. 111–115, 2010.

[37] D. Wen and Y. Ding, “Experimental investigation into convective heat transfer of nanofluids at the entrance region under laminar flow conditions,” *Int. J. Heat Mass Transf.*, vol. 47, no. 24, pp. 5181–5188, 2004.

[38] L. Fedele, L. Colla, S. Bobbo, S. Barison, and F. Agresti, “Experimental stability analysis of different water-based nanofluids.,” *Nanoscale Res. Lett.*, vol. 6, no. 1, pp. 300, 2011.

[39] A. Nasiri, M. Shariaty-Niasar, A. Rashidi, A. Amrollahi, and R. Khodafarin, “Effect of dispersion method on thermal conductivity and stability of nanofluid,” *Exp. Therm. Fluid Sci.*, vol. 35, no. 4, pp. 717–723, 2011.

[40] M. J. Pastoriza-Gallego, C. Casanova, R. Páramo, B. Barbés, J. L. Legido, and M. M. Piñeiro, “A study on stability and thermophysical properties (density and viscosity) of Al2O3 in water nanofluid,” *J. Appl. Phys.*, vol. 106, no. 6, pp. 064301, 2009.

[41] M. Sivasubramanian, K. Nedunjezhian, S. Murugesan, and R. Kalpoondi Sekar, “Sub-micron dispersions of sand in water prepared by stirred bead milling and ultrasonication: A potential coolant,” *Appl. Therm. Eng.*, vol. 44, pp. 1–10, 2012.

[42] M. Chopkar, S. Sudarshan, P. K. Das, and I. Manna, “Effect of particle size on thermal conductivity of nanofluid,” *Metall. Mater. Trans. A*, vol. 39, no. 7, pp. 1535–1542, 2008.

[43] X. Li, D. Zhu, and X. Wang, “Evaluation on dispersion behavior of the aqueous copper nano-suspensions,” *J. Colloid. Interf. Sci.*, vol. 310, pp. 456–463, 2007.

[44] Y. H. Hung, T. P. Teng, and B. G. Lin, “Evaluation of the thermal performance of a heat pipe using alumina nanofluids,” *Exp. Therm. Fluid Sci.*, vol. 44, pp. 504–511, 2013.

[45] W. Duangthongsuk and S. Wongwises, “An experimental study on the heat transfer performance and pressure drop of TiO2 -water nanofluids flowing under a turbulent flow regime,” *Int. J. Heat Mass Transf.*, vol. 53, no. 1–3, pp. 334–344, 2010.

[46] T. Yousefi, E. Shojaeizadeh, F. Veysi, and S. Zinadini, “An experimental investigation on the effect of pH variation of MWCNT – H2O nanofluid on the efficiency of a flat-plate solar collector,” *Sol. Energy*, vol. 86, no. 2, pp. 771–779, 2012.

[47] P. Garg, J. L. Alvarado, C. Marsh, T. A. Carlson, D. A. Kessler, and K. Annamalai, "An experimental study on the effect of ultrasonication on viscosity and heat transfer performance of multi-wall carbon nanotube-based aqueous nanofluids," *Int. J. Heat Mass Transf.*, vol. 52, no. 21–22, pp. 5090–5101, 2009.

[48] M. Abareshi, E. K. Goharshadi, S. Mojtaba Zebarjad, H. Khandan Fadafan, and A. Youssefi, "Fabrication, characterization and measurement of thermal conductivity of Fe3O4 nanofluids," *J. Magn. Magn. Mater.*, vol. 322, no. 24, pp. 3895–3901, 2010.

[49] H. Yu, S. Hermann, S. E. Schulz, T. Gessner, Z. Dong, and W. J. Li, "Optimizing sonication parameters for dispersion of single-walled carbon nanotubes," *Chem. Phys.*, vol. 408, pp. 11–16, 2012.

[50] B. Derjaguin, "A theory of interaction of particles in presence of electric double layers and the stability of lyophobe colloids and disperse systems," *Prog. Surf. Sci.*, vol. 43, no. 1–4, pp. 1–14, 1993.

[51] B. Derjaguin and L. Landau, "Theory of the stability of strongly charged lyophobic sols and of the adhesion of strongly charged particles in solutions of electrolytes," *Prog. Surf. Sci.*, vol. 43, no. 1–4, pp. 30–59, 1993.

[52] E. J. W. Verwey, "Theory of the Stability of Lyophobic Colloids.," *J. Phys. Colloid Chem.*, vol. 51, no. 3, pp. 631–636, 1947.

[53] B. W. Ninham, "Long-range vs. short-range forces. The present state of play," *J. Phys. Chem.*, vol. 84, no. 12, pp. 1423–1430, 1980.

[54] N. V Churaev and B. V Derjaguin, "Inclusion of structural forces in the theory of stability of colloids and films," *J. Colloid Interface Sci.*, vol. 103, no. 2, pp. 542–553, 1985.

[55] B. W. Ninham, “Hierarchies of forces: The last 150 years,” *Adv. Colloid Interface Sci.*, vol. 16, no. 1, pp. 3–15, 1982.

[56] P. G. de Gennes, “Polymers at an interface; a simplified view,” *Adv. Colloid Interface Sci.*, vol. 27, no. 3, pp. 189–209, 1987.

[57] F. T. Hesselink, A. Vrij, and J. T. G. Overbeek, “Theory of the stabilization of dispersions by adsorbed macromolecules. II. Interaction between two flat particles,” *J. Phys. Chem.*, vol. 75, no. 14, pp. 2094–2103, 1971.

[58] Napper, *Polymeric stabilization of colloidal dispersions.* New York: Academic Press, 1983.

[59] J. Israelachvili and H. Wennerström, “Role of hydration and water structure in biological and colloidal interactions.,” *Nature*, vol. 379, no. 6562. pp. 219–225, 1996.

[60] W. van Megen and I. Snook, “Solvent structure and solvation forces between solid bodies,” *J. Chem. Soc. Faraday Trans. 2*, vol. 75, no. 0, pp. 1095–1102, 1979.

[61] D. Y. C. Chan, D. J. Mitchell, B. W. Ninham, and B. A. Pailthorpe, “Short-range interactions mediated by a solvent with surface adhesion,” *Mol. Phys.*, vol. 35, no. 6, pp. 1669–1679, 1978.

[62] A. K. Doerr, M. Tolan, T. Seydel, and W. Press, “The interface structure of thin liquid hexane films,” *Phys. B Condens. Matter*, vol. 248, no. 1–4, pp. 263–268, 1998.

[63] C.-J. Y. and A. G. R. and J. K. and A. D. and P. Dutta, “X-ray diffraction evidence of ordering in a normal liquid near the solid-liquid interface,” *EPL (Europhysics Lett.*, vol. 50, no. 4, pp. 487, 2000.

[64] A. Grabbe and R. G. Horn, “Double-Layer and Hydration Forces Measured between Silica Sheets Subjected to Various Surface Treatments,” *J. Colloid Interface Sci.*, vol. 157, no. 2, pp. 375–383, 1993.

[65] S. Leikin and A. A. Kornyshev, “Theory of hydration forces. Nonlocal electrostatic interaction of neutral surfaces,” *J. Chem. Phys.*, vol. 92, no. 11, pp. 6890–6898, 1990.

[66] V. A. Parsegian and T. Zemb, “Hydration forces: Observations, explanations, expectations, questions,” *Curr. Opin. Colloid Interface Sci.*, vol. 16, no. 6, pp. 618–624, 2011.

[67] D. C. Rau, B. Lee, and V. A. Parsegian, “Measurement of the repulsive force between polyelectrolyte molecules in ionic solution: hydration forces between parallel DNA double helices.,” *Proc. Natl. Acad. Sci. U. S. A.*, vol. 81, no. 9, pp. 2621–2625, 1984.

[68] I. K. Snook and D. Henderson, “Monte Carlo study of a hard‐sphere fluid near a hard wall,” *J. Chem. Phys.*, vol. 68, no. 5, pp. 2134–2139, 1978.

[69] J. Faraudo and F. Bresme, “Anomalous dielectric behavior of water in ionic Newton Black films,” *Phys. Rev. Lett.*, vol. 92, no. 23, pp. 236102–1, 2004.

[70] S. Marčelja, J. N. Israelachvili, and H. Wennerström, “Hydration in electrical double layers,” *Nature*, vol. 385, no. 6618, pp. 690–690, 1997.

[71] S. State, “Polysaccharides Xanthan and Schizophyllan,” vol. 249, no. 1975, 1990.

[72] I. K. Snook and W. van Megen, “Calculation of solvation forces between solid particles immersed in a simple liquid,” *J. Chem. Soc. Faraday Trans. 2 Mol. Chem. Phys.*, vol. 77, no. 1, pp. 181–190, 1981.

[73] P. Tarazona and L. Vicente, “A model for density oscillations in liquids between solid walls,” *Mol. Phys.*, vol. 56, no. 3, pp. 557–572, 1985.

[74] A. O. P. and C. J. Boulter, “Susceptibility critical amplitude ratios and tests of the stiffness instability at wetting transitions,” *Europhysics Lett.*, vol. 28, no. 4, p. 251, 1994.

[75] P. Y. and A. O. P. and S. Kalliadasis, “Complete prewetting,” *J. Phys. Condens. Matter*, vol. 28, no. 27, p. 275001, 2016.

[76] P. Y. and N. S. and S. Kalliadasis, “Density functional study of condensation in capped capillaries,” *J. Phys. Condens. Matter*, vol. 27, no. 27, p. 275104, 2015.

[77] M. F. A.-S. and H. Rahnejat, “Physics of lubricated impact of a sphere on a plate in a narrow continuum to gaps of molecular dimensions,” *J. Phys. D. Appl. Phys.*, vol. 35, no. 18, p. 2311, 2002.

[78] W. W. F. C. and M. T. and H. Rahnejat, “Effect of lubricant molecular rheology on formation and shear of ultra-thin surface films,” *J. Phys. D. Appl. Phys.*, vol. 44, no. 16, pp. 165302, 2011.

[79] D. W. and M. Schoen, “The wetting of planar solid surfaces by symmetric binary mixtures near bulk gas–liquid coexistence,” *J. Phys. Condens. Matter*, vol. 16, no. 28, pp. 4761, 2004.

[80] R. E. and M. C. Stewart, “The local compressibility of liquids near non-adsorbing substrates: a useful measure of solvophobicity and hydrophobicity?,” *J. Phys. Condens. Matter*, vol. 27, no. 19, pp. 194111, 2015.

[81] A. O. P. and P. S. Swain, “Correlation function algebra for inhomogeneous fluids,” *J. Phys. Condens. Matter*, vol. 9, no. 11, pp. 2351, 1997.

[82] J. N. Israelachvili and R. . Pashley, “Measurement of the hydrophobic interaction between two hydrophobic surfaces in aqueous electrolyte solutions,” *J. Colloid Interface Sci.*, vol. 98, no. 2, pp. 500–514, 1984.

[83] J. C. Eriksson, S. Ljunggren, and P. M. Claesson, “A phenomenological theory of long-range hydrophobic attraction forces based on a square-gradient variational approach,” *J. Chem. Soc.{,} Faraday Trans. 2*, vol. 85, no. 3, pp. 163–176, 1989.

[84] Y. I. Rabinovich and B. V Derjaguin, “Interaction of hydrophobized filaments in aqueous electrolyte solutions,” *Colloids and Surfaces*, vol. 30, no. 3, pp. 243–251, 1988.

[85] E. Ruckenstein and N. Churaev, “A possible hydrodynamic origin of the forces of hydrophobic attraction,” *J. Colloid Interface Sci.*, vol. 147, no. 2, pp. 535–538, 1991.

[86] P. M. Claesson and H. K. Christenson, “Very long range attractive forces between uncharged hydrocarbon and fluorocarbon surfaces in water,” *J. Phys. Chem.*, vol. 92, no. 6, pp. 1650–1655, 1988.

[87] J. Israelachvili and R. Pashley, “The hydrophobic interaction is long range, decaying exponentially with distance.,” *Nature*, vol. 300, no. 5890. pp. 341–342, 1982.

[88] K. Ingersent, J. Klein, and P. Pincus, “Forces between surfaces with adsorbed polymers. Calculations and comparison with experiment,” *Macromolecules*, vol. 23, no. 2, pp. 548–560, 1990.

[89] S. T. Milner, T. A. Witten, and M. E. Cates, “Theory of the grafted polymer brush,” *Macromolecules*, vol. 21, no. 8, pp. 2610–2619, 1988.

[90] K. Ingersent, J. Klein, and P. Pincus, “Interactions between surfaces with adsorbed polymers: poor solvent. Calculations and comparison with experiment,” *Macromolecules*, vol. 19, no. 5, pp. 1374–1381, 1986.

[91] J. N. Israelachvili, M. Tirrell, J. Klein, and Y. Almog, “Forces between two layers of adsorbed polystyrene immersed in cyclohexane below and above the θ temperature,” *Macromolecules*, vol. 17, no. 2, pp. 204–209, 1984.

[92] F. T. Hesselink, “Theory of the stabilization of dispersions by adsorbed macromolecules. I. Statistics of the change of some configurational properties of adsorbed macromolecules on the approach of an impenetrable interface,” *J. Phys. Chem.*, vol. 75, no. 1, pp. 65–71, 1971.

[93] J. W. Cahn, “Critical point wetting,” *J. Chem. Phys.*, vol. 66, no. 8, pp. 3667–3672, 1977.

[94] A. Vrij, “Polymers at interfaces and the,” *Pure Appl. Chem.*, vol. 48, pp. 471–483, 1976.

[95] Y. Liang, N. Hilal, P. Langston, and V. Starov, “Interaction forces between colloidal particles in liquid: Theory and experiment,” *Adv. Colloid Interface Sci.*, vol. 134–135, pp. 151–166, 2007.

[96] Y. Hwang, J.-K. Lee, J.-K. Lee, Y.-M. Jeong, S. Cheong, Y.-C. Ahn, and S. H. Kim, “Production and dispersion stability of nanoparticles in nanofluids,” *Powder Technol.*, vol. 186, no. 2, pp. 145–153, 2008.

[97] Y. Hwang, J. K. Lee, C. H. Lee, Y. M. Jung, S. I. Cheong, C. G. Lee, B. C. Ku, and S. P. Jang, “Stability and thermal conductivity characteristics of nanofluids,” *Thermochim. Acta*, vol. 455, no. 1–2, pp. 70–74, 2007.

[98] X. Wang, D. Zhu, and S. yang, “Investigation of pH and SDBS on enhancement of thermal conductivity in nanofluids,” *Chem. Phys. Lett.*, vol. 470, no. 1–3, pp. 107–111, 2009.

[99] X. F. Li, D. S. Zhu, X. J. Wang, N. Wang, J. W. Gao, and H. Li, “Thermal conductivity enhancement dependent pH and chemical surfactant for Cu-H2O nanofluids,” *Thermochim. Acta*, vol. 469, no. 1–2, pp. 98–103, 2008.

[100] Y. J. Hwang, Y. C. Ahn, H. S. Shin, C. G. Lee, G. T. Kim, H. S. Park, and J. K. Lee, “Investigation on characteristics of thermal conductivity enhancement of nanofluids,” *Curr. Appl. Phys.*, vol. 6, no. 6, pp. 1068–1071, 2006.

[101] L. Jiang, L. Gao, and J. Sun, “Production of aqueous colloidal dispersions of carbon nanotubes,” *J. Colloid Interface Sci.*, vol. 260, no. 1, pp. 89–94, 2003.

[102] D. Zhu, X. Li, N. Wang, X. Wang, J. Gao, and H. Li, “Dispersion behavior and thermal conductivity characteristics of Al2O3–H2O nanofluids,” *Curr. Appl. Phys.*, vol. 9, no. 1, pp. 131–139, 2009.

[103] M. N. Pantzali, A. A. Mouza, and S. V Paras, “Investigating the efficacy of nanofluids as coolants in plate heat exchangers (PHE),” *Chem. Eng. Sci.*, vol. 64, no. 14, pp. 3290–3300, 2009.

[104] M. J. Assael, I. N. Metaxa, J. Arvanitidis, D. Christofilos, and C. Lioutas, “Thermal Conductivity Enhancement in Aqueous Suspensions of Carbon Multi-Walled and Double-Walled Nanotubes in the Presence of Two Different Dispersants,” *Int. J. Thermophys.*, vol. 26, no. 3, pp. 647–664, 2005.

[105] J. Antonio, A. Júnior, and J. B. Baldo, “The Behavior of Zeta Potential of Silica Suspensions,” *New J. Glas. Ceram.*, vol. 4, pp. 29–37, 2014.

[106] H. Xie, H. Lee, W. Youn, and M. Choi, “Nanofluids containing multiwalled carbon nanotubes and their enhanced thermal conductivities,” *J. Appl. Phys.*, vol. 94, no. 8, pp. 4967–4971, 2003.

[107] H. Jia, Y. Lian, M. O. Ishitsuka, T. Nakahodo, Y. Maeda, T. Tsuchiya, T. Wakahara, and T. Akasaka, “Centrifugal purification of chemically modified single-walled carbon nanotubes,” *Sci. Technol. Adv. Mater.*, vol. 6, no. 6, pp. 571–581, 2005.

[108] E. Tang, G. Cheng, X. Ma, X. Pang, and Q. Zhao, “Surface modification of zinc oxide nanoparticle by PMAA and its dispersion in aqueous system,” *Appl. Surf. Sci.*, vol. 252, no. 14, pp. 5227–5232, 2006.

[109] N. S. Bell, A. L. Frischknecht, and M. Piech, “Grafted low molecular weight polymers as steric stabilizers of commercial titania nanoparticles in polydimethylsiloxane fluids,” *J. Dispers. Sci. Technol.*, vol. 32, no. 1, pp. 128–140, 2010.

[110] Z. Zhang, A. E. Berns, S. Willbold, and J. Buitenhuis, “Synthesis of poly(ethylene glycol) (PEG)-grafted colloidal silica particles with improved stability in aqueous solvents,” *J. Colloid Interface Sci.*, vol. 310, no. 2, pp. 446–455, 2007.

[111] B. Wang, J. Hao, and H. Li, “Remarkable improvements in the stability and thermal conductivity of graphite/ethylene glycol nanofluids caused by a graphene oxide percolation structure,” *Dalt. Trans.*, vol. 42, no. 16, pp. 5866–5873, 2013.

[112] M. Mehrali, E. Sadeghinezhad, S. T. Latibari, S. N. Kazi, M. Mehrali, M. N. B. M. Zubir, and H. S. C. Metselaar, “Investigation of thermal conductivity and rheological properties of nanofluids containing graphene nanoplatelets.,” *Nanoscale Res. Lett.*, vol. 9, no. 1, pp. 15, 2014.

[113] M. Mehrali, E. Sadeghinezhad, M. A. Rosen, A. Reza, S. Tahan, M. Mehrali, H. Simon, and C. Metselaar, “Heat transfer and entropy generation for laminar forced convection flow of graphene nanoplatelets nano fl uids in a horizontal tube,” *Int. Commun. Heat Mass Transf.*, vol. 66, pp. 23–31, 2015.

[114] Shanthi. R, “Heat transfer enhancement using nanofluids – an overview,” *Thermal science*, vol. 16, no. 2, pp. 423-444, 2012.

[115] D. H. Napper, “Polymeric stabilization of colloidal dispersions. Academic Press, London, 1984.

[116] S. Leikin and A. A. Kornyshev, “Theory of hydration forces . Nonlocal electrostatic interaction of neutral surfaces,” *J. Chem. Phys,*. vol. 6890, no. 1990, pp. 6890, 2016.

[117] W. Evans, J. Fish, P. Keblinski, W. Evans, and J. Fish, “Role of Brownian motion hydrodynamics on nanofluid thermal conductivity,” *Appl. Phys. lett.*, vol. 093116, no. 2006, pp. 2004–2007, 2016.

[118] R. Prasher, I. Corporation, W. Chandler, and V. Boule, “Effect of aggregation kinetics on the thermal conductivity of nanoscale colloidal solutions (nanofluid),” *Nano. Lett.*, vol. 6, pp. 8–12, 2006.

[119] P. Keblinski, S. R. Phillpot, S. U. S. Choi, and J. A. Eastman, “Mechanisms of heat flow in suspensions of nano-sized particles (nanofluids),” *Int. J. Heat. Mass. Tran.*, vol. 45, pp. 855–863, 2002.

[120] A. Kotia, S. Borkakoti, P. Deval, and S. Kumar, “Review of interfacial layer’s effect on thermal conductivity in nanofluid,” *Heat Mass Transf.*, vol. 53, no. 6, pp. 2199–2209, 2017.

[121] H. Han, S. Merabia, and F. Müller-plathe, “Thermal transport at a solid – nano fluid interface : shift of rapid boiling,” *Nanoscale*, pp. 8314–8320, 2017.

[122] W. Yu and S. U. S. Choi, “The role of interfacial layers in the enhanced thermal conductivity of nanofluids : A renovated Maxwell model,” *J. Nanopart. Res.*, pp. 167–171, 2003.

[123] L. Yang, X. Chen, M. Xu, K. Du, L. Yang, X. Chen, M. Xu, and K. Du, “Roles of surfactants and particle shape in the enhanced thermal conductivity of TiO2 nanofluids,” *Aip. Adv.*, vol. 6, pp. 095104, 2016.

[124] B.-X. Wang, L.-P. Zhou, and X.-F. Peng, “A fractal model for predicting the effective thermal conductivity of liquid with suspension of nanoparticles,” *Int. J. Heat Mass Transf.*, vol. 46, no. 14, pp. 2665–2672, 2003.

[125] N. R. Karthikeyan, J. Philip, and B. Raj, “Effect of clustering on the thermal conductivity of nanofluids,” *Mater. Chem. Phys.*, vol. 109, pp. 50–55, 2008.

[126] R. Prasher, W. Evans, P. Meakin, J. Fish, P. Phelan, and P. Keblinski, “Effect of aggregation on thermal conduction in colloidal nanofluids,” *Appl. Phys. Lett.*, vol. 89, no. 14, pp. 143119, 2006.

[127] C. T. Nguyen, F. Desgranges, N. Galanis, G. Roy, T. Maré, S. Boucher, and H. A. Mintsa, “Viscosity data for Al2O3 – water nanofluid — hysteresis : is heat transfer enhancement using nanofluids reliable ?,” *Int. J. Therm. Sci.*, vol. 47, pp. 103–111, 2008.

[128] C. T. Nguyen, S. Boucher, and H. A. Mintsa, “Temperature and particle-size dependent viscosity data for water-based nanofluids – Hysteresis phenomenon,” *Int. J. Heat. Fluid. Fl.*, vol. 28, pp. 1492–1506, 2007.

[129] Y. He, Y. Jin, H. Chen, Y. Ding, D. Cang, and H. Lu, “Heat transfer and flow behaviour of aqueous suspensions of TiO2 nanoparticles (nanofluids) flowing upward through a vertical pipe,” *Int. J. Heat. Mass. Tran.*, vol. 50, pp. 2272–2281, 2007.

[130] P. K. Namburu, D. K. Das, K. M. Tanguturi, and R. S. Vajjha, “Numerical study of turbulent flow and heat transfer characteristics of nanofluids considering variable properties,” *Int. J. Therm. Sci.*, vol. 48, no. 2, pp. 290–302, 2009.

[131] J. Chevalier, O. Tillement, and F. Ayela, “Rheological properties of nanofluids flowing through microchannels,” *Appl. Phys. Lett.*, vol. 91, no. 23, p. 233103, 2007.

[132] W.-Q. Lu and Q.-M. Fan, “Study for the particle’s scale effect on some thermophysical properties of nanofluids by a simplified molecular dynamics method,” *Eng. Anal. Bound. Elem.*, vol. 32, no. 4, pp. 282–289, 2008.

[133] K. B. Anoop, S. Kabelac, T. Sundararajan, and S. K. Das, “Rheological and flow characteristics of nanofluids: Influence of electroviscous effects and particle agglomeration,” *J. Appl. Phys.*, vol. 106, no. 3, pp. 034909, 2009.

[134] E. V Timofeeva, A. N. Gavrilov, J. M. Mccloskey, Y. V Tolmachev, S. Sprunt, L. M. Lopatina, and J. V Selinger, “Thermal conductivity and particle agglomeration in alumina nanofluids : Experiment and theory,” *Phys. Rev. E. Stat Nonlin. Soft. Matter. Phys.*, pp. 28–39, 2007.

[135] S. Ferrouillat, A. Bontemps, O. Poncelet, O. Soriano, and J. A. Gruss, “Influence of Nanoparticle Shape Factor on Convective Heat Transfer of Water-Based ZnO Nanofluids . Performance Evaluation Criterion,” *Int. J. Mecha. Indust. Engi.*, no. 2231, pp. 7–13, 2011.

[136] R. Prasher, D. Song, J. Wang, P. Phelan, R. Prasher, D. Song, J. Wang, and P. Phelan, “Measurements of nanofluid viscosity and its implications for thermal applications Measurements of nanofluid viscosity and its implications,” *Appl. Phys. Lett.*, vol. 133108, no. 2006, pp. 1–4, 2009.

[137] S. K. Das, N. Putra, and W. Roetzel, “Pool boiling characteristics of nano-fluids,” *Int. J. Heat Mass Transf.*, vol. 46, no. 5, pp. 851–862, 2003.

[138] W. Duangthongsuk and S. Wongwises, “Measurement of temperature-dependent thermal conductivity and viscosity of TiO2 -water nanofluids,” *Exp. Therm. Fluid Sci.*, vol. 33, no. 4, pp. 706–714, 2009.

[139] A. J. Schmidt, M. Chiesa, D. H. Torchinsky, J. A. Johnson, A. Boustani, G. H. McKinley, K. A. Nelson, and G. Chen, “Experimental investigation of nanofluid shear and longitudinal viscosities,” *Appl. Phys. Lett.*, vol. 92, no. 24, pp. 244107, 2008.

[140] M. Chandrasekar, S. Suresh, and A. C. Bose, “Experimental investigations and theoretical determination of thermal conductivity and viscosity of Al2O3/water nanofluid,” *Exp. Therm. Fluid Sci.*, vol. 34, no. 2, pp. 210–216, 2010.

[141] H. Chen, Y. Ding, and C. Tan, “Rheological behaviour of nanofluids,” *New J. Phys.*, vol. 9, no. 10, pp. 367–367, 2007.

[142] F. Duan, D. Kwek, and A. Crivoi, “Viscosity affected by nanoparticle aggregation in Al2O3-water nanofluids,” *Nanoscale. Res. Lett.*, vol. 6, pp. 248, 2011.

[143] S. Harikrishnan and S. Kalaiselvam, “Experimental investigation of solidification and melting characteristics of nanofluid as pcm for solar water heating systems,” *Int. J. Eng. Tech. Adv. Eng.*, vol. 3, pp. 628–635, 2013.

[144] S. Wu, D. Zhu, X. Zhang, and J. Huang, “Preparation and melting/freezing characteristics of Cu/Paraffin nanofluid as phase change material (PCM),” *Energy & Fuels*, vol. 24, no. 3, pp. 1894–1898, 2010.

[145] A. Karaipekli and A. Sarı, “Capric – myristic acid / vermiculite composite as form-stable phase change material for thermal energy storage,” *Sol. Energy*, vol. 83, no. 3, pp. 323–332, 2009.

[146] A. Karaipekli, A. Sarı, and K. Kaygusuz, “Thermal conductivity improvement of stearic acid using expanded graphite and carbon fiber for energy storage applications,” vol. 32, pp. 2201–2210, 2007.

[147] C. J. Ho and J. Y. Gao, “Preparation and thermophysical properties of nanoparticle-in-paraf fi n emulsion as phase change material,” *Int. Commun. Heat Mass Transf.*, vol. 36, no. 5, pp. 467–470, 2009.

[148] J. Wang, H. Xie, and Z. Xin, “Thermal properties of paraffin based composites containing multi-walled carbon nanotubes,” *Thermochim. Acta*., vol. 488, pp. 39–42, 2009.

[149] S. Zhou and R. Ni, “Measurement of the specific heat capacity of water-based Al2O3 nanofluid,” *Appl. Phys. Lett.*, vol. 093123, pp. 2006–2009, 2008.

[150] C. Link, H. O. Hanley, J. Buongiorno, T. Mckrell, and L. Hu, “Measurement and model validation of nanofluid specific heat capacity with differential scanning calorimetry” *Adv. Mech. Eng.*, vol. 2012. 2018.

[151] S. Okawa, A. Saito, and R. Minami, “The solidification phenomenon of the supercooled water containing solid particles,” *Int. J. Refrig.*, vol. 24, pp. 108–117, 2001.

[152] S. Wu, D. Zhu, X. Li, H. Li, and J. Lei, “Thermal energy storage behavior of Al2O3–H2O nanofluids,” *Thermochim. Acta*, vol. 483, no. 1–2, pp. 73–77, Feb. 2009.

[153] V. Kumaresan, P. Chandrasekaran, M. Nanda, A. K. Maini, and R. Velraj, “Role of PCM based nanofluids for energy efficient cool thermal storage system,” *Int. J. Refrig.*, vol. 36, no. 6, pp. 1641–1647, 2013.

[154] Q. He, S. Wang, M. Tong, and Y. Liu, “Experimental study on thermophysical properties of nanofluids as phase-change material (PCM) in low temperature cool storage,” *Energy Convers. Manag.*, vol. 64, pp. 199–205, 2012.

[155] J. Ivall, M. Hachem, S. Coulombe, and P. Servio, “Behavior of surface-functionalized multiwall carbon nanotube nano fluids during phase change from liquid water to solid ice,” *Cryst. Growth. Des.*, vol. 15. pp. 3969-3982, 2015.

[156] B. J. Murray, S. L. Broadley, T. W. Wilson, S. J. Bull, R. H. Wills, H. K. Christenson, and E. J. Murray, “Kinetics of the homogeneous freezing of water,” *Phys. Chem. Chem. Phys.*, pp. 10380–10387, 2010.

[157] J. Pasieka, R. Nanua, S. Coulombe, and P. Servio, “The crystallization of sub-cooled water : Measuring the front velocity and mushy zone composition via thermal imaging,” *Int. J. Heat Mass Transf.*, vol. 77, pp. 940–945, 2014.

[158] P. Chandra and M. Sayantan, “A brief review on viscosity of nanofluids,” *Int. Nano. Lett.*, pp. 109–120, 2014.

[159] J. J. Stickel and R. L. Powell, “Fluid Mechanics and Rheology of Dense Suspensions,” *Annu. Rev. Fluid Mech.*, vol. 37, no. 1, pp. 129–149, 2005.

[160] S. Özerinç, S. Kakaç, and A. G. Yazıcıoğlu, “Enhanced thermal conductivity of nanofluids: a state-of-the-art review,” *Microfluid. Nanofluidics*, vol. 8, no. 2, pp. 145–170, 2009.

[161] E. V Timofeeva, J. L. Routbort, D. Singh, E. V Timofeeva, J. L. Routbort, and D. Singh, “Particle shape effects on thermophysical properties of alumina nanofluids,” *J. Appl. Phys.*, vol. 014304, no. 2009, 2013.

[162] C. Nan, Z. Shi, and Y. Lin, “A simple model for thermal conductivity of carbon nanotube-based composites,” *Chem. Phys. Lett.*, vol. 375, pp. 666–669, 2003.